Dissertation
zur Erlangung des Doktorgrades
der Naturwissenschaften

vorgelegt beim Fachbereich 14
der Johann Wolfgang Goethe -Universität
in Frankfurt am Main

von
Christoph Kaiser
aus Hanau
Frankfurt 2009

Improving methods for the study of membrane proteins by solid-state NMR

vom Fachbereich 14 der Johann Wolfgang Goethe - Universität als Dissertation angenommen.

Dekan: Prof. Harald Schwalbe
Gutachter : Prof. Clemens Glaubitz
Datum der Disputation :

Diese Doktorarbeit wurde von Prof. Dr. Clemens Glaubtiz betreut und in der Abteilung Membranbiophysik und Festkörper NMR des Instituts für biophysikalische Chemie der Johann Wolfgang Goethe Universität Frankfurt am Main durchgeführt.

Be excellent to each other

Bill & Ted

Contents

Abbreviations

ADP	Adenosine Diphosphate
AHT	Average Hamiltonian Theory
ATP	Adenosine Triphosphate
ATR-IR	Attenuated Total Reflection Infrared
BR	Bacteriorhodopsin
CDP	Cytosine Diphosphate
CL	Cardiolipine
CP	Cross Polarization
CS	Chemical Shift (always relative to TMS at 4°C)
CSA	Chemical Shift Anisotropy
CW	Continuous Wave
Da	Dalton
DAG	Diacylglycerol
DGK WT	Diacylglycerol Kinase
DM	n-Dodecyl-β-D-Glucopyranoside
DOAM	Double quantum filtering After Mixing
DOPC	Dioleoylphosphatidylcholine
DOPE	DOuble quantum filtering Prior to Evolution
DPC	Dodecylphosphocholine
DQC	Double Quantum Coherence
DTD	Dual Transforation Denoising
DTT	Dithiothreitol
EDTA	Ethylendiamintetraacetate
FID	Free Induction Decay
FSLG	Frequency Switched Lee-Goldburg
FT-IR	Fourier Transform Infrared
HEAT	Half Echo Alternating Transformation
IPTG	Isopropyl-β-D-thiogalactoside
IST	Irreducible Spherical Tensor
LB	Luria Broth
MAS	Magic Angle Sample Spinning
MDO	Membrane Derived Oligosaccharides
NADH	Nicotinamide Adenine Dinucleotide
Ni-NTA	Nickel-Nitrilotriacetate
NMR	Nuclear Magnetic Resonance
OD	Optical Density
OG	n-Octyl-β-D-Glucopyranoside
PAS	Principal Axis System
PDSP	Proton Driven Spin Diffusion
PE	Phosphoethanolamine
PG	Phosphoglycerine
PMLG	Phase Modulated Lee-Goldburg

POPC	Palmitoyloleoylphosphatidylcholine
ppm	Parts per Million
RELOAD	Relaxation Enh. by Lower Overall Adjacent Spin Temp. Distrib.
RF	Radio Frequency
RT	Room Temperature
S/R	Signal to Noise
SDS	Natriumdodecylsulfate
SDS-PAGE	SDS-Polyacrylamidgelelekrophorese
SW	Single Quantum
SQC	Single Quantum Coherence
TEMED	N,N,N',N'-Tetramethylene Diamine
TMS	Tetramethylsilane
TPPM	Two Phase Pulse Modulation
TROSY	Transverse Relaxation Optimized Spectroscopy
UV/VIS	Ultraviolet / Visible Spectrum
V / V	Volume per Volume
W / V	Weight per Volume

Abstract

Solid state NMR (ssNMR) is an emerging technique for the study of biological samples. It has been used on a variety of different molecules, ranging from ligands of low molecular weight, over lipid molecules up to large transmembrane protein complexes. The advantages of ssNMR are many fold: it is possible to study molecules in a variety of states, as ssNMR is not limited by the rotation correlation time of the sample under investigation. Even more useful are the properties of ssNMR in combination with magic angle spinning (MAS). Here, the sample is rapidly spun around an angle of 54.7° relative to the outside magnetic field. For this angle the anisotropic interactions of the nuclei are zero. Using specialized pulse sequences, it is possible to recouple certain selected parts of the nuclear Hamilton operator, which would normally vanish under MAS. These so called combined rotation and multi pulse sequences (CRAMPS) offer the unique possibility to tailor the Hamiltonian to a form desirable for the experiment in question. Thus it is possible to, for instance, allow evolution of the spin system under the influence of the homonuclear dipolar coupling, for a certain time during the experiment, to obtain very precise distance measurements through space. Subsequently, the dipolar coupling can be removed during acquisition, allowing for high resolution spectra to be obtained.

A potential problem with the approach outlined above is that, although the different nuclear interactions can be suppressed to a high degree, they cannot be fully eliminated, without the use of excessive radio frequency (RF) power levels. Therefore certain experiments, such as ^{1}H detected sequences cannot usually be implemented in the solid state, as the residual interactions lead to broad spectral lines, compared to solution state NMR. This necessitates the use of low γ nuclei, which feature nuclear interactions of reduced magnitude, and the application of multidimensional experiments, to overcome spectral overlap.

These factors, together with the special properties of biological samples in the solid state, which usually feature a range of different structural sub populations, leading to inhomogeneous line broadening, results in an overall low sensitivity of ssNMR experiments. Corroborating these problems are technical requirements of the MAS-NMR setup, which do not allow for probe sensitivities usually obtained with solution state NMR hardware.

The net result are excessively long measuring times, especially if experiments of higher dimensionality are desired.

To address these problems a variety of different approaches was investigated to optimize solid state NMR spectroscopy on biological samples.

For shortening the time needed to recover magnetization until a given experiment can be conducted anew, the RELOAD (Relaxation Enhancement by Lower Overall Adjacent spin temperature Distribution) experiment is introduced, which is a technique utilizing unused magnetization in a band selective experiment. By decreasing the time needed between two successive scans the sensitivity per unit time is increased.

Next, for hetero-nuclear transfer, the symmetry based, hetero-nuclear, through bond polarization transfer sequence $R70_{6}^{16,16}$ is presented, which features reduced pref-

erence for a certain motional regime, as compared to the classical polarization transfer schemes, cross polarization and INEPT.

Furthermore the DOPE (Double quantum filtering Prior to Evolution) and DOAM (DOuble quantum filtering After Mixing) experiments are demonstrated, which are used to eliminate the strong contribution of natural abundance background to the diagonal of a homo-nuclear correlation experiment. This is especially useful for samples, in which a small isotope labeled molecule is to be observed in presence of a large number of unlabeled compounds.

During detection the HEAT (Half Echo Alternating Transformation) scheme is introduced, which can be used to enhance the signal for samples, for which T_2^* is lower than T_2, by the acquisition and addition of spin echos.

For processing DTD (Dual Transformation Denoising) is demonstrated. This scheme uses the properties of two different methods of transformation from the time to the frequency domain, fast Fourier transform (FFT) and covariance, to reduce spectral noise and eliminate truncation artifacts from single quantum homo-nuclear correlation spectra.

Finally, the effect of different labeling schemes and reconstitution protocols on the spectral quality of the integral membrane protein diacylglycerol kinase is demonstrated. Furthermore the methods outlined above are applied to this sample, if applicable (for instance, if the signal of this sample is usually strong relative to the lipid background, the application of DOPE or DOAM is unnecessary).

Zusammenfassung

Festkörper-Kernmagnetische Resonanzspektroskopie (im Folgenden auch als solid state NMR oder ssNMR bezeichnet) ist eine Methode die sich in den letzten Jahren rapide weiterentwickelt hat. Sie wurde erfolgreich sowohl zur Untersuchung von anorganischen Substanzen als auch für Strukturstudien an Proteinen, die entweder als Mikrokristalle [1–10], Fibrillen [11–15] oder in eine Membran rekonstituiert [16–20] vorlagen, eingesetzt.

Ein einzigartiger Vorteil von ssNMR liegt darin, das über Methoden wie magic angle spinning (MAS) und/oder bestimmte Radiofrequenz (RF) Pulsfolgen spezifische Interaktionen zwischen den Kernen ent-, aber auch rückgekoppelt werden können. Dies kann dazu benutzt werden, bestimmte Interaktionen für z.B. den Transfer von Magnetisierung zu nutzen, sie aber während der Aufnahme des Signals zu unterbinden, da sie dort die Auflösung negativ beeinflussen würden.

Obwohl diese Möglichkeiten sehr nützlich sind, treten in der Praxis jedoch oft Probleme auf, die die Auswertung der gewonnenen Spektren verkomplizieren.

Die nützlichsten Interaktionen, die man mittels der ssNMR beobachten kann, die anisotropen Kernspininteraktionen, stellen hierbei zugleich die grössten Herausforderungen. Während es möglich ist, die Interaktionen der Kerne untereinander weitestgehend zu unterdrücken, gelingt dies jedoch nie ganz. Dies führt wiederum zu Termen im Kernspinhamiltonoperator, die eine homogene Linienverbreiterung zur Folge haben. Das Resultat sind oft signifikante Überschneidungen der Resonanzen im Spektrum.

Die Notwendigkeit, bestimmte Kernspininteraktionen zu unterdrücken impliziert des weiteren, das die Probe während der Messung starken RF Feldern ausgesetzt ist. Dies kann zu einer Erwärmung der Probe führen, im Speziellen, wenn ein salzhaltiger Puffer verwendet wurde, wie es oft bei Proteinproben der Fall ist.

Das Einfrieren der Probe beseitigt dieses Problem, hat aber wiederum den Nachteil, das es zu einer inhomogenen Linienverbreiterung kommt, wenn die Probe mehrere energetisch ähnliche Konformationen besitzt, die unter normalen Umständen bei Raumtemperatur in schnellem Austausch miteinander stehen.

Speziell betroffen von diesen Effekten sind die ^1H Kerne, die nicht nur die stärksten Kerninteraktionen zeigen, was durch ihr hohe γ bedingt ist, sondern auch eine geringe Bandbreite an chemischen Verschiebungen aufweisen. Dies macht ^1H ungeeignet für eine direkte Detektion in der ssNMR.

Daraus resultiert, das die Sensitivität deutlich niedriger ist, als in der Lösungs NMR, da nur Kerne mit vergleichsweise niedrigem γ detektiert werden können. Aber auch hier tragen anisotrope Kerninteraktionen, wie zum Beispiel die homo- und heteronukleare Dipol-Dipol Kopplung und chemische Verschiebungsanisotropie zu einer Linienverbreiterung bei, so das die Sensitivität in der Regel eingeschränkt ist.

In Fällen, in denen die Probenmenge limitiert ist, kann dies zu extrem langen Messzeiten von mehreren Tagen bis Wochen führen.

Das Problem der mangelnden spektralen Auflösung durch Linienverbreiterung kann zwar durch höherdimensionale Spektroskopie behoben werden, allerdings nur zum

Preis von noch längeren Messzeiten.

Ein weiteres Problem bei der Untersuchung von biologischen Proben, ist deren oft sehr eingeschränkte Verfügbarkeit und Lebensdauer, die zusammen mit den oben genannten Kompikationen bestimmte Experimente nur mit grossen Mühen durchführbar macht.

Um solche Proben erfolgreich mittels ssNMR untersuchen zu können, muss die Sensitivität der Messungen drastisch gesteigert werden. In der vorliegenden Arbeit werden mehrere Ansätze vorgestellt, deren Ziel es ist, die Sensitiviät pro Zeiteinheit von ssNMR Experimenten zu steigern.

Hierbei ist es wichtig zu unterscheiden, ob die Messzeitverkürzung durch eine echten Gewinn an Signal pro Zeiteinheit geschieht, oder nur Signal gegen Messzeit eingetauscht wird, so wie es bei vielen Methoden in der Lösungs NMR der Fall ist. Bei dieser Art der Spektroskopie ist dieses Vorgehen oft sinnvoll, da die gemessenen Signale oft sehr stark sind. Bei der ssNMR ist ein solcher Ansatz, bis auf Ausnahmen, zum Scheitern verurteilt, da ssNMR Experimente nahezu ausnahmslos durch ihre Sensitivität limitiert sind.

Um einen echten Gewinn an Sensitivität zu erreichen, wurden die einzelnen Phasen eines mehrdimensionalen NMR Experimentes untersucht, bezüglich der Optimierungsmöglichkeiten.

Ein konventionelles, zweidimensionales NMR Experiment wird in vier Phasen unterteilt: Präparation, Evolution, Mischen und Detektion.

In der Präparationsphase wird die Polarisation der Kernspins in die transversale Ebene gebracht, oft nach einem Magnetisierungstransfer zwischen Kernen mit einem unterschiedlichen γ.

Während der Evolution wird zumeist die spektrale Information über die chemische Verschiebung in der indirekten Dimension aufgezeichnet, wobei auch andere Interaktionen codiert werden können, abhängig von der Pulssequenz.

Im Mischschritt werden Korrelationen hergestellt, oft unter Zuhilfenahme der homo- oder heteronuklearen Dipol-Dipol Kopplung oder der J-Kopplung.

Bei der Detektion schliesslich wird das resultierende Signal in Form eines free induction decay (FID) aufgezeichnet. Um die Analyse der Spektren zu erleichtern, folgt hierauf oft eine Fouriertransformation in einer oder mehrerer Dimensionen.

In der vorliegenden Arbeit werden mehrere Methoden vorgestellt, die während dieser Phasen wirken.

Wie eingangs erwähnt, ist die Präparationsphase zu einem grossen Teil für die Sensitivtät der Messung verantwortlich. Es gibt deshalb auch viele Methoden, die während der Präparationsphase wirken, wie z.B. Kreuzpolarisation [21] oder INEPT [22]. Hierbei wird Polarisation von einer Kernspezies mit hohem γ auf eine mit niedrigem γ übertragen, was bei einem Transfer von ^1H zu ^{15}N einen Faktor von zehn ausmacht. Dies resultiert in einer um 100 niedrigeren Messzeit.

Die Methode, die in der vorliegenden Arbeit vorgestellt wird, bedient sich eines anderen Mechanismus, um die Messzeit zu verkürzen.

RELOAD (Relaxation Enhancement by Lower Overall Adjacent spin temperature Distribution) setzt nicht die heteronukleare, sondern die homonukleare Dipol-Dipol Kopplung ein, aus der eine sog. Spindiffusion resultiert.

Die Methode basiert auf der Beobachtung, das es viele Experimente gibt, bei denen nur ein Teil der Kernspins als Informationsträger relevant ist. Dies ist zum Beispiel in vielen heteronuklearen Korrelationsexperimenten, aber auch in bandselektiven homonuklearen Korrelationsexperimenten der Fall .

In der RELOAD Adaption dieser Experimente wird zuerst eine konventionelle heteronukleare Magnetisierungstransfermethode, z.B. Kreuzpolarisation, eingesetzt, die die Polarisation aller Heterokerne erhöht, ungeachtet ob diese Kerne im gegebenen Experiment Informationsträger sind oder nicht.

Das eigentliche Korrelationsexperiment wird dann bandselektiv durchgeführt, wobei darauf geachtet wird, die Kernspins ausserhalb der zu erforschenden Regionen des Spektrums (der region of interest (ROI)) möglichst ungestört auf der z-Achse des rotierenden Koordinatensystems zu belassen.

Nachdem das Experiment durchgeführt wurde und er FID aufgezeichtnet ist, wird eine kurze Zeit gewartet, um dem Spinsystem zu erlauben, sich über Spindiffusion zu equilibrieren. Hierbei fliesst Polarisation von den nicht detektierten Kernen in die ROI. Danach wird das Experiment erneut ausgeführt, jedoch ohne den heteronuklearen Polarisationstransferschritt.

Wie im Kapitel 3 gezeigt werden wird, ist es dadurch möglich, die Einzelexperimente wesentlich schneller zu wiederholen, solange die Kernspins ausserhalb der ROI noch signifikant polarisiert sind. Nachdem diese Polarisation verbraucht ist, wird dem Experiment wieder ein heteronuklearer Magnetisierungstransfer, zusammen mit einer längeren Relaxationsphase für die ^1H Kerne vorgeschaltet.

Es resultiert also eine äussere Schleife mit heteronukelarem Transfer, die äquivalent zum konventionellen Experiment ist, in der eine innere Schleife ausgeführt wird, bei der die ROI nur durch die Residualmagnetisierung der Sie umgebenden Kernspins polarisiert wird.

Diese Methode wird mittels Inversion Recovery Experimenten an einem Peptid charakterisiert und der Einfluss von verschiedenen experimentellen Faktoren untersucht. Des weiteren werden bandselektive homo- und heteronukleare Korrelationsexperimente eingeführt, die sich den RELOAD Effekt zu nutze machen und der Gewinn an Sensitivität gegenüber der Ursprungsexperimente bestimmt, wiederum unter verschiedenen experimentellen Bedingungen.

Wie bereits erwähnt, eignet sich RELOAD zur Durchführung von homo- sowie heteronuklearen Festkörperkorrelationsexperimenten.

In der Mischphase des Experiments werden Korrelationen zwischen den Resonanzen im Spektrum aufgebaut, und somit ein Grossteil der spektralen Information kodiert. Unglücklicherweise wird die Analyse dieser Informationen oft durch den Einfluss der Eigendynamik der Probe erschwert, da es zu Interferenzeffekten zwischen den RF Feldern und der Bewegung der Probe, aber auch zu einer allgemeinen Skalierung der benötigten Interaktionen kommen kann.

Dies gilt im Besonderen für Membranproteine, die in halbfester, gelartiger membranrekonsituierter Form gemessen werden sollen. Hier werden zum Teil die Dipolinteraktionen so stark skaliert, das ein Polarisationstransfer mittels Kreuzpolarisation so gut wie unmöglich wird.

Um diesen Effekt auf den Polarisationtransfer zu unterbinden, wurde ein heteronuklearer Polarisationstransfer gesucht, der sich die J-Kopplung zu Nutze macht, aber gleichzeitig insensitiv gegenüber residualen Dipolkopplungen ist. Dies ist speziell für integrale Membranproteine interessant, da dort die Loopdomänen eine signifikant höhere Dynamik aufweisen können als die Transmembrandomänen.

Zu diesem Zweck wurden die Symmetrieprinzipien benutzt, die von Carravetta und Levitt [23] eingeführt wurden, und von Brinkmann [24] auf mehrere Kanäle erweitert wurden.

Diese erlauben eine sehr feine Kontrolle über den effektiven Kernspinhamiltonoperator.

Um einen effektiven Polarisationstransfer zu gewährleisten, wurde ein solcher Hamiltonoperator gesucht, in dem die homo- und heteronukleare Dipolwechselwirkung zu einer möglichst hohen Ordnung unterdrückt werden, die heteronukleare J-Kopplung aber erlaubt ist.

Zu diesem Zweck wurden numerische Simulationen und Experimente verwendet um die beste Kombination aus allen, theoretisch möglichen Symmetrienummern zu finden.

Die daraus resultierende Sequenz wird optimalerweise für einen ^1H zu ^{13}C oder ^{15}N Transfer eingesetzt, kann aber auch für einen ^{13}C zu ^{15}N Transfer benutzt werden.

Nicht die Sensitivtät, sondern die Auflösung steht im Fokus einer weiteren Methode, die in dieser Arbeit vorgestellt wird. Die DOAM (Double quantum filtering After Mixing) und DOPE (DOuble quantum filtering Prior to Evolution) Sequenzen werden im Kapitel 5 erläutert und führen einen zusätzlichen Doppelquantenfilter in ein homonukleares Einzelquantenkorrelationsexperiment ein.

Die Motivation hierbei entstand aus Beobachtungen bei der Messung von kleinen, pharmakologisch relevanten Substanzen heraus.

Eine wichtige Fragestellung ist die Interaktion zwischen einem kleinen Wirkstoffmolekül und einer Membran oder einem Membranprotein. Ist hierbei nur das Wirkstoffmolekül markiert, können dessen Signale, speziell nahe der Diagonalen des Spektrums, leicht von der natürlichen Häufigkeit z.B. der Membranlipide überdeckt werden. Des weiteren erschweren zusätzliche Resonanzen auf der Diagonalen die Auswertung von homonuklearen Korrelationsspektren durch den full matrix approach [25].

Die Verbesserung in der Auflösung, die durch DOPE und DOAM erziehlt werden können, werden in Kapitel 5 diskutiert, und es wird gezeigt, das die Qualität der Spektren durch den zusätzlichen Filter nicht beeinträchtigt wird.

In der ssNMR ist die Unterdrückung von anisotropen Kernspininteraktionen oft unvollständig. Besonders in echten Festkörpern kann dies zu transversalen Relaxationszeiten führen, die im Vergleich zur Lösungs-NMR sehr kurz sind (1-50 ms im Vergleich zu 100-1000 ms).

Dennoch kann die eigentliche, wesentlich langsamere T_2 Zeit durch eine Folge von 180° Pulsen gemessen werden. Dieses Experiment heisst Carr-Purcell Meiboom-Gill (CPMG) [26]. Hierbei werden nur die Maxima der Echos gemessen, um die Einhüllende der T_2 Relaxation zu erhalten.

Aber diese Echos können nicht nur zur Differenzierung von T_2 und T_2^* genutzt werden, sondern auch um die Sensitivität des Experimentes zu erhöhen, die, genau wie die Auflösung, negativ durch T_2^* beeinflusst wird.

Bei der HEAT (Half Echo Alternating Transformation) Methode werden die, sich durch die Folge von 180° Pulsen ergebenen, Echos aufgezeichnet und nach der Signalaquisition in Einzel-FID's zerlegt.

Nachdem jedes zweite Halbecho zeitinvertiert wurde, werden alle Echos addiert, um einen Teil der Intensität zurückzugewinnen, der durch die T_2^* Relaxation verloren gegangen ist.

Leider ist es mittels dieser Methode jedoch nicht möglich, die Auflösung gegenüber dem Ursprungsspektrum zu verbessern, da die Linienbreite der Einzel-FID's immer noch durch T_2^* gegeben ist.

DTD (Dual Transformation Denoising) ist eine Methode zum Prozessieren von Daten, die die Eigenschaften von FFT und Kovarianz kombiniert und in Kapitel 7 vorgestellt wird.

Kovarianz wurde zuerst von Brüschweiler et al. in der NMR eingesetzt [27, 28] um die Messzeit von NMR Experimenten zu verkürzen.

Hierbei werden zweidimensionale NMR Experimente in der direkten Dimension mit FFT und in der indirekten Dimension mit Kovarianz prozessiert, was in einer Verminderung von Artefakten resultiert, die bei der Fouriertransformation von kurzen Zeitreihen auftreten.

Es kann hierbei aber zu falschpositiven Signalen kommen, die durch eine Multiplikation mit dem ganz FFT prozessierten Spektrum aber gut unterdrückt werden können (W. Bermel unveröffentlichte Ergebnisse).

In Kapitel 7 wird eine weitere Eigenschaft der Kombination von FFT mit Kovarianz untersucht, das unterschiedliche Verhalten beider Methoden bei der Transformation von weissem Rauschen. Es wird sowohl an synthetischen als auch experimentellen Datensätzen gezeigt, das es durch die Kombination von FFT und Kovarianz

möglich ist, einen Teil des Rauschens zu unterdrücken, wobei die positiven Eigenschaften bezüglich der Unterdrückung von Schnittartefakten erhalten bleiben.

Des weiteren wird eine Methode vorgestellt, die es ermöglicht, Aufbaukurven unter Benutzung von DTD zu messen.

Ausser spektroskopischen Methoden haben noch die Art der Probenpräparation und des Markierungsschemas einen grossen Einfluss auf die Qualität von NMR Spektren.

Um die Effekte zu untersuchen, die verschiedene Präparationsmethoden auf die Auflösung und Sensitivität von Festkörper-NMR Spektren haben, wurde das integrale α-helikale Membranprotein Diacylglycerol Kinase (DGK) unter Verwendung von verschiedenen Rekonstitutionsmethoden und Markierungsschemata präpariert.

Wie in Kapitel 8 gezeigt, weist DGK eine starke Dynamik auf, so denn die Probe nicht gefroren ist. Dies führt, wie oben erwähnt zu Interferenzproblemen während der Messung.

Der Effekt der Probentemperatur auf die Dynamik in den Loop- und Transmembrandomänen wird untersucht, sowie deren Einfluss auf verschiedene, häufig in der ssNMR angetroffene Pulsesequenzen.

Es werden Alternativen zu etablierten Methoden vorgeschlagen, die bei einer Probe von der Dynamik von DGK einen höheren Wirkungsgrad erziehlen, wie z.B. das Ersetzen von Kreuzpolarisation durch den heteronuklearen Overhauser Effekt, oder die Benutzung von TOBSY gegenüber PDSD, so denn es nur um die Zuordnung von Aminosäuren geht.

Des weiteren werden die Methoden, die bislang in dieser Arbeit vorgestellt wurden auf DGK angewandt, sofern dies plausibel ist.

Die Methoden zur Sensitivitätserhöhung, die in dieser Arbeit vorgestellt werden, können in vielen Fällen kombiniert werden, und es ist somit möglich, die Messzeit für bestimmte ssNMR Experimente signifikant zu verringern, speziell wenn es sich um höherdimensionale Experimente handelt.

Dies könnte dazu beitragen, ssNMR Untersuchungen auch an schwierigen Proben zu ermöglichen.

Chapter 1

Introduction

Structural studies of membrane proteins is of great interest for biologists, biochemists and biophysicists alike. Their wide variety of properties and functions is at the same time of great biological relevance and can give insight into the molecular mechanisms of many phyisologic processes.

The function, or non-function of certain membrane proteins can lead to severe diseases. For example the integral membrane protein Cystic Fibrosis Mediating Factor (CFMF) plays a central role in the pathogenesis of cystic fibrosis, P-Glycoprotein (PGP) is discussed as a cause for resistance in cancer cells to chemotherapy, the prion protein PrP is presumed to be at least membrane associated during one stage of its existence and the B2 receptor plays a key role in pain reception. Similar to the examples above there are many integral membrane proteins, which play central roles in severe diseases. Therefore knowledge about these targets is of scientific, as well as commercial interest.

Despite their great relevance, relatively little structural data is available on membrane proteins, as compared to their soluble counterparts. The reason for this are the unique challenges one faces, if 3D structural data of membrane proteins is to be elucidated. These challenges arise firstly from the high efforts needed for the biochemical preparation of most membrane proteins, which ultimately results in a very limited availability of sample. This poses a severe limit to both NMR, as well as x-ray spectroscopy, which are the two main methods used for structural studies on biological samples. Furthermore, for x-ray crystallography, the unique physical properties of membrane proteins complicate the crystallization process, often leading to an insufficient resolution of the resultant diffraction pattern.

The problems one faces in NMR have different origins, though are no less severe. The exact nature of these complications depends on the particular flavor of NMR which is chosen for the study. In solution state NMR for example, the properties of most membrane proteins dictate, that they cannot be brought into solution, without some sort of membrane mimetic environment. Here certain types of detergents like DDM or LPPG are chosen to overcome this limitation. Still, the large size of the resultant protein-micelle complex often leads to very long rotation correlation times. These negatively influence the sensitivity and resolution of the resultant solution state NMR spectra, often to the point, where only little structurally relevant data can be extracted.

In solid state NMR on the other hand, the rotation correlation time plays no significant role, and therefore the membrane proteins can be studied in their natural environments, or at least in membranes with a close resemblance and has therefore seen rapid development in recent years. Solid state NMR was successfully applied to the study of inorganic compounds, as well as for structural investigations of proteins

in a micro crystalline [1–10] , fibrillar [11–15] or membrane reconstituted state [16–20]. Solid state NMR, in combination with techniques such as magic angle spinning (MAS) and/or certain radio frequency (RF) irradiation schemes, furthermore possesses the unique advantage that a selection of the interactions, which act on the spin system can be achieved. For instance it is possible to use the homo- and hetero-nuclear dipolar couplings as mediators of long range, through space polarization transfer, and then remove some or all of these interactions during detection, yielding a well resolved set of signals during acquisition.

For this type of NMR spectroscopy, the primary source of the complications is at the same time one of its greatest strengths: anisotropic interactions, like the anisotropic chemical shift and the homo-nuclear and hetero-nuclear dipole-dipole coupling.

While providing a great deal of information, if the experiment is designed to take advantage of these interactions, they can lead to significant relaxation, resulting in severely homogeneously broadened spectral peaks.

Although it is possible to suppress the interactions of the nuclear spins to a certain degree, this suppression is by no means perfect. These interactions lead to residual terms in the nuclear spin Hamiltonian, which in turn lead to homogeneous line broadening, resulting in severe spectral overlap in the spectra.

The need for decoupling of strong nuclear interactions also implies continual irradiation of the sample with strong RF fields, during most experiments. This results in considerable heating effects in samples containing water and ions, such as most protein preparations.

Freezing these samples mostly eliminates this problem, but often leads to new complications, when multiple conformations of the sample are frozen out, which would normally inter-convert rapidly at room temperature.

This sample order problem leads to severe inhomogeneous line broadening which due to the slightly different chemical environments of the constituent atoms of various conformations coexistent in the frozen sample. This effect further enlarges the already broad spectral resonances. The overlap caused by the combination of these phenomena often results in a spectrum, where the individual resonances merge and therefore important structural information is obscured. Furthermore the sensitivity is negatively impacted by the very large (in-) homogenous linewidths.

Especially affected by these effects are the ^{1}H spins, which feature not only the strongest internuclear interactions, but also a narrow chemical shift dispersion, making direct proton detection unfeasible in solid state NMR.

Therefore the low sensitivity, caused by the need to detect low γ nuclei such as ^{13}C or ^{15}N, and line broadening effects caused by anisotropic interactions, such as homonuclear and heteronuclear dipolar couplings and chemical shift anisotropies, result in a small signal-to-noise (S/N) ratio. This in turn leads to measuring times which become inconveniently long for multidimensional experiments.

The line broadening, which causes a lack in spectral resolution, can normally be mitigated by recording spectra of higher dimensionality, but again at the cost of an increased measuring time.

Further complicating the situation, is the fact that biological samples tend to have an upper limit of the concentration at which they can be prepared, limiting the amount of sample which may be contained in the MAS rotor.

Some of these problems can be partially alleviated in the solid state, by measuring non-frozen, semisolid samples. These often feature significant interconversion rates between the different conformations of similar energy, which are normally frozen out, thereby reducing the inhomogeneous broadening. Furthermore the homogenous linewidth is also reduced, by merit of the same dynamics, as anisotropic interactions are partially averaged out.

Still, all is not well if a non-frozen sample preparation is measured: Most clas-

sical solid state NMR techniques, such as cross polarization (CP), are dependent on the dipolar coupling and are highly perturbed, if it is strongly scaled down. Therefore many experiments become more challenging. Additionally there may be cases, where the dynamics of the sample are on the timescale of the NMR radio-frequency (RF) irradiation and/or the magic angle sample spinning (MAS). In these cases the experimental parameters have to be adjusted, and between sample requirements and hardware limitations an often suboptimal compromise has to be found, which again impacts on the achievable sensitivity of the experiment.

On the other hand, non-frozen samples, by merit of the different dynamics of the individual domains, provide a wealth of additional spectroscopic information, as compared to frozen samples, if these differences in spectroscopic behavior are considered in the planning of the experiments.

Nevertheless, regardless whether frozen or non-frozen samples are chosen for solid state NMR investigations, the sensitivity is vastly inferior to the one provided by solution state NMR, leading to measuring times which are often an order of magnitude higher than these for the corresponding solution state experiment.

These long measuring times are especially problematic, if an integral membrane protein, which is usually hard and costly to prepare and therefore of limited availability, is to be measured. That most membrane proteins have very limited lifetimes of a few days at 4°C, until irreversible degradation occurs, doesn't help either.

It is therefore imperative to find means to overcome these limitations, which are posed by solution, as well as solid state NMR. In solution state NMR the rotation correlation time problem mentioned above can be strongly attenuated using the TROSY technique by Wthrich et.al. Although this technique requires strong magnetic fields to be optimally effective, these alone, together with cryoprobe technology, in which the measuring coils and electronics are kept at very low temperature (???) together with advances in the Q-factor of the measurement coils have lead to a significant increase in sensitivity in solution state NMR. Another avenue lies in the use of the solution state dynamic nuclear polarization (DNP) effect, about which at the time of writing pioneering work is done [29–31] by the European DNP Project, of which in Frankfurt the group of Prof. Prisner is a member.

DNP has been used more extensively in solid state NMR so far, especially by the group of Robert Griffin. Here the samples are measured deep frozen, which circumvents the heating problem faced when using strong microwave irradiation of the sample. Similar to solution state NMR, stronger fields, faster MAS and cryo-MAS probes provide ever increasing sensitivities.

One feature all of these approaches have in common, is that, for most laboratories, extensive hardware upgrades are required, to utilize these methods to best effect. The costs for such an upgrade can range from 50.000 Euro for a new probe up to several million Euro for the current generation of very high field NMR spectrometers. Therefore most laboratories cannot afford to employ the full wealth of available methodologies, especially if NMR is not the main method being employed by the laboratory.

The methods and experiments described in this work, aim at the decluttering of the NMR spectra, thus lowering the need for higher dimensional experiments, or an increase of sensitivity per unit time. The increase in sensitivity per unit time is an important concept here, as often a "rearrangement" of one dimensional intensity onto a higher dimensional plane is discussed as a way for shortening experiment times. While this works well in a non sensitivity limited case, sensitivity limitation is nearly always given in studies on biological solids. Therefore the aforementioned methods, for which single scan two dimensional NMR is an experimental and projection reconstruction an processing method example, will be difficult to implement when applied in solid state studies of membrane protein samples, often resulting in no net gain in the overall experiment time.

Methods with a true gain in sensitivity per unit time have to work differently to

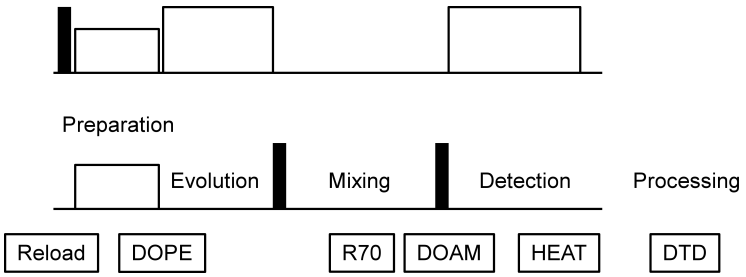

Figure 1.1: Schematic diagram of the phases of a two dimensional NMR experiment. For clarity the phases are shown superimposed on a typical solid state NMR pulse sequence, the proton driven spin diffusion (PDSD) experiment. Below the sequence, the methods introduced in this work are listed, according to the phase of the experiment in which they take effect.

be effective. Rather than "spreading out" magnetization or information across the spectrum, these methods have to "concentrate" the magnetization in spectral areas of interest, or use the properties of specific experiments and transformations to effect a separation of the signal from the spectral noise. The development of methods of the latter kind is the main goal of this thesis. The methods that will be presented in the following were specifically developed, but are not limited to, the study of biological samples in the solid or semi-solid state.

It is important to note that all methods, that will be presented in the following, do not require any additional equipment or sample preparation, to be effective. It is the stated aim of this thesis to introduce methods that are applicable with the hardware already present in most NMR capable laboratories, with no additional finacial overhead required. Therefore all methods described in this thesis work solely through modification and optimization of existing and introduction of new experimental or processing techniques for solid state NMR studies.

To effect genuine gains in the sensitivity, the different phases of a typical multidimensional experiment were analyzed for their potential for improvement.

A two dimensional NMR experiment is usually divided into four phases, preparation, evolution, mixing and detection.

In the preparation phase, the spin polarization is brought to the transverse plane, possibly after a magnetization transfer from a nucleus with a higher γ and thus higher Zeeman energy, prior the next step, the evolution. Here the spins evolve, usually but not necessarily under the effect of the chemical shift Hamiltonian. Then the mixing step, which usually relies on the homo- or hetero-nuclear dipolar coupling or the J-coupling is performed, to create nuclear correlations. Finally the free induction decay (FID) is detected.

The resulting time domain signal is processed and transformed into a frequency domain signal using the fast Fourier transform (FFT).

In this work, several methods will be introduced that take effect in the individual phases of a solid state NMR experiment.

The first phase of an experiment, the preparation phase, is to a large degree responsible for the sensitivity which can be achieved with the experiment. It is therefore the subject of many methods usually using polarization transfer from high γ to low γ nuclei, which can lead to enormous gains in sensitivity (in typical biological samples up to a factor of 10 for a ^1H to ^{15}N transfer). Such methods include INEPT [22], cross polarization (CP) [21] and the hetero-nuclear Overhauser effect [32]. The gain in sensitivity directly impacts the time needed to arrive at a spectrum of good signal to noise (S/N) ratio, as doubling the signal leads to a fourfold reduction in measuring

time, if the same S/N is to be achieved.

The method introduced in this work, which acts during the preparation phase of the experiment, uses a different approach to reduce the time needed for an experiment of a given S/N.

The RELOAD (Relaxation Enhancement by Lower Overall Adjacent spin temperature Distribution) scheme does not use hetero-nuclear polarization transfer to enhance the sensitivity of an experiment, but makes use of homo-nuclear transfer, which occurs naturally in most solid state samples, in the form of spin diffusion.

The basis for this is, that there are many experiments, in which only information about a subset of all spins present in the spin system is desired. This is the case for many hetero-nuclear correlation experiments, but also for band selective homo-nuclear experiments.

In the RELOAD adaptation of these experiments, a conventional hetero-nuclear polarization enhancement scheme like CP is used, which enhances the magnetization of all nuclei of the target species, irrespective if they are of interest for the experiment in question or not.

The actual correlation experiment is then conducted in a band selective manner, with great care being taken to assure that the spins outside the spectral region of interest (ROI) are left unperturbed on the z-axis of the rotating frame.

After the experiment is finished, and the free induction decay (FID) is recorded, a short time is allowed for the spin polarizations of the spins in the ROI and those outside the ROI to equilibrate. Then, the experiment is conducted again, but this time omitting the hetero-nuclear polarization transfer during preparation.

It will be shown in chapter 3 that this allows for a much more rapid repetition of the experiment, than conventionally possible, as long as there is significant polarization outside the ROI. After this magnetization is depleted, the pulse sequence is repeated in a conventional manner, including the polarization enhancement during preparation which is preceded by a comparatively long recycle delay time for ^1H relaxation.

This results in a nested loop arrangement of the RELAOD sequence, where the inner sequence consists of experiments fueled by magnetization acquired from all resonances outside the ROI, and an outer loop which is similar to the conventional experiment, where hetero-nuclear polarization transfer replenishes all spins of the species of interest, inside and outside of the ROI.

This method is characterized using inversion recovery experiments on a peptide and the dependence on a variety of experimental factors is investigated. Furthermore, band selective homo- and hetero-nuclear correlation experiments are implemented and the possible gains in sensitivity evaluated, again with respect to several different experimental parameters.

As mentioned before, this experiment is applicable to homo-nuclear as well as hetero-nuclear solid state correlation experiments.

The mixing phase of an experiment serves to create a correlation between the resonances in the spectrum, and thus encodes the spectral information about nuclear inter-connectivity. Unfortunately, this information is sometimes obscured by detrimental influences of, for instance, sample dynamics on the RF pulses of the mixing block, or a scaling of the nuclear interactions involved.

Especially in membrane proteins in a semi solid state, the homo- and hetero-nuclear dipolar couplings are strongly attenuated, making polarization transfer via cross polarization difficult, of not impossible.

To overcome the effects of sample dynamics on hetero-nuclear correlation, a hetero-nuclear through bond polarization transfer scheme was sought, which improves the efficiency of magnetization transfer for non frozen samples featuring a considerable degree of dynamics, such as membrane proteins.

Here, the symmetry principles introduced by Carravetta and Levitt [23] and adapted for multi channel application by Brinkmann [24], are used to tailor the effective Hamil-

tonian during mixing.

To yield an efficient polarization transfer, an effective Hamiltonian is sought, in which homo- and hetero-nuclear dipolar couplings, as well as isotropic and anisotropic chemical shifts are suppressed to a high degree, while allowing for evolution under the hetero-nuclear J-coupling.

To this end, numerical simulations and experiments under a variety of conditions are conducted to identify the best symmetry amongst all theoretically possible candidates, as shown in chapter 4.

The set of symmetry numbers that results from these investigations is ideally used for ^{1}H to ^{13}C or ^{15}N polarization transfer, but could in principle also be employed in ^{13}C to ^{15}N correlation experiments.

Not enhancing the sensitivity, but instead the spectral resolution are the DOAM (Double quantum filtering After Mixing) and DOPE (DOuble quantum filtering Prior to Evolution) sequences introduced in chapter 5, which introduce an additional double quantum filter (DQF) into a homo-nuclear, single quantum correlation experiment.

The motivation for doing this is a reduction of the natural abundance background, as it can lead to an dramatic increase of the diagonal intensity in a homo-nuclear correlation experiment, if a dilute, ^{13}C labeled compound (such as a small ligand) is to be investigated in presence of a large number of unlabeled molecules (i.e. a membrane reconstituted protein).

This is often the case if the interactions of small, pharmacological relevant compounds with the membrane or their receptor are to be investigated in the solid state.

Natural abundance is a problem in these spectra, because albeit it usually only yields diagonal peaks, the large intensity can obscure cross peaks close to the diagonal.

Furthermore the real diagonal intensities of the labeled compound are buried under the natural abundance background, which results in severe problems in the evaluation of the cross relaxation rates, using methods such as the full matrix approach [25].

The efficiency of these schemes is shown and the retention of the buildup rates investigated, to assure the fidelity of the cross relaxation rates obtained from DOAM or DOPE spectra.

In solid state NMR, the suppression of anisotropic interactions is often less than perfect. Especially in rigid solids, this leads to transverse relaxation times, which are often very short (ms) as compared to those observable in solution state NMR (up to a second), where T_2 can approach T_1 for small molecules.

Still, the real T_2 time can be measured using a train of 180° pulses, as employed in the Carr-Purcell Meiboom-Gill (CPMG) [26] sequence. Here, only the maxima after each echo are of interest, as these outline the envelope of T_2 relaxation.

These echos can not only be used to measure T_2, but also to enhance the signal of the experiment. The reason for this is that a longer T_2 time will not only influence the linewidth obtained, but also the signal to noise of the experiment.

The application of echos during acquisition cannot restore the resolution of the experiment, which is still given by T_2^*, but is well suited to, at least partially, restore the sensitivity normally lost to transverse relaxation due to T_2^*.

Exploiting this fact is the HEAT (Half Echo Alternating Transformation) method, which is introduced in chapter 6. HEAT employs successive spin echos, generated by a train of 180° pulses and acquired during detection. Then the individual echos are separated during processing, with every other half-echo being time inverted. Then all echos are added, which increase the S/N for those samples in which T_2^* is smaller than T_2.

The DTD (Dual Transformation Denoising) processing scheme, introduced in chapter 7, combines the properties of covariance and fast Fourier transform (FFT).

The covariance has first been used in NMR by Brüschweiler et. al. [27, 28] as a method for speeding up NMR measurements.

Summarizing briefly, homonuclear, two dimensional spectra are processed with FFT in the direct dimension and covariance in the indirect dimension. This results in a reduction of truncation artifacts, as compared to the use of FFT in the indirect dimension.

The tradeoff for this can be false positive peaks, as covariance is a method very different from Fourier transform, in which insufficient data leads to this different kind of artifact.

A solution for this is the multiplication of the resultant data sets, of FFT and covariance, as the artifacts of both methods are different in nature.

This leads to a high fidelity of the resultant data set (W. Bermel unpublished results).

In this work, an additional property of the combination of FFT with covariance is investigated, the differences of the two methods when transforming spectral noise. As will be shown in chapter 7, the combination of FFT and covariance can reduce the intensity of the spectral noise, while retaining the ability to reduce truncation artifacts.

This property is investigated, using synthetic, as well as experimental data sets, and a modification of the method, which retains relative peak intensities for buildup measurements is presented.

Additionally to spectroscopic methods, sample preparation and the labeling scheme used have a tremendous influence on the quality of NMR spectra.

To explore the possibilities offered by different preparation methods on the resolution and sensitivity of solid state NMR spectra, the integral α-helical membrane protein diacylglycerol kinase (DGK) was prepared using a variety of different labeling patterns and reconstitution protocols, as shown in chapter 8.

DGK shows strong dynamics when measured in a semi solid state, which can complicate the measurements as dynamics can scale the anisotropic interactions conventionally used in solid state NMR. Furthermore, interference effects of sample dynamics with the RF irradiation of the sample, can be detrimental to the sensitivity of the recorded spectra.

The effect of temperature on the dynamics of the loop and transmembrane regions of the protein is investigated, as well as the influence on different pulse sequences. Alternatives to classical solid state NMR pulse sequence elements are suggested, such as replacing the conventional cross polarization [21] by nuclear Overhauser enhancement [32] or proton driven spin diffusion [33] by TOBSY [34], if no through space constrains are required. Furthermore, the effects of the methods introduced in this work are explored on the sample of DGK, when applicable.

The methods for sensitivity enhancement introduced in this work can be combined in many cases and could therefore result in a considerable reduction of the measurement time, especially for higher dimensional experiments, making the routine application of ssNMR to spectroscopically difficult samples feasible.

Chapter 2

General Solid State NMR Theory

2.1 Introduction

To better understand NMR conducted on rotating solids, it is useful to introduce several concepts. NMR theory is mainly concerned with the interaction of spins with the magnetic field or other spins. To describe these interactions in solids, it is advantageous to introduce a description amenable to rotation, such as irreducible spherical tensors. This simplifies the treatment of anisotropic interactions and their effect on solid state NMR spectra. For static solids this can be performed using the time independent Schroedinger equation. The same approach is not applicable to solids rotating at the magic angle:

$$\beta_m = tan^{-1}\sqrt{2} \tag{2.1}$$

In this case, which is very common in solid state NMR, the time dependent Schroedinger equation has to be solved, as there is a periodic time dependency on the rotation of the sample

$$\frac{d}{dt}\psi = -iH(t)\psi \tag{2.2}$$

Here, ψ is a wave function, describing the spin state and H(t) is a Hermitian operator called the *Hamiltonian*, which shows a periodic time dependency under MAS. It is associated with the energy state of the system, as its eigenvalues multiplied with $\hbar$ correspond to the energy levels of the system in Joules. To solve this equation, two approaches are commonly used, Floquet theory and averaged Hamiltonian theory. The latter is used in this work and will be described in this chapter.

In the following, the theory necessary for a treatment of the averaged Hamiltonian theory (AHT) is given.

Then the AHT itself is discussed and symmetry based sequences are introduced. The symmetry principles which are used by these sequences were derived by Levitt et al. [23], using the different mathematical tools introduced in this chapter. Application of the AHT results in a set of rules, which allow a selective recoupling of nuclear spin interactions.

2.2 Angular Momentum Operators

To facilitate the description of rotations in this work, it is helpful to give a short summary of the definitions of angular momentum operators. Let ψ be a wave function to be rotated. This rotation shall be carried out by the rotation operator $R(\vec{n},\theta)$, with $\vec{n}$ being the axis and θ the angle of rotation, so that ψ is rotated into a new state ψ' according to

$$\psi' = R(\vec{n},\theta)\psi \tag{2.3}$$

The rotation operator $R(\vec{n},\theta)$ performs a unitary transformation, that is, a linear homogeneous transformation in which lengths and angles (and thus the scalar product) are conserved, and

$$R(\vec{n},\theta)^{-1} = R(\vec{n},\theta)^{\dagger} \tag{2.4}$$

holds.
The rotation matrix can be identified as

$$R(\vec{n},\theta) = e^{-iS(\vec{n},\theta)} \tag{2.5}$$

This can be seen by first considering the following definition of exponential operators

$$e^{S} = \sum_{n=0} \frac{1}{n!} S^n \tag{2.6}$$

and the following proof, which shows that e^{-iS} is unitary, if S is Hermitian

$$\left(e^{-iS}\right)^{\dagger} = \sum_n \frac{1}{n!}\left[(-iS)^n\right]^{\dagger} = \sum_n \frac{1}{n!}\left[(-iS)^{\dagger}\right]^n \tag{2.7}$$

$$= \sum_n \frac{1}{n!}(iS^{\dagger})^n = \sum_n \frac{1}{n!}(iS)^n = \left(e^{-iS}\right)^{-1} \tag{2.8}$$

Therefore

$$R(\vec{n},\theta)^{\dagger} = e^{iS(\vec{n},\theta)} \tag{2.9}$$

$$R(\vec{n},\theta)^{-1} = e^{iS(\vec{n},\theta)} \tag{2.10}$$

Thus, the only quantity yet to be determined is $S(\vec{n},\theta)$. To find $S(\vec{n},\theta)$, it is useful to look at rotations around an infinitesimal angle, for which the change of the system can be considered linear. This allows us to drop any power from the Taylor series given in Eqn. (2.6) higher than one. Therefore the rotation of ψ by the rotation operator $R(\vec{n},\theta)$ can be described, with the use of Eqn. (2.5), as

$$R(\vec{n},\theta)\psi = (1 - iS(\vec{n},\theta))\psi \tag{2.11}$$

Now let J_x, J_y and J_z be Hermitian operators for the three Cartesian components of angular momentum, which form a complete set, so that any angular momentum can be expressed as a linear combination of the three, with the general angular momentum denoted as $\mathbf{J}$. With the assumption of infinitesimal rotation, one may write

$$R(\vec{n},\theta)\psi - \psi = -i\theta(\vec{n}\mathbf{J})\psi \tag{2.12}$$

Comparing Eqn.(2.12) to Eqn.(2.11), it can be seen that

$$S(\vec{n},\theta) = \theta(\vec{n}\mathbf{J}) \tag{2.13}$$

and thus

$$R(\vec{n},\theta)\psi = e^{-i\theta(\vec{n}\mathbf{J})}\psi \tag{2.14}$$

As is known from quantum mechanics, angular momentum is quantized, and therefore the angular momentum operators have certain properties, when applied to wave functions or each other. J^2 commutes with every other component and a complete basis can be constructed from the eigenfunctions of J^2 and J_z. The other angular momentum operators do not commute with one another, but there a relationship called cyclic commutation holds

$$[J_i, J_j] = i\varepsilon_{ijk}J_k \tag{2.15}$$

$$[J^2, J_i] = 0 \tag{2.16}$$

A system can now be expressed in a basis using the eigenvalues and eigenfunctions of J^2 and J_z, using the so called Dirac notation

$$J^2|j,m>= \hbar^2 j(j+1)|j,m> \tag{2.17}$$

$$J_z|j,m>= \hbar m|j,m> \tag{2.18}$$

with j and m being the eigenvalues of J^2 and J_z respectively. Furthermore, rising and lowering operators may be defined as

$$J_+ = J_x + iJ_y \tag{2.19}$$

$$J_- = J_x - iJ_y \tag{2.20}$$

with the following eigenvalues

$$J_\pm = \hbar\sqrt{j(j+1) - m(m\pm 1)}|j,m\pm 1> \tag{2.21}$$

This eigenbasis is well suited for the description of the operators encountered in NMR. Generally there are $2j+1$ eigenstates of the system with j being one of $\frac{1}{2}, 1, \frac{3}{2}, \ldots$. For spin $\frac{1}{2}$ particles such as ${}^1H$ the eigenstates of $J_z, m = \pm\frac{1}{2}$ are often called α and β in the literature and the eigenbasis is referred to as *Zeeman Eigenbasis*, so that

$$J_z = \hbar\frac{1}{2}|\alpha> \tag{2.22}$$

$$J_z = -\hbar\frac{1}{2}|\beta> \tag{2.23}$$

In this basis, it is possible to express every spin state as a superposition of the basis states

$$|\psi(t)>= c_\alpha(t)|\alpha> + c_\beta(t)|\beta> \tag{2.24}$$

where $c_\alpha(t)$ and $c_\beta(t)$ are complex, time dependent coefficients that are normalized so that for each t $|c_\alpha(t)|^2 + |c_\beta(t)|^2 = 1$ holds.

If a spin system consisting of a multitude of spins is considered, the corresponding eigenfunctions can be obtained by using the direct product of the individual Zeeman states. In the case of N_s spin $\frac{1}{2}$ particles, there will be $N = 2^{N_s}$ eigenstates of the system, denoted as

$$|\psi>= |m_1, m_2, \ldots, m_{N_s}> \tag{2.25}$$

These states are simultaneous eigenstates of the individual J_z^n operators and the operator for the z-component of the total spin angular momentum J_z, which is defined as

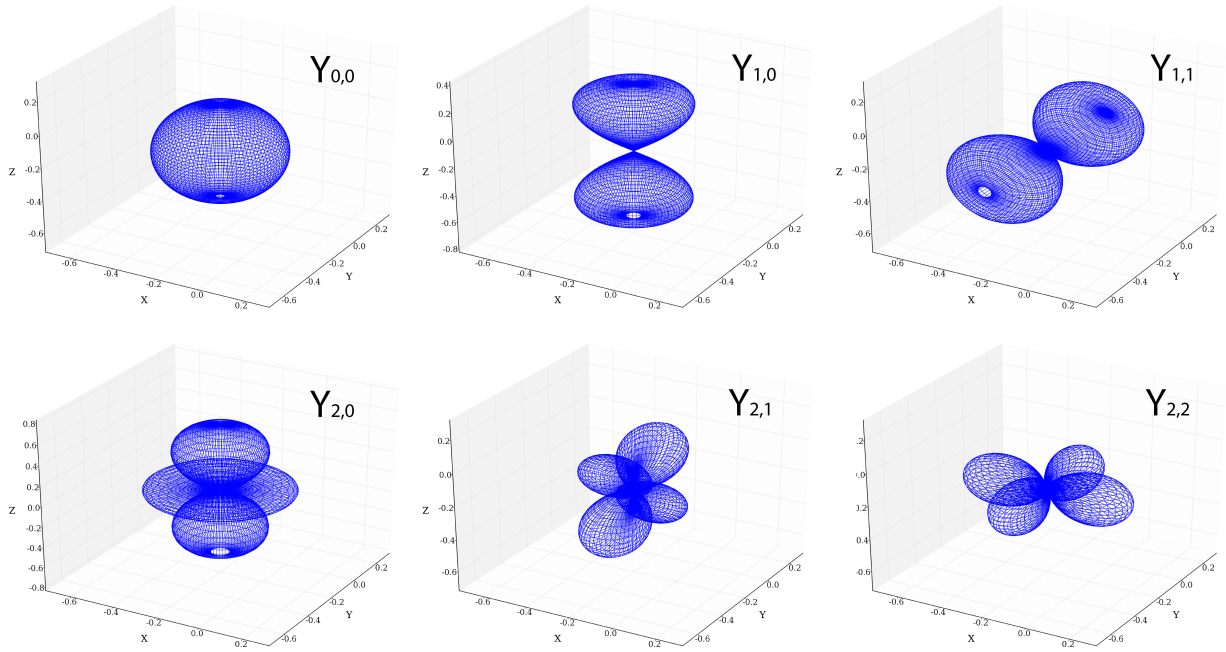

Figure 2.1: Plot of the spherical harmonics $Y_{0,0}$ (upper left), $Y_{1,0}$ and $Y_{1,1}$ (upper middle and upper right) and $Y_{2,0}$ to $Y_{2,2}$ (lower left to lower right)

$$J_z = \sum_{n=1}^{N_s} J_z^n \tag{2.26}$$

applying this operator to the wave function of a multi spin system results in

$$J_z|\psi >= M_\psi|\psi > \tag{2.27}$$

with

$$M_\psi = \sum_{n=1}^{N_s} m_n \tag{2.28}$$

again, a spin state $|\Psi(t) >$ can be expressed as

$$|\Psi(t) >= \sum_{n=1}^{N} c_n(t)|n > \tag{2.29}$$

in analogy to the case for a single spin $\frac{1}{2}$.

If the value of j is an integer, the eigenfunctions are given by the spherical harmonics

$$Y_{lm}(\theta,\phi) = P_l(cos\theta)e^{im\phi} = \frac{1}{2^l l!}\frac{d^l}{d(cos\theta)^l}[(cos\theta^2 - 1)^l] \tag{2.30}$$

with P_l being the Legendre polynomials. The symmetry of spherical harmonics reflects the symmetry of atomic orbitals as shown in Fig. 2.1.

2.3 Propagators

Once a wave function describing the state of the system is found, it is interesting to look at the time evolution of said system. To facilitate this, the Schroedinger equation has to be applied, which is accomplished by applying a so called *propagator* $U(t, t_a)$ to the wave function of the spin system. This propagator is defined as the operator transforming the spin state $|\psi(t_a)>$ into the spin state at a later time point $|\psi(t)>$.

$$|\psi(t)>= U(t, t_a)|\psi(t_a)> \tag{2.31}$$

where $U(t, t_a)$ has to solve

$$\frac{d}{dt}U(t, t_a) = -iH(t)U(t, t_a) \tag{2.32}$$

$$\frac{d}{dt}U(t_a, t_a) = \mathbb{1} \tag{2.33}$$

To derive the propagator, different cases of time dependency of the Hamiltonian have to be considered.

- If H is time independent the propagator is given by:

$$U(t, t_a) = exp\{-iH(t - t_a)\} \tag{2.34}$$

- if H is time dependent in a fashion that $[H(t'), H(t'')] = 0$ for all time points $t_a \leq t', t'' \leq t$, this case is called as inhomogeneous and the propagator becomes:

$$U(t, t_a) = exp\left\{-i\int_{t_a}^{t} dt' H(t')\right\} \tag{2.35}$$

- if H is time dependent so that $[H(t'), H(t'')] \neq 0$ for at least one time point $t_a \leq t', t'' \leq t$, then the propagator cannot generally be derived analytically. The propagator can still be derived if the interval $[t, t_a]$ can be divided into n small fragments τ_k with $k = 1, 2, \ldots, n$ in which the Hamiltonian is piecewise time independent. The propagator is then given by:

$$U(t, t_a) = exp(-iH_n\tau_n)\ldots exp(-iH_2\tau_2)exp(-iH_1\tau_1) \tag{2.36}$$

  with H_k being the time independent Hamiltonian operative during the interval τ_k. If the Hamiltonian cannot be considered time independent during these intervals, one can still use the solution given in Eqn.(2.36) as an approximation, if n is sufficiently large.

In solid state NMR, the Hamiltonian is often given in a certain frame of reference and must be transformed into the laboratory frame before it can be applied to the wave function of the spin system, in the manner given above. To accomplish this, it is useful to employ Euler angles, Wigner matrices and the irreducible spherical tensor representation of the Hamiltonian. These tools will be outlined in the following.

2.4 Euler Angles and Wigner Matrices

There are multiple ways of describing a rotation in space. In solid state NMR it is common to make use of the so called Euler Angles. Here, the rotation (in Cartesian space) about an arbitrary axis is decomposed into a set of three rotations.

- a rotation about the z-axis by an angle α
- a rotation about the new y-axis (denoted as y') by an angle β

- a rotation about the new z-axis (z") by an angle γ

This set of angles $\Omega = (\alpha, \beta, \gamma)$ is called Euler angles. Alternatively the initial frame can be kept, but then the order of rotations has to be inverted. If a spherical basis is chosen, a rotation by a set of Euler angles can be accomplished by the application of a Wigner matrix

$$\begin{aligned} D^j_{lm}(\Omega) &= < jm'|e^{-i\alpha J_z} e^{-i\beta J_y} e^{-i\gamma J_z}|j,m > & (2.37)\\ &= e^{-im'\alpha} < jm'|e^{-i\beta J_y}|j,m > e^{-im\gamma} & (2.38)\\ &= e^{-im'\alpha} d^j_{m'm}(\beta) e^{-im\gamma} & (2.39) \end{aligned}$$

where $d^j_{m'm}(\beta)$ is called the reduced Wigner matrix element. These elements are given by

$$d^1 = \begin{pmatrix} \frac{(1+cos\beta)}{2} & \frac{-sin\beta}{\sqrt{2}} & \frac{(1-cos\beta)}{2} \\ \frac{sin\beta}{\sqrt{2}} & cos\beta & \frac{-sin\beta}{\sqrt{2}} \\ \frac{(1-cos\beta)}{2} & \frac{sin\beta}{\sqrt{2}} & \frac{(1+cos\beta)}{2} \end{pmatrix} \tag{2.40}$$

and

$$d^2 = \begin{pmatrix} \frac{(1+cos\beta)^2}{4} & \frac{-(1+cos\beta)sin\beta}{2} & \frac{1}{2}\sqrt{\frac{3}{2}}sin^2\beta & \frac{-(1-cos\beta)sin\beta}{2} & \frac{(1-cos\beta)^2}{4} \\ \frac{(1+cos\beta)sin\beta}{2} & \frac{2cos^2+cos\beta-1}{2} & -\sqrt{\frac{3}{2}}sin\beta cos\beta & -\frac{2cos^2\beta-cos\beta-1}{2} & \frac{-(1-cos\beta)sin\beta}{2} \\ \frac{1}{2}\sqrt{\frac{3}{2}}sin^2\beta & \sqrt{\frac{3}{2}}sin\beta cos\beta & \frac{3cos^2\beta-1}{2} & -\sqrt{\frac{3}{2}}sin\beta cos\beta & \frac{1}{2}\sqrt{\frac{3}{2}}sin^2\beta \\ \frac{(1-cos\beta)sin\beta}{2} - & -\frac{2cos^2\beta-cos\beta-1}{2} & \sqrt{\frac{3}{2}}sin\beta cos\beta & \frac{2cos^2\beta+cos\beta-1}{2} + & -\frac{(1+cos\beta)sin\beta}{2} \\ \frac{(1-cos\beta)^2}{4} & \frac{(1-cos\beta)sin\beta}{2} & \frac{1}{2}\sqrt{\frac{3}{2}}sin^2\beta & \frac{(1+cos\beta)sin\beta}{2} & \frac{(1+cos\beta)^2}{4} \end{pmatrix} \tag{2.41}$$

Although higher order Wigner matrices exist, these are not used in the context of this work.

2.5 Tensors

Different physical terms need to be described with the correct dimensionality, for instance mass is a scalar, and thus has the dimension of zero. Momentum is described as a vector with three dimensions. Magnetic susceptibility, on the other hand, needs to be described by a matrix as an applied field (described by a vector) results in a different vector. Generally all these interactions can be described with tensors of different ranks, whereas scalar quantities are rank 0 tensors, vectors rank 1 and matrices, such as the susceptibility, are rank 2. In solid state NMR theory, the tensor representations of the individual physical quantities are normally given in a spherical basis, for ease of later manipulation, which often consists of a series of rotations. Thus a 3×3 Cartesian tensor T is decomposed into three spherical tensors, that are chosen to be irreducible, and consist of a rank 0 tensor, corresponding to the trace of T, an asymmetric rank 1 tensor and a symmetric rank 2 tensor. As a consequence of the spherical basis, rotations of these tensors may be conducted by using the Wigner matrices, outlined in the previous section. Therefore

$$T^{F_2}_{JM} = R(\vec{n},\theta) T^{F_1}_{JM} R(\vec{n},\theta)^{-1} = \sum_{M'} D^J_{MM'}(\Omega) T^{F_1}_{JM'} \tag{2.42}$$

with $M' = -J, -J+1, \ldots, J$ and where F_1 and F_2 denote two different frames that are linked by a rotation around Ω. In solid state NMR it is customary to describe an interaction in the so called Principal Axis Frame (PAS) in which the symmetric part of the Cartesian tensor is diagonal.

2.6 The Nuclear Spin Hamiltonian

The Hamiltonian for a system in NMR is normally given by the sum over all Hamiltonians of the different spin interactions:

$$H = \sum_{\Gamma} H^{\Gamma} \tag{2.43}$$

These terms H^{Γ} of the individual interactions are normally given in the Cartesian coordinate system by the multiplication of a second rank tensor with two vectors, describing the interacting physical entities.

$$H^{\Gamma} = C^{\Gamma}(\boldsymbol{X}^{\Gamma})^{T}\mathbb{A}^{\Gamma}\boldsymbol{Y}^{\Gamma} = C^{\Gamma}\left(X_x^{\Gamma}X_y^{\Gamma}X_z^{\Gamma}\right)\begin{pmatrix}\mathbb{A}_{xx}^{\Gamma} & \mathbb{A}_{xy}^{\Gamma} & \mathbb{A}_{xz}^{\Gamma}\\ \mathbb{A}_{yx}^{\Gamma} & \mathbb{A}_{yy}^{\Gamma} & \mathbb{A}_{yz}^{\Gamma}\\ \mathbb{A}_{zx}^{\Gamma} & \mathbb{A}_{zy}^{\Gamma} & \mathbb{A}_{zz}^{\Gamma}\end{pmatrix}\begin{pmatrix}Y_x^{\Gamma}\\ Y_y^{\Gamma}\\ Y_z^{\Gamma}\end{pmatrix} \tag{2.44}$$

These entities can be two nuclear spins or a spin and the external magnetic field. The constant C^{Γ} is characteristic for the individual spin interactions. To describe the Hamiltonian in its spherical representation, it can be decomposed into irreducible spherical tensors so that

$$\mathbb{A}^{\Gamma} = \mathbb{A}_0^{\Gamma} + \mathbb{A}_1^{\Gamma} + \mathbb{A}_2^{\Gamma} \tag{2.45}$$

as outlined above. At this point, it is convenient to separate the Hamiltonian into two irreducible spherical tensors $\hat{A}$ and $\hat{T}$, where $\hat{T}$ is derived from the vectors $\boldsymbol{X}$ and $\boldsymbol{Y}$ given in Eqn.(2.44). $\hat{A}$ is referred to as the *spatial tensor* and $\hat{T}$ as the *spin tensor*, if $\boldsymbol{X}$ and $\boldsymbol{Y}$ are two interacting spins, or as *spin-field tensor* if one of the vectors represents the external magnetic field. Therefore the Hamiltonian is given by

$$H^{\Gamma} = C^{\Gamma}\sum_{l=0}^{2}\sum_{q=-l}^{l}(-1)^{q}[\hat{A}_{lq}^{\Gamma}]^{F}[\hat{T}_{l-q}^{\Gamma}]^{F} \tag{2.46}$$

where $[\hat{A}_{lq}^{\Gamma}]^{F}$ and $[\hat{T}_{l-q}^{\Gamma}]^{F}$ refer to the representations of $\hat{A}^{\Gamma}$ and $\hat{T}^{\Gamma}$ in a frame F.

2.7 Reference Frames

Interactions are normally described in solid state NMR using the *Principal Axis System* (PAS). This frame is defined in such a way that the symmetric part of the spatial tensor in its Cartesian representation is diagonal. The interaction in this frame has to be transformed into the laboratory frame by a rotation around the Euler angle Ω_{PL}. For the sake of clarity, this rotation is divided into a set of sequential rotations into different frames, as certain frames can change their orientation with respect to one another during the experiment, i.e. under MAS. Thus, it is customary to first rotate a given interaction Γ from the PAS into the *Molecular Frame* describing the orientation of the interaction with respect to the normal of the molecule (Ω_{PM}) and further into the *Rotor Frame*, yielding the orientations of the molecules with respect to the rotor director (Ω_{MR}). Finally, the interaction is transformed into the *Laboratory Frame* (Ω_{RL}). Under MAS conditions, this rotation is generally time dependent. A pictorial representation of the different frames of reference and the transformations between them is given in Fig. 2.2.

A combination of Eqns. (2.46) and (2.42) yields

$$H^{\Gamma} = C^{\Gamma}\sum_{l=0}^{2}\sum_{q,q'=-l}^{l}(-1)^{q}[\hat{A}_{lq'}^{\Gamma}]^{P}D_{q'q}^{l}(\Omega_{PL}^{\Gamma})[\hat{T}_{l-q}^{\Gamma}]^{L} \tag{2.47}$$

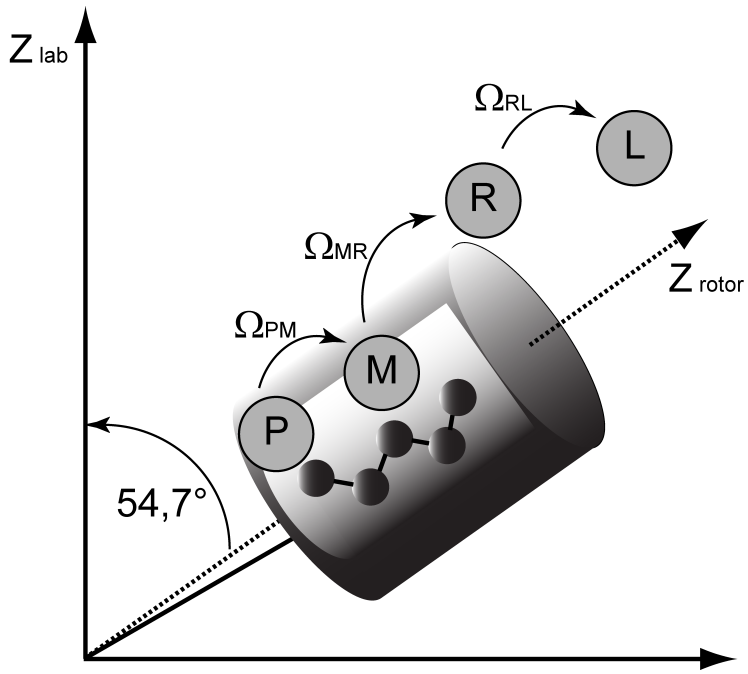

Figure 2.2: Schematic representation of the frames commonly used in solid state NMR and the sets of Euler angles used for transformations between them.

Generally the components of $\hat{A}$ are given by

$$\begin{aligned}
\hat{A}_{00} &= -(1/\sqrt{3})[\mathbb{A}_{xx} + \mathbb{A}_{yy} + \mathbb{A}_{zz}] && (2.48)\\
\hat{A}_{10} &= -(i/\sqrt{2})[\mathbb{A}_{xy} - \mathbb{A}_{yx}] && (2.49)\\
\hat{A}_{1\pm1} &= -1/2[\mathbb{A}_{zx} - \mathbb{A}_{xz} \pm i(\mathbb{A}_{zy} - \mathbb{A}_{yz})] && (2.50)\\
\hat{A}_{20} &= (1/\sqrt{6})[3\mathbb{A}_{zz} - Tr(\mathbb{A})] && (2.51)\\
\hat{A}_{2\pm1} &= \mp 1/2[\mathbb{A}_{xz} + \mathbb{A}_{zx} \pm i(\mathbb{A}_{yz} + \mathbb{A}_{zy})] && (2.52)\\
\hat{A}_{2\pm2} &= 1/2[\mathbb{A}_{xx} - \mathbb{A}_{yy} \pm i(\mathbb{A}_{xy} + \mathbb{A}_{yx})] && (2.53)
\end{aligned}$$

The components of $\hat{T}$ depend on whether it represents a spin tensor or a spin-field tensor. In the former case, $\hat{T}$ for the two spins I and S is given by:

$$\begin{aligned}
\hat{T}_{00} &= -(1/\sqrt{3})[I_xS_x + I_yS_y + I_zS_z] && (2.54)\\
\hat{T}_{10} &= -(i/\sqrt{2})[I_xS_y - I_yS_x] && (2.55)\\
\hat{T}_{1\pm1} &= -1/2[I_zS_x - I_xS_z \pm i(I_zS_y - I_yS_z)] && (2.56)\\
\hat{T}_{20} &= (1/\sqrt{6})[3I_zS_z - (I_xS_x + I_yS_y + I_zS_z)] && (2.57)\\
\hat{T}_{2\pm1} &= \mp 1/2[I_xS_z + I_zS_x \pm i(I_yS_z + I_zS_y)] && (2.58)\\
\hat{T}_{2\pm2} &= 1/2[I_xS_x - I_yS_y \pm i(I_xS_y + I_yS_x)] && (2.59)
\end{aligned}$$

For a spin-field tensor it is more convenient to express the Hamiltonian as the product of two vectors, as B_0 is fixed in space and not subject to spin rotations. Therefore Eqn. (2.44) can be written as

$$H^{\Gamma} = \boldsymbol{I}^{\Gamma} * \mathbb{A}^{\Gamma} * \boldsymbol{B_0} = \boldsymbol{I}^{\Gamma} * \boldsymbol{B_{\mathbb{A}}}^{\Gamma} \qquad (2.60)$$

the Hamiltonian is then expressed as

$$H^{\Gamma} = \sum_{q=-1}^{q=1} (-1)^q \hat{A}^{\Gamma}_{1q} \hat{T}^{\Gamma}_{1-q} \tag{2.61}$$

With $\boldsymbol{B_0} = (0, 0, B_0)$, $\hat{A}$ and $\hat{T}$ are, for this case, given by

$$\begin{aligned}
\hat{A}_{10} &= \mathbb{A}_{zz} B_0 && (2.62)\\
\hat{A}_{1\pm1} &= \mp(1/\sqrt{2})(\mathbb{A}_{xz} B_0 + i\mathbb{A}_{yz} B_0) && (2.63)\\
\hat{T}_{10} &= I_z && (2.64)\\
\hat{T}_{1\pm1} &= (1/\sqrt{2})(I_x \pm i I_y) && (2.65)
\end{aligned}$$

Generally, the explicit form of $\hat{A}^{\Gamma}$ and $\hat{T}^{\Gamma}$ depends on the specific interaction in question, if for example the tensor is symmetric, the terms $\hat{A}_{10}$ and $\hat{A}_{1\pm1}$ are zero.

2.8 Spin Interactions

The Hamiltonian during an experiment is often the sum of contributions from spin interactions and radio frequency (RF) fields applied to the sample. Therefore, the full Hamiltonian during the experiment is given by

$$H(t) = H_{int}(t) + H_{RF}(t) \tag{2.66}$$

2.8.1 The Secular Approximation

H_{int} normally contains a plethora of interactions, which can affect the magnetic field at the site of the nucleus in all possible directions in space. To simplify this complicated situation, it is generally assumed in NMR that only field contributions that directly enhance or diminish the outside magnetic field B_0 have an effect on the spectrum (this excludes effects of relaxation). Thus only terms that commute with the z component of the spin angular momentum operator in the laboratory frame (I_z) are considered. This is called the *secular* or *high-field approximation*. Thus the internal Hamiltonian can be split into two parts

$$H_{int} = H^{sec}_{int} + H^{nonsec}_{int} \tag{2.67}$$

with

$$[I_z, H^{sec}_{int}] = 0, \; [I_z, H^{nonsec}_{int}] \neq 0 \tag{2.68}$$

Therefore, the interaction Hamiltonian for a single spin can be written, with the definitions given above, as

$$H_{int}(t) = \sum_{\Gamma, l_A, l_T} \sum_{q=-l}^{l} [\hat{A}^{\Gamma}_{l_A q}]^P D^l_{q0}(\Omega^{\Gamma}_{PL}) T^{\Gamma}_{l_T 0} \tag{2.69}$$

If two spins I and S are involved in the interaction, Eqn. (2.69) becomes

$$H_{int}(t) = \sum_{\Gamma, l_A, l_{TI}, l_{TS}} \sum_{q=-l}^{l} [\hat{A}^{\Gamma_{IS}}_{l_A q}]^P D^l_{q0}(\Omega^{\Gamma_{IS}}_{PL}) T^{\Gamma_I}_{l_{TI} 0} T^{\Gamma_S}_{l_{TS} 0} \tag{2.70}$$

For the two spin case, the Hamiltonian transforms as rank l_A with respect to rotations in space, with rank l_{TI} with respect to rotations of spin I and rank l_{TS} for rotations of spin S.

2.8.2 Zeeman and Chemical Shift Interactions

The Zeeman interaction of a spin I with the outside magnetic field B_0 is given by

$$\begin{aligned} H_I^Z &= \boldsymbol{I}\hat{Z}\boldsymbol{B_0} && (2.71)\\ &= \boldsymbol{I}(-\gamma_I)\mathbb{1}\boldsymbol{B_0} && (2.72)\\ &= \omega_0 I_z && (2.73)\\ &= \hat{A_{00}}\hat{T_{10}} && (2.74) \end{aligned}$$

with ω_0 being the *Lamor frequency* and $\mathbb{1}$ the unity matrix. The chemical shielding interaction is normally described with a *deshielding tensor* $\hat{\delta}$, yielding

$$H^{CS} = -\gamma \boldsymbol{I}\hat{\delta}\boldsymbol{B_0} \tag{2.75}$$

In its irreducible Cartesian form the chemical shift interaction is the sum of a rank 0 tensor, called the *isotropic chemical shift* and a rank 2 tensor, called *chemical shift anisotropy* (CSA). Although $\hat{\delta}$ is not necessarily symmetric, the influence of the rank 1 tensor can usually be ignored. The CSA is diagonal in its PAS and the diagonal values δ_{xx}, δ_{yy} and δ_{zz} in this frame are determined according to

$$|\delta_{zz} - \delta_{iso}| \geq |\delta_{xx} - \delta_{iso}| \geq |\delta_{yy} - \delta_{iso}| \tag{2.76}$$

with the isotropic chemical shift being

$$\delta_{iso} = \frac{1}{3}(\delta_{xx} + \delta_{yy} + \delta_{zz}) \tag{2.77}$$

the CSA is often described with the anisotropy (ω_{aniso})and asymmetry (η) parameters. These are defined as follows

$$\omega_{aniso} = \omega_0(\delta_{zz} - \delta_{iso}) \tag{2.78}$$

and

$$\eta = \frac{\delta_{yy} - \delta_{xx}}{\delta_{zz} - \delta_{iso}} \tag{2.79}$$

Thus the chemical shift Hamiltonian is given by

$$H^{CS} = ([\hat{A}_{00}^{CS}]^L + [\hat{A}_{20}^{CS}]^L)\hat{T}_{10} \tag{2.80}$$

2.8.3 Dipolar Interaction

The dipolar couplings are represented by a symmetric, traceless Cartesian tensor $\mathbb{D}$. For the homo-nuclear case of two spins I^s and I^k coupling, the Hamiltonian is given by

$$\begin{aligned} H^{DD} &= \boldsymbol{I}^s\mathbb{D}\boldsymbol{I}^k && (2.81)\\ &= [\hat{A}_{20}^{DD}]^L T_{20} && (2.82)\\ &= -\frac{\mu_0}{8\pi}\frac{\gamma_I^2\hbar}{r_{sk}^3}(3cos^2\theta - 1)(3I_z^sI_z^k - \boldsymbol{I}^s\boldsymbol{I}^k) && (2.83) \end{aligned}$$

for the hetero-nuclear case of two coupled spins I and S, the analog expression is

$$\begin{aligned} H^{DD} &= \boldsymbol{I}\mathbb{D}\boldsymbol{S} && (2.84)\\ &= [\hat{A}_{20}^{DD}]^L T_{10}^I T_{10}^I && (2.85)\\ &= -\frac{\mu_0}{8\pi}\frac{\gamma_I\gamma_S\hbar}{r_{sk}^3}(3cos^2\theta - 1)(2I_zS_z) && (2.86) \end{aligned}$$

2.8.4 J-coupling

The J-couplings are indirect dipolar couplings, mediated by the electrons of the coupled nuclei. The J-coupling is described by a Cartesian tensor $\mathbb{J}$, which may be decomposed into rank 0, 1 and 2 tensors. The rank 0 tensor is called the *isotropic J-coupling*, the rank 1 tensor is normally ignored and the rank 2 tensor is referred to as the *J-anisotropy*. The Hamiltonian for the homo-nuclear isotropic J-coupling between two coupled spins I^s and I^k is given by

$$\begin{aligned} H^J &= \boldsymbol{I}^s \mathbb{J} \boldsymbol{I}^k && (2.87) \\ &= [\hat{A}^J_{00}]^L T_{00} && (2.88) \end{aligned}$$

in the hetero-nuclear case of two coupled spins I and S, Eqn. (2.88) becomes

$$\begin{aligned} H^J &= \boldsymbol{I} \mathbb{J} \boldsymbol{S} && (2.89) \\ &= [\hat{A}^J_{00}]^L T^I_{10} T^S_{10} && (2.90) \end{aligned}$$

The J-anisotropy has the same transformation characteristics as the dipolar coupling, but is much smaller for the case of light nuclei.

2.9 Radio Frequency Pulses

During NMR experiments the spins are subjected to irradiation with radio frequency waves of their Lamor frequency B_{RF}. This imposes an additional Hamiltonian on the spin system as shown in Eqn. (2.66). This Hamiltonian, acting on a spin I can be described as

$$H_{RF}(t) = -\frac{1}{2}\gamma_I B_{RF}(cos(\omega_{ref}t + \phi_p)I_x + sin(\omega_{ref}t + \phi_p)I_y) \qquad (2.91)$$

where ω_{ref} is the reference frequency of the spectrometer, which determines the center of the spectrum and ϕ_p is the phase of the radio frequency pulse. The spin evolution is often described in the *rotating frame*. Here, the spectrometer reference frequency and phase are subtracted from the spin evolution

$$H_{rot} = R_z(-(\omega_{ref}t + \phi_{ref}))HR_z(\omega_{ref}t + \phi_{ref}) - \omega_{ref}I_z \qquad (2.92)$$

upon transformation into the rotating frame, and assuming $\phi_{ref} = 0$, Eqn. (2.91) simplifies to

$$H_{RF}(t) = -\frac{1}{2}\gamma_I B_{RF}(cos(\phi_p)I_x + sin(+\phi_p)I_y) \qquad (2.93)$$

2.10 Magic Angle Spinning

Manipulation of the spin interactions and their influence on the spectrum is often mandatory to obtain a spectrum containing the desired information with sufficient clarity. One general approach is the time dependent manipulation of interactions in spin space with RF pulses, through manipulation of the $\hat{T}$ component of the Hamiltonian. Another method, mostly used in solid state NMR, is called *Magic Angle Spinning* (MAS). Here, the sample is rotated around a "magic angle" of $\beta_m = tan^{-1}\sqrt{2}$ with respect to the outside magnetic field B_0. This introduces a time dependency into the real space part $\hat{A}$ of the interactions. Therefore the rotation of the secular, real space part of the Hamiltonian from the PAS to the laboratory frame under MAS can be expressed as

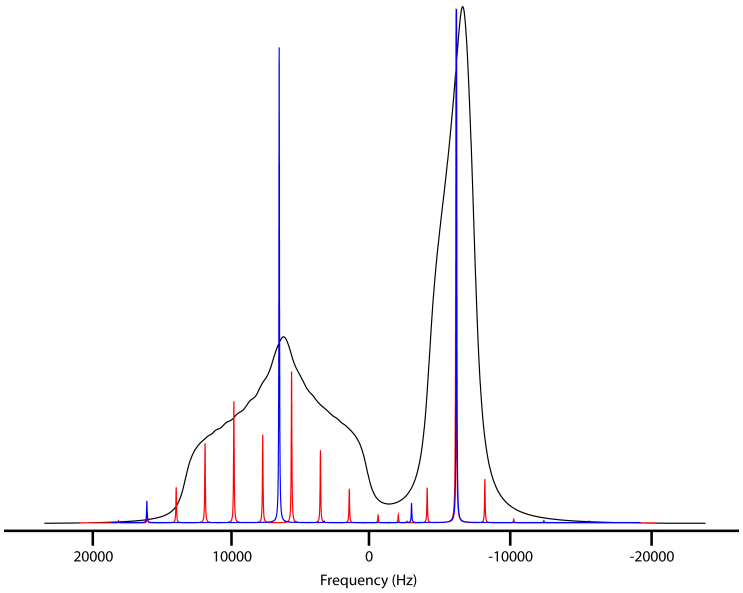

Figure 2.3: The effect of MAS on solid state NMR spectra: Shown above are the spectra of two spins ($\delta_{iso1} = -7300Hz, CSA_1 = -7000Hz, \eta_1 = 0.90$ and $\delta_{iso2} = 6100Hz, CSA_2 = -2000Hz.\eta_2 = 0.43$) at different spinning speeds. Spectra are shown for an MAS rate of 0Hz (black) 2000Hz (red) and 10000Hz (blue). The spectra have been scaled to the same maximum intensity.

$$H^{\Gamma} = C^{\Gamma} \sum_{l=0}^{2} \sum_{q,q',q''=-l}^{l} (-1)^q [\hat{A}^{\Gamma}_{lq''}]^P D^l_{q''q'}(\Omega^{\Gamma}_{PM}) D^l_{q'q}(\Omega^{\Gamma}_{MR}) d^l_{q0}(\beta_m)\ exp\{iq(\omega_R t - \alpha^0_{RL})\} \tag{2.94}$$

where Ω_{MR} is random for a powder sample and $D^l_{q0}(\Omega^{\Gamma}_{RL})$ was written in explicit form, to highlight the time dependence introduced to Ω_{RL} with MAS. It is worth noting that $d^l_{00}(\beta_m) = 0$ thus eliminating the influence of the secular part of the CSA and the dipolar couplings on the spectrum, as can be seen from Eqns. (2.80) and (2.83). The effect of MAS on the spectrum of a simulated two spin system is shown in Fig. 2.3 for 0, 2000 and 10000 Hz MAS frequency.

2.11 The Density Matrix

So far only one or two spins were considered. The spin systems involved in most NMR experiments are usually much larger, although a given spin commonly interacts with but a small subset of all spins present in the system. To describe such systems, one uses the *density operator* ρ. For the definition of this operator, one first has to find all states, which the spin system can assume. These are given by

$$|\psi_j(t)> = \sum_{i=1}^{N} c^j_i(t)|i> \tag{2.95}$$

with $c^j_i(t)$ being a factor determining the contribution of the spin state $|i>$ to the overall state of the spin system. With this definition the density operator for a point in time t can be described as

$$\rho(t) = \sum_{s,k} p_{sk}(t)|s><k| \tag{2.96}$$

with p_j being the probability of finding the spin system in the state j. If the density operator for a spin system is known, the quantum mechanical expectation value for an operator $\mathbf{O}$ is given by

$$< \boldsymbol{O} > (t) = Tr\{\rho(t)\boldsymbol{O}\} \tag{2.97}$$

the matrix elements of $\rho(t)$ can be determined using

$$\rho_{sk}(t) =< s|\rho(t)|k > \tag{2.98}$$

for $\rho_{sk}(t)$ it holds that

$$\rho_{sk}(t) = \overline{c_s^j(t)c_k^j(t)^*} = \overline{|c_s^j(t)||c_k^j(t)|exp\{i(\phi_s(t) - \phi_k(t))\}} \tag{2.99}$$

with $\overline{c_s^j(t)c_k^j(t)^*}$ representing the ensemble average. This implies the existence of two types of matrix elements in the density operator. The first are called populations and are situated at the diagonal ($s = k$). These elements represent the z-components of the individual spin states and are proportional to $\overline{|c_s^j(t)|^2}$. The second type of matrix elements are called *coherences* ($s \neq k$) and are given by the off diagonal elements. For these elements to occur, the two states $|s >$ and $|k >$ must form a superposition state (both factors $c_s^j(t)$ and $c_k^j(t)$ must be nonzero for at least one state of the spin system $|\psi_j(t) >$) and the phases $\phi_s(t)$ and $\phi_k(t)$ must be correlated over the ensemble. The so called *coherence order* depends on the position of the coherence in the matrix. For a system of two spins there can be zero, single and double-quantum coherences. These correspond to the following spherical spin operators

- zero-quantum coherence : $I_s^+ I_k^-$, $I_s^- I_k^+$
- single-quantum coherence : I_s^+, I_s^-, I_k^+, I_k^-
- double-quantum coherence : $I_s^+ I_k^+$, $I_s^- I_k^-$

At thermal equilibrium, using the high temperature limit ($k_B T \gg |\hbar\omega_0|$), which is allowed at room temperature, the initial density operator for an ensemble of N spins I is often approximated by

$$\rho_{eq} \approx \frac{1}{2^{N_I}}\mathbb{1} + \frac{1}{2^{N_I}}\frac{\hbar\gamma_I B_0}{k_B T} I_z \tag{2.100}$$

Dropping the first term with $\mathbb{1}$, which has no influence on the NMR spectrum and the prefactor of the second term, which only gives the overall signal intensity, Eqn.(2.100) is simplified to

$$\rho_{eq} \approx I_z \tag{2.101}$$

2.11.1 Time Evolution and Propagators

The time evolution of the density matrix is described by the *Liouville-von Neumann equation*

$$\frac{d}{dt}\rho(t) = -i[H(t), \rho(t)] \tag{2.102}$$

The evolution of the state of a density matrix at a point in time t_1, $\rho(t_1)$ to a state at a later time point t_2 can be calculated using propagators, if the state at t_1 is known

$$\rho(t_2) = U(t_2, t_1)\rho(t_1)U(t_2, t_1)^\dagger \tag{2.103}$$

with the propagators fulfilling the conditions given in Eqns. (2.32) and (2.33). For example, the propagator for a RF pulse is given by

$$\begin{aligned} U(t_2,t_1) &= exp\{-i\omega_{RF}(cos\phi I_x + sin\phi I_y)(t_2-t_1)\} && (2.104)\\ &= R_z(\phi)R_x(\xi)R_z(-\phi) && (2.105)\end{aligned}$$

with ω_{RF} being the nutation frequency of the RF pulse, the flip angle ξ being $\omega_{RF}(t_2-t_1)$ and ϕ being the phase of the RF pulse.

2.11.2 The NMR Signal

Using the density matrix the complex NMR signal at a point in time t can be calculated using

$$s(t) \sim 2iTr\{\rho(t)\sum_{j=1}^{N} I_j^+\}exp\{-i(\phi_{rec}+\phi_{dig})\} \quad (2.106)$$

where ϕ_{rec} and ϕ_{dig} are the receiver and digitizer phases of the spectrometer.

2.12 The Average Hamiltonian Theory

In most NMR experiments the Hamiltonian cannot be considered time independent, for any length of time. This is especially true for MAS, as the sample is continually subjected to rotation, changing the orientation of individual crystallites with respect to the outside magnetic field B_0. This problem is corroborated by the application of RF pulses, which change the spin part of the Hamiltonian. Often these time dependencies cannot be solved analytically and have to be approximated by the *Averaged Hamiltonian Theory* (AHT). Given a time dependent Hamiltonian, using the AHT, a piecewise, time independent analytical approximation called the *effective Hamiltonian* $\overline{H}$ can be calculated using the *Magnus expansion*. The precision of the approximation is governed by the order to which the approximation is calculated, as the effective Hamiltonian can be written as

$$\overline{H} = \overline{H}^1 + \overline{H}^2 + \overline{H}^3 \ldots \quad (2.107)$$

The first, second and third order effective Hamiltonians are given by

$$\overline{H}^1 = \tau^{-1}\int_{t_0}^{t_0+\tau} dt H(t) \quad (2.108)$$

$$\overline{H}^2 = (2i\tau)^{-1}\int_{t_0}^{t_0+\tau} dt' \int_{t_0}^{t'} dt[H(t'),H(t)] \quad (2.109)$$

$$\overline{H}^3 = (6\tau)^{-1}\int_{t_0}^{t_0+\tau} dt'' \int_{t_0}^{t''} dt' \int_{t_0}^{t'} dt \left\{[H(t''),[H(t'),H(t)]] + [[H(t''),H(t')],H(t)]\right\} \quad (2.110)$$

with t_0 being the starting point and τ the interval, for which the effective Hamiltonian is calculated. Higher order terms exist, but are seldom included into the considerations, as their effect is generally small, as compared to the first and second order terms.

2.12.1 The Interaction Frame

If several time dependent interactions are present in a given system, it can be convenient to switch to a so called *interaction frame*. Consider for example a Hamiltonian consisting of two time dependent components, called $H_\phi(t)$ and $H_\psi(t)$ in the following. These components do not have to be commutable. Then a propagator can be constructed, such that

$$\frac{d}{dt}U_\phi(t_1,t_0) = -iH_\phi(t)U_\phi(t_1,t_0) \tag{2.111}$$

and

$$U_\phi(t_0,t_0) = \mathbb{1} \tag{2.112}$$

With this propagator, $H_\psi(t)$ can be expressed in the interaction frame as follows

$$\tilde{H}_\psi(t) = U_\phi(t_1,t_0)^\dagger H_\psi(t)U_\phi(t_1,t_0) \tag{2.113}$$

The propagator for $H_\psi(t)$ is then given by

$$\frac{d}{dt}\tilde{U}^\psi(t_1,t_0) = -i\tilde{H}_\psi(t)\tilde{U}_\psi(t_1,t_0) \tag{2.114}$$

and

$$\tilde{U}^\psi(t_0,t_0) = \mathbb{1} \tag{2.115}$$

This results in a propagator for the total Hamiltonian given by

$$U(t_1,t_0) = U_\phi(t_1,t_0)\tilde{U}(t_1,t_0) \tag{2.116}$$

This representation of the Hamiltonian can be used in conjunction with the AHT, by replacing the respective Hamiltonian operators in Eqns. (2.108) and (2.109). This can enhance the convergence of the Magnus expansion considerably, if a suitable Hamiltonian component is chosen to construct the interaction frame.

2.13 Theory of symmetry based recoupling sequences

The concepts discussed above are not only useful to explain the effects observed in NMR, but also serves as a powerful tool in the development of new solid state NMR pulse sequences.

The interplay of sample rotation, RF irradiation and nuclear spin interactions has been used in a variety of ways by Levitt at al. [23, 35–37]

The most important result of this work is that simple rules can be derived, governing which interactions are present, after each interval, for which the averaged Hamiltonian is calculated.

By employing the effects of sample rotation in real space and radio-frequency irradiation, which results in a rotation in spin space, on the averaged Hamiltonian, spin-spin and/or spin-field interactions can be selectively suppressed or recoupled, depending on the relative values of sample rotation, RF power and RF phase alterations.

The control over the nuclear spin interactions is even more elaborate, as only those parts of a given interaction can be recoupled, which show a distinct symmetry in real- or spin-space.

Together with coherence selection, this allows a high degree of control during the experiment.

In the following, a short introduction to these selection rules is given. A more elaborate treatment can be found in [37], where dual synchronized, symmetry based

Interaction	Space Rank l	Space Component m
Iso CS	0	0
CSA	2	-2,-1,1,2
homonuclear DD coupling	2	-2,-1,1,2
homonuclear J coupling	0	0
Interaction	Spin Rank λ	Spin Component μ
Iso CS	1	-1,0,1
CSA	1	-1,0,1
homonuclear DD coupling	2	-2,-1,0,1,2
homonuclear J coupling	0	0

Table 2.1: Homo-nuclear space and spin symmetry numbers for solids rotating at the magic angle

pulse sequences are described in great detail. These constitute a generalization of the theory of symmetry based pulse sequences to two or more channels. For better comparison the nomenclature from this work will be used in the following, with l corresponding to l_A, and λ corresponding to l_T in Eqn. 2.69.

As was discussed before in this chapter, the Hamiltonian describing the time evolution of the spin system can be divided into an internal and an external (RF) component.

$$H(t) = H_{int}(t) * H_{RF}(t) \tag{2.117}$$

Typical internal interactions are the homo-nuclear and hetero-nuclear dipolar coupling, the chemical shift and its anisotropy, J and possibly also quadrupole interactions. For a detailed analysis of the internal Hamiltonian, it is advantageous to employ a description of the involved interactions in terms of spherical harmonics. These are detailed above and are especially suited to describe the spin system under spatial and/or spin rotation.

Thus, the internal Hamiltonian can be described as:

$$H(t) = \sum_{I,l,m,\lambda,\nu} H^I_{l,m,\lambda,\nu}(t) \tag{2.118}$$

Here, I is the interaction in question and l is its rank regarding rotations in space (with the components m = -l, -l+1,,l) and λ the rank concerning rotations in spin-space (μ = -λ, -λ+1,, λ). To describe the selection rules used by the sequences introduced by Levitt, first the type of recoupling sequence has to be chosen. There are two types: the C and the R type of recoupling sequences. The difference between the two is that in a C sequence the phase of the RF pulses is continually incremented by a certain constant amount, while during a R sequence the phase of the RF irradiation is switched back and forth between $\pm$ a constant value. These phase values, together with the other parameters of the recoupling sequence can be calculated as follows:

First, three symmetry numbers need to be chosen: N is the number of basic elements in one complete recoupling block of the pulse sequence (which can be concatenated if a longer recoupling time is desired), n is the number of space rotations during that time and ν is the proportional to the phase change from one element within the recoupling block to the next. During a C type sequence, the individual elements of the recoupling block consist of 2π pulses. These are often implemented as composite pulses, such as $\pi/2_0 - 2\pi_{180} - 3\pi/4_0$ to increase the fidelity of the spin rotation angle, and thus the stability of the overall recoupling.

From one element to the next, the phase is incremented by $2\pi\nu/N$. The RF power of the pulses is chosen such that N of those elements fit in n number of rotation periods of the MAS rotor.

Interaction	Space Rank l	Space Component m
Heteronuclear DD coupling	2	-2,-1,1,2
Heteronuclear J coupling	0	0
Interaction	I Spin Rank λ_I	I Spin Component μ_I
Heteronuclear DD coupling	1	-1,0,1
Heteronuclear J coupling	1	-1,0,1
Interaction	S Spin Rank λ_S	S Spin Component μ_S
Heteronuclear DD coupling	1	-1,0,1
Heteronuclear J coupling	1	-1,0,1

Table 2.2: Hetero-nuclear space and spin symmetry numbers for solids rotating at the magic angle

Employing a C-type recoupling sequence selects those terms of the effective Hamiltonian, for which the following equation holds:

$$\bar{H}^I_{l,m,\lambda,\nu} \neq 0 \; if \; mn - \mu\nu = NZ \tag{2.119}$$

In the case of R symmetries the recoupling block is constructed by concatenating N/2 pairs of R elements, R and $R\prime$. Each element R and $R\prime$ effects a net rotation of the spins by π. The phase of R is given by $\pi\nu$/N and the phase of $R\prime$ is -$\pi\nu$/N. The complete recoupling block is then constructed by applying N/2 pairs of R and $R\prime$ elements, during n rotor periods. As with C-type symmetries, it is advisable to use composite pulses instead of simple π pulses during a R sequence. One example would be the $\pi/2_0 - 3\pi/2_{180}$ composite pulse described in [38, 39]. These pulses are reported to increase the tolerance of the recoupling block to RF offsets.

The major drawback of these composite pulses, which can be easily seen from their structure, is that generally the RF irradiation power has to be doubled. This can become problematic at higher spinning speeds, and in some cases a compromise between pulse flipangle fidelity and MAS speed has to be found.

To calculate the interactions which are active in the effective Hamiltonian of a R-type recoupling sequence, the following formula can be used:

$$\bar{H}^I_{l,m,\lambda,\nu} \neq 0 \; if \; mn - \mu\nu = \frac{N}{2} Z_\lambda \tag{2.120}$$

With Z_λ being an integer with the same parity as λ and H being the averaged Hamiltonian to first order. The values of l, m, λ and for the internal interactions are given in table 2.1.

From the equations given above, it can be seen that R sequences, in contrast to C sequences, are sensitive to the parity of λ, making R sequences more selective. This is especially important for the exclusion of the isotropic chemical shift, as here l is zero and thus in C type recoupling sequences, the m=0, μ=0 part is always recoupled. This part can be suppressed using R sequences, which is a very desirable property in most recoupling sequences.

The methodology presented so far is only concerned with single channel RF irradiation. This implies that only a single spin species is observed and interactions to other types of nuclei can be neglected. The latter point is generally untrue in solid state NMR, and thus usually at least hetero-nuclear decoupling is needed, even if the recoupling sequence itself is only concerned with a single RF channel. In this case, care has to be taken that proton channel decoupling or other pulse sequence elements do not perturb the performance of the recoupling sequence. This is normally achieved by using power levels well above the ones used for the recoupling sequence. As C- or R-type sequences tend to have a rather high power requirement at the spinning speeds

usually employed in the study of biological solids, this is not always an option. Thus in some cases a reduction of the recoupling performance has to be accepted, when hetero-nuclear decoupling is mandatory.

Extending the theory of symmetry based pulse sequences to more than one channel thus offers the highly useful possibility of incorporating hetero-nuclear decoupling or even hetero-nuclear polarization transfer into a recoupling sequence, as the interactions of different nuclei in the spin system are explicitly treated.

Here, only the resulting formula is given, which can be used to compute the symmetry numbers N,n and ν for a dual channel synchronized R-type recoupling sequence:

$$\bar{H}^I_{l,m,\lambda_S,\nu_S,\lambda_K,\nu_K} \neq 0 \; if \; mn - \mu_S\nu_S - \mu_K\nu_K = \frac{N}{2} Z_{\lambda_S+\lambda_K} \tag{2.121}$$

In this formula, s and k denote the recoupling blocks on the two channels. A list of symmetry numbers for hetero-nuclear interactions that can be recoupled in this manner is given in table 2.1.

It is also possible to use the C symmetry or even to mix R and C symmetries on the different channels of the recoupling block. The resultant symmetries are then denoted by $C/RN^{\nu,\nu}_n$.

The rules for the symmetry allowed terms in the effective Hamiltonian in case of a dual channel C-type or mixed C/R or R/C-type sequence can be easily derived from Eq. 2.121 by using the single channel rules for C sequences given in Eq. 2.119.

It is therefore always prudent to employ the rules for a multichannel sequence even for recoupling blocks designed for a single channel, as in some cases it turns out that no decoupling on the hetero channel is required. In these cases, all undesirable hetero-nuclear terms are removed by sample spinning and the RF irradiation on the channel of interest alone.

It is noteworthy, that the selection rules given above where derived, using the first order averaged Hamiltonian. Although mostly correct, the exact evolution of the spin system can only be described by using the second and higher order averaged Hamiltonian terms. There are also symmetry selection rules for the second order averaged Hamiltonian [37], but upon inspection it turns out that the selection in the second order is far less stringent than in the first order, which in some cases can lead to a significant contribution of terms, which are not symmetry allowed in the first order averaged Hamiltonian.

In addition to the points made above, it is important that all rules discussed in this section are based on the implicit assumption, that the RF-field applied to the sample is equal or greater than the spin interactions present.

Although this assumption is not used in the mathematical derivation of the formulas, the time interval which is to be calculated using the averaged Hamiltonian gets long if low RF power levels are used (assuming a constant symmetry). If this time interval is significant, compared to the evolution periods of the nuclear interactions, the first order averaged Hamiltonian does not approximate the active Hamiltonian very well, leading to a deviation of the calculated from the experimental results.

Chapter 3

Sensitivity Enhancement for ssNMR Spectra: RELOAD

3.1 Introduction

An especially important class of experiments for the study of membrane proteins with solid state NMR (ssNMR) are those that yield sequential assignments, which connect a given amino acid with its neighbors. The assignment of individual resonances to single amino acids in the protein primary sequence forms the basis for structural studies and is therefore indispensable, if a three dimensional model for a protein is to be elucidated.

This information can be gained by several experiments, for example the $C\alpha - N - CO - C\alpha$ introduced in [40], or the $C\alpha - C\alpha$ correlation experiments introduced in [5].

Generally, the main factor limiting the applicability of ssNMR is its comparatively low sensitivity, which can be particularly problematic in multidimensional experiments on biological samples. Low sensitivity implies long measuring times which can be a serious issue for samples with limited stability, for example peptides and proteins.

Therefore, sensitivity enhancement is vital for solid state NMR and is routinely achieved by a combination of magic angle spinning (MAS) and cross polarization (CP) [21]. In magic angle sample spinning the sample is rotated around an axis of 54,7° with respect to the outside magnetic field, to average anisotropic interactions, such as the dipolar coupling or the chemical shift anisotropy as outlined in chapter 2. Cross polarization is used to transfer ^1H polarization to a hetero-nucleus, typically ^{13}C or ^{15}N, resulting in a sensitivity gain of 4 or 10, respectively.

There are several other ways to decrease measuring time for solid state NMR spectra. Cryo MAS-NMR and dynamic nuclear polarization[41–45] are two methods to increase the polarization of the sample dramatically, but special equipment is needed for these methods to work, which is not generally available. Paramagnetic relaxation enhancement [46, 47] has also been employed in solid state NMR spectra for an increase of sensitivity per unit time, for samples that have been doped with a relaxation agent such as Cu^{2+}. A variety of processing schemes exist, that can decrease measuring time of certain spectra, such as covariance [27, 28, 48–53], harmonic inversion [54–56] or dual transformation denoising [57] and chapter 7. Another way to enhance sensitivity per unit time utilizes the fact that, although all hetero-nuclei of the same type are polarized with CP, there are experiments where not all of these spins are of interest.

A way to exploit this and decrease measuring time for multidimensional spectra is band selectivity. Here only a certain region of the spectrum, henceforth referred to as the region of interest (ROI), of the full spectrum is excited, and therefore the sweep

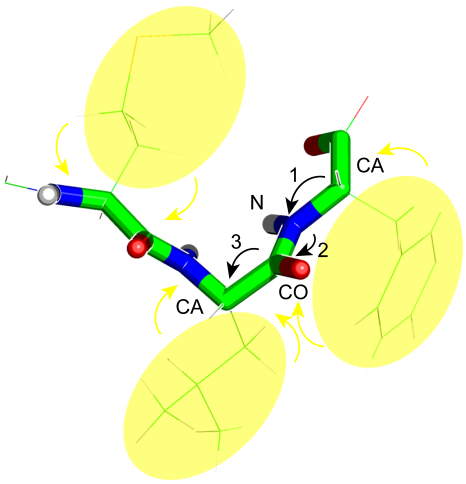

Figure 3.1: Transfer of magnetization during an $C\alpha - N - CO - C\alpha$ assignment experiment along the backbone of MLF as described in [40]. The order of the individual transfer steps is indicated by numbers. During this experiment, only the backbone resonances are of interest and the side chain atoms are usually not detected. Therefore it is possible to use the magnetization of the side chain ^{13}C atoms, which has been enhanced by cross polarization along with the backbone ^{13}C's, to lower the spin temperature of the backbone between two consecutive experiments via spin diffusion (as indicated in the picture with yellow arrows). This allows for a rapid repetition of the experiment, as long as there remains significant polarization on the side chain spins, as will be shown in the following.

width can be reduced dramatically. A potential problem for this approach in solid state NMR is, that an effective gain in S/N can only be achieved if the experiment in question is not sensitivity limited.

As sensitivity limitation is usually given in solid state NMR spectra, band selective experiments are normally not employed. A possible way around this limitation, leading to an effective gain in sensitivity per unit time lies in the aforementioned selectivity of band limited spectra.

For example, in the $C\alpha - N - CO - C\alpha$ experiment, only the backbone carbons and nitrogen are investigated, omitting the side chain resonances from the spectrum. Similarly $C\alpha - C\alpha$ sequential assignment experiments could be performed with a region of interest omitting CO and side chain resonances from the spectrum.

As only the region of interest is excited, the remainder of the spin system can be left unperturbed. In the following this unperturbed spin population will be referred to as the spin bath. This spin bath, although not relevant to the spectrum in question, still carries magnetization, which is enhanced via cross polarization in the same way as the excited spin population in the region of interest, as noted above.

During the course of the experiment, the region of interest is detected and thus dephased by T_2 relaxation, while the spin bath retains its full starting polarization, as long as it is stringently kept on the z-axis of the rotating frame.

This implies, that a given homo-nuclear experiment can be adjusted to make use of the aforementioned facts, as long as it is possible to conduct the experiment in a band selective fashion, the remaining magnetization of the spin system is left unperturbed and the spin system shows a cross relaxation sufficiently strong to replenish the ROI in a short time. Furthermore it is possible to extend this concept to hetero-nuclear spectra, in which case the transfer needs to start from a abundant spin species showing

strong cross relaxation, and the hetero-nuclear transfer is conducted in such a fashion, that the polarization of the majority of spins of the source species is retained.

A way to achieve this is to employ selective pulses, to affect only certain regions of the spectrum and leave others unperturbed. Thus, most pulses of a given sequence have to be replaced by selective pulses, which is especially simple in sequences relying almost exclusively on hard pulses.

The spin species, which is most amenable to the experiment outlined above is ^{13}C in biological samples, which due to its abundance, good spectral resolution and usually close proximity to ^{1}H nuclei is ideally suited as an abundant source.

The latter point is especially important for the given experiment, as a close proximity to protons will firstly lead to a good cross-polarization efficiency in solids, and secondly to a very broad zero quantum lineshape. This effects a high rate of spin diffusion via zero quantum "flip-flop" transitions, making the flow of spin order from the bath to the region of interest faster, and more efficient.

One example for an experiment, which would highly benefit from the aforementioned experimental setup, is a $C\alpha - N - CO - C\alpha$ correlation, schematically shown in Fig. 3.1. Here only the backbone magnetization is of interest and the side chains are normally not observed. At the end of this experiment, given the magnetization of the side chain nuclei is still intact, it is possible to transfer this magnetization to the backbone via spin diffusion, replenishing the spins of interest in a time shorter than ^{1}H T_1.

As relaxation of ^{1}H is normally the limiting factor for the recycle delay between two consecutive scans, using cross polarization, lowering this requirement can significantly shorten the time needed for an experiment with a good signal to noise (S/N).

For a description of the effects presented in this chapter, it is useful to introduce the term spin temperature. This term is used to reference to spin order and hence polarization. "Hot" spins show no, or only slight polarization, whereas "cool" spins have a high degree of order.

The main effect, which is employed in this chapter, is one of cross relaxation in a coupled spin bath, meaning the apparent relaxation of one subgroup of spins is enhanced, on the expense of the other spins in the system.

Thus, in a system of coupled spins, using selective pulses and keeping the polarization of the majority of the nuclei intact, it should be possible to exploit cross relaxation to enhance the apparent T_1 relaxation of a subgroup of spins.

In this chapter, the RELOAD (Relaxation Enhancement by Lower Overall Adjacent spin temperature Distribution) experiments are introduced, which in general are band limited correlation experiments, making extensive use of selective pulses and spin diffusion delays, to increase the scan rate in comparison to the conventional experiment, from which the RELOAD version is derived.

The utility of homo-nuclear, as well as hetero-nuclear RELOAD experiments are shown on the tripeptide f-MLF [58, 59] and it is demonstrated that a reduction of the measuring time by a factor of up to 2,6 is possible using the RELOAD adaption, instead of the conventional experiments.

A similar scheme has been employed by Brutscher et al. in solution state NMR, observing amide protons and using the remaining protons to cool the amides via spin diffusion in the so called SOFAST experiment [60–62].

To describe the RELOAD adaption of the proton driven spin diffusion (PDSD), double cross polarization (DCP) and rotational echo double resonance (REDOR) experiments, first the selective pulses, which have been used, will be introduced shortly.

Then the recovery rates will be compared for RELOADed and non-RELOADed inversion recovery (IR) experiments, to attain a measure of the factor by which the apparent relaxation of certain groups of nuclear spins can be enhanced.

Next, homo-nuclear RELOAD experiments are shown and the enhancement of the signal to noise is evaluated, which can be achieved via RELOAD.

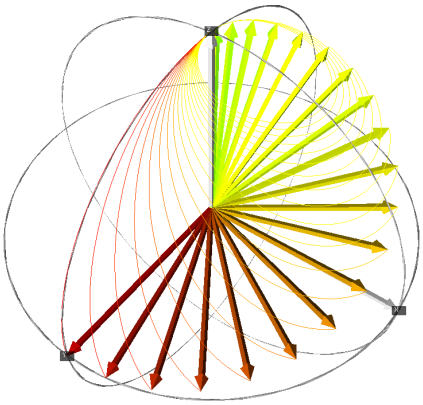

Figure 3.2: The effect of a finite carrier offset (off resonance irradiation) on the trajectories of magnetization rotation. Here the effect is shown for a 90° pulse. With an increasing offset from resonance, the spins are rotated by an effective field with an angle $\theta = arctan(\Delta B/B_1)$ from the x-y plane and a strength of $B_{eff} = (\Delta B^2 + B_1^2)^{1/2}$. This leads to cyclic trajectories, which can result in a rotation back to the z-axis for large offsets. Spins, for which this holds, are said to be outside the excitation range of the pulse. The relative magnitudes of B_1 and ΔB govern at which offset from resonance the spins are no longer excited. As the flip angle is given by $\omega_{nut} * \tau_{pulse}$, the use of a long pulse with a small B_1 field can be employed for selective excitation.

Finally the hetero-nuclear application of RELOAD is explored, and two commonly employed hetero-nuclear correlation techniques (DCP and REDOR) are compared as to their compatibility to RELOAD enhancement.

3.2 Selective Pulses

An integral part of band selective experiments are selective pulses. These pulses allow for the selection of certain regions of the spectrum, permitting the specific manipulation of individual spins or groups of spins. The simplest of all selective pulses is a soft rectangular pulse. For this pulse the radio frequency field, used for irradiation of the sample, is reduced while the pulse length is increased proportionally. This leaves the overall flip angle on resonance unperturbed, according to $\phi = \omega_{nut} * \tau_{pulse}$. Differences between this pulse and a hard pulse (with a high ω_{nut} and short τ) arise at frequencies removed from the carrier frequency (the center frequency) of the pulse. In the rotating frame, off resonance spins evolve under an additional field ΔB along the z-axis, which can be positive or negative, according to the sense of spin rotation. The magnitude of the field is given by $\Delta\omega$, which is the difference or offset of the spins resonance frequency from the RF carrier.

For on resonance spins, this field is zero and arbitrary combinations of ω_{nut} and τ can be used, as long as the product yields the desired flip angle, if only the isotropic chemical shift and the B_1 field interaction are considered. For off resonance spins this is no longer true, due to the presence of ΔB. Upon application of a B_1 field, the spins evolve under an effective field with a magnitude of $B_{eff} = (\Delta B^2 + B_1^2)^{1/2}$ and angle $\theta = arctan(\Delta B/B_1)$ with respect to the x-y plane. This results in a cyclic trajectory, which eventually carry the spins back to the z-axis at large offset frequencies, as shown in Fig. 3.2.

These spins show minimal rotation by the end of the soft pulse and are said to be

outside the excitation range of the pulse. Therefore the ratio of B_1 to ΔB governs the excitation range of a soft pulse.

Although rectangular pulses can be used for selective excitation and inversion of spins, there are drawbacks to this pulse shape. The sharp edges at the beginning and the end of the rectangular pulse cause wiggles in the excitation spectrum of the pulse. This can be appreciated by the Fourier transform of the shape, as shown in Fig. 3.3 a). It can be seen that the frequency excitation profile shows local maxima outside the main excitation area, which can lead to the selection of unwanted magnetization, especially in spectra with many resonances of considerable dispersion.

It has to be mentioned that the Fourier transform gives only a rough first approximation of the frequency excitation profile of a shaped pulse, as the assumption of a linear excitation response is only justified for small flip angles, so that $sin\alpha \approx \alpha$. Still, Fourier transformation is an easy way to get an idea about the frequency characteristics of a pulse shape.

To get rid of these wiggles, the edges of the rectangular pulse are removed in so called sinc pulses. The sinc shape is defined by $|sinx/x|$, and is often truncated after the first zero crossing. This results in a strong attenuation of the off resonance excitation.

Another possibility is the use of a Gaussian pulse shape, as the Fourier transform of a Gaussian results in another Gaussian. This property can be appreciated from the excitation profile shown in Fig. 3.3 b). Here it can be seen that only the region around the carrier is significantly excited, leading to a much better profile for this shape, as compared to the rectangular pulse.

Although unwanted excitation outside the desired region can be suppressed using a sinc or Gaussian shape, these profiles are still not optimal if larger spectral regions are to be excited. The reason for this is the influence of the ΔB field inside the selected region. It causes a tilt of the effective field, which leads to phase errors and non uniform excitation intensities, as the circular magnetization trajectories result in a distribution of the spins according to their offset from resonance, as shown in Fig. 3.2.

To circumvent these problems several shapes have been reported in the literature, such as half Gaussian [63] or Gaussian cascades [64]. The latter uses a combination of time shifted Gaussian pulse shapes to effect selective excitation or inversion. The time and Fourier transformed frequency profile of a Gaussian cascade is shown in Fig. 3.3 c). Here it can be seen, that the Gaussian cascade, in addition to the good phase behavior reported in the literature, features a so called top hat excitation profile. The splitting seen in Fig. 3.3 c) is a consequence of the Fourier transform, and does not appear if a better method for pulse profile evaluation, such as explicit calculation of magnetization trajectories using the Bloch equations, is employed (see [64]). This profile is favorable, as now a good phasing behavior and a uniform excitation response can be achieved for the whole region selected by the shaped pulse.

To optimize the selective pulses for the following experiments the pulse sequences shown in Fig. 3.4 were used. The sequence used in a) is a simple 90° pulse sequence using a selective pulse of the desired shape for excitation. The sequence shown in b) uses a selective inversion pulse to rotate the magnetization in the selected region to the -z-axis and then excites the whole spin system with a hard 90° pulse. In all cases the spectral region was selected with a carrier offset jump. No phase modulation was employed to shift the excitation frequency for any of the pulses.

The results for the optimizations are shown in Figs. 3.5 and 3.6, for selective excitation and inversion, respectively. It can be seen that the CO, $C\alpha$ and $C\beta$ spectral regions could be excited specifically, with high fidelity in phase and intensity. Selective inversion was optimized for $C\alpha$, $C\beta$, the side chain resonances (defined here as all carbons in the side chain beyond $C\beta$) and combinations thereof. The selectivity is good in all cases and the relaxation losses due to the use of shaped pulses were small.

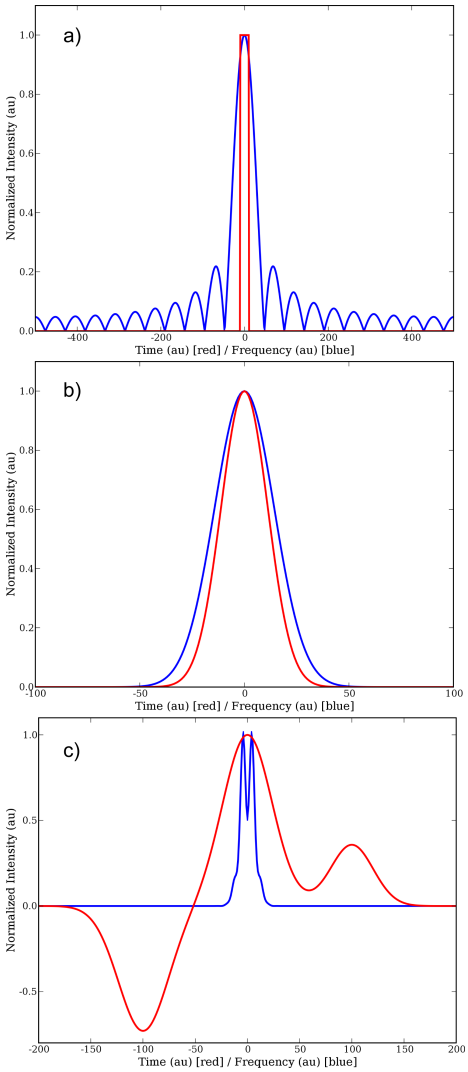

Figure 3.3: Fourier analysis of different pulse shapes: a) Time trace of a rectangular pulse (red), along with its Fourier transform (blue). Besides the main region of excitation around the carrier offset, multiple areas adjacent to the carrier offset show finite excitation. This sinc profile ($|sinx/x|$) stems from the sharp edges of the rectangular pulse leading to an overall poor selectivity of the shape. b) Time trace of a Gaussian pulse ($exp[-a(t-t_0)^2]$) along with its Fourier transform. Although Gaussian pulses afford good selectivity, the phase and the flip angle in the excited region are not uniform. A Gaussian cascade shape is shown in c). In the region of excitation the flip angle is nearly uniform and phase errors of the excited magnetization are minimal. The Gaussian cascade shown was calculated using $A[i] * exp(-\sigma[i] * (t - t_{offs}[i]))^2$, with an amplitude A of -1, 1.37, 0.49, the pulse width σ of 0.0009, 0.0009, 0.0012 and an offset time t_{offs} of 0.4, 0.5 and 0.6 seconds for the three pulses the Gaussian cascade comprises.

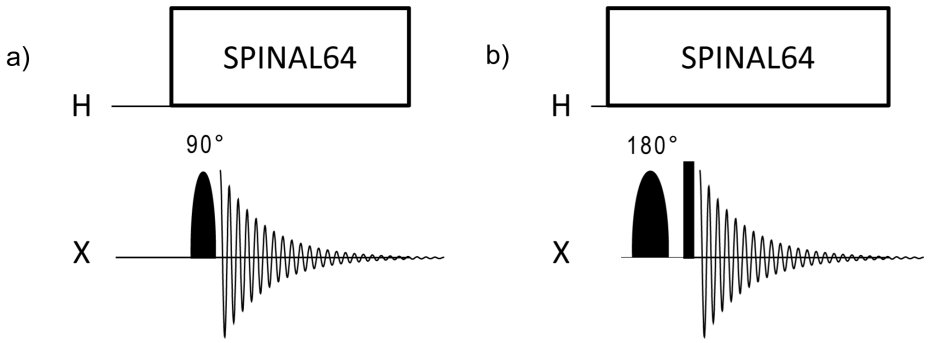

Figure 3.4: Sequences used for the optimization of selective pulses. In a) the sequence for the optimization of selective excitation pulses is shown. The selective pulse is applied and the resultant signal detected under ^1H decoupling. In b) the sequence for the optimization of selective inversion pulses is shown. Here, a region of the spectrum is inverted with a selective inversion pulse and the magnetization is read out with a 90° hard pulse immediately following the selective pulse. The signal is detected under ^1H decoupling.

In the following, sinc pulses have been mainly used for CO excitation and inversion, as for this region, the small spectral dispersion does not necessitate the use of more elaborate schemes, and Gaussian cascades for all other resonances.

3.3 Inversion Recovery

To assess the speed of magnetization recovery via spin diffusion using the RELOAD experiment, as compared to the normal relaxation of the sample, a variety of inversion recovery (IR) experiments were recorded.

The sequences used are shown in Fig. 3.7. To first investigate by how much the recovery of ^{13}C magnetization is sped up, using spin diffusion as compared to the normal spin relaxation, the ^{13}C relaxation of the sample was measured using the sequence shown in Fig. 3.7 a). Here, after polarization enhancement by CP, the ^{13}C magnetization is rotated from the x-y plane to the -z-axis. Following a certain inversion recovery time, which is incremented in the indirect dimension of the experiment, the magnetization is rotated back to the x-y plane and detected. The intensity of the signal is then observed to evaluate the return of the spin polarization to the positive z-axis.

Inversion recovery spectra of MLF are shown in Figs. 3.8 and 3.9, for short (10 nsec to 50 msec) and long (10 nsec to 10 sec) inversion recovery times. The steps were increased logarithmically in both cases. As can be seen from Fig. 3.8, no significant relaxation happens for the resonances of MLF in the time frame up to 50 msec, despite the presence of multiple fast relaxing methyl groups. Only at longer inversion recovery times do the resonances relax back to the positive z-axis, with the relaxation being 90% complete after 3 sec. This is more obvious in Fig. 3.10, where the inversion recovery has been plotted for all resonances in Fig. 3.9.

To observe the spin diffusion assisted relaxation, selective inversion recovery experiments, as shown in Fig. 3.7, were conducted. Here, after CP, all magnetization is stored along the positive z-axis using a hard 90° pulse. After selective inversion of a group of resonances, an inversion recovery time is allowed, which is sequentially increased along the indirect dimension of the experiment. After this time, the magnetization of the whole spin system is read out using a 90° hard pulse.

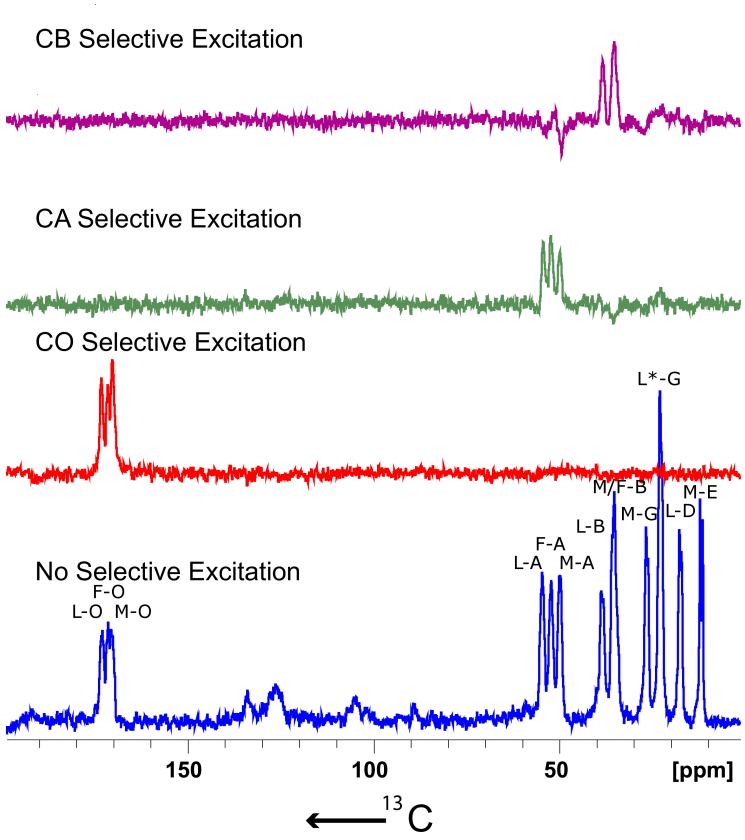

Figure 3.5: 1D ^{13}C selective excitation spectra of MLF. The blue spectrum is a MLF CP experiment shown for reference, with the assignments of the individual peaks. The red spectrum was recorded with the pulse sequence shown in Fig. 3.4 a). A sinc shape consisting of only the central lobe of the sinc pattern (see Fig. 3.3) has been used for excitation. The shaped pulse was 200 μsec long, and applied with an offset of 11000 Hz from the carrier, which was set to 100 ppm, to selectively excite the CO resonances. In the green spectrum the sinc shape was replaced by a Q5 Gaussian cascade, of 3.5 msec length and an offset of -7250 Hz from the carrier set to 100 ppm. This lead to selective $C\alpha$ excitation. To selectively excite the $C\beta$ resonances, the same Q5 pulse used for the $C\alpha$ region was employed, only with an offset of 9470 Hz with respect to the carrier frequency, as shown in the purple spectrum. All spectra were acquired at 600MHz ^1H frequency, 10 kHz spin rate, 295K and 4 scans.

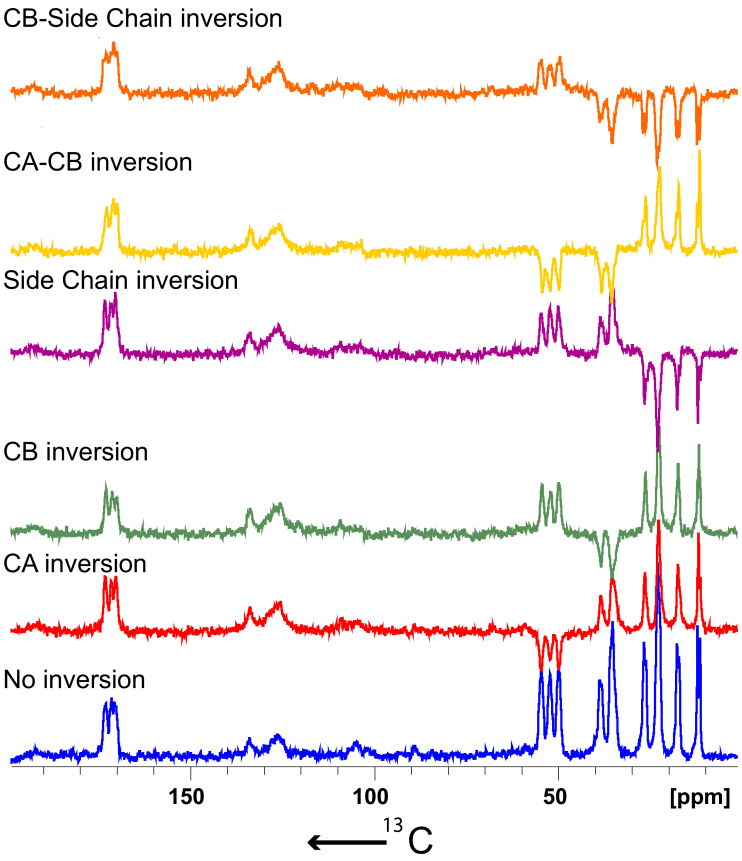

Figure 3.6: 1D ^{13}C selective inversion spectra of MLF. The blue spectrum is a MLF CP experiment shown for reference. All other spectra were recorded with the pulse sequence depicted in Fig. 3.4 b). In all spectra a Q3 Gaussian cascade was used, with a length and offset from the carrier (which was set to 100 ppm) of: 3.25 msec and -7250 Hz for selective $C\alpha$ inversion (red spectrum), 3 msec and -9470 Hz for selective $C\beta$ inversion (green spectrum), 1.5 msec and -12200 Hz for selective side chain inversion (purple spectrum), 1.3 msec and -8350 Hz for selective $C\alpha$ and $C\beta$ inversion (yellow spectrum) and 0.8 msec and -11250 Hz for selective $C\beta$ and side chain inversion. All spectra were acquired at 600MHz ^{1}H frequency, 10 kHz spin rate, 295K and 4 scans.

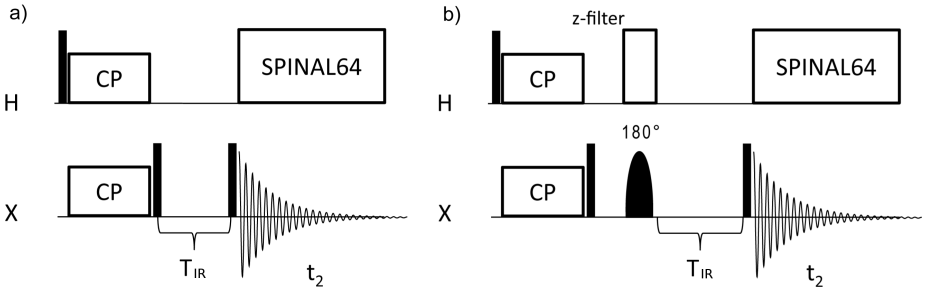

Figure 3.7: Comparison of an unselective and a selective inversion recovery sequence. In a) an unselective inversion recovery sequence is shown. After CP, the transverse magnetization is flipped to the -z-axis with a hard 90° pulse. After an inversion recovery time, which is varied along the indirect dimension of the two dimensional experiment, the magnetization is returned to the x-y plane for detection by a second 90° pulse. In the selective inversion recovery experiment shown in b), all magnetization is stored on the +z-axis by applying a hard 90° pulse directly after CP. Residual x-y magnetization is then purged using a z-filter. The spectral region to be investigated is inverted with a selective 180° pulse, which is followed by an inversion recovery period. The magnetization is read out after this delay with a hard 90° pulse.

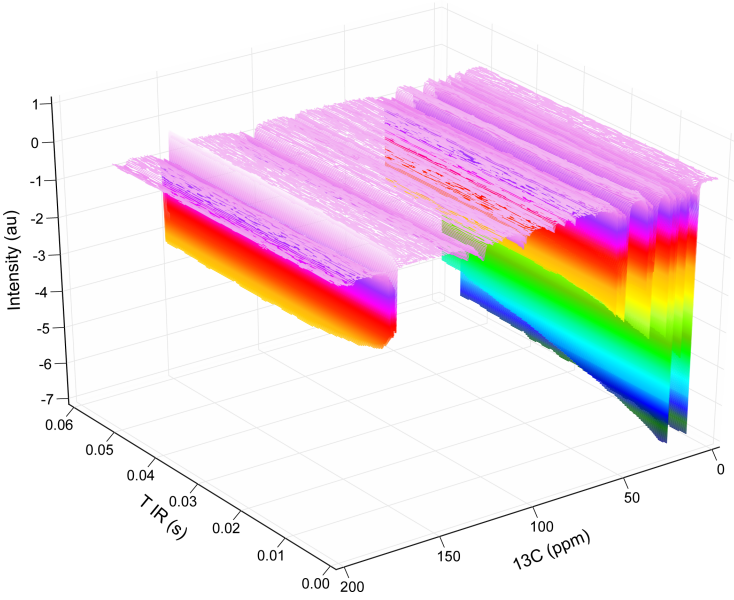

Figure 3.8: Inversion recovery experiment using the pulse sequence shown in Fig. 3.7 a). Here, the magnetization for all residues is inverted and the recovery back to the positive z-axis observed. Inversion recovery times of 10 nsec to 50 msec were used and 32 logarithmically increasing time steps were acquired. It can be seen that for this time frame, no significant relaxation of any of the resonances back to the positive z-axis can be observed. The spectrum was recorded with 32 scans per increment, 10kHz spin rate at 295K. The spectrum was processed with exponential line broadening of 20Hz in the direct dimension.

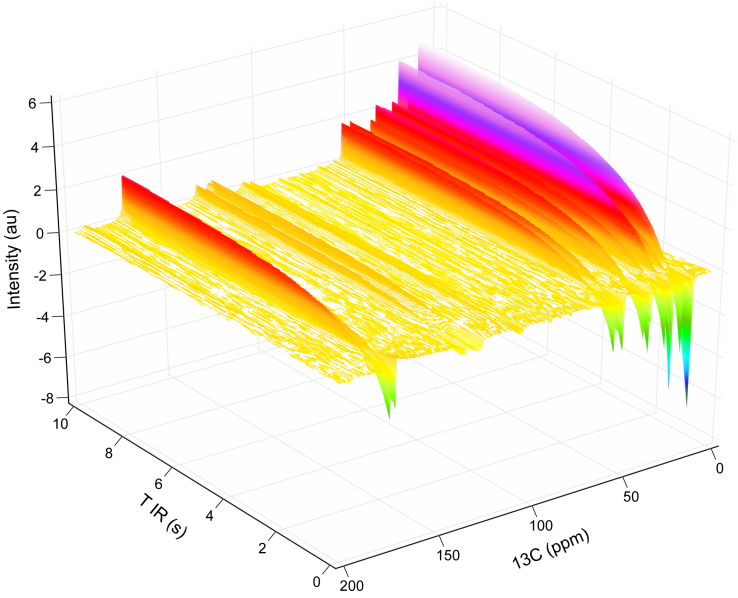

Figure 3.9: Inversion recovery experiment using the pulse sequence shown in Fig. 3.7 a), similar to the experiment shown in Fig. 3.8, but with inversion recovery times ranging from 10 nsec to 10 sec in 32 increments (the time steps were increased logarithmically). With the longer inversion recovery times, the relaxation of the MLF resonances can be determined to be mostly completed after 3 seconds. The spectrum was recorded with 32 scans per increment, 10kHz spin rate at 295K and processed with an exponential line broadening of 20Hz in the direct dimension.

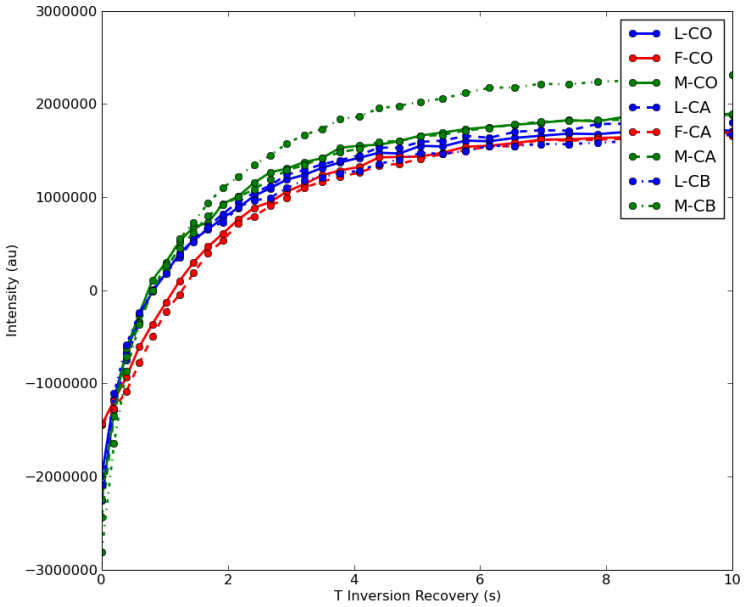

Figure 3.10: Evaluation of Fig. 3.9. The intensity for all resonances is plotted over the inversion recovery time. The inversion recovery is 90% complete after 3 seconds.

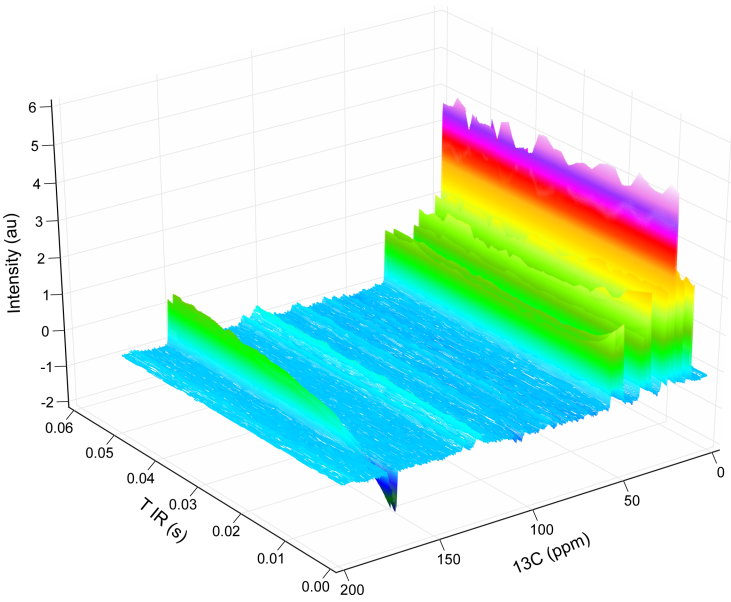

Figure 3.11: Selective inversion recovery experiment on the CO region of MLF, recorded with the sequence shown in Fig. 3.7 b). A Q3 Gaussian cascade was used for selective inversion. Inversion recovery times of 10 nsec to 50 msec were used in 32 increments (the time steps were increased logarithmically). The spectrum was recorded with 32 scans per increment, 10kHz spin rate at 295K and processed with exponential line broadening of 20Hz in the direct dimension.

The resultant spectrum for an selective CO inversion is shown in Fig. 3.11. It can be seen that the magnetization of the CO resonance recovers much faster than in the unselective case, with a concomitant decrease of the $C\alpha$ and, to a lesser extend, $C\beta$ residues.

This becomes clearer in Fig. 3.12. In this picture the fast return to the z-axis for the CO resonances can be appreciated, being 90 % complete after 25 msec. Furthermore a decrease of the $C\alpha$ magnetization, proportional to the CO recovery is observable, implying a transfer of spin polarization. The same effect occurs for the $C\beta$ residues, although with reduced magnitude.

For Phe, the effect on the $C\alpha$ is much more pronounced and the recovery of magnetization of the CO residues stops at the point of spin-thermal equilibrium of the CO and $C\alpha$ residues. This corroborates the assumption that magnetization transfer from neighboring nuclei is the main mediator of CO relaxation in this short time frame. The stronger effect on the Phe $C\alpha$ nuclei might be explained by ring flips of the phenyl moiety, which strongly perturbs spin diffusion from its nuclei to the rest of the MLF molecule, together with the absence of a bound proton on the $C\beta$ residue. For the other two residues, Leu and Met, the presence of strongly coupled $C\beta$ and side chain nuclei might help with the relaxation of the CO spins, via direct transfer of spin polarization and/or replenishment of the neighboring $C\alpha$ nuclear magnetization, thereby leading to a relayed transfer of polarization.

To corroborate these results and to investigate the behavior of the other resonances in the MLF spectrum, the above experiment was repeated with selective $C\alpha$ inversion. The resultant spectrum is shown in Fig. 3.13. This spectrum is evaluated in Fig. 3.14. Here it can be seen that the recovery of the magnetization is even faster than for the CO spins, most probably owing to the stronger coupling and smaller spectral

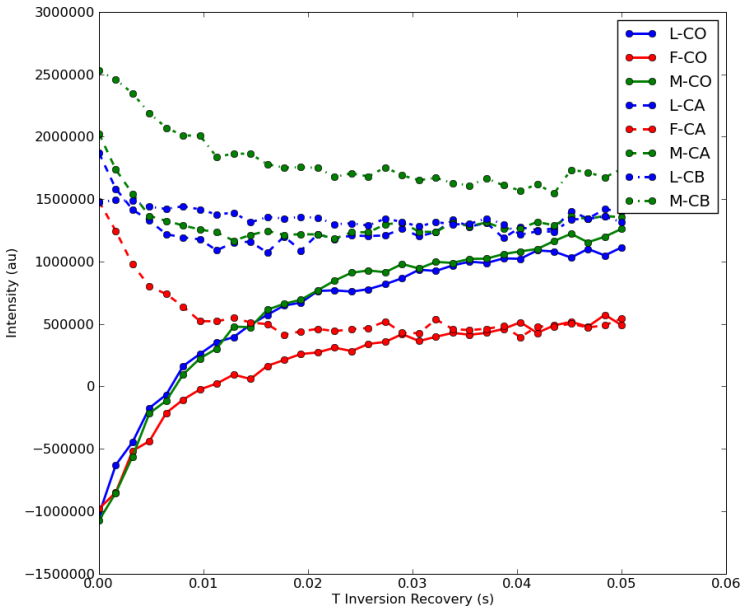

Figure 3.12: Evaluation of the spectrum shown in Fig. 3.11. Here, the magnetization of the inverted CO region is plotted with solid lines. The recovery of the inverted magnetization is rapid and nearly complete after 20 msec. The transfer of magnetization from the neighboring $C\alpha$ nuclei can be seen by the decrease of magnetization observed for these resonances, as the CO resonances return to the positive z-axis. The same effect is apparent for the $C\beta$ resonances, although the slope is not as steep as for the $C\alpha$. After 15 msec a significant portion of the CO resonances is recovered and the decline of the magnetization of the $C\alpha$ and $C\beta$ spins levels off as well.

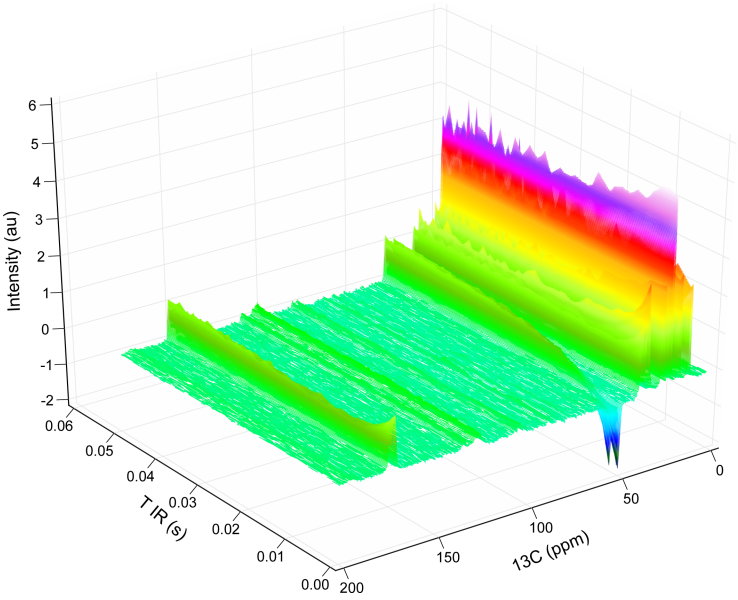

Figure 3.13: A similar experiment to the one shown in Fig. 3.11, but with selective inversion of the $C\alpha$ residues instead of the CO spins.

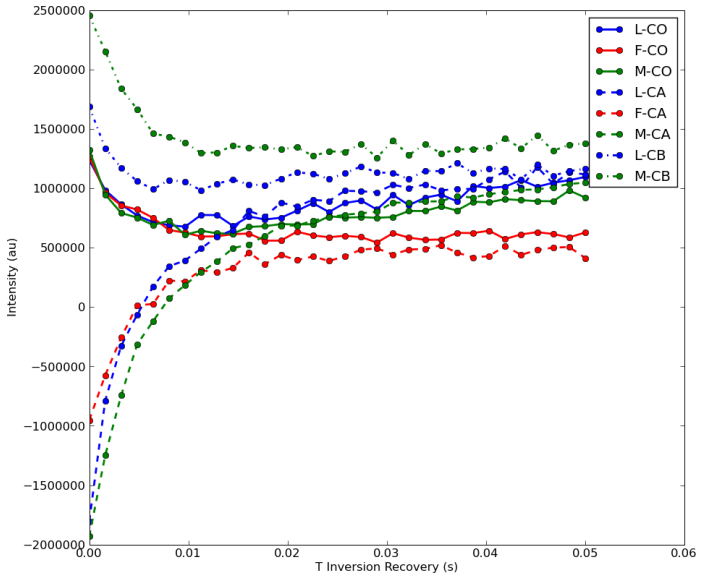

Figure 3.14: Evaluation of the spectrum shown in Fig. 3.13. Comparison with Fig. 3.12 reveals a faster magnetization recovery of the $C\alpha$ spins, as compared to the CO resonances. This is expected, as the directly bound proton and the spectral proximity to the side chain resonances lead to fast spin diffusion for the $C\alpha$ nuclei. Furthermore the decrease of the $C\beta$ nuclei is stronger than the one observed in Fig. 3.12, again probably due to the close proximity to the $C\alpha$ as compared to the CO resonances.

separation of the $C\alpha$ nuclei from the rest of the spinsystem. It is also noteworthy that the decrease of the adjacent nuclei CO and $C\beta$ is more uniform during the restoration of the $C\alpha$ magnetization. This corroborates the observation that the spacial, as well as spectral proximity of the spins acting as sources of magnetization plays an important role in the speed of magnetization recovery. Interestingly the recovery of the Phe $C\alpha$ resonance is more complete for this experiment, than for the selective CO inversion. Still the recovery is significantly reduced as compared to the Leu or Met resonances.

A slow, steady rise of magnetization is observable after the initial, fast recovery has been completed (after 20 msec in Fig. 3.14). This might indicate an equilibration of the magnetization of the inverted spins and its direct neighbors with more distant spins, leading to a recovery of polarization with a rate reduced by the distance to the source spins. The absence of this slow rise of magnetization for the Phe residue may indicate that the side chain nuclei are responsible for this phase of magnetization recovery.

The experiment was also performed with selective inversion of the $C\beta$ residues as shown in Figs. 3.15 and 3.16. Here, a behavior similar to the inversion recovery experiments selective on the CO region of the spectrum is observed, with the $C\alpha$ spins acting as a main source of magnetization and the CO resonances yielding only a small contribution.

A comparison of the relative rates of inversion recovery is shown in Fig. 3.17. Here, the inversion recovery is plotted for the Leu CO resonance, without (solid line) and with (dotted line) selective inversion. From this plot it is obvious, that the recovery of magnetization can be sped up by more than an order of magnitude, if a significant portion of the resonances of the spin system can be left on the z-axis, to act as sources of magnetization for the spins detected during the experiment.

In the context of the CP experiment, the ^1H T_1 relaxation is more important

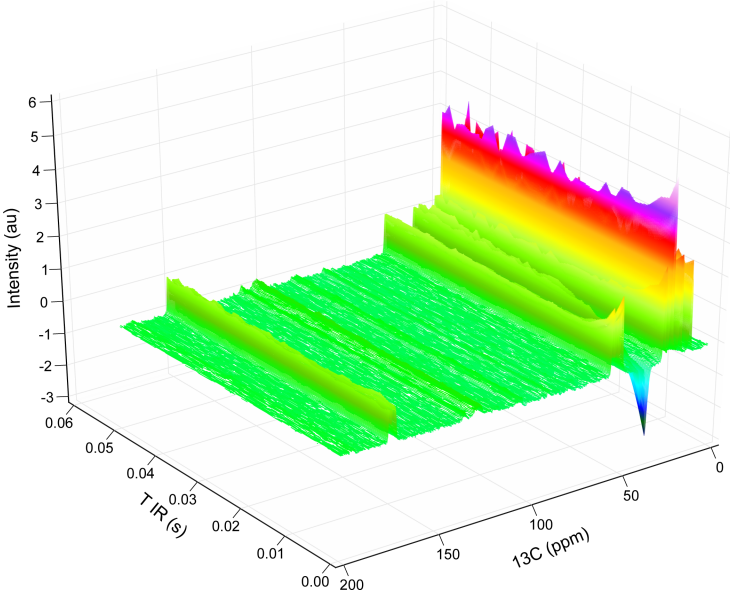

Figure 3.15: Same experiment as shown in Fig. 3.11, but with selective inversion of the $C\beta$ residues.

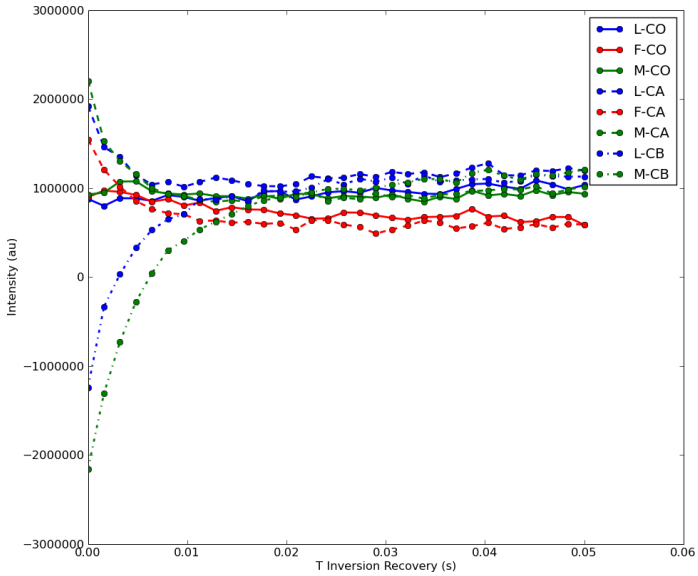

Figure 3.16: Evaluation of the spectrum shown in Fig. 3.15. Comparison with Fig. 3.12 and Fig. 3.14 shows a magnetization recovery with a rate similar to the $C\alpha$ spins. The decrease of magnetization is much more pronounced on the $C\alpha$ nuclei, as compared to the CO spins. This corroborates the observation in Fig. 3.12, that the spacial and spectral proximity of the resonances is an important factor for magnetization transfer for a given inversion recovery time.

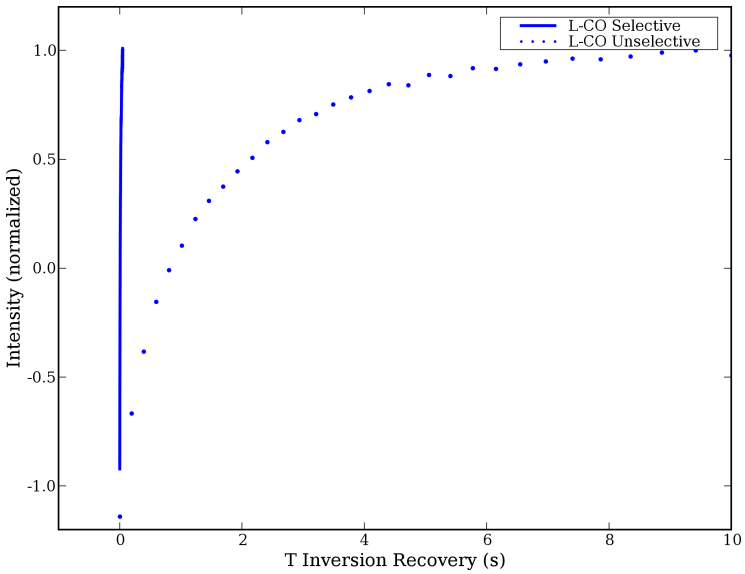

Figure 3.17: Comparison of the relative rates of the unselective and selective inversion recovery traces for the Leu *CO* resonance. The relaxation of the selectively inverted trace (solid line) is nearly complete after 30 msec, whereas the magnetization for the unselective experiment takes about 3 seconds to relax back to the positive z-axis. This indicates that considerable gains in the measuring time should be achievable using selective excitation in the context of RELOAD experiments.

than the ^{13}C relaxation. Due to the lack of resolution in solid state NMR spectra of protons, a study of similar detail to the one presented above was not possible. Still, optimization of the recycle delay time of a CP experiment show that the magnetization of the ^{1}H nuclei takes 1,5 to 2 sec to recover, for the given sample of MLF (data not shown). Although shorter than the recovery measured for ^{13}C, this is still significantly longer than the recycle delay times made possible by spin diffusion assisted relaxation.

3.4 RELOAD CP

To employ the effect observed in the previous section, and to investigate which gains in sensitivity per unit time are possible using RELOAD, one dimensional CP experiments were recorded using the pulse sequences depicted in Fig. 3.18.

In a) a normal CP sequence is shown, in which the ^{1}H magnetization is flipped to the x-y plane, via a 90° pulse, followed by a spin lock. An additional spin lock field is applied to the hetero-nuclear channel according to the Hartmann-Hahn condition under MAS: $\omega_{1\,H} = \omega_X \pm n * \omega_r$, where $\omega_{1\,H}$ and ω_X are the nutation frequencies of the spin lock fields applied to the proton and hetero-nuclear channel and ω_r is the MAS rotation frequency. n is any (usually small) integer. Following the cross polarization the signal is detected under ^{1}H decoupling. For signal accumulation the sequence is repeated with a recycle delay between experiments. This recycle delay depends on the ^{1}H relaxation of the sample. For proteins this is typically in the range of 1.5-3 seconds. In b) the RELOAD adaption of the CP sequence is shown. Here, the sequence is expanded with a hard pulse, directly after the cross polarization, which stores all magnetization on the z-axis. After a z-filter of 20-50 msec duration, which purges residual x-y magnetization, and later doubles as the RELOAD mixing time (the z-

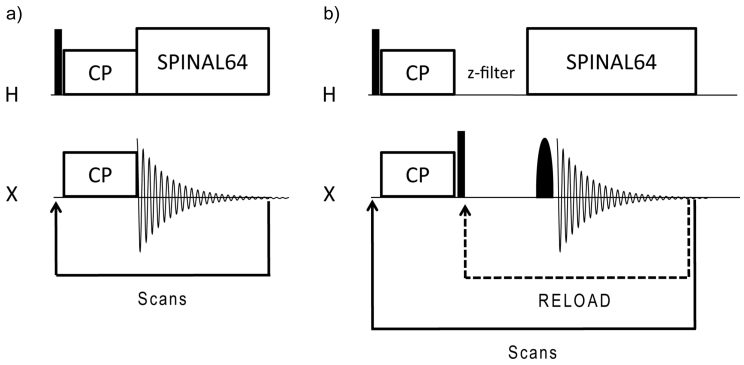

Figure 3.18: Comparison of a conventional CP sequence and its adaption to RELOAD. In a) a conventional CP sequence is shown, which employs a CP step for polarization enhancement on the hetero-nuclear channel. Then the signal is detected under ^1Hdecoupling. The recycle delay time for this kind of experiment is typically in the range of 1.5-3 seconds. In b) the RELOAD adaption of the CP sequence is shown. The sequence is expanded with a hard pulse, z-filter (20-50 msec) and a selective pulse, which only excites the region of interest. After detection, the sequence is cycled in an inner loop, pointing to the beginning of the z-filter (which therefore doubles as the RELOAD mixing time). In the following z-filter time, the magnetization of the region of interest is replenished and can be read out anew using the shaped pulse. This inner loop is repeated, until the magnetization outside the region of interest is depleted. Then the outer loop is executed, which corresponds to the normal scan loop of the conventional CP experiment. After the magnetization of the whole spin system is replenished, via CP, new set of inner loops can be conducted.

filter and the RELOAD mixing time can be considered synonymous for the rest of this chapter, as all z-filters used, double as reload mixing times, unless explicitly stated otherwise), the spectral region of interest is excited with a selective pulse, which leaves the rest of the magnetization unperturbed. After detection of the FID from the region of interest, the sequence is cycled in an inner loop, which returns the execution of the sequence to the point directly after the hard 90° pulse. In the following z-filter time, residual x-y magnetization is purged and the magnetization of the region of interest is replenished via spin diffusion from neighboring nuclei. After this RELOAD mixing time, the region of interest is read out anew using a shaped pulse. This inner loop is repeated, until the magnetization outside the region of interest is depleted. Then the sequence executes an outer loop, which comprises the recycle delay time and the cross polarization in the same way as in the non-RELOADed sequence shown in a). After cross polarization the magnetization of the whole sample is restored and a new set of inner loops can be conducted.

Therefore the total measuring time for experiment b) computes to:

$$T_{exp} = N * [T_{rec.del.} + T_{CP} + M * (T_{RELOAD} + T_{aq})] \tag{3.1}$$

as compared to:

$$T_{exp} = N * (T_{rec.del.} + T_{CP} + T_{aq}) \tag{3.2}$$

for the conventional CP experiment a). Here, T_{exp} is the total time the experiment needs, $T_{rec.del.}$ is the recycle delay time needed for ^1H relaxation between two successive cross polarization experiments, T_{CP} is the contact time of the cross polarization experiment, T_{RELOAD} is the time needed in between RELOAD experiments, to replenish the ROI magnetization from the bath and T_{aq} is the acquisition time.

So, assuming a typical recycle delay time of 2 seconds, a contact time of 1 msec, a RELOAD time of 50 msec and a acquisition time of 30 msec and 4 RELOAD cycles, the ratio $fracT_{exp}(RELOAD)T_{exp}(CP)$ works out to be 1.14.

The total enhancement of a RELOAD experiment needs to be divided by this factor, to obtain the sensitivity gain per unit time. s

To assess the gain in signal to noise ratio achieved with RELOAD, several spectra were recorded for the CO, $C\alpha$ and $C\beta$ resonances of MLF using the RELOAD CP sequence shown in Fig. 3.18. The evaluation of these spectra is shown in Figs. 3.19, 3.20 and 3.21 for selective CO, $C\alpha$ and $C\beta$ excitation, respectively. The z-filter was 50 msec in all cases. It can be seen that the gain in signal to noise (obtained by dividing the signal intensity relative to the conventional experiment, by the square root of the number of inner loops), is between 1.3 and 1.9 for all resonances, with the curve flattening off for a higher number of RELOAD cycles. This is to be expected, as the bath magnetization is depleted over multiple RELOAD cycles, yielding increasingly less effective recovery of the magnetization in the excited region of the spectrum.

To quantify this effect, and to assess how many RELOAD cycles can be performed using a certain RELOAD mixing time, several spectra of the CO region were recorded, using different combinations of RELOAD cycles and RELOAD mixing times with the sequence shown in Fig. 3.22. In this sequence, the RELOAD is repeated n times, with all FID's save the last one discarded by dephasing during the RELOAD mixing time. After (n-1) RELOAD cycles, the last FID is recorded, to assess the polarization received by the target spins after a certain amount of RELOAD loops.

The resultant spectra are shown in Fig. 3.23. It is apparent that for one RELOAD cycle the replenishment of the CO resonances is incomplete for short mixing times, with longer mixing times resulting in a better restoration of the magnetization. Furthermore, for a larger number of RELOAD cycles, the overall signal intensity decreases dramatically for short mixing times. Increasing the mixing time again alleviates this problem and the signal gain for a large number of RELOAD cycles stabilizes at a higher overall signal intensity. There are two possible reasons for this behavior. First, as was previously seen, longer recovery times lead to a second phase in the equilibration of the magnetization, which possibly stems from the slow interaction of the depleted spins of the excited region and its nearest neighbors with the more distant side chain resonances. A second reason could be an equilibrium between magnetization transfer and auto-relaxation of the spins, leading to a stabilization of the spin polarization which may be transferred at longer RELOAD mixing times.

Corroborating the measurements shown in Fig. 3.23, are the measurements of the effect of the RELOAD mixing time on the signal gained, with the sequence shown in Fig. 3.18 b). As shown in Fig. 3.24, for a small number of RELOAD cycles, the magnetization of the neighboring spins (the bath magnetization) is only mildly drawn upon and the diffusion to the CO resonances is the major step deciding on the efficiency of the RELOAD. Thus the RELOAD intensity, relative to the starting mixing time of 5 msec, increases for longer mixing times, but levels out quickly. For a higher number of RELOAD cycles, the RELOAD mixing time is more important, as can be seen from the marked increase in signal intensity for a given number of RELOAD cycles with longer mixing times. This is in accordance with the measurements shown in Fig. 3.23, where the RELOAD transfer is more efficient for a longer mixing time, given a large number of RELOAD cycles is employed.

It is noteworthy, that the increase in signal intensity for zero reload cycles in Fig. 3.24 stems from the equilibration of the differential polarization enhancements for the CO and $C\alpha$ residues, using CP at the spin lock time employed in the experiment. This effect is also apparent in Fig. 3.8.

The different spin diffusion pathways, which lead to magnetization recovery during a RELOAD mixing time, are shown in Fig. 3.25. Here, the direct transfer of magnetization is depicted as black arrows, originating from the spins directly adjacent to

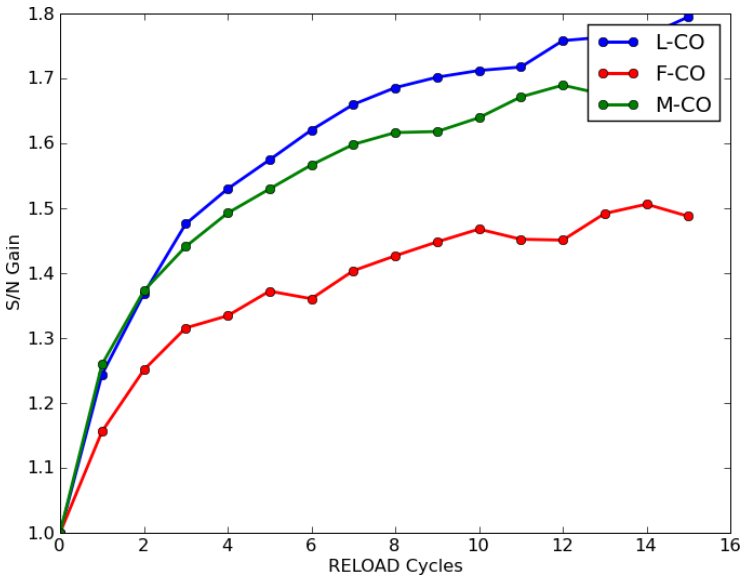

Figure 3.19: RELOAD CP gains: To investigate the gain which can be obtained for the ^{13}C resonances of the MLF backbone, the S/N is plotted over the number of RELOAD cycles for the CO resonances of MLF, using the sequence shown in Fig. 3.18 b). The number of RELOAD cycles was linearly increased from 1-16 in steps of 1. The RELOAD time was chosen to be 50 msec and 16 scans (outer loops) were recorded per increment. The spinning speed was 10kHz and the temperature 295K. It can be seen that the best enhancement of about 1.8 can be achieved for the Leu resonance, which is situated in the center of the peptide.

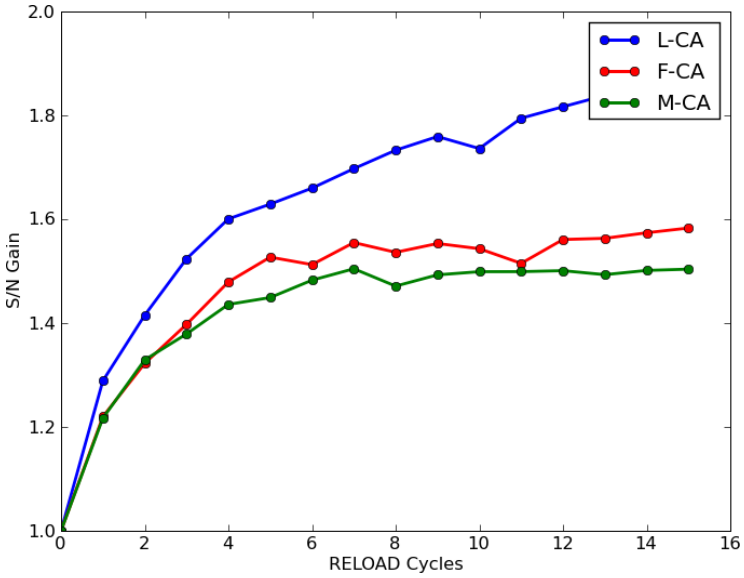

Figure 3.20: RELOAD CP gains: Same evaluation as shown in Fig. 3.19 but this time for the $C\alpha$ residues. Again the Leu residue shows the highest enhancement with about 1.8.

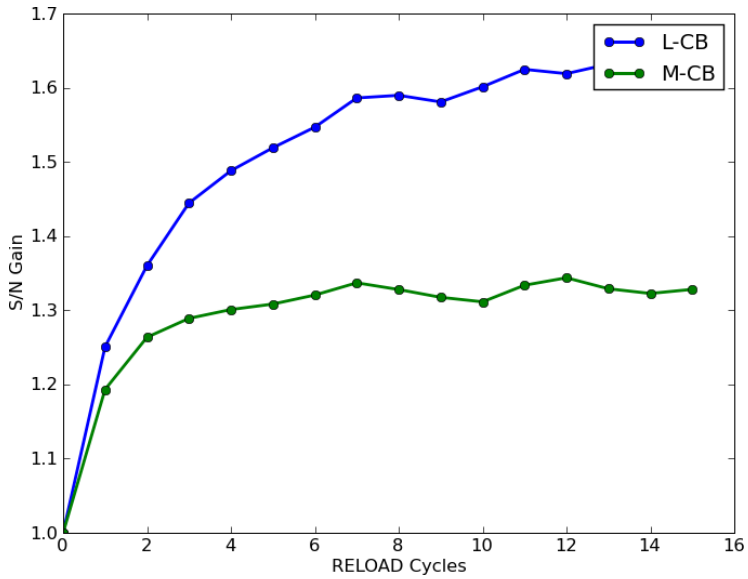

Figure 3.21: RELOAD CP gains: Same evaluation as shown in Fig. 3.19 but this time for the $C\beta$ residues. Again the Leu residue shows the highest enhancement with about 1.6. The Phe resonance was not resolved.

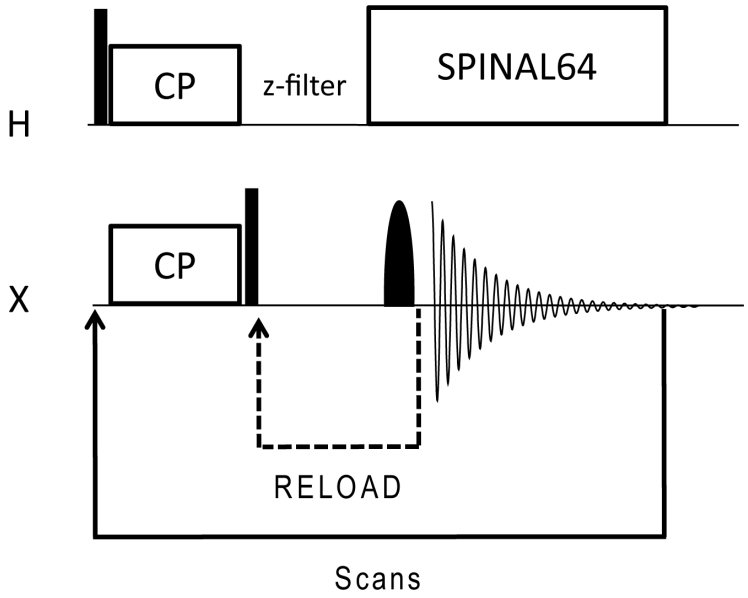

Figure 3.22: Investigation of the N-th RELOAD cycle: To test the efficiency of RELOAD, depending on mixing time and the number of RELOAD cycles, the sequence in Fig. 3.18 b) has been modified as shown above. Here, the RELOAD loop begins before the acquisition and the signal, which would be normally acquired, is dephased during the z-filter. Only after the last RELOAD cycle, the residual signal is acquired, whose intensity depends on the number of preceding RELOAD loops and the RELOAD mixing time, giving a measure of the maximum number of RELOAD cycles which can be employed.

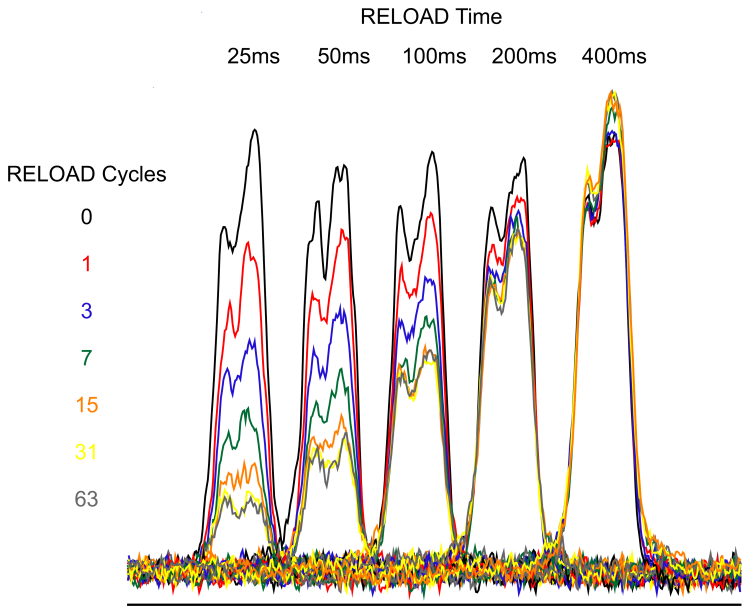

Figure 3.23: Investigation of the N-th RELOAD cycle: Spectra of the MLF *CO* region, acquired for several mixing times and RELOAD cycles using the sequence shown in Fig. 3.22. As can be seen from the spectra, short (25 msec) RELOAD mixing times lead to incomplete reloading of the *CO* resonances (signal loss after one RELOAD cycle) and rapid depletion of the bath magnetization (higher number of RELOAD loops lead to a accumulating attenuation of the signal). This behavior is reduced, if longer RELOAD mixing times are chosen, as can be seen from the overall higher signal after one RELOAD cycle and the reduced loss of signal after multiple RELOAD loops. At 400 msec the reloading and the relaxation of the system are in equilibrium and no further loss in signal upon successive RELOAD loops can be observed. At this long mixing time the difference between the RELOAD and a typical recycle delay is only of a factor 2-4 and thus for optimal gains in performance a compromise between sample relaxation and RELOAD mixing time has to be found. All spectra were acquired at 600MHz ^{1}H frequency, 10 kHz spin rate, 295K and 32 scans and processed with 20 Hz exponential line broadening.

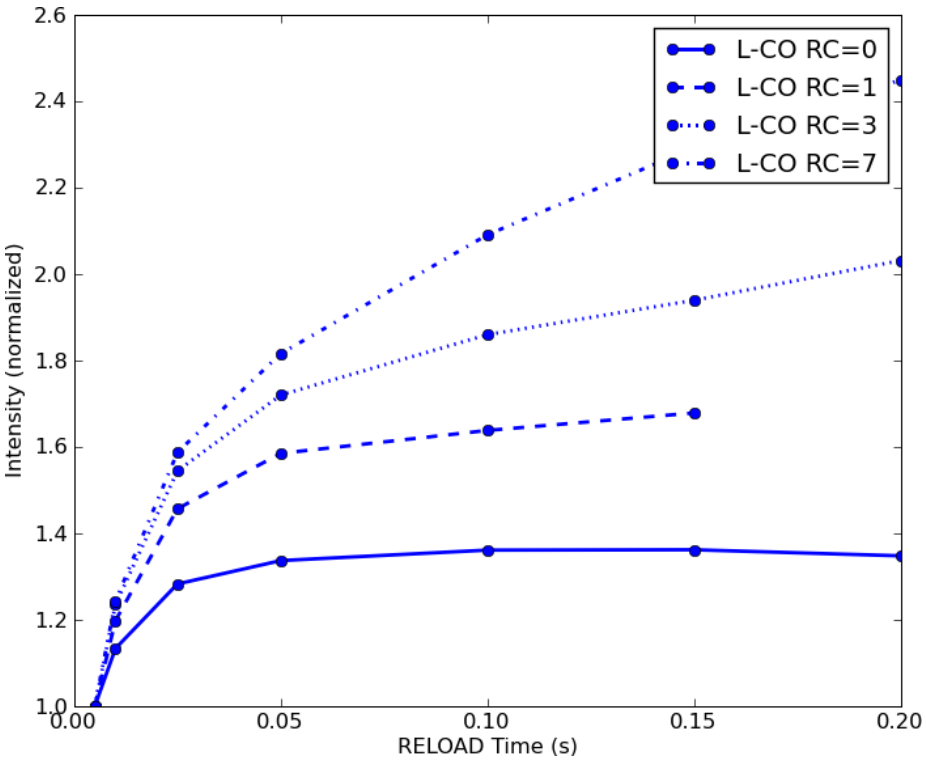

Figure 3.24: Buildup of the CP signal intensity for the MLF Leu CO resonance, for a range of reload cycles in dependence on the RELOAD mixing time. It can be observed that for a rising number of RELOAD loops the length of the RELOAD mixing time gains in importance for the signal enhancement that can be achieved. For a small number of RELOAD cycles (denominated as RC in the figure), the depletion of the bath magnetization is low and the transfer to the CO resonance is the dominating feature. Thus the enhancement quickly levels out. For a larger number of RELOAD cycles the bath magnetization is significantly depleted and thus the replenishment of the bath via relayed spin diffusion and auto-relaxation plays a bigger role. Thus longer RELOAD mixing times are required until the enhancement is saturated. The increase in signal intensity for zero reload cycles stems from the equilibration of differential polarization enhancements for the CO and $C\alpha$ residues at the CP spin lock time employed, an effect also apparent in Fig. 3.8.

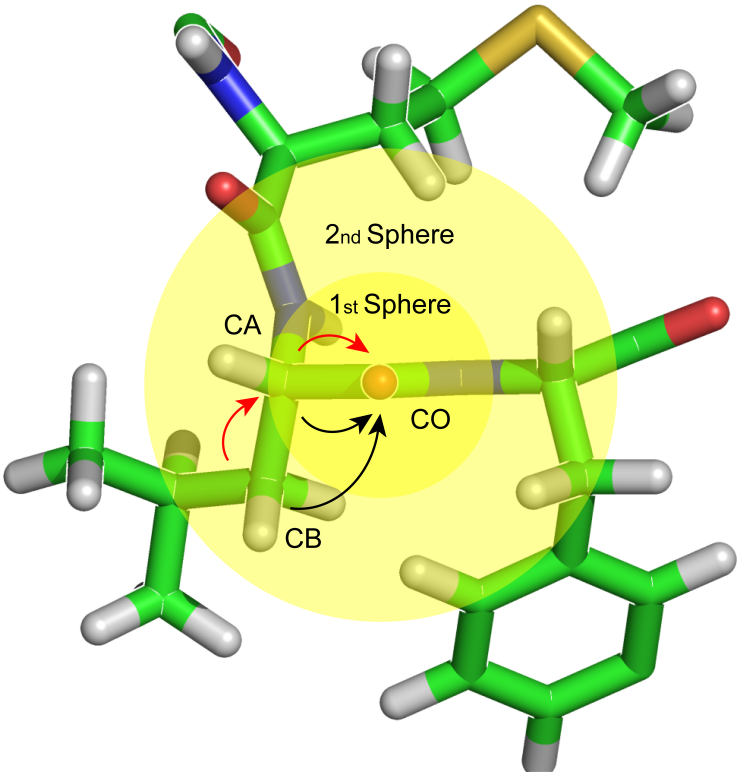

Figure 3.25: Scheme of transfer pathways contributing to RELOAD. The buildup of spin polarization during a RELOAD delay can be mediated by multiple factors. The strongest contribution is expected to result from spin cooling, mediated by spin diffusion from neighboring atoms of the same species. Above spin diffusion from the $C\alpha$ and $C\beta$ atoms to the CO of the Leu in MLF is indicated with black arrows. The range for which a significant contribution to the spin cooling of the CO spin can be expected is a function of the RELOAD delay, which acts as a mixing time for the spin diffusion. This is indicated in a simplified fashion by the spheres depicted above, which in reality would be more of a gradient, whose exact properties are given by the RELOAD delay time, the proton density, the resonance frequencies of the involved nuclei and the dynamic properties of the molecular area in question. Another effect, expected to occur in addition to the direct spin diffusion is relayed spin diffusion. Here, the nearest neighboring nuclei cool one another, which results in an indirect transfer of spin temperature along the side chain, indicated as red arrows between spheres 1 and 2. The auto-relaxation of the peaks excited during the experiment also plays a role, but is expected to result in a negligible contribution during a typical RELOAD delay (20-50ms) for the CO or $C\alpha$ resonances usually investigated via RELOAD. Auto-relaxation of side chain resonances could contribute to the recovery in this time frame, especially in close proximity to methyl groups.

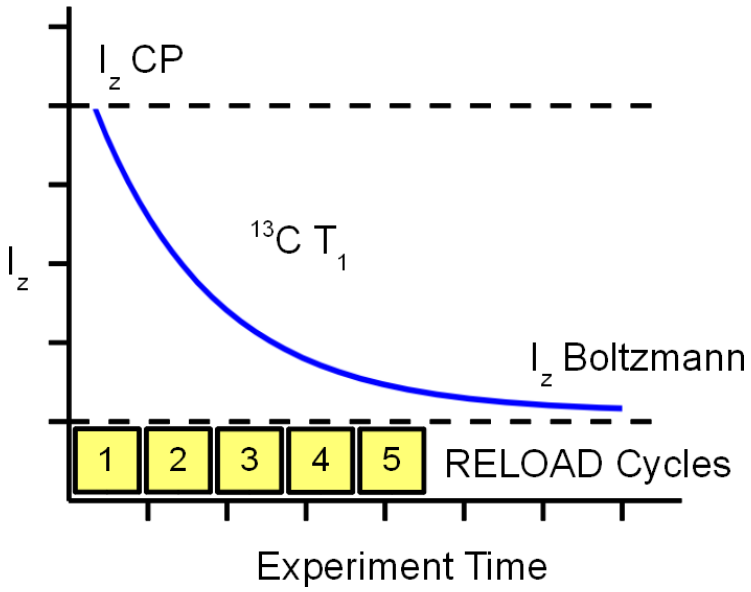

Figure 3.26: Schematic depiction of the decay of CP induced hyperpolarization with a decay rate governed by ^{13}C T_1. This decay of the complete sample magnetization back to the Boltzmann level, sets an absolute upper limit to the number of RELOAD cycles, which may be meaninfully employed for signal enhancement.

the nucleus to be RELOADed (schematically shown as first sphere) and spins more distant to the RELOADed nucleus (second sphere). The number of spheres which contribute to this effect is determined by the RELOAD mixing time. A second effect is the polarization transfer from the second to the first sphere, which in turn transfers its polarization to the nucleus to be RELOADed. This is shown as red arrows. For longer mixing time this effect can extend to a large number of successive spheres, which would explain the slower second phase of magnetization recovery observed in Figs. 3.12, 3.14 and 3.16. In addition to these effects the auto-relaxation of the involved spins is active, which might play a role for longer RELOAD mixing times, especially for fast relaxing methyl groups and their direct neighbors. For these spins an equilibrium between auto-relaxation and spin diffusion might be reached, explaining the stabilization of the RELOAD intensity with longer mixing times.

The sphere description given above is obviously only a simplified model. In a more realistic approximation the spheres would correspond to a spin diffusion gradient, whose exact properties are given by the RELOAD delay time, the proton density, the resonance frequencies of the involved nuclei and the dynamic properties of the molecular area in question.

Furthermore it is important to point out that the longitudinal relaxation of ^{13}C after CP polarization transfer, leads to an decay of the overall magnetization of the sample. This decay, together with the time each RELOAD cycle takes, sets an absolute upper boundary to the number of cycles which may be meaningfully employed to enhance the signal of the sample, irrespective of all other effects. This is depicted in Fig. 3.26.

In summary RELOAD could be confirmed to lead to signal enhancement for band selective CP spectra. Furthermore the RELOAD mixing time was found to be an important parameter, if a large number of RELOAD cycles is to be employed. As a longer mixing time leads to longer experiments, the time advantage offered by RELOAD is

lessened, as compared to a normal experiment without RELOAD. Therefore a compromise between the mixing time and the number of RELOAD cycles has to be found for optimal sensitivity gain per unit time. Our measurements so far indicate that such a compromise, which also has to take the maximum duty cycle of the probe into account, is likely to result in a reduction of the measurement time of a factor of 2-3 (the square of the signal to noise enhancement of 1.4 to 1.8 for a RELOAD time of 50 msec).

3.5 Application of RELOAD to homo-nuclear correlation spectra

In the previous section, it was shown that a RELOAD adaption of the CP experiment leads to a significant gain in sensitivity per unit time. It is therefore interesting to investigate the applicability of RELOAD to multidimensional experiments.

Homo-nuclear correlation experiments play an important role in NMR, as these spectra not only offer superior resolution, as compared to one dimensional experiments, but yield additional information about the spacial proximity of two residues in the spectrum, if the dipolar coupling is used as a mediator of spin interaction.

One important experiment of this type in solid state NMR is the proton driven spin diffusion (PDSD) experiment [33], the sequence of which is shown in Fig. 3.27 a).

In this experiment, the ^1H magnetization is transferred to a hetero-nucleus via cross polarization. Following the CP the indirect dimension is evolved under ^1H decoupling. After evolution, a 90° hard pulse is applied, which rotates the magnetization perpendicular to the pulse phase back to the z-axis. Next, the proton decoupling is switched off. This leads to a dephasing of all magnetization not on the z-axis, resulting in an effective selection of magnetization and encoding of the frequency information in the indirect dimension. Furthermore, the deactivation of the proton decoupling leads to a broadening of the energy levels of the individual resonances, by merit of the couplings of each hetero-nucleus to the surrounding protons. The resultant energy overlap facilitates a homo-nuclear zero quantum transfer of magnetization from the resonances selected by the 90° pulse (the source spins) after evolution to their neighboring nuclei. After a certain mixing time, the proton decoupling is reactivated and the magnetization is read out using a hard 90° pulse. As with the CP experiment the experiment is repeated multiple times and the signal is co added with a 1.5-3 sec recycle delay between experiments for most biological samples.

The pulse sequence used for a RELOADed, band-selective version of PDSD is shown in Fig. 3.27 b). The sequence of the normal PDSD is expanded by a z-filter of 20-50 msec length, prior to the evolution period, which serves the twin purpose of purging magnetization left on the x-y plane after the hard 90° pulse and as a mixing time for the RELOAD experiment. Furthermore all hetero-nuclear hard 90° pulses are replaced by shaped pulses.

After a 90° pulse on ^1H, magnetization is transferred to a hetero-nucleus (in this case ^{13}C) via cross-polarization. The magnetization of the whole spin system is then stored on the z-axis, via a 90° hard pulse. After a z-filter, used to remove artifacts from pulse imperfections from the spectrum, the spectral band of interest in the indirect dimension is excited using a shaped pulse.

Sinc shapes of $200\mu s$ and Gaussian Cascades (Q5) of 5ms length have been found to yield good selectivity and sensitivity for the carbonyl and $C\alpha$ region of the spectrum, respectively. After excitation and t_1 evolution of the carbonyl (for $CO - C\alpha$ correlation) or the $C\alpha$ (for $C\alpha - C\alpha$ correlation experiments) spins, the excited resonances are flipped back to the z-axis for PDSD zero quantum mixing, again using a selective pulse.

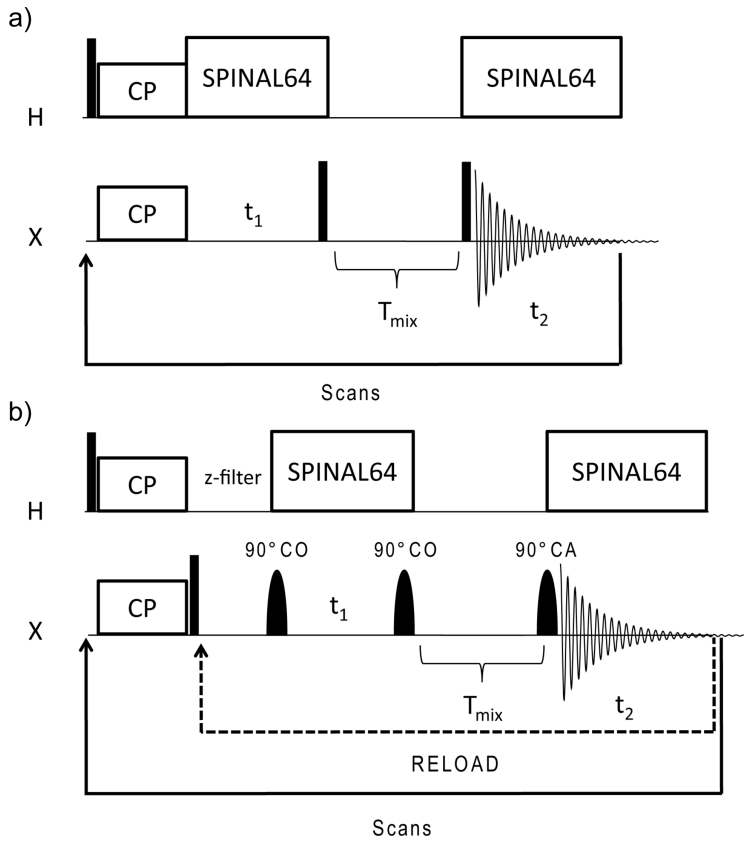

Figure 3.27: Comparison of a conventional PDSD sequence and its adaption to RELOAD. In a) a normal PDSD sequence is shown, in which the hetero-nuclear polarization is enhanced via CP. After evolution in the indirect dimension a 90° hard pulse rotates the magnetization to the z-axis. Next, proton decoupling is switched off, leading zero quantum mixing. After a set mixing time, the proton decoupling is switched back on and the magnetization is read out with a hard 90° pulse. In b) the RELOAD adaption of the PDSD sequence is shown. The sequence is expanded with a hard 90° pulse, a z-filter (20-50 msec) and a selective excitation pulse, which selects the spectral region of interest in the indirect dimension. Following evolution, the magnetization is rotated to the z-axis by another selective pulse. After PDSD mixing, the transferred magnetization is read out using an excitation pulse on the region of interest in the direct dimension. As with the RELOAD-CP experiment (Fig. 3.18), a nested inner loop is executed, which points to the beginning of the z-filter.

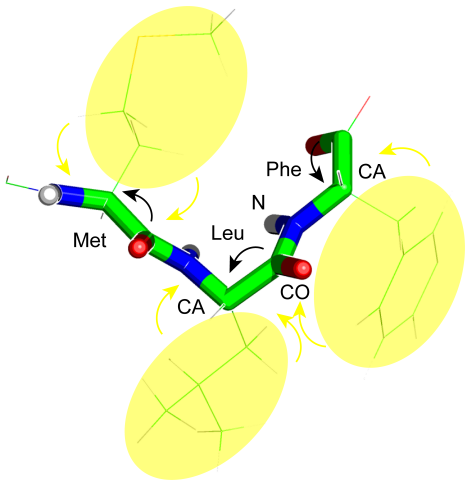

Figure 3.28: Polarization transfer during the two dimensional band selective $CO-C\alpha$ experiment. Here all spins are rigorously kept on the z-axis, save the spectral region of interest. In the experiment depicted above, the CO resonances are excited in the indirect dimension of the experiment and the $C\alpha$ spins are excited in the direct dimension, resulting in a band limited experiment, which keeps the side chain magnetization unperturbed. This allows for spin cooling of the backbone spins during a short delay, which is mediated by spin diffusion.

After the mixing time, the spectral band of interest in the direct dimension (in this case $C\alpha$) is rotated to the x-y plane for detection. It is noteworthy, that during mixing and both evolution periods, all spins outside the region of interest remained on the z-axis, and therefore still carry their initial magnetization acquired during the CP step.

To utilize this magnetization to replenish the region of interest, the pulse program loops back to the beginning of the z-filter, in an inner loop. During this time (typically 20-50ms) spin diffusion from the bath magnetization (consisting of the side chain carbons for the presented experiments) to the backbone (CO or $C\alpha$) takes place, restoring the magnetization spent during the first experiment. Then the whole experiment onwards from this point is repeated, adding the signals of the first and second cycle.

This whole procedure is repeated, until the bath magnetization is depleted, and no further net gain in S/N can be achieved. Thus, the z-filter serves the twin purposes of artifact suppression and RELOAD spin diffusion. Subsequently, an outer loop is conducted, which incorporates the full experiment, including the recycle delay of 2s for proton T_1 relaxation and the cross polarization step, which is followed by a 90° hard pulse on ^{13}C.

The flow of magnetization for such a band limited, RELOADed $CO-C\alpha$ PDSD experiment on MLF is schematically depicted in Fig. 3.28.

Using this procedure, the band-selective RELOAD version of PDSD can increase the effective sensitivity per unit time, as multiple scans can be performed in the inner loop of the sequence using a much shorter recycle delay time than traditionally required, if full proton T_1 relaxation is to be completed between repetitions of a given experiment. If the PDSD mixing time is long enough (greater than 20ms), the RELOAD delay prior to each inner loop is unnecessary, as the source magnetization is replenished concurrently with the PDSD mixing (data not shown).

This shortens experiment time even further and thus increases sensitivity per unit

time. This possibility was not used in the experiments presented in this work, for reasons of maximum duty cycle of the probes used.

A PDSD spectrum overlaid with band selective RELOAD versions on MLF is shown in Fig. 3.29. The conventional PDSD spectrum is shown in black, the band selective $CO-C\alpha$ RELOAD-PDSD in red, the $C\alpha-C\alpha$ RELOAD-PDSD in blue, the $C\alpha-CO$ RELOAD-PDSD in green and the $CO-C\beta$ RELOAD-PDSD in yellow. As can be seen from the figure, in all cases the selected resonances overlay well with the conventional PDSD spectrum and no artifacts or ghost peaks are introduced by the use of shaped pulses or the modifications of the pulse sequence. No inner RELOAD loops were used for any of these spectra.

To further assess the gain obtained by using RELOAD in PDSD experiments, a three dimensional plot of the peaks in a $C\alpha-CO$ RELOAD PDSD, which was RELOADed three times (red) and the same sequence without inner RELOAD loops (in blue) is shown in Fig. 3.30. From this figure the enhancement of the peaks is evident. Furthermore, the line shapes are not changed or distorted by consecutive RELOAD cycles. It is noteworthy at this point, that the shaped pulses used lead to slight phase distortions of the peaks, irrespective of whether RELOAD loops are executed or not.

The enhancements as a function of RELOAD cycles are shown in Fig. 3.31 for the $C\alpha-CO$ RELOAD-PDSD experiment, where the gain in signal to noise is plotted over the number of RELOAD cycles. Enhancements up to 1.75 could be observed for 3 RELOAD cycles. Although signal is still gained with a higher number of RELOAD cycles, the gain is not constant but is slightly diminished with consecutive RELOAD scans. This is expected, as during RELOAD the bath magnetization is depleted and the polarization present at the start of successive RELOAD cycles therefore reduced, as seen before. Still the slope of the curve suggests that significant further gains can be achieved by increasing the number of RELOAD loops.

Table 3.1: Signal to noise enhancements for the band selective PDSD-RELOAD spectra, for different amounts of RELOAD cycles. The second set of columns gives the multiplier of the number of scans needed for a conventional PDSD, to reach the same signal to noise ratio. The final set of columns gives the factor by which the RELOAD version is faster than the conventional version if the additional time required for the RELOAD experiment is taken into account: (NS*(recycle delay+PDSD mixing+acquisition) vs. NS*(recycle delay+RELOAD delay+PDSD mixing+acquisition+RELOAD cycles*(RELOAD delay+PDSD mixing+acquisition)) (table adapted from the diploma thesis of S. Asami [65])

		$(S/R)^{RELOAD}$			N^{PDSD}			t^{PDSD}/t^{RELOAD}		
Selection	Peak	$L_1 = 1$	$L_1 = 2$	$L_1 = 4$	$L_1 = 1$	$L_1 = 2$	$L_1 = 4$	$L_1 = 1$	$L_1 = 2$	$L_1 = 4$
C'-C^{α}	M	1.00	1.67	1.88	1.00	2.79	3.53	1.0	2.6	3.0
C'-C^{α}	L	1.00	1.16	1.39	1.00	1.35	1.93	1.0	1.3	1.7
C'-C^{α}	F	1.00	1.17	1.45	1.00	1.37	2.10	1.0	1.3	1.8
C^{α}-C'	M	1.00	1.32	1.72	1.00	1.74	2.96	1.0	1.6	2.5
C^{α}-C'	L	1.00	1.40	1.86	1.00	1.96	3.46	1.0	1.8	3.0
C^{α}-C'	F	1.00	1.28	1.69	1.00	1.64	2.86	1.0	1.5	2.4
C'-C^{β}	M	1.00	1.32	1.52	1.00	1.74	2.31	1.0	1.6	2.0
C'-C^{β}	L	1.00	1.33	1.75	1.00	1.77	3.06	1.0	1.6	2.6
C^{α}-C^{α}	M	1.00	-	1.43	1.00	-	2.04	1.0	-	1.7
C^{α}-C^{α}	L	1.00	-	2.11	1.00	-	4.45	1.0	-	3.6
C^{α}-C^{α}	F	1.00	-	2.02	1.00	-	4.08	1.0	-	3.3

The enhancement gained for all resonances of the $C\alpha-C\alpha$ experiment is plotted in Fig. 3.32. From these and the previous plots, it can be seen that there are differences in the RELOAD behavior of the different amino acids, depending on the type and experiment performed. For the $C\alpha-CO$ experiment, large enhancements are seen for the RELOAD time used (50ms). These nearly reach the theoretical optimum S/N enhancement of 2 for an experiment with three following RELOAD cycles, corresponding

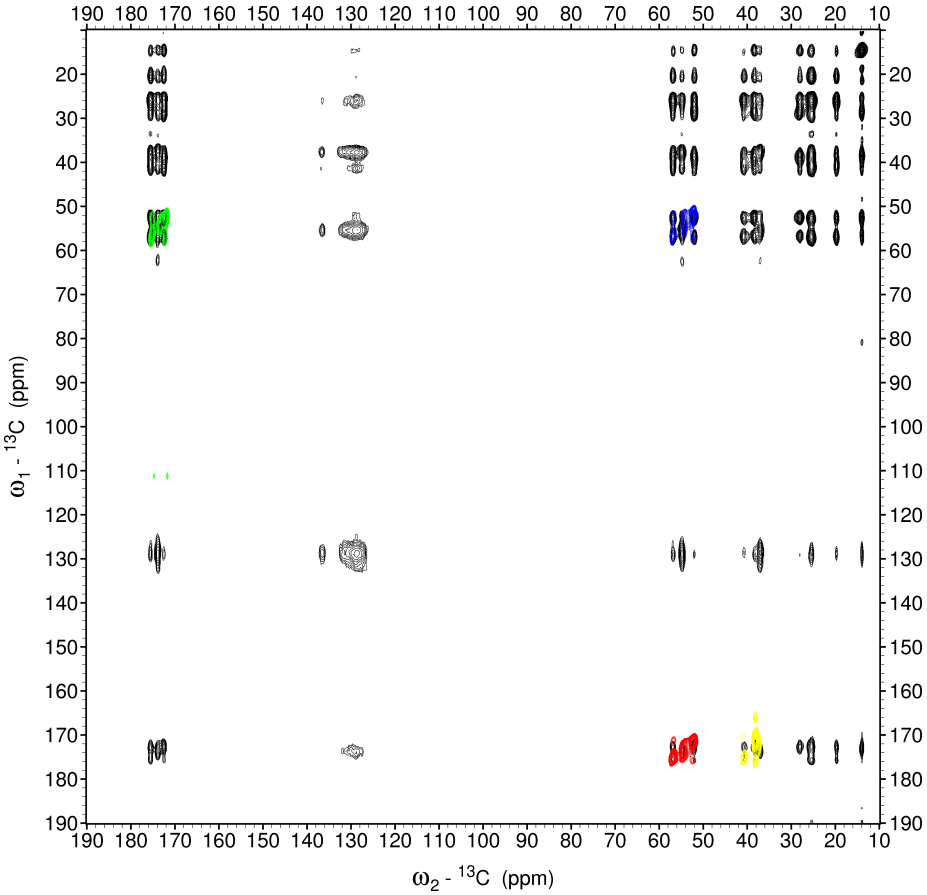

Figure 3.29: Overlay of a full and several band selective PDSD experiments on MLF. Plotted in black is a PDSD experiment recorded with the sequence shown in Fig. 3.27 a) and a mixing time of 200 msec. Overlaid in red is the band selective RELOAD-PDSD experiment shown in Fig. 3.27 b), with selective pulses on CO in the indirect and $C\alpha$ in the direct dimension and a mixing time of 50 msec. In blue, green and yellow, $C\alpha$-$C\alpha$, $C\alpha$-CO and CO-$C\beta$ band selective RELOAD-PDSD experiments are shown, with a mixing times of 100, 50 and 50 msec, respectively. It is important to point out that, even though a RELOAD capable sequence was used to record the band selective spectra, no actual RELOAD cycles were performed during the experiment. Only the the signals stemming from conventional CP polarization were recorded, as the primary goal of the spectra shown is to investigate the fidelity of band selection in both spectral dimensions for the RELOAD adapted two dimensional sequence. Although the sweep width for these experiments could have been reduced, due to the band selectivity, this option was not employed. Full sweep width spectra were recorded, to investigate the occurrence of artifacts outside the selected range, caused by the pulse sequence. As can be seen, no artifacts were introduced into the spectra for any of the experiments. The full PDSD was acquired with 32, the band selective PDSD with 36 scans per increment. All spectra were acquired with 128 increments in the indirect dimension, with 10 kHz spin rate at 600MHz and 295K. For selective excitation of the CO region of the spectrum, sinc pulses with a length of 200 μs where used. For selective $C\alpha$, Cβ and side chain excitation, Q5 Gaussian Cascades with a length of 5 msec where employed. The spectra were processed with 50 Hz exponential line broadening in both dimensions.

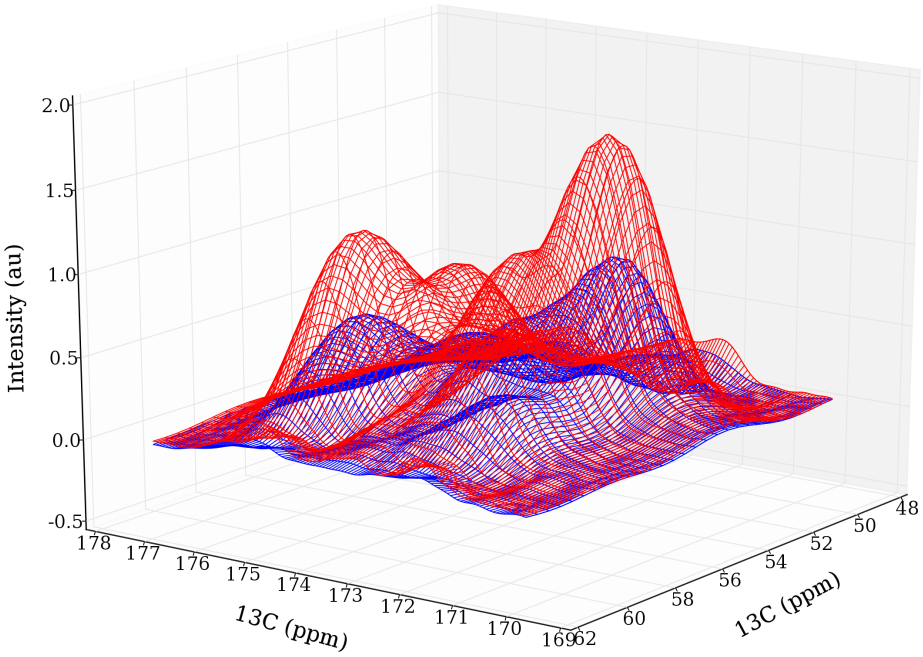

Figure 3.30: Representative three dimensional plot of the $C\alpha$-CO band selective RELOAD-PDSD, without RELOAD (blue) and with three RELOAD cycles (red). The enhancement can be clearly observed and the peak shape is not perturbed by conducting multiple RELOAD cycles. The enhancements in signal to noise range from 1.75 for the Leu $C\alpha - CO$ intra-residue cross peak to 1.6 for the Phe $C\alpha - CO$ intra-residue cross peak. Both experiments were recorded with a PDSD mixing time of 50 msec, a RELOAD delay of 50 msec, 36 scans per increment, 128 increments in the indirect dimension, 10kHz spin rate at 295K. Both spectra were processed with 50 Hz exponential line broadening in both dimensions.

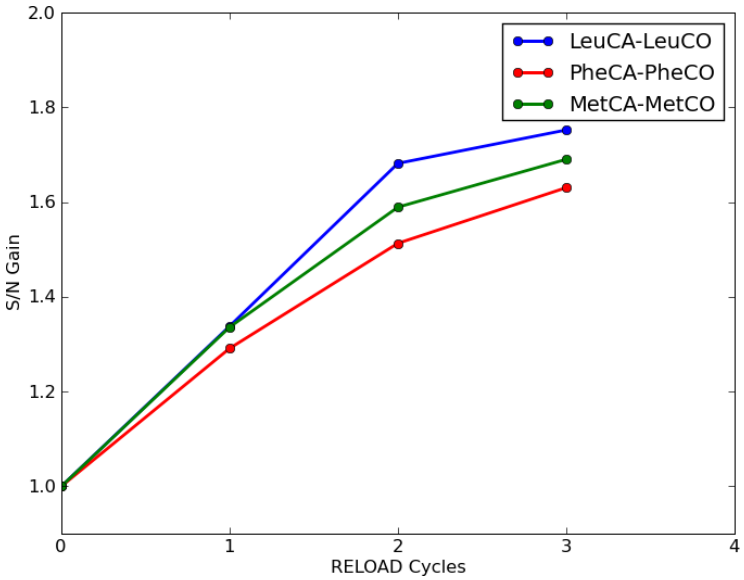

Figure 3.31: Signal to noise enhancement for band selective RELOAD PDSD spectrum shown in Fig. 3.30. The signal to noise is plotted over the number of RELOAD cycles for the Leu, Phe and Met $C\alpha - CO$ intra-residue cross peaks.

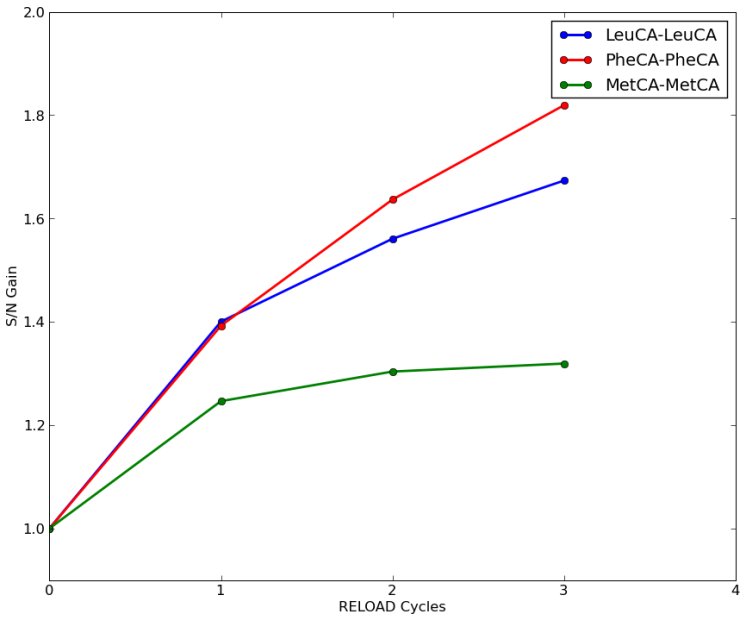

Figure 3.32: Signal to noise enhancement for a band selective $C\alpha - C\alpha$ RELOAD PDSD spectrum. The signal to noise is plotted over the number of RELOAD cycles for the Leu, Phe and Met $C\alpha - C\alpha$ diagonal peaks.

to 4 scans, for the Leu $C\alpha - CO$ cross peak. On the other hand, for Met $C\alpha - C\alpha$ diagonal peak, the enhancement is less pronounced. While still comparable for the first RELOAD cycle, it diminishes much faster, reaching a maximum at a factor of only about 1.3. Surprising in this context is the apparent strong intensity of the Phe $C\alpha - C\alpha$ diagonal peak. This has to be interpreted with caution, as for this peak, the correct intensity is difficult to determine. This is due to spectral overlap, which also complicated the evaluation shown in Fig. 3.21.

A reason for the differences between the experiments could be that the $C\alpha$ spins are stronger contributors to the RELOAD effect than the CO resonances. During the PDSD mixing time, the $C\alpha$ spins are already being RELOADed, thus doubling the effective RELOAD time (the PDSD mixing, as well as RELOAD mixing times were 50 msec each). This only works, if the $C\alpha$ nuclei are not detected in the direct dimension of the experiment, which would dephase them.

This additional RELOAD time during mixing, in which the RELOAD effect has time to relax the $C\alpha$ spins, likely contributes to the overall gain for multiple RELOAD cycles, which in turn could explain the better performance of the band selective $CO - C\alpha$ as compared to the $C\alpha - C\alpha$ experiments.

The situation is similar for the $CO - C\alpha$ spectra, although there the maximum enhancement is generally lower and reaches factors of 1.25 for Phe to 1.6 for Leu $CO - C\alpha$ cross peaks, with three RELOAD cycles.

The cause for this could be the slower return to equilibrium of the CO resonances, seen in Fig. 3.12. This, together with the influence of multiple RELOAD cycles at short RELOAD mixing times, as seen in Fig. 3.24, diminishes the enhancement.

Higher gains are expected if the RELOAD or PDSD mixing times are prolonged, without increasing the time needed for the whole experiment by more than a few percent.

As seen before, the differences in signal to noise gain for different amino acids most likely arise from the accessibility different of ^{13}C nuclei acting as bath magnetization during a given RELOAD spin diffusion step. Therefore it is not surprising that Leu, situated at the center of the molecule, consistently shows the strongest and most stable enhancements, while those of Met and Phe, at the ends of the peptide, are less pronounced. It is important to note that the sample of MLF used was not diluted with unlabeled MLF, so there may be effects from the crystal packing of the individual MLF molecules.

Overall the effect of the amino acid location should be lessened in a larger peptide, although the type of amino acid, especially the length and protonation of the side chain, is expected to give rise to differences in the maximum enhancement that can be achieved with RELOAD.

The efficiency of RELOAD for other combinations of nuclei, such as $CO - C\beta$ or $CO - C\alpha + C\beta$, was also investigated. There, the enhancements gained were similar, with less enhancement gained in the case of $CO - C\alpha + C\beta$, as here a significant portion of the side chain is excited, and thus not available as bath magnetization (data not shown).

The number of RELOAD cycles was kept low in all experiments, although the traces shown imply that higher gains could be achieved for a higher number of RELOAD loops. This was avoided to limit the duty cycle of the probe used in the experiments. A significant increase in the number of RELOAD cycles is expected to be achievable with Efree technology.

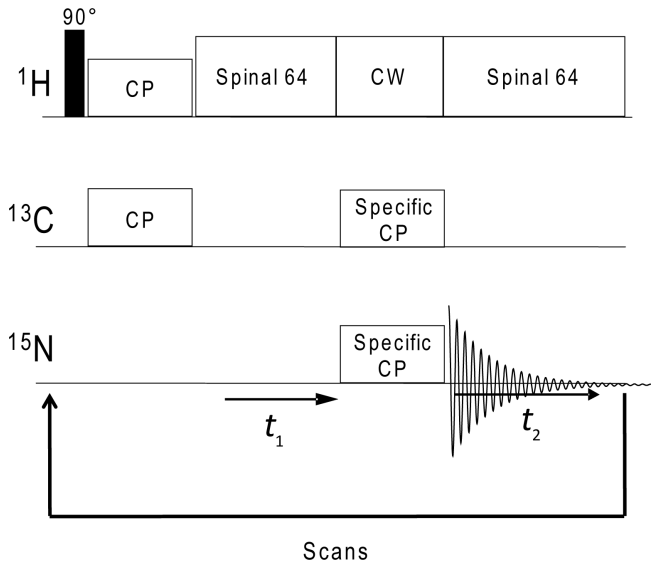

Figure 3.33: The double CP sequence: ^1H magnetization is transferred to a hetero-nucleus via cross polarization. Following the CP indirect chemical shift evolution, another cross polarization is applied, between the hetero-nuclei. Here, specific CP is often used, which allows selective transfer between the amide ^{15}N and the CO or $C\alpha$ atoms in the backbone of a protein. After acquisition and a recycle delay for ^1H T_1 relaxation, the sequence is repeated number of scans times and the FIDs are co added.

3.6 Application of RELOAD to hetero-nuclear correlation spectra

In the previous section, RELOAD was successfully applied to homo-nuclear correlation spectra, with enhancements of the signal to noise of up to 1.75.

To test the applicability and possible gains achievable with RELOAD for hetero-nuclear correlation spectra, two sequences commonly used for hetero-nuclear polarization transfer in solid state NMR were tested as to their compatibility with RELOAD enhancement. These experiments will be shortly outlined in the following.

3.6.1 Hetero-nuclear Correlation via Cross Polarization

One way of transferring magnetization between two hetero-nuclei, which is commonly used in solid state NMR is the double CP (DCP) experiment [66, 67]. This sequence is shown in Fig. 3.33. Here, the proton magnetization is first transferred to a hetero-nucleus, whose chemical shift is recorded under proton decoupling in the indirect dimension of the experiment. Then the magnetization parallel to the spin lock field is transferred to another hetero-nucleus via cross polarization. It is important to stringently select the nutation frequencies on the individual channels, so that $\omega_{nut1} = \omega_{nut2} \pm n * \omega_r$ is fulfilled for the two hetero-nuclear channels, but not for the proton channel, which would lead to a strong attenuation and the appearance of artifacts in the spectrum.

The specific CP method introduced by Baldus et al. [68] is often used to make the polarization transfer from ^{15}N to ^{13}C selective for the $C\alpha$ or CO resonances in proteins. Here, the contact field on the ^{13}C channel during the second CP step is set on resonance with the CO or $C\alpha$ spins. These spins then experience the CP condition

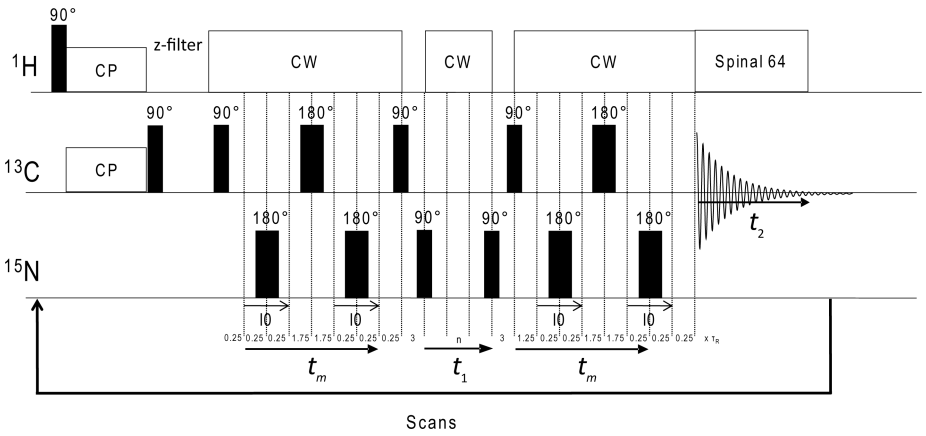

Figure 3.34: The Redor sequence. Briefly, magnetization is transferred from the protons to a hetero-nucleus (in this case ^{13}C). Then, through recoupling of the hetero-nuclear dipolar interactions by rotor synchronized 180° pulses, antiphase magnetization is created on ^{15}N and evolved in the indirect dimension of the experiment. After evolution, the magnetization is returned to inphase by a recoupling block symmetric to the first and detected in the direct dimension.

outlined above. For the other resonances, the large offset leads to an effective field with a magnitude of $B_{eff} = (\Delta B^2 + B_1^2)^{1/2}$. This puts these spins outside of the CP condition and thus prevents magnetization transfer. This works especially well for hetero-nuclei, as the small relative size of the homo-nuclear dipolar couplings, as compared to ^1H, leads to a very narrow CP condition.

The transferred magnetization is then detected in the direct dimension of the experiment, yielding a chemical shift correlation of the two hetero-nuclei.

3.6.2 Hetero-nuclear Correlation via REDOR

Rotational Echo Double Resonance (Redor) [69] has been used as a very sensitive tool to measure distances in solid state NMR.

Furthermore it can be employed to record hetero-nuclear correlation spectra [58]. This latter application is implemented using a pulse sequence as shown in Fig. 3.34.

In the Redor sequence shown, the ^1H magnetization is transferred to a hetero-nucleus via cross polarization. Following the CP, a 90° hard pulse is applied followed by a z-filter. This is not necessary at this point and was only incorporated into the sequence for better comparison with the RELOADed version of this experiment, shown later. After the z-filter, the magnetization is rotated back to the x-axis and after a quarter of a rotor cycle a sequence for $^{13}C -^{15} N$ recoupling is commenced. Here, every half rotor period a hard 180° pulse is applied to the ^{15}N channel. This perturbs the averaging of the hetero-nuclear dipolar coupling to the ^{13}C nuclei and thus leads to a Hamiltonian of the form $B(r,\theta)(2I_zS_z)$ (see chapter 2, Eqn. 2.86). Then a delay of an integer number of rotor periods is applied, which leads to a 180° flip of the effective field experienced by the ^{13}C nucleus. During this time the ^{13}C chemical shift is refocused using a 180° hard pulse. This delay of an odd integer number of rotor periods, with the ^{13}C refocusing pulse in the middle, assures that the Hamiltonian is not refocused during the second half of the recoupling sequence, as a consequence of the chemical shift refocusing on ^{13}C. After a number of repetitions of the second $0.25\tau_R - 180^\circ_{^{15}N} - 0.25\tau_R$ recoupling block, the initial I_x magnetization has evolved into an I_yS_z antiphase term. At this point, a 90° pulse is applied to ^{13}C to yield

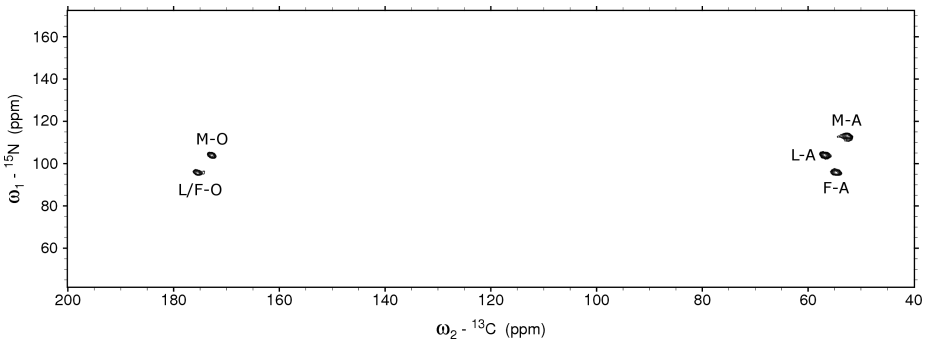

Figure 3.35: Heteronuclear $^{13}C-^{15}N$ correlation spectrum of MLF, acquired with the Redor sequence shown in Fig. 3.34. The spectrum was recorded at 600MHz, 8 kHz spin rate, 295K, 256 increments in the indirect dimension and 64 scans per increment. 20 Hz exponential line broadening and qsine (SSB = 2) processing were applied in the direct and indirect dimension, respectively. Peak assignments are given as text in the figure.

I_zS_z magnetization. Next a z-filter is applied, to purge the spin system of residual x-y magnetization. After reactivation of the proton decoupling, a ^{15}N 90° pulse is applied, yielding an I_zS_x term. After chemical shift evolution in the indirect dimension, which must have an length of an integer number of rotor periods, another 90° pulse is applied to ^{15}N which gives I_zS_z. Next, another z-filter is applied and the ^{13}C magnetization is returned to the x-y plane with a 90° pulse. A recoupling block symmetric to the first is applied, converting the ^{13}C magnetization back to an inphase $-I_x$ term. Following acquisition and a recycle delay of 1.5-3 sec, the sequence is repeated and the signals co added number of scans times.

During acquisition spinal64 decoupling is used, whereas during the recoupling a continuous wave field is applied. The reason for this is, that the large number of strong pulses applied during the recoupling can lead to a Hartmann-Hahn match, severely perturbing the performance of the sequence. As continuous wave decoupling is insensitive to the exact strength of the decoupler field, above a certain threshold (with the exception of certain sharp recoupling conditions at integer multiples of the spinning speed), the decoupling field can be easily adjusted to avoid Hartmann-Hahn matching on the ^{15}N, as well as ^{13}C channel. Although more intricate to set up, more advanced decoupling schemes could yield better sensitivities for the experiment, if applied during recoupling.

A Redor $^{13}C-^{15}N$ correlation spectrum of MLF is shown in Fig. 3.35.

3.6.3 Double CP RELOAD

The first sequence investigated regarding its compatibility to RELOAD is the double CP (DCP) sequence, which is often used in solid state NMR spectra of proteins, to effect the polarization transfer from backbone ^{13}C to ^{15}N nuclei, or vice versa.

The RELOAD version of the DCP sequence shown in b) with the conventional DCP sequence shown in a) for comparison. Several adjustments had to be implemented to make RELOAD enhancement possible. A z-filter was incorporated and the indirect dimension evolution was flanked by two selective pulses (here on $C\alpha$) to leave the bath magnetization unperturbed. After the spins in the region of interest are returned to the z-axis by the second selective pulse, all spins are rotated to the axis of the double CP spin lock field. The reason for this is that leaving the bath magnetization on the z-axis would lead to a rotation of the bath magnetization during the spin lock of the

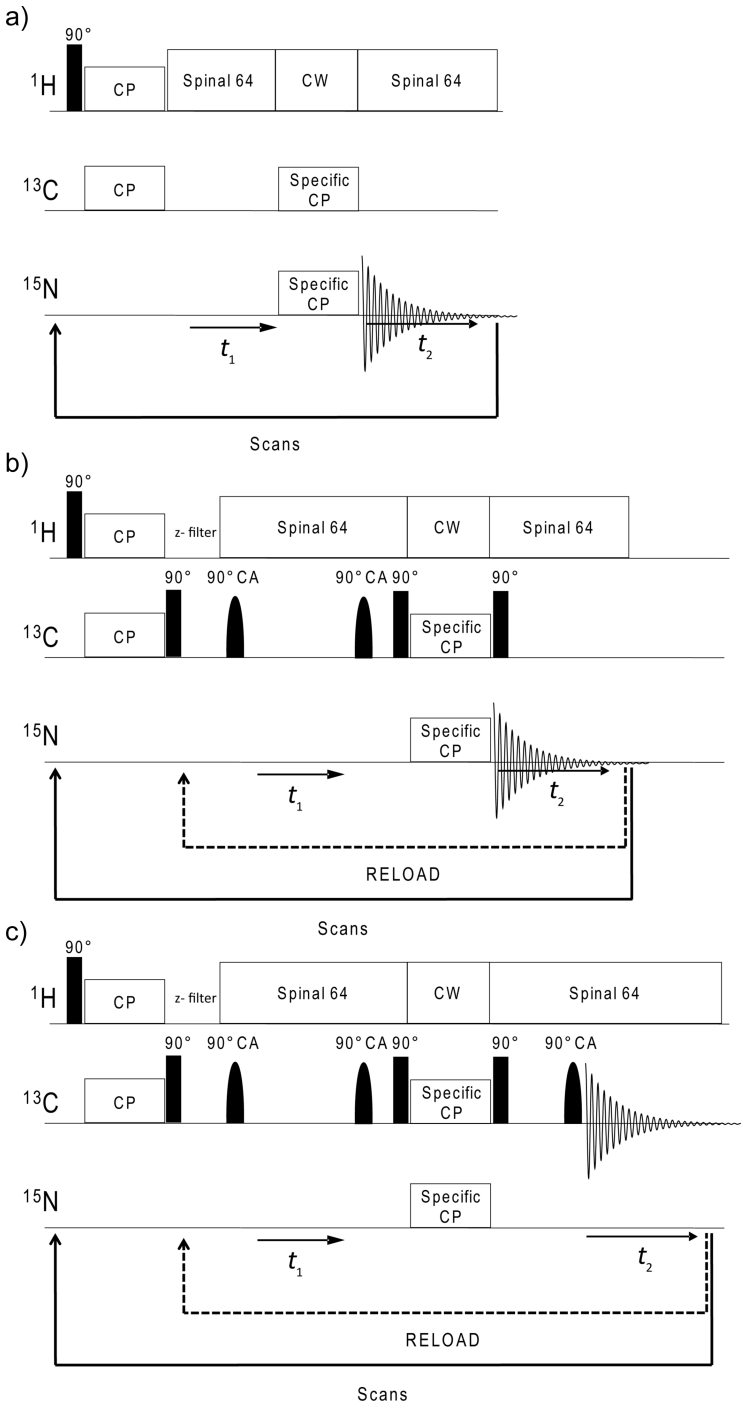

Figure 3.36: Comparison of a conventional DCP sequence and its adaption to RELOAD. In a) a conventional DCP sequence is shown, with its RELOAD version shown in b). Here a z-filter was incorporated and the indirect dimension evolution is flanked by two selective pulses, the last of which is followed by a hard 90° pulse. After DCP, another 90° hard pulse on the ^{13}C channel returns the bath spins to the z-axis. The effect of the shaped pulses and the spin lock field on the bath magnetization was investigated with the sequence shown in c). Here the magnetization on the ^{13}C channel is detected after a certain number of RELOAD cycles were executed.

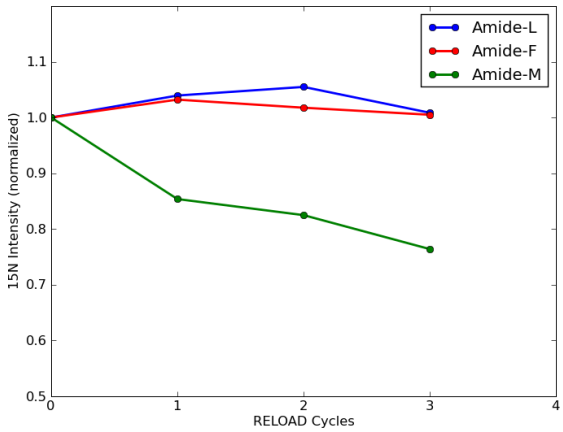

Figure 3.37: Plot of the RELOAD enhancement for the ^{15}N magnetization in an $^{1}H -^{13} C -^{15} N$ DCP experiment. The evolution time in the indirect dimension was set to zero and only the first increment of the, normally two dimensional, experiment recorded, yielding a one dimensional spectrum. All spectra for this evaluation were recorded at 600 MHz, 10 kHz spin rate, 295K and 4096 scans. A Q5 Gaussian cascade of 5 msec length was used for selective $C\alpha$ excitation at -3500 Hz off resonance (which was set to 75ppm). 20 Hz exponential line broadening was applied to all spectra. It can be seen that the signal to noise is not enhanced for the amide Leu and Phe resonances and even decreases for Met, with a larger number of RELOAD cycles. Each cycle adds a constant amount of noise, but the quickly declining signal looses intensity faster than the the noise rises in the spectrum.

spins selected using the shaped pulses. This would first lead to a strong attenuation of the bath, caused by B_1inhomogeneity, and second leave the bath spins with an unknown angle to the z-axis after the double CP block, making a rotation back to the z-axis difficult. As this is required for optimal RELOAD performance, strong losses of bath magnetization are expected, if the soft pulse-hard pulse combination is not applied prior to double CP.

After the magnetization is transferred between the hetero-nuclei, another 90° hard pulse on the ^{13}C channel returns the bath spins to the z-axis. After acquisition a nested inner loop is performed leading back to the point in the sequence just prior to the z-filter.

The enhancement gained with the RELOAD DCP sequence shown in Fig. 3.36 b) for a $^{1}H -^{13} C -^{15} N$ transfer, is plotted in Fig. 3.37.

From these plots it is obvious that RELOADing of the spectra does not improve the sensitivity . Quite in the contrary, the signal to noise decreases for the Met resonance.

A reason for this could be that the RELOAD efficiency is marginal and the constant contribution of the noise to the spectrum with every RELOAD cycle quickly overshadows the addition of signal in consecutive loops.

To investigate the reason for this effect further, the bath magnetization on the ^{13}C channel after a number of RELOAD cycles was observed, using the sequence shown in Fig. 3.36 c).

Here, the magnetization on the ^{13}C channel is detected after a certain number of RELOAD cycles are co added. This was done to assess why RELOAD yields no enhancement on the ^{15}N channel.

If there is signal left on the ^{13}C channel after the second CP step, as can be seen in Fig. 3.38 for zero RELOAD cycles, this signal is expected to accumulate and enhance the signal to noise ratio for successive RELOAD loops. If the magnetization is severely

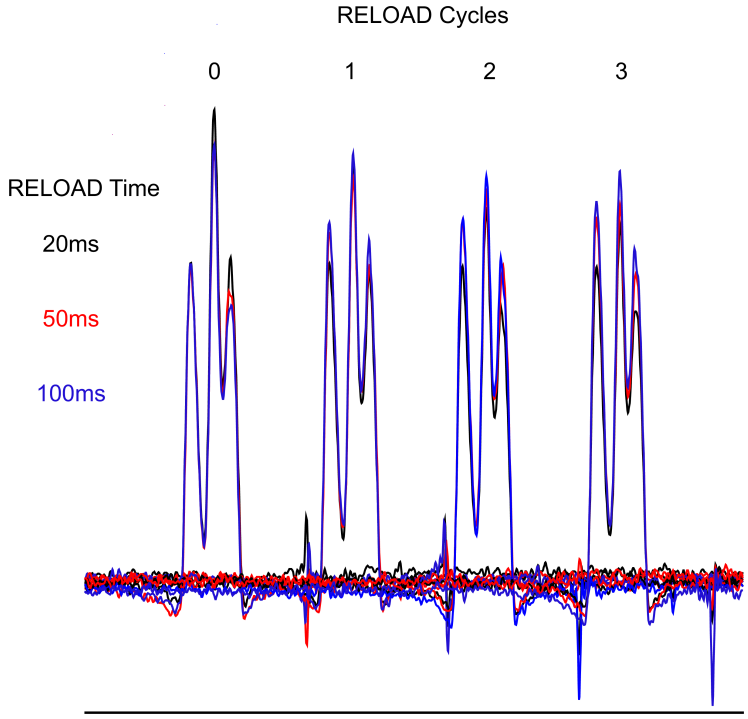

Figure 3.38: Spectrum of the $C\alpha$ resonances after n RELOAD cycles are co added. The signals were acquired following the second CP step in a $^{1}H -^{13} C -^{15} N$ DCP experiment. The ^{13}C magnetization was observed to see if there is an accumulation of intensity with a rising number of RELOAD loops. If ^{13}C intensity is retained after the second CP step, as seen for 0 RELOAD cycles, this intensity is expected to increase with successive loops. Instead the signal to noise declines with rising number of loops (all spectra were scaled to the same noise level). This indicates a perturbation of the bath magnetization, with a concomitant deficiency in the RELOAD effect. The evolution time in the indirect dimension was set to zero and only the first increment of the, normally two dimensional, experiment recorded, yielding a one dimensional spectrum. All spectra were recorded with at 600 MHz, 10 kHz spin rate, 295K and 1728 scans. A Q5 Gaussian cascade of 5 msec length was used for selective $C\alpha$ excitation at -3500 Hz off resonance (which was set to 75ppm). 20 Hz exponential line broadening was applied to all spectra.

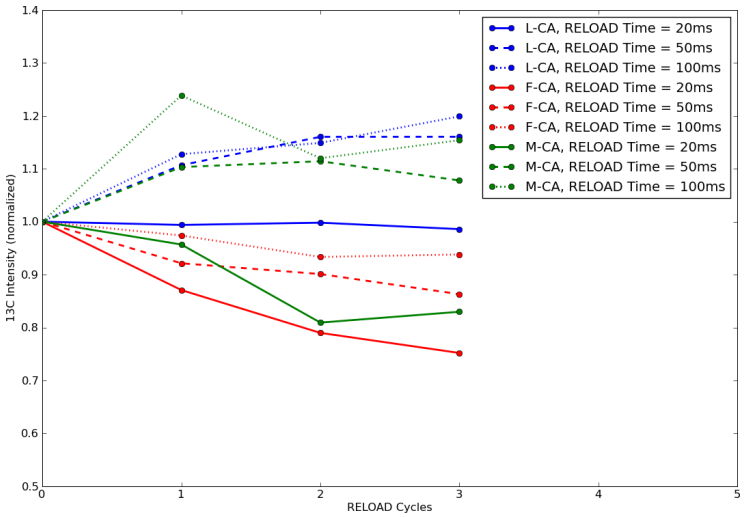

Figure 3.39: Evaluation of the spectra shown in Fig. 3.38. Here, the decline in signal to noise ratio for a rising number of RELOAD cycles can be seen. Although longer RELOAD mixing times partially alleviate this problem, no satisfactory enhancement could be achieved. For this evaluation, the spectra have not been scaled to the same noise level, as is the case in Fig. 3.38.

weakened, the RELOADed signal to noise ratio is expected to decline. As can be seen from Fig. 3.38, the signal to noise indeed decreases, if RELOAD is employed. This can be partially alleviated by the use of longer mixing times, but even at 100 msec, the decline is still significant.

This is even more clear if the intensities of the spectra shown in Fig. 3.38, are plotted without the scaling to the same noise level, as is shown in Fig. 3.39. For short RELOAD mixing times the magnetization declines, which strongly suggests a perturbation of the bath magnetization during the second CP step.

Reasons for that could be B_1 inhomogeneity, or an insufficient spin lock, leading to a severe dephasing of the bath magnetization, which should remain exactly on axis if effective RELOAD is to be achieved.

Further corroborating this point are the spectra shown in Fig. 3.40, in which the contact time for the second CP step between ^{13}C and ^{15}N has been increased from 3 to 5 msec. This increase significantly perturbed the residual ^{13}C magnetization, without a concomitant gain in ^{15}N intensity (data not shown).

In the light of these results, DCP does not seem to be suited for RELOAD experiments, as the second CP step is highly perturbing to the residual ^{13}C magnetization, which acts as a bath and therefore as a source for RELOAD enhancement.

3.6.4 Redor RELOAD

As DCP did not yield gains in signal to noise, when adapted for RELOAD enhancement, the Redor sequence was considered. As was seen before for the RELOAD-PDSD experiments, shaped pulses alone seem to be minimally perturbing to the bath magnetization, in contrast to the spin lock field used during DCP. Therefore it should be possible to achieve significant RELOAD enhancement, if only shaped pulses are used in context of the correlation experiment. Thus the Redor sequence is an ideal candidate.

In Fig. 3.41 b) the RELOAD adaption of the Redor sequence is shown. Here, all

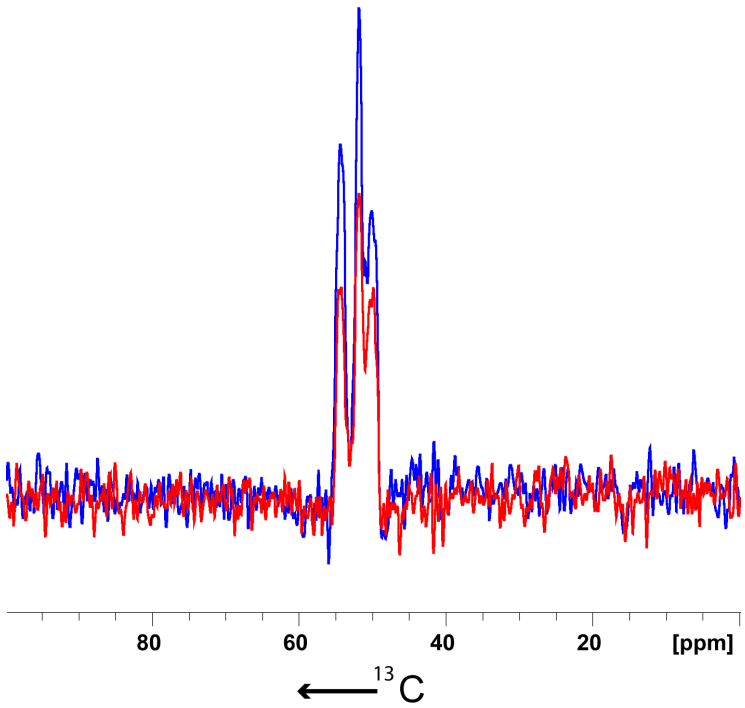

Figure 3.40: Spectra showing the effect of an increase of the second spin lock time from 3 msec to 5msec in an $^{1}H-^{13}C-^{15}N$ DCP experiment. A significant decrease in ^{13}C magnetization remaining after the $^{13}C-^{15}N$ contact can be observed, without an accompanying rise in polarization on the ^{15}N channel (not shown). This suggests a perturbing effect of the spin lock field on the ^{13}C magnetization. No RELOAD was used for either spectrum. Both spectra were recorded with at 600 MHz, 10 kHz spin rate, 295K and 72 scans. A Q5 Gaussian cascade of 5 msec length was used for selective $C\alpha$ excitation at -3500 Hz off resonance (which was set to 75ppm). 20 Hz exponential line broadening was applied to all spectra.

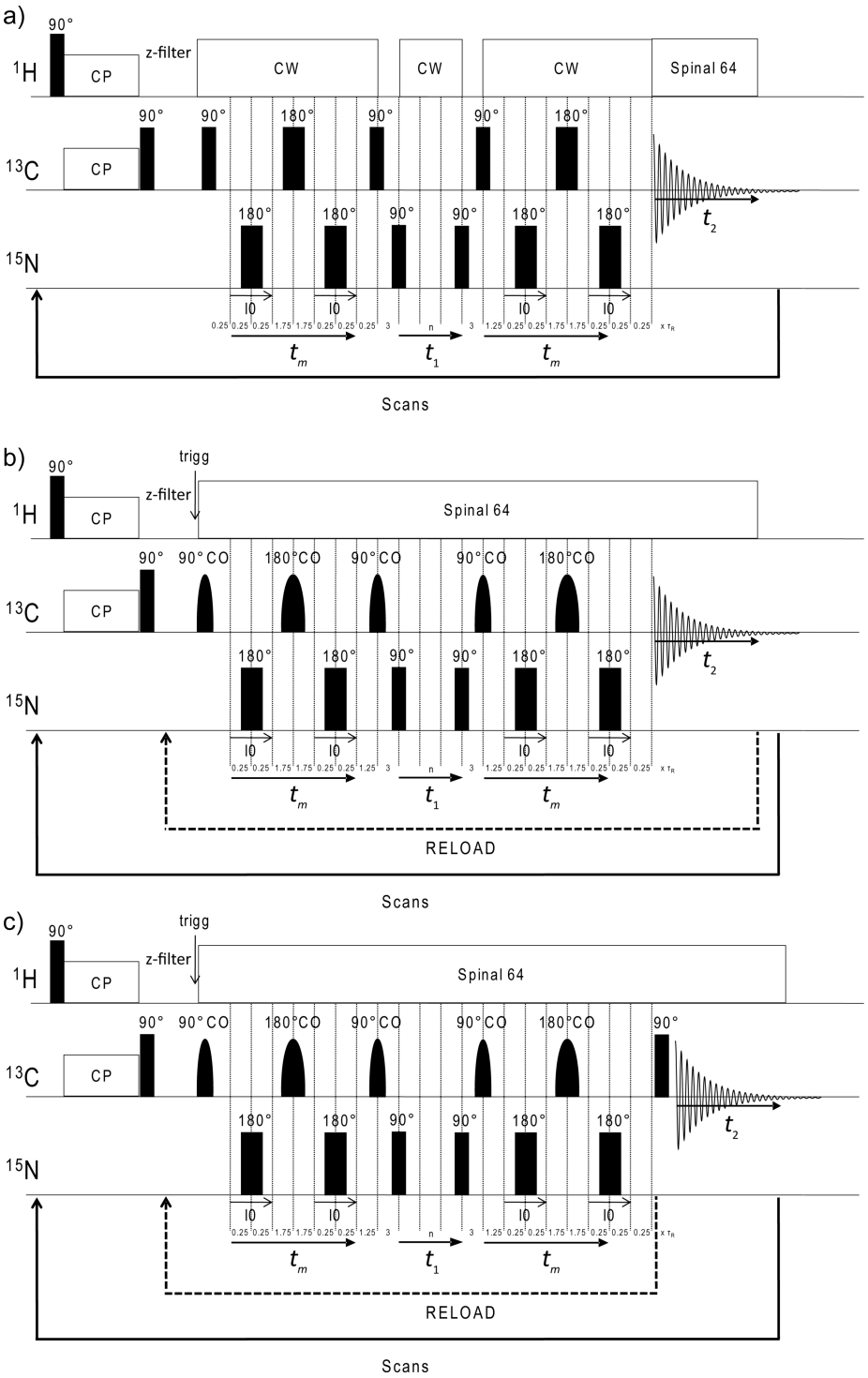

Figure 3.41: Comparison of a conventional Redor sequence and its adaption to RELOAD. In a) a conventional Redor sequence is shown, for sake of comparison, with its RELOAD version shown in b). All pulses on the ^{13}C channel (save for the pulse prior to the first z-filter) have been replaced by selective pulses. After acquisition, a nested inner loop is performed. To investigate the effect of multiple shaped pulses on the bath magnetization, sequence b) was modified as shown in c). Here, the RELOAD cycle commences before the acquisition. After the last RELOAD loop the bath magnetization is read out using a hard 90° pulse on ^{13}C.

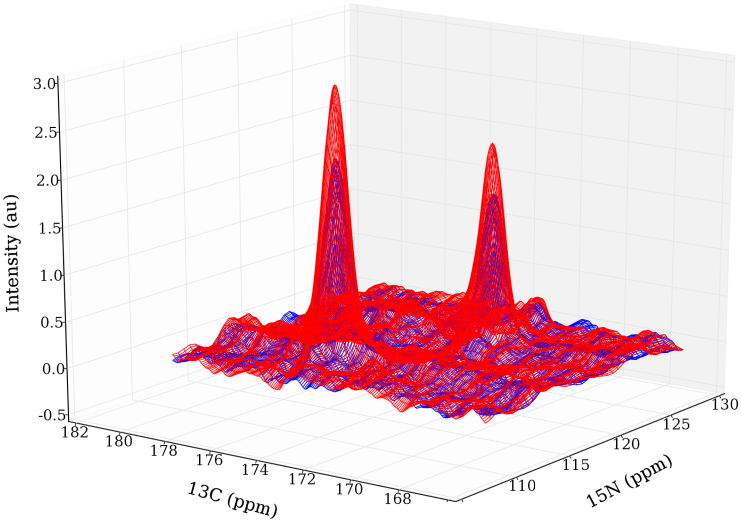

Figure 3.42: Overlay of a *CO* band selective Redor spectrum, recorded with the sequence shown in Fig. 3.41 b) without RELOAD (blue) and with three RELOAD cycles (red). The signal to noise ratio is significantly enhanced, without any perturbation of the peak shape. The spectra have been scaled to the same level of noise. Both spectra were recorded with at 600 MHz, 8 kHz spin rate, 295K and 128 increments in the indirect dimension and 120 scans. Sinc pulses of 250 usec were used with different power levels for selective *CO* excitation and inversion, 11000 Hz off resonance (which was set to 100ppm). 50 Hz exponential line broadening was applied in both dimensions.

pulses on the ^{13}C channel (save for the pulse prior to the first z-filter) were replaced by selective pulses (for the experiments performed here, *CO* selective sinc pulses have been used), and the delays in the sequence have been adjusted to accommodate the much longer shaped pulses. The z-filters applied prior and after the indirect evolution have been omitted, as no significant effect on the spectra was observed. After acquisition, an nested inner loop is executed, which returns the execution of the sequence to the point directly after the hard pulse after cross polarization. During this time the *CO* magnetization is replenished via spin diffusion from the surrounding ^{13}C nuclei. Then the sequence is repeated and the signals co added. After the magnetization of the neighboring nuclei is depleted, an outer loop, similar to the one in the normal Redor experiment, is performed, including a recycle delay for ^{1}H T_1 relaxation and cross polarization. This repolarizes the whole spin system and a new set of inner loops can be performed. For this sequence, a rotor trigger was implemented directly after the z-filter to assure rotor synchronization of the sequence, irrespective of acquisition and RELOAD delays.

The enhancement gained for a band selective *CO* Redor RELOAD as depicted in Fig. 3.41 is shown in Fig. 3.42. In this figure it can be seen that the signal to noise ratio is significantly increased, without perturbation of the overall peak shape. The spectra have been scaled to the same level of noise.

The rise in signal to noise ratio with a increasing number of RELOAD cycles is shown in Fig. 3.43. Although the enhancement is not as pronounced as for the PDSD-RELOAD experiments shown in Figs. 3.31 and 3.32, enhancements of 1.4 in signal to noise could be achieved using four RELOAD cycles. The slope of this curve suggests even higher enhancements are possible, using a larger number of RELOAD cycles. As before, this possibility was not tested, due to concerns regarding the maximum duty cycle of the probe used.

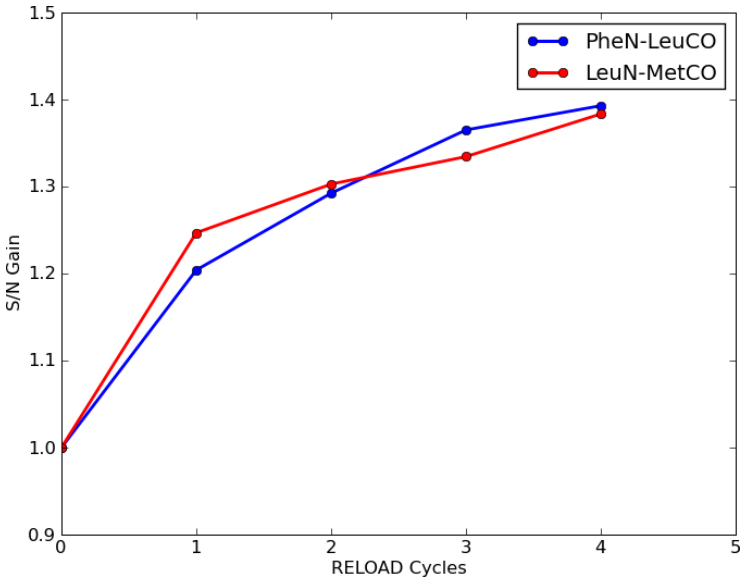

Figure 3.43: Evaluation of the signal to noise enhancement over the number of RELOAD cycles for the spectrum shown in Fig. 3.42. The increase in signal to noise is significant, although it is less pronounced than for the RELOAD PDSD experiments shown in Fig. 3.31. Still an enhancement of 1.4 can be achieved for four RELOAD cycles.

The decrease in relative enhancement for the Redor-RELOAD, as compared to the PDSD-RELOAD, can be explained by the larger number of shaped pulses used in the former sequence. These could lead to a slight perturbation of the bath magnetization. This perturbation is by far less pronounced as for the DCP-RELOAD experiment, and therefore significant gains in signal to noise can be achieved.

To investigate to which degree the bath magnetization is preserved, the experiment shown in Fig. 3.41 c) was employed. The sequence shown in b) was modified, so that the RELOAD cycle commences before the acquisition. Only after the last RELOAD loop, the bath magnetization is read out using a hard 90° pulse on ^{13}C.

Therefore the method of investigating the bath magnetization is a bit different to the one employed for the DCP experiment. Whereas, for the DCP, the accumulation of residual magnetization on the ^{13}C channel was observed, here the ^{13}C magnetization is dephased during the z-filter for all RELOAD cycles, save the last, where the magnetization for all ^{13}C spins is read out after all selective pulses have been applied for the last RELOAD loop. Insofar, this experiment can be regarded as even more stringent, as only the magnetization left after the last RELOAD cycle is recorded. The result of these measurements are shown in Fig. 3.44. Here, the residual magnetization of all ^{13}C resonances of the MLF spectrum is shown after the last RELOAD loop, as a function of total RELOAD loops. It is apparent that for most resonances, more that 50% of the initial magnetization is retained, even after five successive RELOAD cycles. This suggests that the Redor RELOAD sequence is only mildly perturbing to the bath magnetization, explaining the good gains in signal to noise ratio seen in Fig. 3.43.

These measurements suggest that Redor is a much better hetero-nuclear correlation sequence to be employed in conjunction with RELOAD, yielding significant enhancements, which allow a reduction in measurement time by about a factor of 2, with the current implementation.

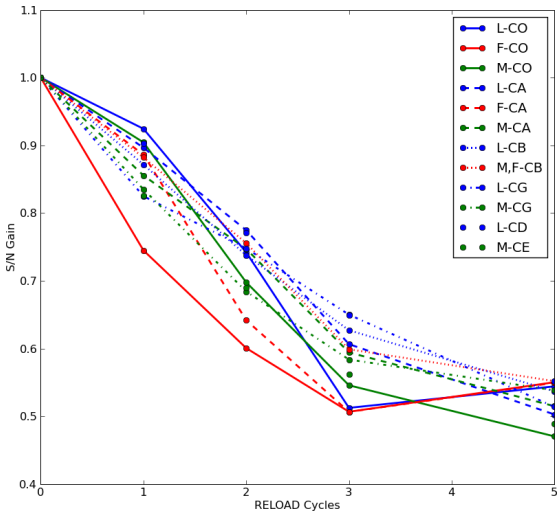

Figure 3.44: Plot of the residual ^{13}C magnetization after the last RELOAD cycle over the total number of RELOAD cycles, for all resonances of the MLF spectrum. It is apparent, that even after five RELOAD loops, more than 50% of the initial magnetization is retained for most resonances. This implies a minor perturbation of the bath magnetization by the Redor RELOAD sequence. All spectra were recorded with at 600 MHz, 8 kHz spin rate, 295K and 4 scans. 50 Hz exponential line broadening was applied to all spectra.

3.6.5 The multi-spin problem

An additional advantage of the band selective Redor RELOAD sequence worth pointing out is that it eliminates the multi-spin problem of the Redor experiment, if exact distances are to be measured. A correct interpretation of the Redor oscillation, obtained upon increasing the Redor recoupling time, usually requires the assumption of a two spin system for an optimal fit. In uniformly labeled molecules, this assumption is often unreasonable, leading to severe complications in the interpretation of the measured curves. This can be alleviated by using selective pulses on the ^{13}C channel, which select only a certain spectral band, with the interaction of all other ^{13}C nuclei, outside the selected band, being refocused during the second half of each Redor recoupling block. This makes the two spin assumption viable in a multiple labeled system.

The two dimensional Redor RELOAD sequence, shown above, can be easily adapted to a three dimensional experiment, by just increasing the length of the Redor recoupling blocks, for successive experiments. Then Redor oscillation curves are obtained for all resonances in the spectrum in the third dimension, which can be analyzed for the determination of exact distances.

As longer Redor times lead to nontrivial through space connectivities, the exclusion of the multi spin problem from the Redor RELOAD experiment offers interesting possibilities to yield conformational restrains in a significantly reduced time.

3.7 Materials and Methods

3.7.1 Sample

$U^{13}C-^{15}N$ f-Met-Leu-Phe was bought from Euriso-top GmbH, Saarbr/"ucken, Germany and used without further purification. 3 mg of the peptide were transferred to a 4 mm MAS rotor for measurement.

3.7.2 NMR

All experiments were conducted on a Bruker Avance 600 MHz Spectrometer using a 4mm DVT HXY MAS probe. MAS frequencies of 10 kHz were used for all spectra. The samples were kept at 250 K during the measurements. PDSD spectra [28] of MLF were recorded using standard CP (with spinlock field 48,5 kHz on ^{1}H and 38,5 kHz on ^{13}C with a spin locking time of 1,25 ms and a ramped pulse of 80-100% on the 1H channel). ^{1}H and ^{13}C pulse lengths for 90° tilt angles were 3 and 6,5 s, respectively. The mixing time was 50 ms and the protons were decoupled during acquisition with 83 kHz Spinal64 decoupling [29]. The ^{13}C offset was set to 100ppm. CO selective excitation was achieved with a Sinc shape of $200\mu s$ length, with a concomitant carrier frequency shift of 11000 Hz to 173ppm. $C\alpha$ selection was achieved with a Gaussian Cascade (Q5) of 5ms length with a carrier frequency shift of -7250Hz to 52ppm.

All chemical shifts in this work have been referenced to TMS (0 ppm) at 4° C.

3.7.3 Computation

Experimental spectra were processed with Topspin 2.0 (Bruker, Karlsruhe).

3.8 Conclusion and Outlook

The effect of RELOAD for band selective, homo-nuclear and hetero-nuclear correlation experiments was demonstrated on the tripeptide MLF. The signal to noise enhancement factors observed were in the range of 1.4 to 1.8 for homo-nuclear and up to 1.4 for hetero-nuclear spectra, as compared to spectra recorded in a conventional manner. This corresponds to a decrease in measuring time of a factor of 2 to 3.24, and 2 for homo- and hetero-nuclear spectra, respectively.

The origin of the RELOAD effect was shown to result from an enhancement of the relaxation by spin diffusion from neighboring nuclei and the effect of the RELOAD mixing time was discussed, if a large number of RELOAD cycles is to be employed.

The gains achieved can be expected to be achievable in any spectrum in which only a certain region is of interest, and this region is excitable in a band selective manner. Therefore RELOAD should be applicable to a wide range of pulse sequences, yielding a significant reduction in measuring time for the experiments in question.

The presented pulse sequences are easily adaptable to three dimensions, without modification for a ^{15}N-^{13}C correlation, with a Redor oscillation in the third dimension, or with slight modification for a ^{15}N-^{13}C-^{13}C experiment, by a combination of the homo- and hetero-nuclear RELOAD sequences.

Chapter 4

Symmetry Based Hetero-nuclear Polarization Transfer: R70

4.1 Introduction

Solid state NMR is a versatile tool to study a wide variety of biological samples, such as lipids, small ligands or membrane proteins. Still, even though there is no intrinsic limitation imposed on ssNMR experiments by the rotation correlation time of the sample under study, polarization transfer can be complicated by the broad spectrum of motional regimes which may be encountered for a given sample, especially if semi solid preparations are to be investigated.

A polarization transfer step from one nuclear species to another is an integral part of most NMR experiments. Especially in ssNMR, this step plays an important role, as the transfer of spin order from ^1H to a hetero-nucleus is often a necessity to overcome the very low sensitivity offered by ssNMR on biological samples.

The problems encountered when applying conventional polarization transfer schemes to semi solid samples, are caused by effects of motion on the homo-nuclear and hetero-nuclear coupling between the spins. For instance, the hetero-nuclear dipole-dipole coupling (DD-coupling) typically employed in cross polarization (CP) [21, 70], is sensitive to motion, as its isotropic value is 0. J-couplings, on the other hand, are not influenced by mobility, but experiments employing the J-coupling for polarization transfer, such as INEPT [22], contain periods of free evolution, which cause significant relaxation losses, if the DD-couplings are not fully averaged.

This can become problematic for an reconstituted integral membrane protein at room temperature, as these samples exhibit domains with different motional properties. These consist of rigid transmembrane helices at one end of the scale and flexible loop regions on the other. For these cases, motional sensitivity of polarization transfer schemes between homo- and hetero-nuclei can prove to be limiting, if information from all regions of the sample is to be acquired in a single spectrum.

In solid state NMR, polarization transfer schemes such as the NOP-MAS [71, 72] utilizing the hetero-nuclear NOE and homo-nuclear decoupled INEPT [73] have been proposed to address this problem. These sequences have their origin in solution state NMR schemes and have been adapted to solid state NMR, by employing spin diffusion (in case of NOP-MAS) or homonuclear decoupling (INEPT with eDUMBO decoupling).

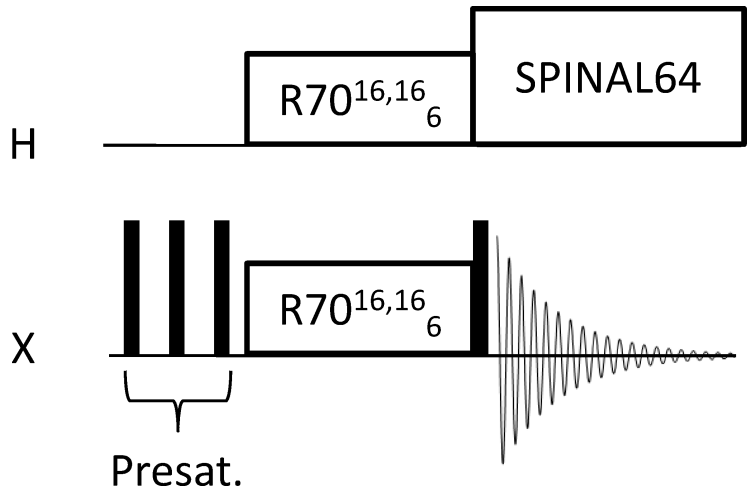

Figure 4.1: Schematic diagram of the pulse sequence for dual synchronized R-transfer used in this work. A presaturation sequence is applied first to eliminate natural abundance artifacts. Then, two double synchronized symmetry based recoupling blocks are applied simultaneously on both channels to transfer magnetization. A final 90° pulse creates observable x-y magnetization.

In this chapter, techniques first developed for solid state NMR are applied to the problem of motional sensitivity of heteronuclear polarization transfer. The heteronuclear J-coupling is chosen as a medium for motional insensitive polarization transfer, as dipole-dipole (DD) couplings are not an option for a motional insensitive sequence. Hetero-nuclear cross relaxation, via the nuclear Overhauser effect, is also unsuited as a mixing step in a two dimensional experiment, as transfer times would typically be in the order of seconds, making the experiment unfeasibly long.

A limiting factor for the application of J-couplings in the solid state is the competition with the other interactions present. The relative strength of the J-coupling, about 100 to 150 Hz, is low compared to the DD couplings in rigid solids, which are typically in the kHz range. To select one interaction for polarization transfer and additionally suppress the effect of other interactions, a reliable method to select the filter out desired interaction is needed. Particularly suited to selecting distinct magnetic interactions are the symmetry based sequences first introduced by Levitt and coworkers [23, 37, 74–76].

These sequences correlate the spinning speed of the MAS rotor with the RF pulse strength, which the nuclei are subjected to during the experiment. By carefully adjusting the pulse phase and RF nutation frequency at a particular MAS rate, certain interactions may be suppressed, while others are selectively reintroduced. This is an elegant method of tailoring the Hamiltonian during the mixing period. Two types of symmetry based sequences exist, referred to as C-type and R-type sequences [37]. The latter were used in the present work, as R-type sequences additionally allow the suppression of the isotropic chemical shift, which is important to avoid introducing phase errors into the spectra. Symmetry based sequences have been used for heteronuclear polarization transfer in MAS NMR before, but so far only for dipolar polarization transfer [37, 75]. In this chapter, dual synchronized, symmetry based pulse sequences, henceforth denoted as $RN_n^{\nu,\nu}$ sequences (with N, ν and n being symmetry numbers), as detailed in [37] have been used.

To identify the sequence best suited for the heteronuclear, through-bond polarization transfer, a large number of symmetries was evaluated in several steps. First,

symmetries from a large parameter space were tested using simulations, on spin systems commonly encountered in biomacromolecules, such as ^1H-^{15}N and ^1H-^{13}C-^1H. This yielded a selection of promising candidates for experimental evaluation. Thereafter, the performance of these sequences was tested experimentally to identify the most efficient and robust symmetry.

In this chapter the sequence $RN70_6^{16,16}$ is presented. Simulations and experiments on the lipid dimyristoylphosphocholine (DMPC) are presented, which show that the motional dependence of $RN70_6^{16,16}$ is intermediate between the classical heteronuclear transfer sequences INEPT and CP. DMPC is an ideal sample for these investigations, as DMPC shows a wide variety of dynamics, along its chain and headgroup. These motions can be further controlled by exploiting the phase transition of DMPC from the liquid crystalline to the gel phase, as this transition greatly influences the overall mobility of the lipid molecules [77]. These properties can be used to model a wide range of motional regimes.

The pulse sequence used in this work is shown in Fig. 4.1. First, a train of 90° pulses is applied to the heteronuclear channel, to eliminate natural abundance magnetization. Then, the $R70_6^{16,16}$ sequence is applied to both channels, to effect the polarization transfer. Finally, a 90° pulse creates observable x-y magnetization. The two dimensional version of this experiment, adds a ^1H $90^/circ$ pulse and a proton evolution period prior to transfer. Hetero-nuclear J-decoupling is achieved there by a 180° pulse on the heteronuclear channel in the middle of the ^1H evolution period.

4.2 Simulations

The program suite used in this chapter consists of several individual programs, which allow for a rapid identification of the most suitable set of symmetry numbers, in the large parameter space of possible combinations. The first routine in the program suite generates sets of symmetry numbers from a range of possible values specified by the user, iterating over all possible combinations. With a given set of symmetry numbers, the parameters for the simulation program SIMPSON are generated. The theory, which has been employed in the design of this testing algorithm, is discussed in [37] and briefly summarized in chapter 2. After the result is obtained, in the form of a buildup curve (magnetization on the hetero-nucleus over time), a second program performs an analysis, which consists of a check of the overall excitation efficiency and the time, after which the transfer maximum was reached. This routine is repeated, until the whole set of possible combinations is screened. When all symmetry sets have been computed, the results are output in form of a surface plot, giving the excitation efficiency over the symmetry numbers. Here, sequences not fulfilling the minimum limits in excitation efficiency and/or excitation profile can be excluded from the plot. This plot is shown in Fig. 4.2.

From this plot, promising candidates can be selected by the user and be submitted to a program, which will automatically translate the symmetry numbers obtained into a Bruker pulse program.

This procedure makes it feasible to screen a large number of symmetries, which theoretically solve a given recoupling or decoupling problem.

Thus, this approach can be used to find any symmetry based recoupling (or decoupling) sequence suited for a given experiment on one or more channels, as long as the target state is known and can be reliably evaluated by an automated routine.

4.2.1 Symmetry based heteronuclear transfer

To arrive at a set of sequences which fulfill the boundary conditions given above and to limit the number of sequences which have to be considered experimentally,

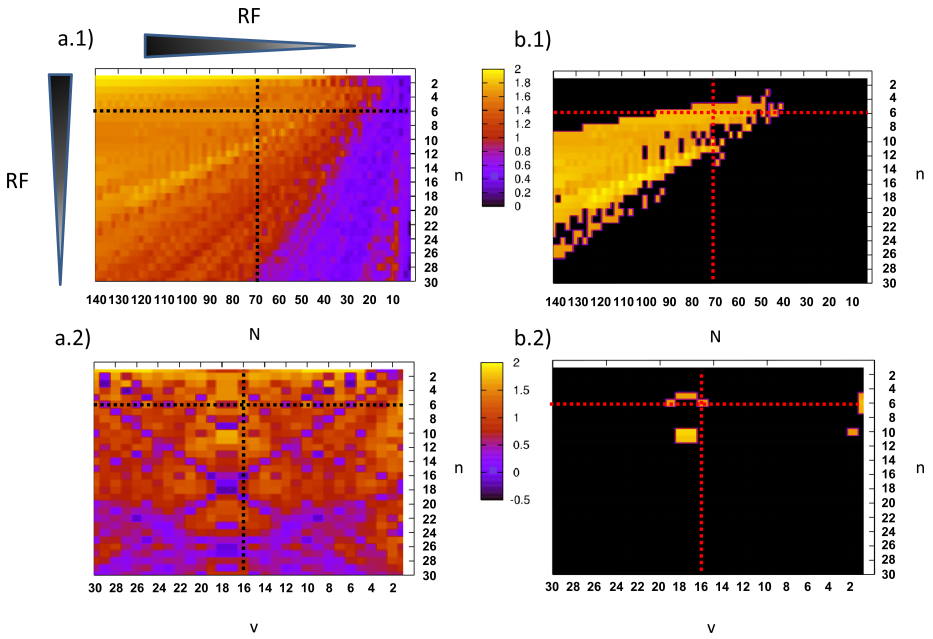

Figure 4.2: Evaluation of the transfer efficiency of 63000 symmetry sets. Buildup curves were simulated using the SIMPSON software package and evaluated for all combinations of N (2-140), n (1-30) and ν(1-30) as shown in a.1) Here, only the maximum efficiency for all possible values of ν has been plotted to reduce dimensionality to two, for sake of clarity. a.2) To arrive at a complete set of symmetry numbers, the slice indicated in a.1) is expanded along ν to find the sequence with the highest efficiency and complete the set of symmetry numbers. b.1) and b.2) are the same as a.1) and a.2) but with the additional selection criterion of a minimum of 0.75 maximal transfer and a RF power requirement of less than 10 x ω_r. The set of symmetry numbers for the sequence $R70_6^{16,16}$ is indicated in red. The spinning speed was set to 10 kHz for all simulations.

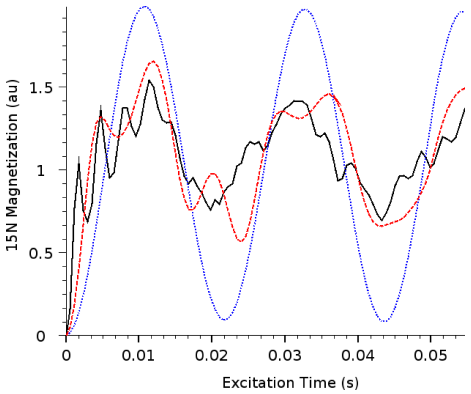

Figure 4.3: Simulated excitation curves for $R70_6^{16,16}$ on a linear NH..H spinsystem using the same J-coupling (-92Hz) for each trace, but with scaled DD-couplings relative to the values used for the simulations shown in Fig.4.2. Full DD-coupling was used for the black solid trace, 0.6 x DD-coupling for the red, broken trace and 0.2 x DD-coupling for the blue, dotted trace. It can be seen that dipolar couplings reduce transfer efficiency by a factor of approx. 0.25.

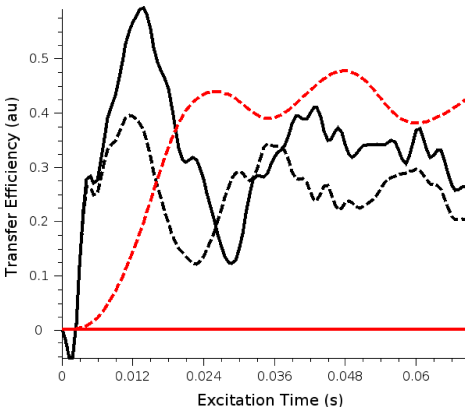

Figure 4.4: Excitation curves for a C-CH_2 group. Black are the traces for the carbon with attached protons, without (solid line) and with homo-nuclear J-coupling (dotted line) between the carbons. The traces for the carbon without directly bound protons are shown in red, without (solid line) and with homo-nuclear J-coupling (dotted line). It is apparent that homo-nuclear ^{13}C-^{13}C magnetization transfer occurs simultaneous to heteronuclear ^{1}H-^{13}C transfer. Dipolar couplings were scaled by a factor of 0.1 for this simulation. Spinning speed was set to 10 kHz for all simulations.

symmetry numbers have to be chosen such that only the terms corresponding to the heteronuclear J-coupling in table 2.2 in chapter 2 are selected. All homo-nuclear terms should be suppressed, including the isotropic chemical shift, as it is desirable to suppress evolution during the transfer. This can be easily done for all interactions, save for the homo-nuclear J-coupling, which is always symmetry allowed, as can be seen from its space- and spin rank of 0. Therefore, the symmetries of interest would yield a multi interaction decoupling, while leaving the heteronuclear J-coupling intact.

Fortunately there are many sequences that exhibit this kind of recoupling profile. Still the experimental performance of these sequences is not identical. The reason for this is, although the first order averaged Hamiltonian given in equations 2.119 and 2.120 in chapter 2 is a good indication to what terms will be symmetry allowed, second and higher order terms of the averaged Hamiltonian influence the experimental performance of a symmetry based sequence as well. Generally, there are many second and higher order terms which are symmetry allowed. This can lead to interference effects, degrading the experimental performance of the sequence, but the extent of these effects are difficult to predict. Therefore numerical simulations were conducted, to assess the transfer efficiency of all sequences in a range of symmetry numbers (N = 2-140, n = 1-30, ν = 1-30) using the SIMPSON simulation package [78], as outlined above. Simulations were performed for a simple linear spin system, in which a ^{15}N nucleus is directly bound to a proton and another distant, non bound proton is present. The interaction strengths were set to typical values found in the literature (see Material and Methods for details). The evaluation of the resultant buildup curves for this spinsystem in presence of all heteronuclear interactions (J and DD) is shown in Fig. 4.2 a1). Here an efficiency landscape is plotted over the symmetry numbers N and n. Efficiency is defined here as the maximum ^{15}N magnetization obtained during the excitation time. For each point shown in Fig. 4.2 a1), only the the best efficiency for ν is plotted to keep the dimensionality to two, for sake of clarity. When a suitable set of N and n is chosen, a slice can be expanded along the chosen value of N, to yield the efficiency landscape in dependence of ν, as shown in Fig. 4.2 a2). Choosing an appropriate ν finally yields a complete set of symmetry numbers. As can be seen from Fig. 4.2 a) there are many sequences that show efficient polarization transfer

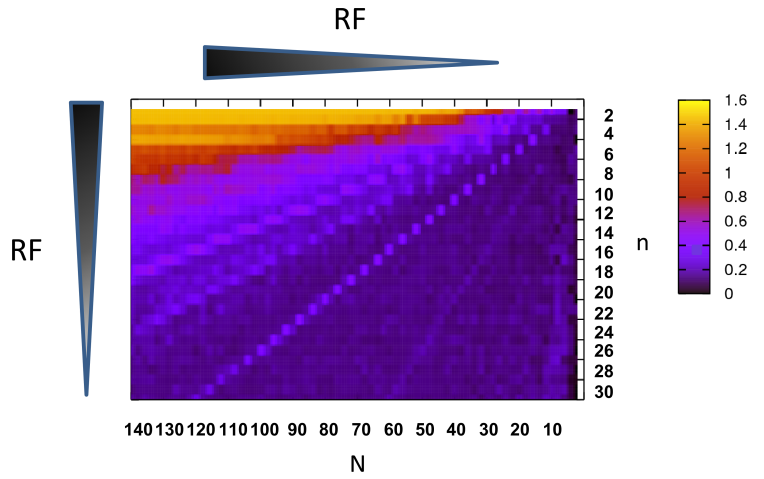

Figure 4.5: Transfer efficiency of the same symmetry sets numbers shown in Fig.4.2, but for a CH_2 spinsystem derived from G35 in Ubiquitin. It is apparent, that for this spinsystem much stronger RF fields are required to yield good transfer, as compared to Fig.4.2. The spinning speed was set to 10kHz for all simulations.

from ^1H to ^{15}N, especially for sequences with higher RF-power requirements. This is expected, as symmetry based suppression of interactions only works reliably, if the radio frequency (RF) irradiation is much stronger than the interactions to be suppressed. If this is not the case, these interactions are still present to a certain degree, leading to attenuation of the transfer efficiency.

To identify the most suitable candidates for experimental implementation, limits were imposed on the radio frequency power requirement of the sequence (less than 10 x the MAS rate (ω_r)) and the transfer efficiency, where the maximum ^{15}N magnetization reached during the excitation time must be greater than 75% of the theoretical optimum. This was done to filter out sequences with unrealistically high demands on the hardware, and those in which competing interactions attenuate the through-bond polarization transfer.

These selection criteria lead to the reduced set of symmetry numbers shown in Fig. 4.2 b). To further differentiate between primarily J-coupling mediated and higher order DD-coupling driven transfer, a variety of different homo- and heteronuclear DD-coupling strengths were simulated, keeping the J-couplings fixed. This was done for the subset of symmetries which performed best in the first simulation run. Only sequences that showed minimal perturbation of the excitation profile with rising DD-coupling strength were considered for experimental evaluation. An example is shown in Fig. 4.3 for $R70_6^{16,16}$, which was identified as the most efficient and robust sequence of the parameter space investigated and which is used for the reminder of this chapter. Here, transfer is simulated in relation to dipolar coupling strength. For this, the J_1NH coupling was left constant at a value of -92Hz, but all DD-couplings present were reduced by 40% (red curve) and 80% (blue curve). The reason for these simulations was to get an estimate of the effect of motional averaging on the sequence. Comparison of the curves shows that the maximum transfer of magnetization to ^{15}N is reduced by 25% under the full strength dipolar coupling, most likely by second order dipolar coupling terms present in the averaged Hamiltonian, for the spin system used.

To verify these results, spin systems with the orientations, distances and chemical shift tensors typically found in proteins were simulated. To this effect, the relative orientations of the nuclei in the backbone of K6 and the side chain of G35 in ubiquitin

(pdb:1D3Z) were used as input for the program SIMMOL [79]. This program calculates all relevant CSA tensors and DD-coupling strengths for the spin system given, using standard values from the literature. The resultant transfer efficiency plot for a CH2 spinsystem, is shown in Fig. 4.5. It can be seen that power requirements are even more stringent here, as is to be expected from the strong modulation of the Hamiltonian by the DD-couplings from two directly bound protons.

As mentioned above, the homo-nuclear J-coupling is always selected for this kind of sequence, regardless of the symmetry numbers chosen. It is therefor interesting to investigate, if this interaction can act as a mediator of relayed transfer.

A simulation of this behavior is shown in Fig. 4.4. Here, a C-CH_2 group was simulated. The solid lines indicate the magnetization buildup on the protonated (black) and non-protonated carbon (red), if no homo-nuclear J-coupling exists between the two carbons. As expected for a through bond polarization transfer, only the protonated carbon is polarized. The dotted lines show the magnetization buildup of the same spin system, upon introduction of a homo-nuclear J-coupling of 55Hz between the two carbons. A polarization buildup on the non-protonated carbon is apparent, which follows the polarization buildup of the protonated carbon with a certain lag. Furthermore, the polarization of the protonated carbon is markedly reduced.

This strongly suggests that a relayed polarization transfer is possible between the two carbon nuclei, via the homo-nuclear J-coupling.

4.3 Materials and Methods

4.3.1 Samples

DMPC was bought from Avanti and used without further purification. A sample of 15 mg was rehydrated with 45 μl D_2O, freeze thawed via bath sonication three times and then packed into a 4mm MAS rotor using high resolution MAS inserts.

4.3.2 Computation

Simulations were performed using the SIMPSON package [78], with different spin systems. The initial set used in Fig. 4.2, consisted of a linear arrangement of a ^{15}N nucleus with a directly bound proton (HN) (J_1NH = -92Hz, DD-coupling = 11146.6) and a distant proton (HD) (DD-coupling to ^{15}N = 1393.32, DD-coupling to HN = -4925.27). For verification two additional spin-systems were calculated using SIMMOL [79] together with the pdb structure of ubiquitin (pdb: 1d3z). Relative orientations and distances for an amide group and a HCα were calculated for the backbone of the residue K6. Similarly a CH2 spin system was calculated from the geometry of the residue G35. The resultant buildup curves were evaluated with the help of the Tcl scripting language [24]. Graphs were plotted using Gnuplot 4.0. Processing of experimental spectra was done in Topspin 1.3 (Bruker, Karlsruhe). The programs used are given in the appendix.

4.3.3 NMR

Experiments were conducted on a Bruker Avance II 400 MHz Spectrometer using a 4mm DVT HXY probe. An MAS frequency of 5 kHz was used in all experiments. The temperature of the DMPC sample was varied between 270 and 310 K, as indicated in the figure captions. The pulse power used for all hard pulses and the $R70_6^{16,16}$ mixing block was 58333 Hz , as given by the quotient of the symmetry numbers N/n and the MAS rate of 5 kHz. The excitation time was optimized to 6.52ms. Presaturation before the $R70_6^{16,16}$ transfer was achieved with 8 $\pi/2$ pulses spaced in intervals of 5ms. The evolution delay for the heteronuclear J-coupling during refocused INEPT transfer

was optimized to 2.27 ms for all experiments. CP contact field strengths were 36 kHz and 41 kHz on ^{13}C and ^{1}H, respectively. CP mixing time was 2 ms. DMPC 2D heteronuclear correlation spectra were recorded with 64 scans per increment and 128 increments in the indirect dimension. All experiments were recorded with an acquisition time of 30 ms and 67 kHz SPINAL64 [80] decoupling during acquisition.

4.4 Experimental Verification and Results

For experimental evaluation, spectra of DMPC were recorded at different temperatures. DMPC is ideally suited for studying the dependence of different polarization transfer schemes on motion, as the phase transition at 24°C from gel to liquid-crystalline phase strongly increases mobility of the lipid molecules, especially in the chain region. Furthermore, it is well known that the order parameters in lipid bilayers vary along the membrane normal, and yield another indication of the polarization transfer efficiency for different motional ranges.

Spectra of DMPC were recorded at different temperatures using $R70_6^{16,16}$, INEPT and CP transfer steps from ^{1}H to ^{13}C, to compare the performance of the symmetry based sequence to established polarization transfer schemes. The spectra for DMPC at 310K and 280K using 5 kHz MAS, are shown in Fig. 4.6 a) and b), respectively. $R70_6^{16,16}$ exhibits good polarization transfer efficiency at high temperature, as predicted by theory and the simulations described above. At 310K, the INEPT and $R70_6^{16,16}$ show a similar performance for all resonances, with the exception of the methyl groups of the DMPC chain (denoted as CH3 in Fig. 4.6) and the headgroup carbons (denoted as α,β,γ), where INEPT is more sensitive by a factor of 2.14 (here a factor of 1 denotes equal intensities), as compared to $R70_6^{16,16}$.

For the chain carbons ($(CH_2)_n$) polarization transfer with INEPT is less effective by a factor of 0.86. CP, on the other hand, is the best sequence to polarize the chain carbons, being more sensitive by a factor of 2.84 as compared to $R70_6^{16,16}$, but transfer efficiency is poor, only 0.11 of $R70_6^{16,16}$ for the methyl carbons of the highly flexible phosphatidylcholine headgroup (γ). A reduction in mobility, brought about by cooling the sample below the lipid phase transition temperature, perturbs the performance of INEPT considerably, for all but the headgroup carbons. CP performs better at lower temperatures, showing more effective polarization transfer for the chain and even chain-terminus carbons, but the headgroup intensity is still low. $R70_6^{16,16}$, on the other hand, shows a performance intermediate between those of INEPT and CP. While the sensitivity for the headgroup is still higher with INEPT transfer by a factor of 1.43, the chain carbons are not polarized at all. Compared to CP, $R70_6^{16,16}$ performs better for the headgroup carbons (CP efficiency is 0.22 as compared to $R70_6^{16,16}$), while the chain region is polarized better by a factor of 5.57 by CP. An explanation could be, that in this more rigid motional regime, the second order dipolar averaged Hamiltonian terms have a stronger influence on the transfer, leading to stronger relaxation during the excitation time. Higher spinning speeds and consequently higher RF power could prove to be advantageous in this regard, but higher MAS rates were not studied in this work, as hardware limitations prevented power levels exceeding 75 kHz on the carbon channel. Thus polarization transfer blocks with reduced RF power requirements would be preferable. To this end other sequences, with reduced RF power requirements were tested, such as $R34_5^{26,26}$. It was found that, even as $R34_5^{26,26}$ is 25% more efficient than $R70_6^{16,16}$ for methyl groups at higher temperatures, the increased influence of second order DD-terms leads to stronger relaxation during transfer. This results in temperature dependence similar to INEPT, even at higher MAS rates. Additional simulations and experiments conducted with super cycled versions of the transfer sequences did not show a significant improvement of the experimental stability, for any of the symmetries tested. To ascertain the performance of $R70_6^{16,16}$ in a two dimensional

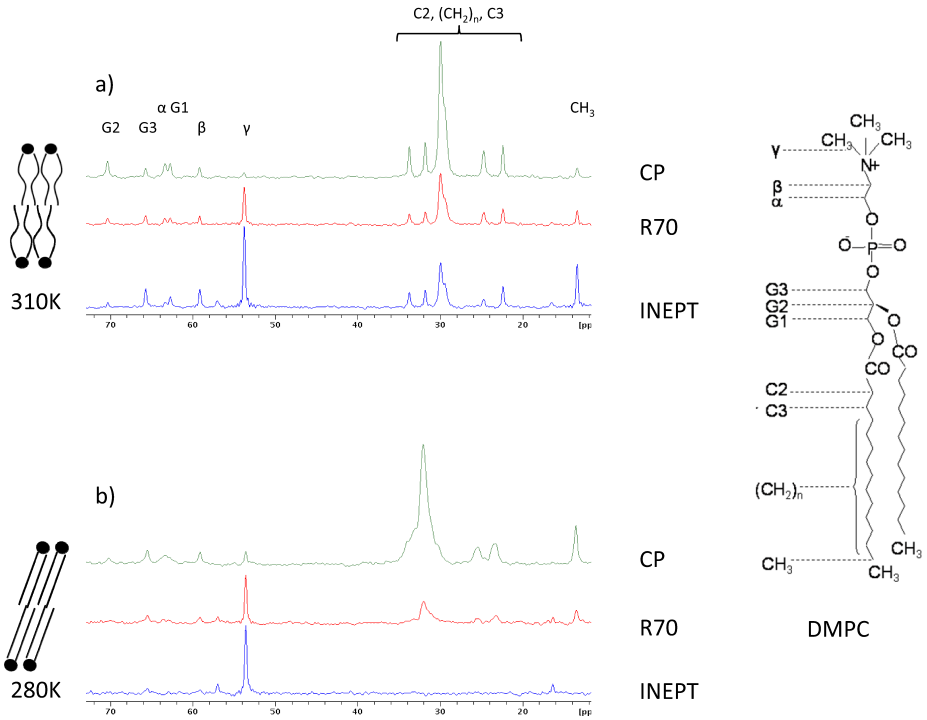

Figure 4.6: a) ^{13}C 1D spectra of DMPC using INEPT, $R70_6^{16,16}$ and CP recorded at 310K with 5 kHz MAS. b) Same spectra as in a) but at 280 K. The structure of DMPC with resonance assignments is shown on the right. A pictorial representation of the phases of DMPC, at the two temperatures used, is given to the right of the spectra.

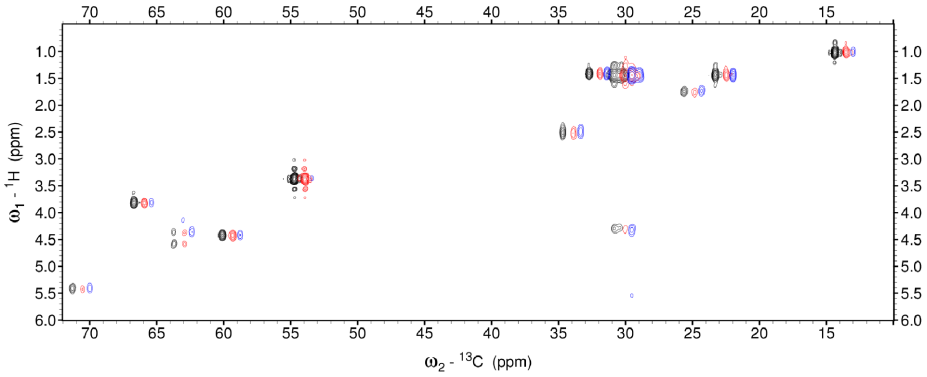

Figure 4.7: 2D $^1H-^{13}C$ heteronuclear correlation spectra of DMPC recorded at 310 K and 5 kHz MAS. The heteronuclear transfer step was INEPT for the black spectrum, $R70_6^{16,16}$ for the red and CP for the blue spectrum (spectra have been offset by 0.8ppm for clarity). The spectra are comparable and no phase errors are introduced by $R70_6^{16,16}$ transfer.

experiment and to exclude the presence of artifacts in our spectra, 2D heteronuclear correlation experiments on DMPC were recorded at 310K, 5 kHz MAS. As shown in Fig. 4.7 the $R70_6^{16,16}$ transfer (red) performs comparable to INEPT (black) and better as CP (blue) for mobile residues, as seen before. Additionally it does not introduce artifacts or phase problems into the spectra, indicating suppression of the isotropic chemical shift evolution during transfer, an important characteristic for good phasing behavior.

Due to the presence of the homo-nuclear J-coupling during excitation, the possibility for relayed transfer to ^{13}C nuclei with no directly bound ^{1}H exists. To investigate this possibility further, the simulations shown in Fig. 4.4 were conducted as described in section 4.2.

It can be seen that, upon addition of the homo-nuclear J-coupling between the two ^{13}C nuclei, polarization is transferred between these spins during the excitation time. Measurements on a fully labeled protein sample corroborates these findings, as shown in chapter 8.

This feature of $R70_6^{16,16}$ could be used to provide H-Cα-CO correlation information for fully labeled proteins. This information can be especially useful in a ^{1}H-^{13}C correlation experiment on membrane proteins reconstituted into phospholipids. Lipids are normally added in a large excess to the protein during reconstitution. A consequence of this are strong peaks from natural abundance ^{13}C lipid background in the spectra, complicating the analysis, especially if complex lipid mixtures were used for reconstitution. Relayed transfer in the fully labeled biomolecule can help to identify genuine protein peaks.

4.5 Conclusion and Outlook

In this chapter a dual synchronized symmetry based sequence $R70_6^{16,16}$ was identified, using a semi automatic routine for rapid screening of a very large number of theoretically possible symmetry based sequences. This sequence is suited for heteronuclear polarization transfer using J-couplings and shows a dependence on molecular motion, which is intermediate between INEPT and CP transfers. This could be shown in one and two dimensional experiments, on a sample of DMPC. $R70_6^{16,16}$ could become especially useful when studying semi solid samples, such as drugs or peptides in a membrane environment or reconstituted membrane proteins, which can show large motional variations in different domains. An additional feature of the sequence is the homo-nuclear J-transfer active during excitation, which allows for polarization transfer to spins with no directly bound proton. This could prove to be advantageous for the identification of a uniformly ^{13}C labeled compound in the presence of a strong ^{13}C background i.e. the lipid matrix of a membrane protein.

4.5.1 Acknowledgments

The author wants to thank Prof. Thomas Vosegaard for helpful discussion and support using SIMPSON, and Prof. Malcolm H. Levitt for helpful discussions.

Chapter 5

Double quantum filtered homonuclear correlation spectra

5.1 Introduction

Homonuclear correlation techniques become an increasingly important method for obtaining structural data from biomolecules in the solid state. Methods, such as ^{13}C-^{13}C proton driven spin diffusion (PDSD) [33] , dipolar assisted rotational resonance (DARR) [81] or CHHC polarization transfer experiments [82], together with uniform isotope labeling of proteins, allow a large number of distance constraints to be obtained simultaneously. As in established liquid state NMR protocols, such constraints are important for protein structure calculations of high resolution. However, the situation becomes rather challenging when such spectra are acquired on small, uniformly labeled molecules embedded into protein/lipid complexes, which are the source of large ^{13}C natural abundance (NA) background signals. Such a situation is typically encountered, for example, with uniformly ^{13}C labeled neuropeptides bound to GPCRs [18, 83], or single ^{13}C labeled amino acids within large membrane proteins [84]. The difficulty here lies in the fact that signals from the labeled compounds are obscured by the large NA peak intensities along the DARR spectrum diagonal, which is typically larger in intensity by several orders of magnitude. In the past, ^{13}C isotope labeling has sufficed for the structural investigation of membrane proteins in reconstituted form [85–87] or peptide/protein complexes [88]. For these examples, the ratio of the signals which stem from labeled sample (SL) and the natural abundance (NA) background (SNA) proves to be SL/SNA 10^{-2}, which is sufficient for ssNMR experiments on protein systems. However, for the case of samples involving large membrane protein/lipid complexes, SL/SNA becomes much smaller, and the signal of the ligand, although labeled, is obscured by the signal background from NA ^{13}C nuclei found in the membrane protein and its reconstitution environment (detergent micelles or lipid membranes). Here, DQ filtering [89–92] has proven to be the crucial step: past ssNMR studies of ligands bound to reconstituted membrane protein receptors were possible only because DQ filtering causes the signals of isolated ^{13}C nuclei to be removed from the NA background spectrum, which lowers the ratio SL/SNA at which ssNMR experiments may be carried out, roughly by two orders of magnitude: SL/SNA 10^{-4} [18]. A solution to this problem are DQ filtered experiments with which chemical shift values of GPCR bound neuropeptides, for example, have lead to backbone structures [18, 83], or the

characterization of single amino acids within multidrug transporters [84]. The DQSQ experiments used in these examples yield protein backbone torsion angle constraints, which is information that is contained in chemical shift values. DARR experiments are complementary, and deliver through space constraints not through chemical shifts, but through relative cross peak intensities and buildup rates. Whilst DQSQ experiments are inherently suited for samples with a high NA ^{13}C background, DARR pulse sequences with DQ filtering are currently not obtainable within the repertoire of existing ssNMR techniques. Here, DARR experiments [81] are described, which are extended by pulse sequence blocks and phase cycling in which DQ coherence is first excited and then reconverted to single quantum coherences. Two schemes for DQ filtering DARR experiments are depicted in Fig. 5.1. In the first (Fig. 5.1 a), DQ filtering occurs after Hartman-Hahn ^{1}H-X magnetization transfer, before chemical shift evolution. In the second (Fig. 5.1 b), DQ filtering is achieved after longitudinal magnetization exchange for a period t_{mix}, before signal acquisition. For convenience, in the remainder of this chapter, the abbreviations DOPE (Double Quantum Filtering Prior to Evolution) and DOAM (Double Quantum Filtering After the Mixing) will be used to distinguish between the two strategies. The pulse sequences introduced here are developed with structural studies of GPCR bound ligands in mind [18, 83]. GPCRs, reconstituted, in a lipid medium, and complexed with a natural ligand, require a large amount of care and effort. Therefore, such mammalian membrane proteins are not used in the context of this chapter. Instead, this study involves two sets of experiments, the first which consists of tests of DQ filtered DARR sequences on the reconstituted, bacterial transmembrane photoreceptor proteorhodopsin (PR, 27 kDa) of which three cysteine residues are uniformly ^{13}C labeled. This sample was kindly provided by Dr. Sarika Shastri. In the second set of experiments, the effect of DQ excitation and reconversion on cross peak intensities in the DARR, DOPE and DOAM are investigated on spectra of the tripeptide MLF, for different mixing times. The experimental details and the results are described in the following.

The results presented in this chapter have been published in [93].

5.2 Materials and Methods

5.2.1 NMR pulse sequences

In the following DARR experiments [81], which are extended by pulse sequence elements designed to first excite DQ coherences and subsequently reconvert them to single quantum coherences, are described. Symmetry theorems for MAS NMR experiments during which radio frequency (RF) pulses are timed to coincide with the MAS rotor revolutions allow the NMR spectroscopist to tailor the Hamiltonian under which the magnetization evolves [35]. Here, for DQ filtering, the symmetry-derived sequence block $SR22_4^9$ is incorporated into the experiment. This block belongs to a class of pulse sequences which may be described with the shorthand notation SRN_n^ν [36] ,where R denotes an element in which the resonant spins are rotated about the x-axis (of the rotating frame) through the angle π. A second element R follows, which is identical to its predecessor R, but with an RF pulse phase of opposing sign (see Fig. 5.1 c). The properties of this particular sequence block (N = 22, ν = 9, n = 4) lead to a γ-encoded CSA-compensated dipolar recoupling between X nuclei [36]. Of course, other established DQ coherence recoupling sequences, such as for example pC7 [23] and SPC5 [94] are expected to give comparable results. For the case of DQ filtering before the chemical shift evolution (Fig. 5.1 a, DOPE), bracketing pulses are placed on either side of the array of R-elements, in order to create longitudinal magnetization before the DQ filtering, and transverse magnetization after the DQ excitation/reconversion, for the ensuing chemical shift evolution (of duration t1). For the case of DQ filtering after magnetization exchange (Fig. 5.1 b, DOAM), bracketing

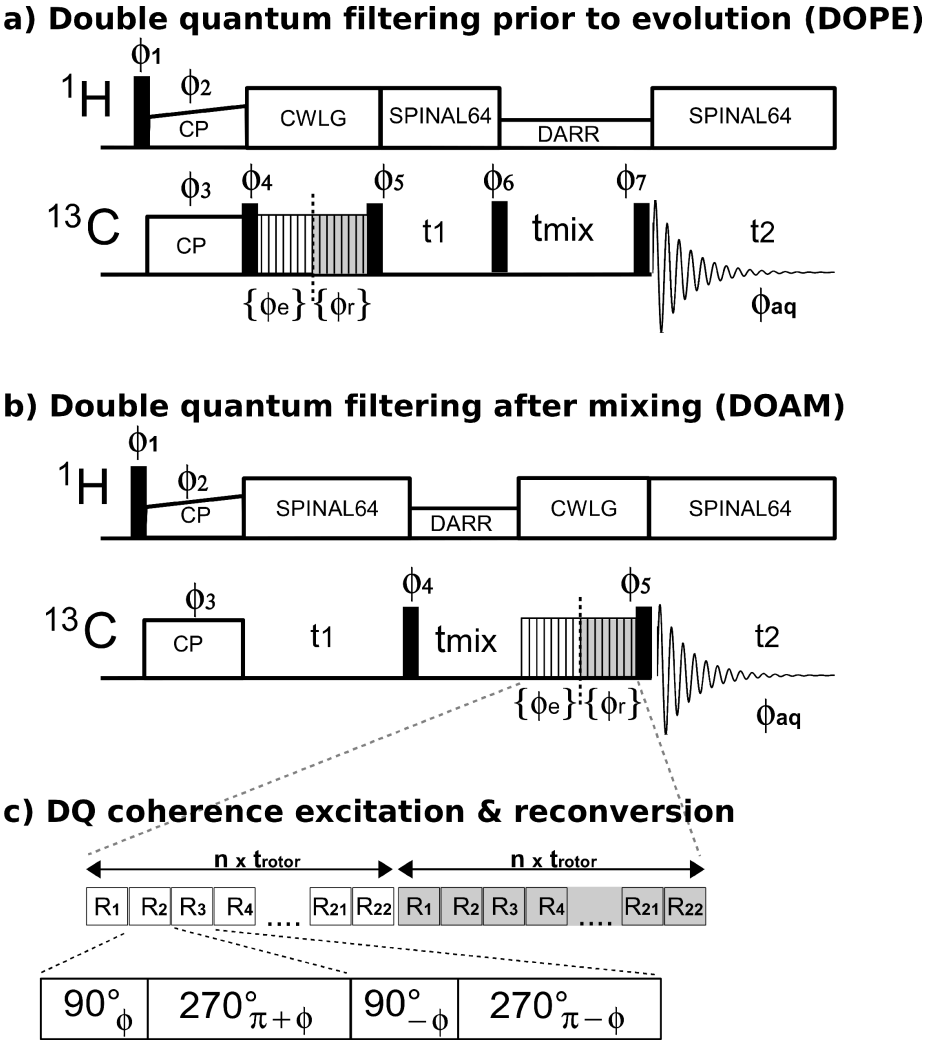

Figure 5.1: DQ filtering schemes for DARR experiments. DQ filtering prior to evolution (DOPE, upper scheme) is achieved before the chemical shift evolution by excitation of magnetization due to DQ coherences, and its immediate rerouting to SQ coherence pathways. For DQ filtering after mixing (DOAM, middle scheme), the DQ excitation-reconversion block is placed at the end of the DARR pulse sequence. $SR22_4^9$ is schematically depicted (lowest scheme), the phases of the R sequences have collectively been summed up in a) and b), for DQ excitation ϕ_e and DQ reconversion (shaded) ϕ_r, in order to describe their super cycling for DQ filtering by phase cycling (see text)

pulses are unnecessary: longitudinal magnetization is already present before filtering, and is converted to transverse magnetization by the readout pulse, for signal acquisition. To avoid interference by a Hartman-Hahn transfer during DQ excitation and reconversion, any ^1H-^{13}C magnetization transfer has been subdued by the application of homonuclear Lee-Goldburg [95, 96] decoupling during DQ excitation and reconversion in both, DOPE and DOAM experiments.

5.2.2 Setup and parameter values

NMR experiments were conducted using two widebore Bruker Avance spectrometers (Bruker Biospin, Karlsruhe, Germany), respectively operating at ^1H frequencies of 400 MHz and 600 MHz, each equipped with a triple-resonance (^1H,^{13}C,^{15}N) MAS DVT probe head (4 mm rotor diameter). Experimental parameters were very similar for all experiments, and are listed respectively in the following, for the 400 MHz and 600 MHz (in brackets) spectrometers: Hartmann-Hahn ^1H to ^{13}C cross-polarization scheme [21] parameters, the contact pulse duration is 1000 μs (750 μs), ^1H spin lock power levels, ramped from 80 % - 100 %: 46 kHz (62 kHz), ^{13}C spin lock power levels: 44 kHz (44 kHz), $\pi/2$ pulse lengths for ^1H: 4.25 μs (3 μs), $\pi/2$ pulse lengths for ^{13}C: 4.55 μs (4 μs). SPINAL64 decoupling [80] was used during chemical shift evolution and signal acquisition, at a power level of 74 kHz (83 kHz). DQ excitation and recoupling were achieved with the symmetry derived pulse sequence block $SR22_4^9$, with equal DQ excitation and SQ reconversion times of 410 μs (500 μs). Lee Goldburg decoupling was set up on adamantane, by varying the ^1H r.f. field strength for a given pulse length until ^1H-^{13}C J-couplings could be resolved. Here, an effective ^1H decoupling field of B1/ $\sqrt{2}$ = 66 kHz (83 kHz) was used. On PR, 2D DARR spectra and the DQ filtered versions thereof were acquired with 2048 (F2) points and 128 (F1) increments (1024 scans per increment). Magnetization buildup curves (Fig.5.3) were obtained on U-^{13}C-MLF by acquiring 2D ^{13}C MAS - DARR, DOPE and DOAM (Fig.5.4) spectra at mixing times of (in seconds): 0.001, 0.005, 0.010, 0.025, 0.050, 0.100, 0.150, and 0.200 per increment. Here, spectra were acquired with 1024 points, 128 increments and 64 acquisitions. All 2D experiments were carried out with phase sensitive detection (STATES-TPPI) at an MAS speed of 10 kHz, with a recycle delay time of 2 s, at a temperature of 290 K.

5.2.3 Phase cycling

In order to ensure that only coherences generated by Hartman Hahn ^1H - ^{13}C magnetization transfer are propagated during the experiment, ϕ1 and ϕaq are synchronously alternated between y and y for each acquisition. DQ filtering is achieved by conventional phase cycling, in which the phases of two pulse sequence blocks are cycled in a concerted manner with respect to each other [97]. For both DOPE and DOAM experiments, the array of R elements which reconvert DQ coherence to SQ coherence (phases ϕr in Fig.5.1, shaded elements), together with the second bracket pulse (phase ϕ5), constitute the first entity to be supercycled. Their phases are incremented by 90° with each acquisition. In order to filter out any magnetization not due to DQ coherence pathways, the pulse positioned at the end of the chemical shift evolution (DOPE, Fig. 5.1 a, ϕ6) and the receiver phase (DOAM, Fig.5.1b, ϕaq) were cycled according to -y x y x. Conclusively, the final phase cycles used in the experiments consists of eight steps, and are listed in table 5.1 (DOPE) and tablw 5.2 (DOAM).

5.2.4 Processing, Analysis and Plotting

If not mentioned otherwise in the figure captions, all spectra were processed by doubling the number of points in each dimension, using zero filling. Automatic baseline

ϕ_1	ϕ_2	ϕ_3	ϕ_4	ϕ_r	ϕ_5	ϕ_6	ϕ_7	ϕ_{aq}
y	y	x	-x	y	y	-y	x	x
y	y	x	-x	-x	-x	-x	x	x
y	y	x	-x	-y	-y	y	x	x
y	y	x	-x	x	x	x	x	x
-y	y	x	-x	y	y	-y	x	-x
-y	y	x	-x	-x	-x	-x	x	-x
-y	y	x	-x	-y	-y	y	x	-x
-y	y	x	-x	x	x	x	x	-x

Table 5.1: Phase cycle of the DOPE pulse sequence (Fig.5.1a)

ϕ_1	ϕ_2	ϕ_3	ϕ_4	ϕ_r	ϕ_5	ϕ_{aq}
y	y	x	x	y	y	-y
y	y	x	x	-x	-x	-x
y	y	x	x	-y	-y	y
y	y	x	x	x	x	x
-y	y	x	x	y	y	y
-y	y	x	x	-x	-x	x
-y	y	x	x	-y	-y	-y
-y	y	x	x	x	x	-x

Table 5.2: Phase cycle of the DOAM pulse sequence (Fig.5.1b)

corrections and window functions were applied in the direct (exponential form, 50 Hz) and indirect dimension (squared sine function, with a sine bell shift of $\pi/2$, corresponding to a pure cosine function). All experimental data were processed with TopSpin 2.0 (Bruker BioSpin, Karlsruhe, Germany). Peak picking and integration was carried out with the help of the software package Cara 1.8.3 [98]. Plotting and data analysis was carried out with the help of scripts written in house, using Python 2.5 (http://www.python.org), more specifically with the library of mathematical functions which are supplied in the python modules pylab (http:// matplotlib.sourceforge.net) and SciPy (http:// www.scipy.org, [99]). With the exception of TopSpin, all software is available for download on the world wide web, at no cost. Data AnalysisBuildup curves (see Fig. 5.3) were calculated with the full matrix rate analysis, [25]. In short, experimentally measured DARR peak volumes, represented by matrix A, at the mixing time t_m, and the cross-relaxation rate R are linked by the following matrix equation.

$$A(t_m) = A(0) * exp(Rt_m) \tag{5.1}$$

The relaxation rate matrix R is calculated by rewriting Eq. 5.1 as follows.

$$R = -\frac{Xln(D)X^{-1}}{t_m} \tag{5.2}$$

Here, X is the matrix of eigenvectors, and D is the diagonal matrix of eigenvalues of the normalized peak volume matrix a(t_m) = A(t_m)[(A(0)-1]. All calculations were carried out with the help of Python 2.5, specifically with the modules pylab and SciPy (www.scipy.org).

5.2.5 Sample Preparation

Two samples were used for NMR measurements: First, the integral membrane protein proteorhodopsin (PR, 27 kDa), reconstituted into DOPC in 2D crystalline form, with

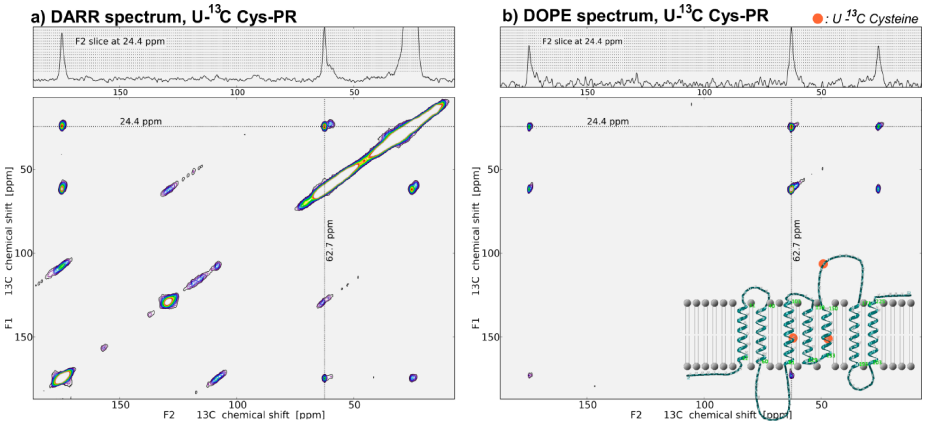

Figure 5.2: DARR and DOPE spectra on reconstituted PR, with selectively ^{13}C labeled cysteines 107, 156 and 175 (marked by orange circles on the protein, see inset picture). For both DARR and DOPE spectra, 16 equidistant contour levels were chosen, with a minimum value just above the baseline, and a maximum value corresponding to the cross peak intensity at 67.7 and 24.4 ppm (see slices, at top). The diagonal intensity is the dominant spectrum characteristic in the conventional DARR spectrum, along with MAS spinning sidebands, and is completely removed in the DOPE spectrum. Any background contribution from ^{13}C NA intensities, stemming from the large membrane protein and its reconstitution environment (lipid bilayer), is removed.

selectively ^{13}C labeled cysteines which are found at positions 107, 156 and 175 (see Fig. 5.2, inset). Second, the chemotactic tripeptide MLF, uniformly ^{13}C and ^{15}N labeled. The expression of wild type PR was essentially carried out as described in [100]. In short, the cells were grown in defined medium with 50 g/ml Kanamycin until the optical density reached 0.8. The cells were then resuspended in a freshly mixed medium with labeled cysteine (50 mg/lit). 1 mM IPTG (isopropyl-beta-D-thiogalactopyranoside) was used for induction along with 0.7 mM all-trans retinal dissolved in ethanol for PR over expression. Cells were harvested after 4 hours of incubation at 37 °C. The harvested cells were broken open using a cell disruptor, and the membrane fraction was obtained after ultracentrifugation. The membranes were solubilized in 1.5% DDM. Detergent solubilised histidine tagged protein was purified using a Ni-NTA (nitrilo-triacetic acid) column and eluted in 0.2% Triton X. The concentration of protein was estimated using UV-Vis spectroscopy, and adjusted to 1 mg/ml. Appropriate lipids (DOPC, 1,2-Dioleoyl-sn-Glycero-3-phosphocholine) were added just prior to setting up the 2D crystalline preparation by means of dialysis for 1 week with regular buffer changes. The crystalline sample was finally pelleted and transferred to a 4 mm MAS rotor. For the measurements, the rotor contained 15 mg of the sample. The sample prepared using the aforementioned protocol was kindly provided by Dr. Sarika Shastri. formyl-[U-13C,15N]-Met-Leu-Phe-OH (MLF) was purchased from euriso-top GmbH, Saarbrcken, Germany, and used without further purification. 3 mg of the peptide were transferred to a 4 mm MAS rotor for measurement.

5.3 Results and Discussion

In the following, the efficacy of DQ filtering a DARR spectrum is shown. Furthermore, the effect of DQ filtering on the cross peak intensities and buildup rates are discussed,

by comparing experimental buildup curves of DARR, DOPE and DOAM experiments, and demonstrating assignment walks obtained with DOAM experiments. DQ-filtering: Spectrum simplification by removal of natural abundance background signals. DARR, DOPE and DOAM spectra were acquired with the membrane protein PR, containing three uniformly ^{13}C labeled cysteines (Fig. 5.2 b, inset). In Fig. 5.2, DARR and DOPE spectra are depicted side by side (DOAM not pictured). To facilitate the comparison, contour levels are adjusted to cover, from top to bottom, the cross peak found at 67.7, 24.4 ppm (see inset of 1D slice, at top) for both contour plots. In the DARR spectrum, NA ^{13}C nuclei occurring in the membrane protein and in its membrane reconstitution environment are the source of diagonal peak intensities which are more than a magnitude larger than that of the cross peak at 62.7 and 24.4 ppm (see Fig.5.2). It is worth mentioning that, for other membrane proteins (GPCRs), this factor is in general much larger (100-1000:1), causing diagonal peak intensities several magnitudes larger. For the purpose of demonstrating the efficacy of the DQ filtering schemes presented here, the results are clear: the DOPE spectrum features peaks stemming only from the ^{13}C labeled cysteines, the diagonal peak intensities are completely missing. It is worth noting that, due to the addition of the DQ filter, the sensitivity of a DOPE or DOAM experiment is reduced in comparison to a DARR spectrum. The DQ filtered experiments yield 40% of the DARR signal strength, and result in a lower signal to noise ratio, as observable on comparing the 1D spectrum slices at the tops of Fig. 5.2 a and b.

5.3.1 Intensities

In ssNMR spectroscopy, a large number of spatial constraints between sites in a protein can be obtained by the acquisition of a single DARR spectrum. In such homonuclear correlation experiments, the cross peak intensities of nuclear pairs are measured at certain mixing times, and subsequently used to estimate distances between nuclear sites. With the introduction of a DQ filter into the DARR experiment, it is necessary to ensure that cross peak intensities can still be used to obtain internuclear distance constraints as shown for PDSD or DARR experiments without DQ filtering. Intensity modulation from DQ buildup curves have been used for precise internuclear distance measurements [36]. In DOPE or DOAM experiments, such intensity changes, manifesting themselves through modulations of cross peak intensities over the course of several mixing periods, would undermine the proportionality between cross peak intensity and internuclear distance. To ensure that DQ filtering of DARR experiments does not affect the relative intensities between cross peaks, DARR, DOPE and DOAM spectra were acquired for a range of different mixing times. Measurements were carried out on the chemotactic tripeptide MLF, a sample which has been thoroughly studied with ssNMR [101, 102], and which lends itself well as a standard, due to well resolved ^{13}C spectra. As depicted in Fig. 5.3, the typical exponential decay of the diagonal peaks, and magnetization buildup and decay of the cross peaks, is readily discernible for DARR, DOPE and DOAM experiments acquired over a range of mixing times. For the sake of clarity, in Fig. 5.3 a, only the buildups of the diagonal peaks and cross peaks which are due to backbone carbons C, Cα and Cβ of the center amino acid leucine are shown. A simultaneous plot of the curves shows that the relative intensities for the case of the DARR and DOPE experiments, with respect to each other, remain comparable. For the relative DOAM intensities, however, this is only the case for nuclei which are not directly bonded. Cross peaks belonging to the neighboring nuclear pairs of C-Cα and Cα-Cβ exhibit their highest signal intensity at the beginning of the buildup curves, due to a magnetization transfer facilitated by the dipolar recoupling of the bonded pairs by the DQ excitation which is achieved during $SR22_4^9$ dipolar excitation.

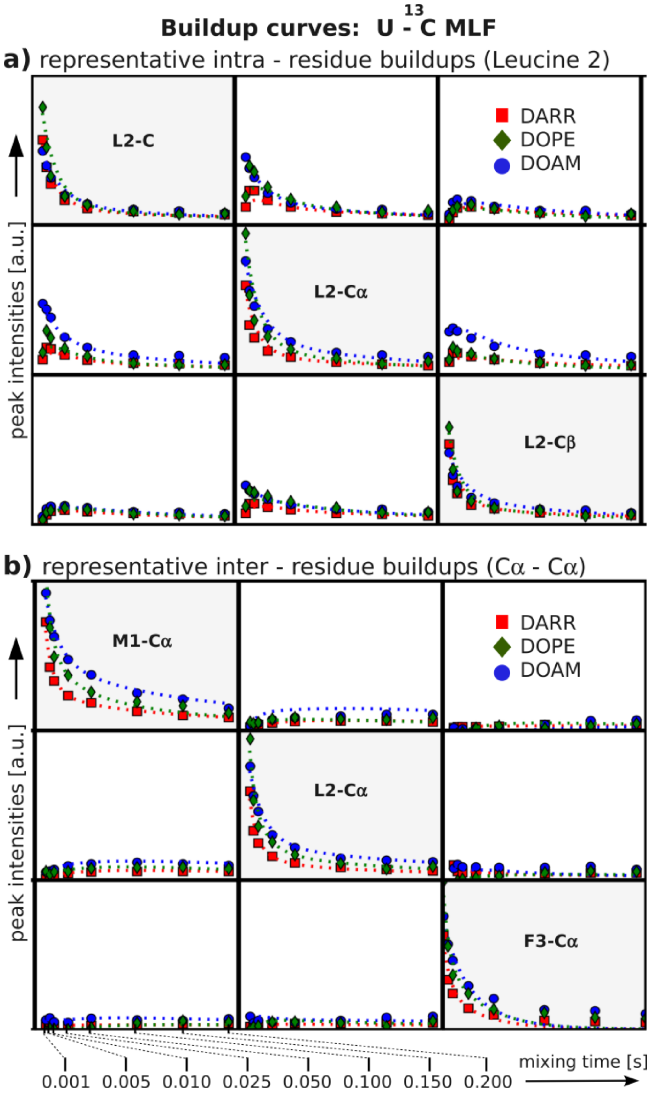

Figure 5.3: A comparison of diagonal and cross peak intensities (a) and buildup rates (b, normalized) within Leu-2 in MLF for DARR, DOPE and DOAM experiments. Dotted lines are the result of curves calculated with magnetization rates that were obtained by fitting with the full matrix approach, and are intended to guide the eye. The intensity curves (above) are plotted over mixing times. In the initial buildup regime, the growth rates of the curves are identical. Buildup rates were unaffected by the addition of DQ filtering pulse elements to the DARR sequence. Spectra were acquired with uniformly ^{13}C labeled MLF. The data for one amino acid, L2, are depicted. The buildup rates for M1 and F3 show the same trend (not shown).

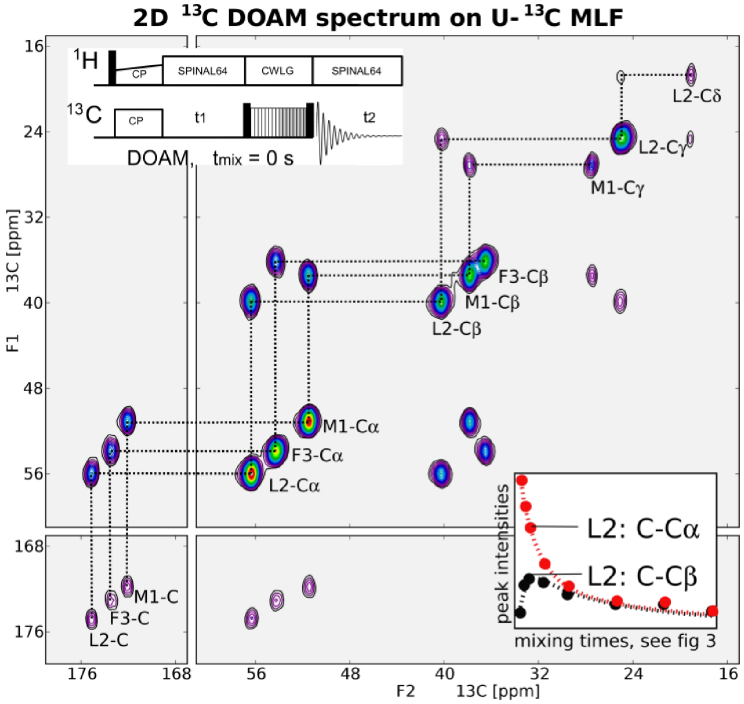

Figure 5.4: DOAM spectrum of uniformly ^{13}C labeled MLF, with a mixing time of 0.001 s. Assignment walks are indicated by horizontal and vertical dotted lines. Cross peaks are visible only for directly neighboring (bonded) nuclei. This is not an effect of choosing appropriate contour levels. At this negligible mixing time, cross peaks are due only to dipolar coupling between adjacent nuclei. Cross peak intensities for non bonded nuclei exhibit negligible intensities for short mixing times (see picture inset).

5.3.2 Buildup rates

Spatial constraints for protein structure calculations can be derived from cross peak buildup curves, as described above for cross peak intensities. It is necessary to ensure that cross peak buildup rates are also not affected by the excitation of DQ coherences during the acquisition of DARR spectra. In Fig. 5.3 b, buildup curves are normalized and displayed in the same subplots. A comparison of the slopes with which the intensities grow before reaching an intensity plateau shows matching buildup curves for the DARR and DOPE experiments. DOAM experimental buildup curves, however, need to be divided into two classes: The profile of DOAM buildup curves for nuclear pairs which are non bonded exhibits rates which are comparable to those of DARR and DOPE experiments (see Fig. 5.3 b). Buildup curves of neighboring nuclei, directly bonded, exhibit a maximum at the beginning of the mixing time, and decay in an exponential manner. Buildup plots for the DARR, DOPE and DOAM experiments for the complete MLF peptide are shown at the end of the chapter (Figs. 5.5, 5.6 and 5.7)

5.3.3 DOAM: assignment walks

As described above, DOAM cross peak intensities for neighboring nuclei have their maxima at the beginning of the intensity buildup curves. As a consequence, the acquisition of 2D DOAM spectra at tmix = 0 s (see inset schematic of the pulse sequence at the top of Fig. 5.4) leads to homonuclear correlation spectra which exhibit cross peaks only from coupled nuclei. As indicated in Fig. 5.4, this leads to the possibility of performing assignment walks, which can simplify the identification and assignment of peaks substantially.

5.4 Summary and Conclusion

The experiments introduced in this chapter fulfill the need for DQ filtered homonuclear correlation spectra in the ssNMR biomembrane toolbox. Of very high interest currently are the interactions between molecules in native lipid membrane systems. Unfortunately, this highly relevant class of samples intrinsically involves a high ^{13}C natural abundance background, due to the lipid bilayer and the size of the membrane proteins, and currently limits the application of ssNMR experiments severely. A typical example is a recent ssNMR study which delivers compelling experimental evidence that the protonation state of a GPCR-bound agonist (Histamine) is able to influence receptor activation [103]. In this important study, the identification of histidine resonances within a PDSD spectrum was obtained by conducting one additional DQ filtered experiment. The pulse sequences introduced here obviate the need for such additional experiments, and deliver the sample information within one experiment. The DOPE and DOAM experiments introduced here allow the identification, assignment and the gathering of spatial information, without being impeded by a large amount of ^{13}C nuclei due to NA. DOPE experiments yield relative cross peak intensities and buildup rates which are unaffected by DQ filtering, as indicated by a comparison to DARR spectra under identical conditions. It is predictable that, of the two possibilities, DOPE will be the more routine experiment when it comes to gathering information concerning structural constraints. DOAM experiments yield buildup curves which may be split into two classes, depending on whether they are from peaks from bound or non bound nuclei. Cross peak intensities originating from bound nuclei are characterized by a maximum intensity for a mixing time of tmix = 0 s, and may mostly be useful in the identification and assignment of amino acid backbone cross peaks, on assignment walks based on the knowledge of the backbone structure.

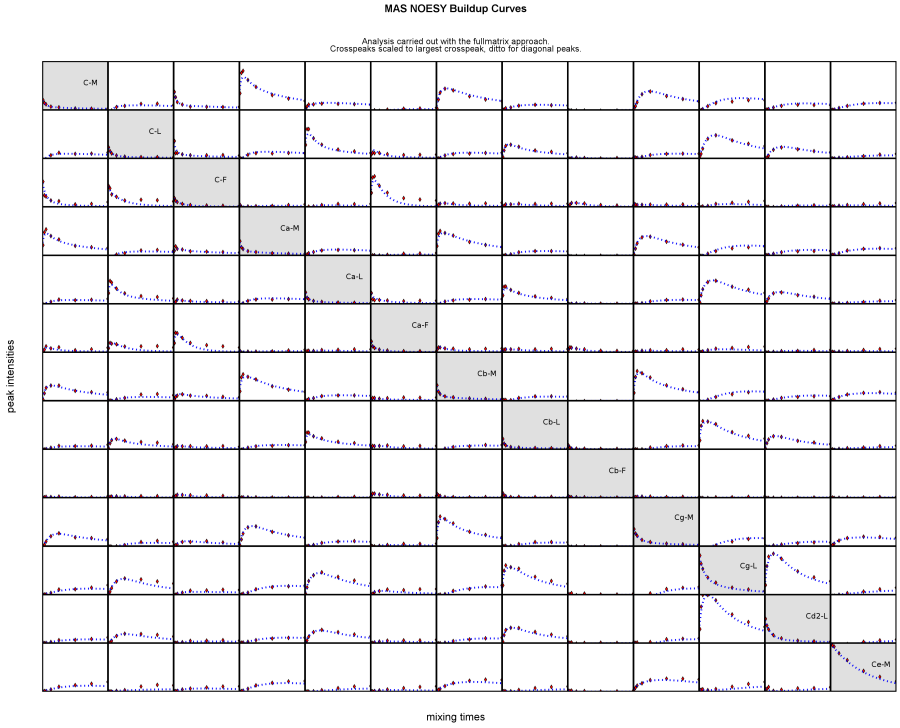

Figure 5.5: Buildup curves for MLF, for a conventional DARR experiment. Cross peak intensities have been normalized with respect to their corresponding diagonal peaks.

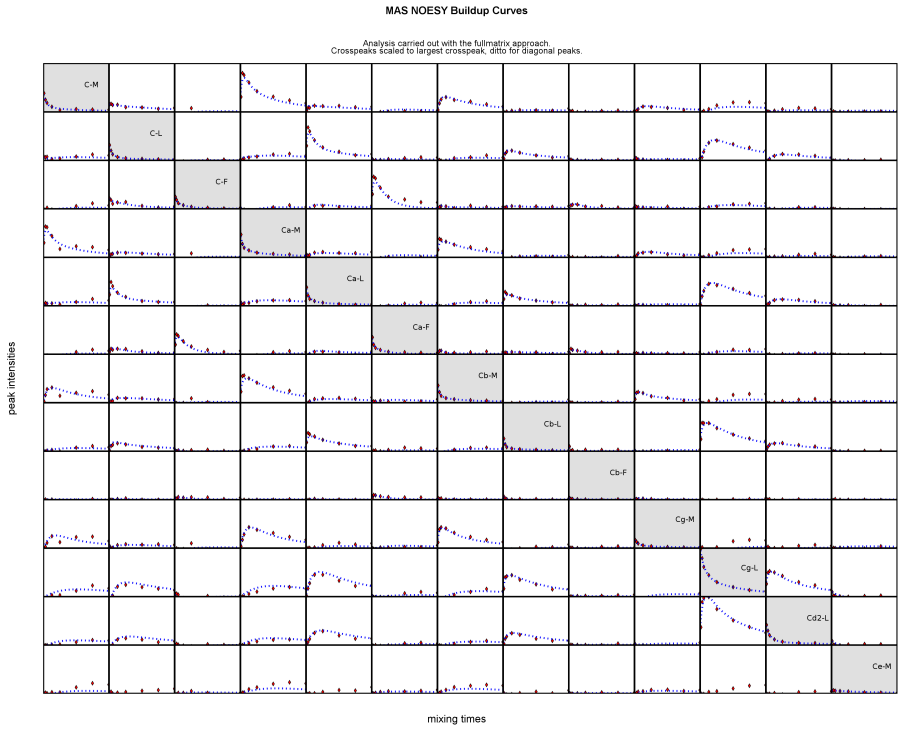

Figure 5.6: Buildup curves for MLF, for a DOPE experiment. Cross peak intensities have been normalized with respect to their corresponding diagonal peaks.

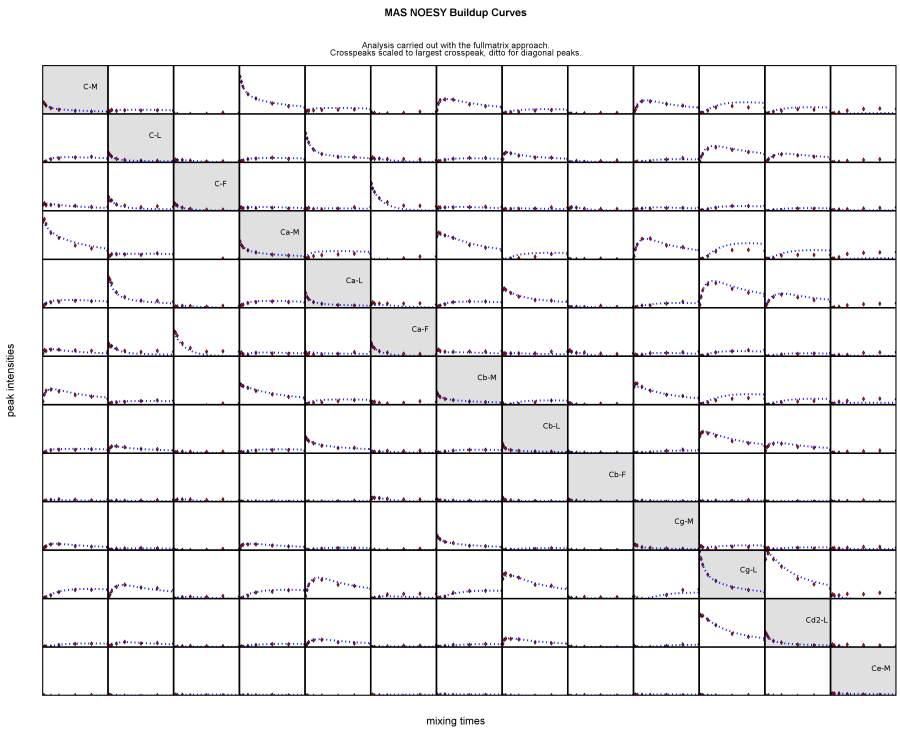

Figure 5.7: Buildup curves for MLF, for a DOAM experiment. Cross peak intensities have been normalized with respect to their corresponding diagonal peaks.

Chapter 6

Minimizing Relaxation Losses during Acquisition: HEAT

6.1 Introduction

One obvious feature of solid state NMR spectra, in comparison to solution state NMR, are the often strongly broadened lineshapes of the spectral resonances. This broadening stems from transverse relaxation, caused by slightly different magnetic fields experienced by the spins, which are in coherence at the start of the experiment. This leads to slightly different precession frequencies of these resonances and ultimately to a loss of the overall coherece of the spins in the ensemble. This means that the net transverse magnetization starts to decay, as the dispersion in the x-y plane of the rotating frame caused by the different precession frequencies of the individual resonances increases leading to a cancellation of the individual components of the net magnetization vector.

In solid state NMR, this effect is especially pronounced, due to the presence of anisotropic interactions, like the chemical shift anisotropy or the homo- and heteronuclear dipolar coupling. These effects lead to significant differences in the magnetic field experienced by the spins in the ensemble, depending on their physical position in the sample, with respect to each other and the outside magnetic field.

Not only does this effect lead to broad spectral resonances, as the exact frequency of the resonances can only be approximated to a certain degree using the Fourier transform of such a shortened free induction decay, but the sensitivity of the measurement is perturbed as well, due to the strong loss of coherence of the individual components of the signal.

Fortunately, not all of this coherence loss is unrecoverable: if the differences in magnetic field, that lead to transverse relaxation are constant over time, or follow a certain periodicity, the loss of coherence can be undone, using a adequately timed 180 $^{/}circ$ pulse and a rephasing time in which coherence is restored. If the local magnetic field at the position of the individual spins change unpredictably, on the other hand, no such recovery is possible.

In almost all cases, these two types of magnetic field change will be active at the same time, but can be disentangled using the Carr-Purcell-Meiboom-Gill (CPMG) experiment [26].

The apparent transverse relaxation, consisting of the recoverable and unrecoverable

parts, is called T_2^*, whereas the unrecoverable part alone is termed T_2.

The HEAT (Half Echo Alternating Transformation) method introduced in this chapter offers the possibility for a signal enhancement on samples, where T_2^* is lower than T_2, during the detection phase of the experiment. This condition is often fulfilled in the solid state for nuclei which are not in the proximity of a fast relaxing moiety, such as the methyl group. For instance ^{15}N nuclei in proteins often fall into this category, as do the carbonyl ^{13}C atoms.

For these nuclei, the difference of T_2 and T_2^* can be exploited by recording a series of spin echos. Here, the intensity of the refocused magnetization depends only on T_2, allowing for a longer acquisition of the FID and henceforth larger S/N ratio. A problem with this straightforward approach is the generation of sidebands by the spin echos, spaced by $1/\tau_{Echo}$ Hz, upon Fourier transformation of the resultant FID. If the spectral lines are broad, this usually doesn't pose a problem and therefore spin echos have been employed before, for spectra of quadrupolar nuclei [104]. In the case of crowded spectra with many narrow but partially overlapping resonances, as for instance found with many biomolecules, these sidebands can complicate the interpretation of the spectra significantly.

Here, a method is presented to obtain the S/N enhancement gained by recording spin echos, without the generation of echo sidebands in the spectrum. The approach for this is straightforward: after the FID containing the spin echos is recorded, but before Fourier transformation, the signals of the individual echos are digitally split. Furthermore every half echo associated with the refocusing of the spins from a dephased state, is time inverted to obtain the correct phase. The necessary information for this post processing step can easily be obtained from the parameters of the pulse sequence, which consists of the duration of one echo, the dead time before and after the 180° pulse and the dwell time.

After every half echo, associated with the refocusing of the magnetization, is time inverted by swapping the position of the data points using a first in / last out operation, the half echos are added, yielding an FID which falls off according to T_2^*. Thus, after Fourier transformation, the spectral shape is retained and no echo sidebands are present in the spectrum. Still the S/N ratio is enhanced and the gain is similar to the one obtained by a straight Fourier transformation of the spin echos. This procedure greatly simplifies the interpretation of the spectra.

The actual gain in S/N ratio, which can be obtained by using the method, strongly depends on the relative magnitudes of T_2 and T_2^*. This can be easily assessed during the experiment, by observation of the intensity of the spin echos. As the signal of typical biomolecules in the solid state at low temperature is usually fully dephased after 10 to 15 msec, but the save maximum acquisition time under ^1H decoupling is about 50 msec, multiple echos can be safely acquired, without any damage to the sample or the setup. This is a major strength of this method, as it is compatible with almost every experiment, given the sample fulfills the criterion outlined above.

An alternative approach, which was not investigated in this work, is to store the magnetization on the z-axis, after the dephasing and rephasing echos have been acquired. Then the ^1H decoupling is switched off for a time approximately equal to the echo time. Following this period the decoupling is switched back on and the magnetization is returned to the x-y plane, to record another echo. This should not influence the properties of the spectrum, given there is no strong spin diffusion happening during the interval between the echos, i.e. for ^{15}N nuclei in proteins. The advantage of this approach is that it greatly reduces the duty cycle of the probe. This could prove to be useful, if the RF power irradiation, and not the T_2 time of the sample sets the limit to the applicability of HEAT.

The experiments presented in this section were conducted in corporation with Nicole Pfleger.

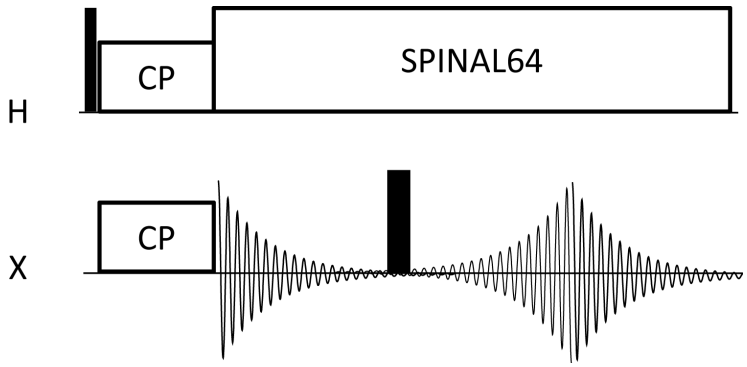

Figure 6.1: Schematic diagram of the pulse sequence of the one dimensional HEAT-CP experiment. First the ^1H magnetization is transferred to a heteronucleus, using a conventional CP step. Then the FID is acquired under ^1H decoupling. After the FID is fully dephased according to T_2^* after a time τ, the receiver is blanked and a 180° pulse is applied on the heteronuclear channel. After probe ringdown, the receiver is unblanked again, and the echo is recorded. The echo intensity is proportional to $e^{2*\tau/T_2}$. This procedure is repeated, until no recoverable magnetization is left, or the save limit of continuous ^1H decoupling is reached.

6.2 Experimental

The pulse sequence for the HEAT adaption of the one dimensional CP experiment is shown in Fig. 6.1. Here, the magnetization is transferred from ^1H to a hetero-nucleus, as usual for the CP experiment. After acquisition has started, and the FID has fully decayed by dephasing caused by T_2^*, the receiver is blanked and a 180° hard pulse is applied. After coil ringdown, the receiver is unblanked again, and the acquisition is continued. The blanking of the receiver during the pulse is necessary to exclude pulse spikes from the FID. Although these could be removed digitally during post processing, it is more elegant to exclude these artifacts in the sequence, making the use of conventional Fourier transform possible if desired, without the need for post processing.

After the re- and subsequent dephasing of the signal, another 180° pulse can be applied. This procedure is repeated, until the signal has fully decayed due to T_2 or the save decoupling time limit is reached.

After the FID is recorded and the full number of scans for the experiment are co added, the FID can be subjected to post processing. In this step every half echo (rephasing and dephasing) is stored separately, as an individual FID. The rephasing echos have to be time inverted, to yield the shape of a conventional FID. This is done by simply inverting the order of the acquired data points. After that, all component FID's are added, to yield a FID which decays with T_2^* but features an increased S/N ratio, due to the summation of the component FID's of the spin echo sequence.

The exact gain which can be achieved using this method greatly depends on the relative magnitudes of T_2 and T_2^*, and therefore on the sample and nucleus observed.

In the solid state, for nuclei that are in proximity to a fast relaxing moiety such as a methyl group, the difference of T_2 and T_2^* is rather small and no significant gains can be obtained. For nuclei that are removed from said groups, such as most ^{15}N backbone resonances in proteins, the gains can be quite large, as is shown in the following.

In Fig. 6.2, a ^{15}N FID of the tripeptide MLF is shown, with one 180° hard pulse used for refocusing. It can be seen that the FID, upon refocusing, shows a reduced intensity as compared to the initial magnetization. It can therefore be concluded that

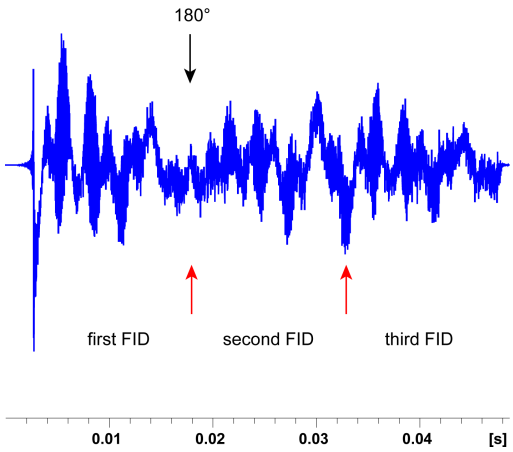

Figure 6.2: Experimental ^{15}N FID of MLF recorded with the sequence shown in Fig. 6.1. The individual phases of the experimental FID, that result from the initial polarization (which will become the first component FID after post processing), the rephasing after the hard 180° pulse (second FID) and the subsequent dephasing (third FID) are indicated below the time trace. The position of the 180° pulse is marked by a black arrow. It can be seen from the relative intensities of the initial magnetization and the spin echo, that, although the echo is reduced due to T_2, a large part of the magnetization could be recovered. Only one echo was recorded, to keep the acquisition time below 50 msec. The FID was recorded at 40MHz ^{15}N resonance frequency and room temperature.

this sample has a pronounced difference in T_2 and T_2^*, although the effect of T_2, which manifests itself as the part of the initial magnetization which cannot be successfully refocused, is still significant in the time period observed (50 msec). This behavior is expected for ^{15}N backbone nuclei in solid peptides, as the averaged distance of these nuclei to groups, that significantly contribute to the spectral density at one or two times the nuclear Lamor frequency, is too large on average to effect fast T_2 relaxation.

The Fourier transform of this experimental FID without any post processing is shown in Fig. 6.3. The expected spectral shape of three nuclei is recognizable, but severely distorted by the appearance of sidebands. These stem from the Fourier transform of the spin echo and complicate the spectrum considerably.

To alleviate this problem, the experimental FID has to be split into its individual components via post processing. First, the three components of the echo are separated, resulting in an first FID, which corresponds to the normal signal without the application of HEAT, a second FID, from the refocusing spin echo and a third component, which stems from the magnetization dephasing again after the echo maximum. Only the second component needs to be further manipulated before the three components can be summed. As the second component corresponds to a rephasing and chemical shift refocusing of the spins, it needs to be time inverted to be comparable to the other components of the experimental FID. This is easily achieved by reversing the order of the data points, as shown in Fig. 6.4. Here the spectra of the three individual components are overlayed. It can be seen that, apart from small phase distortions, the spectra overlay nicely and each spectrum has the three peak shape with a line width given by the T_2^* time, as would be expected from an conventional ^{15}N CP experiment on MLF. The phase distortions result from a small mismatch of the data points with the spin refocusing, caused by the dwell time. After post processing, all components can be added the same way individual scans would be, and the resultant FID subjected

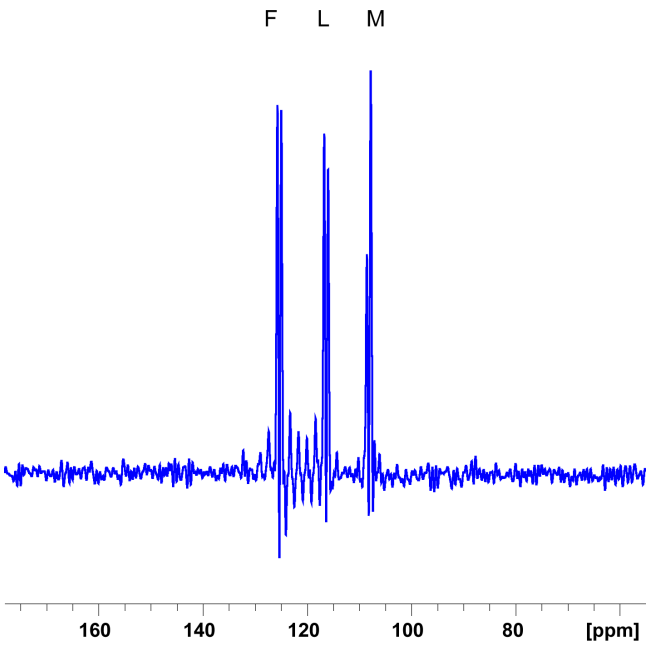

Figure 6.3: Fourier transform of the complete FID shown in Fig. 6.2. The conventional three peak ^{15}N spectrum of MLF is split into sidebands. These sidebands result from the spin echo sequence employed, and would severely complicate spectral interpretation, if a greater number of peaks were present in the spectrum.

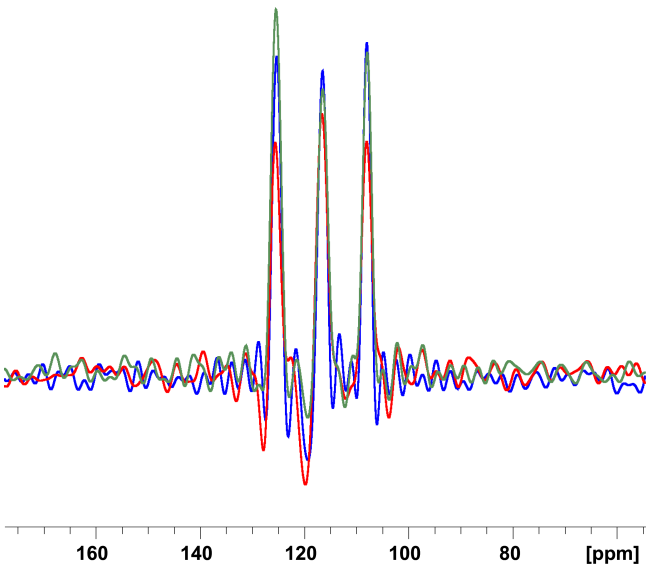

Figure 6.4: Fourier transform of the three component FID's indicated in Fig. 6.2 in the order blue (1st), red (2nd), green (3rd), after post processing. In contrast to Fig. 6.3, it is immediately obvious that the usual appearance of the spectrum is retained for each of the three component spectra. Although the S/N is reduced for the FID's stemming from the spin echo, the signal is still well above the noise.

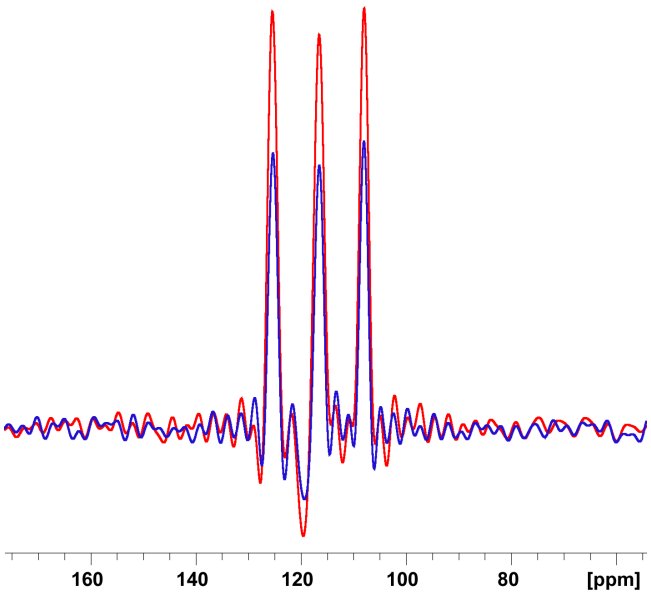

Figure 6.5: Overlay of the sum of the three component spectra, generated by the use of a spin echo shown in Fig. 6.4, and the spectrum of the first FID alone, as indicated in Fig. 6.2, which would be normally acquired in a conventional experiment. It is obvious, that HEAT leads to an significant increase in the S/N ratio of the spectrum, without the detrimental effect of sidebands on the spectral appearance. The gain in S/N is approx. 55%. The spectra have been scaled to the same noise level.

to Fourier transformation.

A comparison of the spectrum resulting from a conventional CP experiment (which is equal to the first component of the HEAT FID), and the sum of the three components recorded in the HEAT experiment shown, is depicted in Fig. 6.5. The enhancement of the signal to noise is obvious, as both spectra have been scaled to the same level of noise. The gain in S/N ratio of approx. 55% is less than the one that would be obtained by co adding three conventional scans, which would result in an S/N increase of 73%. The difference is caused by the influence of the T_2 relaxation during acquisition. This results in a part of the original magnetization not being recoverable by a spin echo and therefore lost for the purpose of the signal enhancement. This part gets larger, the longer the FID is recorded, thereby limiting the maximum gain, which can be theoretically achieved by using HEAT.

Still the S/N enhancement corresponds to a 2.4 fold reduction in measuring time.

The strength of HEAT is that it is not sensitive to the exact type of experiment it is applied to. As long as the T_2^* to T_2 ratio is greater than one for the observed nuclei, a gain can be achieved.

Again, the exact magnitude of this gain depends on the nuclei, their environment and the state of the sample.

Although the enhancements possible and the independence from the exact type of experiment used are advantageous features of HEAT, there are also some drawbacks depending on the sample under investigation.

First, the enhancement is directly proportional to the number of spin echos, which can be acquired. This also means, that for longer FID's a compromise between the achievable enhancement and the sample heating due to the longer decoupling during acquisition has to be struck. This effect gets more pronounced, the longer the FID's

lasts before decaying. In addition this means that often the difference between T_2^* and T_2 gets less favorable for the HEAT experiment. In principle this problem can be circumvented by cutting the FID short, but this leads to a loss of resolution and undesirable truncation artifacts.

In addition to these points, great care has to be exercised in the design of the experiment with regard to the placement of the 180° pulses. If the timing of the pulses is not correct, it is possible that periodic changes, such as MAS, cannot be fully compensated by the pulse train. Furthermore, the dwell time of the experiment and therefore the exact acquisition points of the FID have to be considered for the pulse placements, lest severe phase errors result upon processing of the resultant component FIDs.

In summary, HEAT is best suited for samples with inherently low resolution and strong T_2^* relaxation, which is often the case for solid powder or frozen samples, which do not feature a high degree of internal dynamics. For these samples significant gains in the measuring time (up to a factor of approx. 2) can be gained, for a wide variety of solid state NMR pulse sequences (all sequences, which need no irradiation of the detection channel during acquisition).

With increasing dynamics of the sample, the enhancement factors decrease, due to the smaller difference between T_2^* and T_2. Additionally the number of echos, which can be safely acquired, is less because the longer FIDs lead to a longer total acquisition time, thus the number of echos has to be reduced to stay within the maximum save limit.

Chapter 7

Processing Multidimensional Spectra Twice: DTD

7.1 Introduction

Although solid state NMR has developed rapidly in recent years, one of the chief limiting factors of ssNMR are its inherently low sensitivity. This is due to low γ of the nuclei which are detected e.g. ^{13}C or ^{15}N and line broadening caused by anisotropic interactions, such as homo-nuclear and heteronuclear dipolar couplings and chemical shift anisotropies. The resulting small signal-to-noise (S/N) ratio leads to measuring times which become inconveniently long for multidimensional experiments. Furthermore, biological samples (e.g. membrane proteins) tend to have an upper limit in the concentration at which they can be prepared, limiting the amount of sample which may be contained in the MAS rotor. Line broadening also causes a lack in spectral resolution, which can normally be mitigated by recording spectra of higher dimensionality. The drawback is again an increase in measuring time. Conclusively, a post experimental processing scheme which not only enhances the S/N, but reduces the necessary number of increments in the indirect dimensions of NMR experiments would be highly desirable, and might well play a key role in making multidimensional experiments which are routine in solution state NMR feasible in its solid state counterpart. Approaches that lead to a reduction in experimental time have been investigated before in the field of fast multidimensional solution state NMR. Several strategies to decrease the experimental time needed to obtain a well resolved multidimensional spectrum have been proposed, including single scan 2D NMR [105, 106], Hadamard spectroscopy [107–109], reduced dimensionality NMR [110–112], non-uniform sampling methods [113–117] and covariance processing [27, 28, 48]. Covariance has been used before, e.g. in the deconvolution of spectra of mixtures [49, 50] or the formation of symmetric spectra from heteronuclear experiments [51–53]. The general applicability of covariance makes it interesting for ssNMR, although in many cases the gain in experimental time is not sufficient to make higher dimensional ssNMR experiments feasible. Here, a hybrid approach is suggested which uses the properties of Fourier and covariance transformations as indicated in Fig. 7.1. Two copies of a given homo-nuclear data set are separately transformed from the time to the frequency domain, using conventional Fast Fourier transform (FFT) in one case and covariance transform in the other. The two resulting data sets are multiplied, and result in a spectrum which, compared to

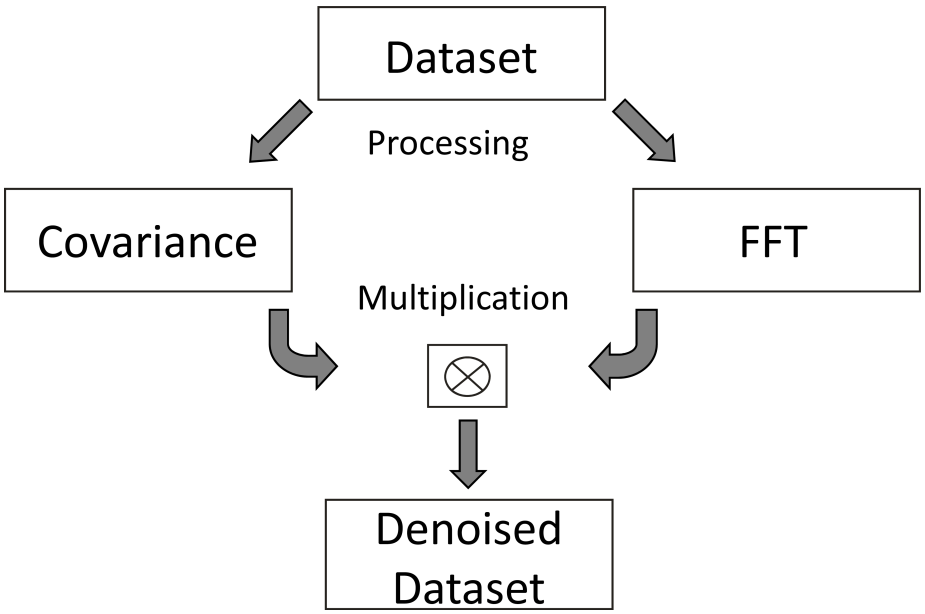

Figure 7.1: Schematic diagram of dual transformation denoising: a homo-nuclear data set is processed separately using covariance and Fourier transformations. The two resultant data sets are then multiplied to yield the final data set featuring an enhanced signal to noise ratio and reduced truncation artifacts.

conventional processing by FFT only, shows overall enhanced sensitivity and a reduction of truncation artifacts in the indirect dimension. This noise reduction is possible by utilizing the fact that noise from FFT spectra and from covariance spectra is not correlated as shown below. For the rest of this thesis, the term Dual Transformation Denoising (DTD) will be used to refer to this processing method.

The multiplication of spectra processed separately by FFT and with covariance has been used before in another context: covariance can produce false correlations, which can be mistaken as crosspeaks. These artifacts are suppressed by multiplication of the covariance spectrum with the Fourier transform spectrum.

The truncation artifacts in the FFT tend to be strongest in the vicinity of the diagonal, whereas the artifacts caused by covariance processing mostly appear well removed from the diagonal. As a result false peaks from both sources in the multiplied spectrum are eliminated (W. Bermel unpublished results). Another method for artifact suppression was demonstrated recently, consisting of the application of a step-function mask derived from the correlation matrix [118]. This suppression of artifacts is an additional advantage gained by choosing multiplication of the FFT and covariance spectra in DTD processing. In this chapter, the performance of DTD is assessed with the help of a calculated dataset, designed to show the effects of signal processing on resolution and sensitivity. This is done for a fully synthetic dataset, created with Scipy [119] and an simulated set, which was calculated with the SIMPSON simulation environment [78]. Then, the combination of denoising, with the possibility of t1 truncation (i.e. reduction of the number of increments in the indirect dimension), is explored using synthetic data sets. The results of the theoretical assessment are then compared to experimental homo-nuclear correlation spectra on the nonapeptide Bradykinin, a neuropeptide activating the B-1 and B-2 receptors [120].

The results shown in this chapter have been published in [57].

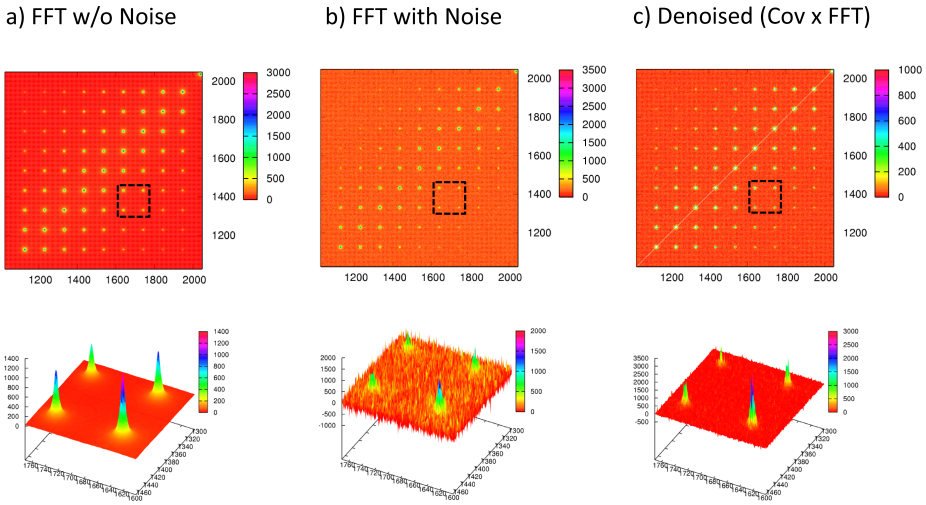

Figure 7.2: To demonstrate the effect of denoising, a two-dimensional FID was calculated. The Fourier transformed data set without added noise shown in (a) features a symmetric crosspeak pattern where the nth peak off the diagonal has an intensity scaled by $\sqrt{2}^n$. Adding Gaussian noise results in the spectrum shown in (b). The differences in S/N between adjacent crosspeaks now correspond to halving the number of scans. This allows a detailed inspection of the effect of dual transformation denoising (c). DTD processing yields an S/N improvement compared to Fourier transformation alone.

7.2 Theory

In the following, a description of the covariance transformation, Fourier transformation and their effect on a set of data is given. Covariance transformation is based on the analysis of correlated changes between signals in a dataset. For the application in NMR, a multidimensional spectrum is Fourier transformed for frequency/frequency covariance, or in all but one dimension for time/frequency covariance. In the former case, the resultant data set can then be examined for common variations (i.e. frequencies) along any dimension, whereas in the latter case the time domain is used for covariance analysis.

The underlying principle is explained most easily using a 2-dimensional data set in which only the direct dimension t_2 (the dimension normally featuring the highest digital resolution) is Fourier transformed, yielding a mixed time/frequency data set S(t1,ω_2):

$$S(t_1, \omega_2) = Re \int_0^{t_{2,max}} dt_2 exp(-i\omega_2 t_2) s(t_1, t_2) \tag{7.1}$$

Using discrete Fourier transform, Eqn.7.1 becomes:

$$S(k, M) = Re \sum_m exp(-iMm) s(k, m) \tag{7.2}$$

here, the data points recorded in the indirect and direct dimensions, t_1 and t_2, are given by the indices k and m respectively, which are denoted K and M upon transformation into the frequency domain. The frequency ω corresponding to each point M is given by:

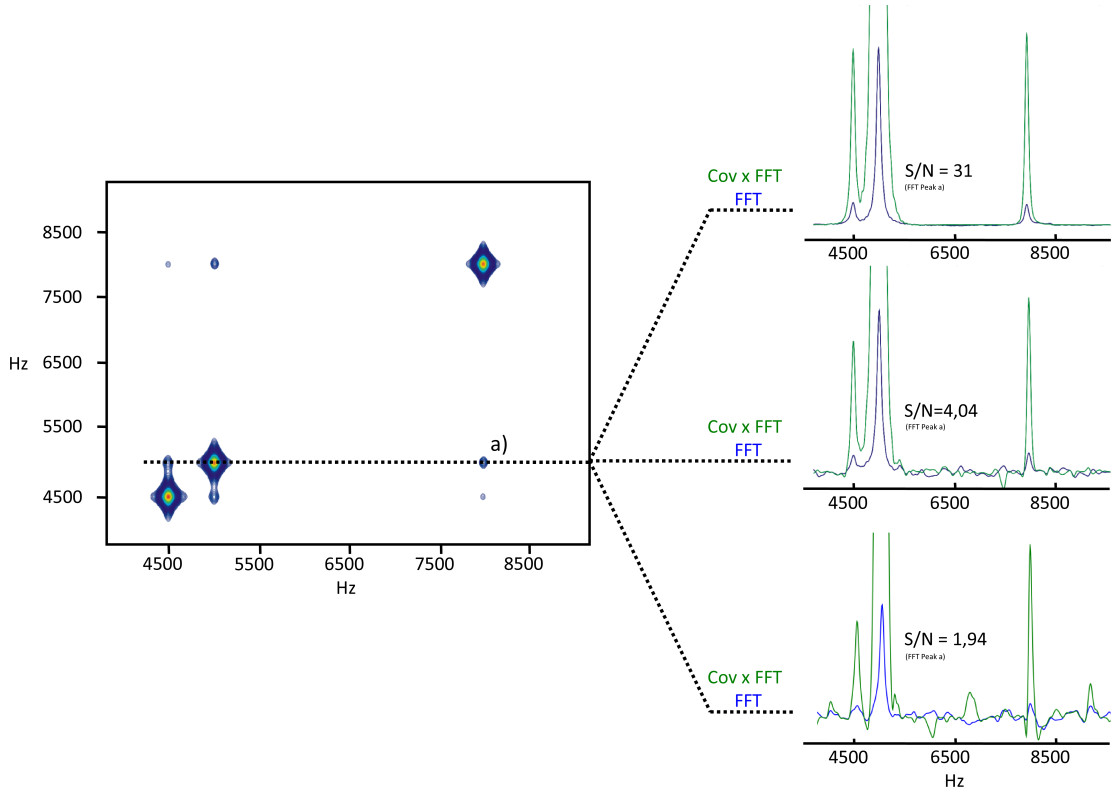

Figure 7.3: 2D RFDR fourier transform spectrum simulated for a 3-spin system (4500Hz, 5000Hz, 8000Hz) using SIMPSON. Varying degrees of synthetic noise were added to the FID of this spectrum before processing, to simulate a real spectrum with different S/N ratios (the intensity of the spectrum is fixed, for example peak a) has a intensity of 186 in all spectra). Slices are shown for three signal to noise levels representing weak, intermediate and strong noise contribution to the spectrum (corresponding to a 2 x Std. Dev. Noise of 6, 46 and 96). Superpositions are shown for FFT processed data (blue) and covariance multiplied with FFT data (green). The signal to noise ratio is given for the Fourier transform of the crosspeak a) as an inset for each slice.

$$\omega(M) = 2\pi\{(-\frac{SW}{2}) + (\frac{SW}{M_{max}} * M)\} \tag{7.3}$$

where M_{max} is the total number of digital points after Fourier transformation and SW is the sweep width. The covariance matrix element with indices (M, N) is now computed according to:

$$C_{MN} = \frac{1}{k_{max} - 1} \sum_k (S(k, M) - \langle S(M)\rangle)(S(k, N) - \langle S(N)\rangle) \tag{7.4}$$

where $\langle S(x)\rangle = k_{max}^{-1} \sum_k S(k, x)$ is a baseline correction factor to exclude false correlations caused by nonzero row sums along the indirect dimension, and k_{max} is the number of increments recorded in the indirect dimension. The definition of C_{MN} implies the generation of a symmetric $M_{max} \times M_{max}$ matrix that features the same resolution in the indirect as in the direct dimension. The covariance matrix thus obtained lists the variances of the resonances in the spectrum, defined as

$$Var(I) = \langle S(M)^2\rangle - \langle S(M)\rangle^2 \tag{7.5}$$

along the diagonal and the covariances, as defined in Eqn.7.4 as off diagonal elements. To correlate this covariance matrix to the Fourier transform spectrum, which would be obtained from conventional two dimensional processing, the following identity has to be taken into account

$$S = 2^{1/2} * C^{1/2} \tag{7.6}$$

Thus, taking the square root of this matrix results in the final symmetric covariance processed spectrum. On the other hand, the two-dimensional discrete Fourier transform generates a pure frequency data set S(K,M) according to:

$$S(K, M) = Re \sum_k \sum_m exp(-iKk)exp(-iMm)s(k, m) \tag{7.7}$$

With the definitions given above, it can be shown that signals from a diagonal symmetric data set should remain unaffected by the choice of transformation, whereas noise (given by a FFT) and the correlation of noise (given by the covariance) are affected differently by the separate transformations, as demonstrated below. This can be used as a means to discern between real signals and noise contribution. To highlight the differences in covariance and FFT and how these can be used to accomplish a reduction in spectral noise, it is useful to consider the two extremes of a diagonal symmetric 2D spectrum without noise, and one consisting only of noise. A real spectrum may be considered as the superposition of these two extreme cases. Consequently, four cases need to be considered: a noiseless spectrum processed with FFT or covariance (cases 1 and 2) and noise processed with FFT or covariance (cases 3 and 4). In the first case, Fourier transformation of a row along the indirect dimension is achieved by multiplying it with a set of complex exponential functions as shown in Eqn. 7.7, scanning over a certain frequency range (the sweep width). All these function are periodic, as can be seen with the Euler formula $exp(ix) = cos(x) + isin(x)$.

In the second case, the covariance transform will compare each spectral row, i.e. the time trace of one point M along all values of k in a mixed time-frequency set, with itself and every other spectral row to generate the covariance matrix as outlined in Eqn. 7.4. As the row index M corresponds to a certain frequency ω(M), as shown in Eqn. 7.3, this can be regarded as an operation similar to that performed in discrete Fourier transform. Hence the time traces used in the covariance transform in principle correspond to the periodic functions used in the FFT. This comparison omits relaxation and additional amplitude modulation that may be present in an experimental time trace, but as the only required property used for further discussion is the periodicity of the trace,

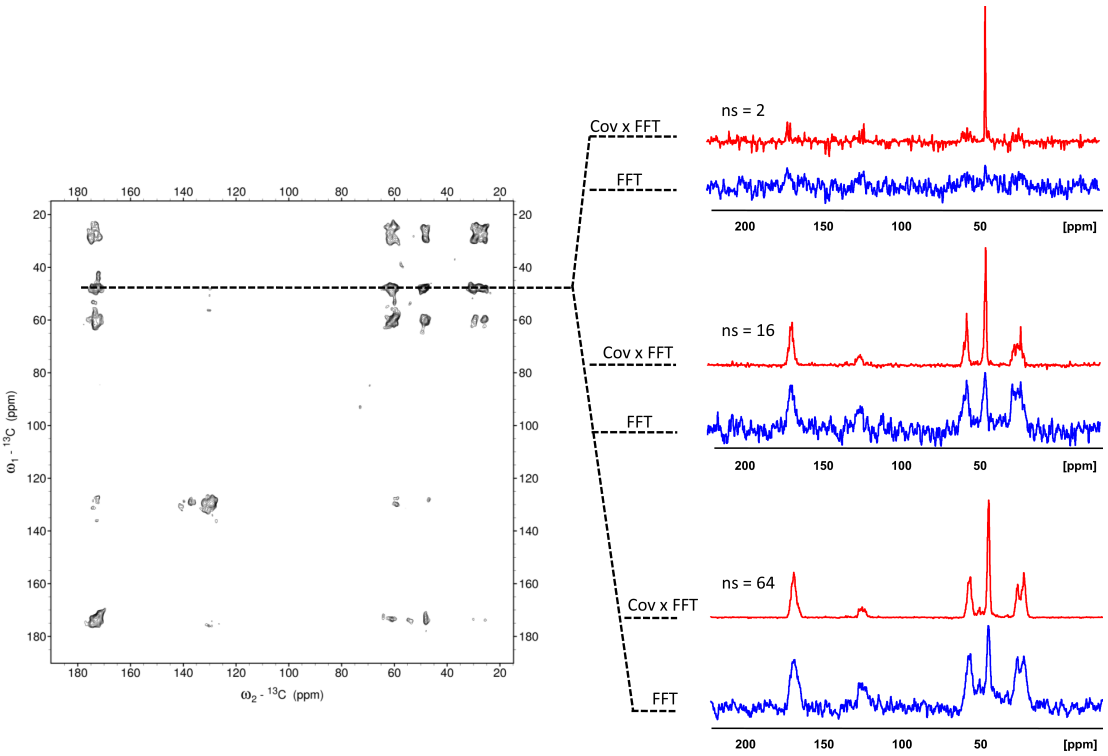

Figure 7.4: (a) A $^{13}C - ^{13}C$ PDSD spectrum of the nonapeptide bradykinin in lyophilized form was recorded using 256 increments with 64 scans and a mixing time of 100 ms (240 K, 8 kHz spin rate). The spectrum was processed using FFT in both dimensions. (b) The same experiment was repeated with 2, 8 and 32 scans and processed using FFT or DTD. Slices at 47 ppm are compared. A significant reduction of experimental noise is already visible after 8 scans using DTD processing and noise is mostly eliminated with 32 scans. The strong diagonal intensity visible in the spectra is a consequence of covariance as a column is always autocorrelated with itself.

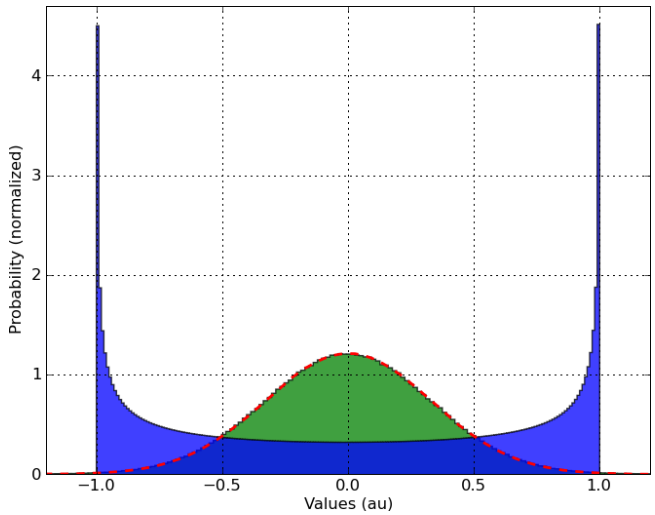

Figure 7.5: Histogram of the distribution of values around zero, for noise which is normal distributed (green) and a sinus wave (blue). To compute these histograms, for the green curve 2000000 samples of gaussian noise with a sigma of 0.33 were evaluated. For the blue curve an equal number of samples were taken from a sin wave in regular intervals for a lenght of 300*pi. The y axis has been normalized to a probability of 1. The distribution on the x axis for the normal distributed noise has been chosen such, that only 0.3 % of the values lie outside the interval from -1 to 1. This plot was generated using Scipy.

this simplification is valid. Therefore, when comparing the two transformations in a spectrum devoid of noise, the position and resolution of peaks will remain unchanged, yielding a symmetric spectrum. For a spectrum containing only noise, the set of exponential multipliers used by the FFT for generating the pure frequency spectrum (see Eqn. 7.7) in case 3, and the experimental time traces covariance uses in case 4 (see Eqn. 7.4) are very different, as the rows in case 4 will invariably be time traces consisting only of noise. These traces show no periodicity whatsoever, as noise is uncorrelated and thus the multiplication factors used to arrive at a pure frequency spectrum in cases 3 and 4 are periodic in one case and stochastic in the other. This dissimilarity leads to a different shape of the transformed noise in the spectra generated with FFT and covariance transform.

This behavior can be further rationalized by the histograms shown in Fig. 7.5. In this figure, the histogram of the probability for values of normal distributed noise (sigma = 0.33, green) is compared to one for a sinus wave (blue). The sigma of the noise was chosen such, that only 0.3 % of the values lie outside of the interval from -1 to 1, to facilitate the comparison. From the comparison of these two histograms, it is obvious that the probability for values around zero is much higher for the normal distributed noise than for the sinus wave, where the disappereance of the first derivative around the extrema leads to an approximately inverse distribution.

From this it follows, that if a given time trace (consisting of noise) is multiplied point per point with a) another time trace of noise and b) with a time trace consisting of a sine wave of arbitrary, nonzero frequency, the results are bound to be different for the majority of points. Now if these results are to be summed (as is the case in the covariance and Fourier transforms), this difference in behavior will most likely lead to different results. Most likely, because the arbitrary nature of noise always allows for constellations, where the results of the two calculations will be identical, although the

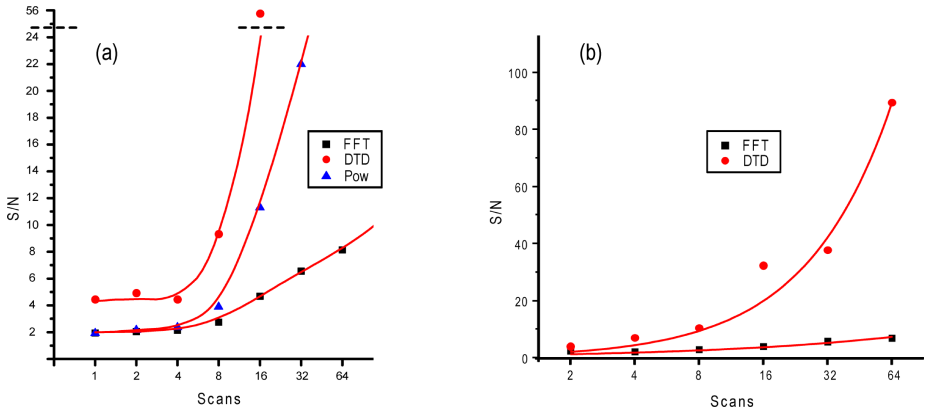

Figure 7.6: (a) Evaluation of the signal-to-noise ratio of the synthetic data set shown in Fig. 7.2: Signals have been evaluated from the topmost row of the spectra and plotted, against number of scans of the signal, defining the peak with the lowest S/N as one scan. The signal to noise ratio is plotted against the number of scans per increment for FFT (squares), DTD (circles) and a power spectrum (triangles). Lines have been added to guide the eye. (b) Evaluation of the signal to noise ratio for the experimental data shown in Fig. 7.4: the effect on S/N for the carbonyl-Cα crosspeak of bradykinin using FFT (squares) and DTD (circles) processed spectra is plotted over the number of scans. (this corresponds to the region between 165 and 180 ppm in the slices shown in Fig. 7.4b).

probability of this occurrence gets smaller, the more points are included into the sum.

These considerations imply, that the exact form of spectral noise, after transformation from the time into the frequency domain, is a function of the mathematical transformation used.

Thus, by multiplication of the two spectra resulting from covariance and FFT, overall noise is reduced, whereas the signals are enhanced. It is important to note, that noise after multiplication is still symmetric about zero but shows a more narrow distribution than the Gaussian noise from both component spectra. This non-Gaussian noise is used in the following to define a signal-to-noise ratio which can be compared to the S/N from FFT spectra to assess sensitivity improvements.

7.3 Materials and Methods

7.3.1 Samples

^{12}C-R-(U13C-15N-PPGFSPF)^{12}C-R bradykinin was synthesised using standard solid phase synthesis. The tripeptide MLF was bought from Eurisotop.

7.3.2 Computation

The pseudo-homonuclear spectra shown in Fig. 7.2 were computed using Python 2.4, using the module scientific python [119]. The resulting spectra were imported into NMRPipe [121] and processed using the covariance binary provided by Rafael Brüschweiler (http://spin.magnet.fsu.edu/software/ covNMR/covNMR.html). Spectra were plotted using GnuPlot 4.0. Processing of experimental spectra was done in Topspin 1.3 (Bruker, Karlsruhe) using the au-program covariance which is part of Topspin versions newer than 1.3 (for the 1.3 compatible version, please contact W.

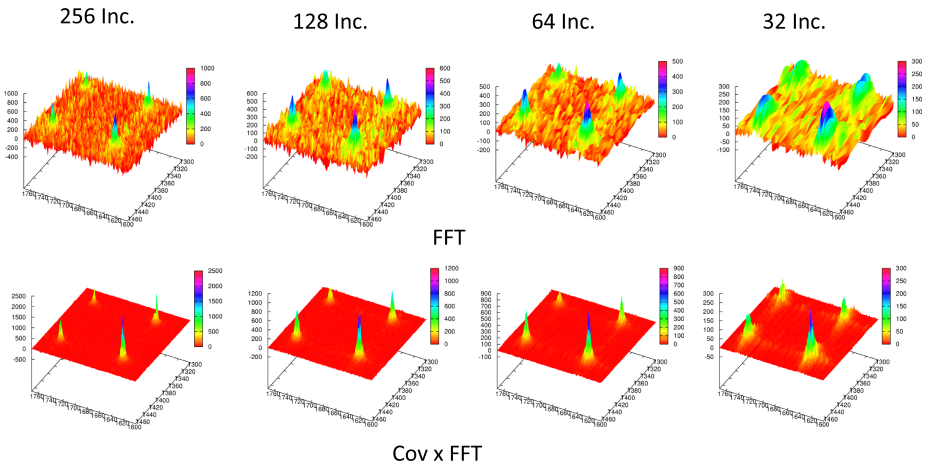

Figure 7.7: Comparison of FFT and DTD on the synthetic data sets shown in Fig. 7.2, with respect to spectral truncation: The calculated data set was truncated to 256, 128, 64 and 32 increments in the indirect dimension and then transformed with FFT (upper row) and DTD (lower row). The region shown is the same as the insets in Fig. 7.2. The broadening of the peaks in the indirect dimension is visible with both processing schemes, but highly attenuated in the case of DTD.

Bermel). The spectra used for measuring buildup curves of MLF were processed using Topspin 1.3 (Bruker, Karlsruhe). The buildup curves were generated using Cara 1.8.4 and then evaluated and plotted using Python 2.4. All software except Topspin 1.3 is open source, public domain, and freely available on the Internet.

7.3.3 NMR

All experiments were conducted on a Bruker Avance II 400 MHz Spectrometer using a 4-mm DVT HXY probe. MAS frequencies of 8 kHz were used for Bradykinin spectra and 10 kHz for MLF spectra. The samples were kept at 240 K during the measurement. PDSD spectra [33] (mixing time 100 ms) of Bradykinin were recorded using standard CP (with spinlock field 55 kHz on 1H and 47 kHz on 13C with a spin locking time of 500 s). 1H and 13C pulse lengths for 90° tilt angles were 4.47 s. The mixing time was 100 ms and the protons were decoupled during acquisition with 100 kHz Spinal64 decoupling [80]. For the MLF sample, DARR mixing [81] was employed using a 10-kHz resonant field during mixing. Values for CP were 47 kHz spin lock for ^{13}C and 57 kHz for ^{1}H with a 700-s spin lock. 90° pulse lengths of 4 and 3 s were employed for ^{13}C and ^{1}H pulses, respectively. Buildup curves were recorded with mixing times of 1, 5, 10, 25, 50, 100, 150 and 200 ms.

7.4 Results and Discussion

To evaluate the performance of DTD with respect to S/N ratio, resolution and truncation artifacts, a calculated data set is used, consisting of a grid of Lorentzian peaks placed symmetrically around the spectrum diagonal. The intensities between neighboring peaks are varied by a factor of $\sqrt{2}$, in order to enable a quick and simple evaluation of the effect of any processing on S/N (Fig. 7.2a). This corresponds to doubling the number of scans in an experimental spectrum, between adjacent cross-peaks. Gaussian noise is added to the spectrum in such a way that the S/N of the

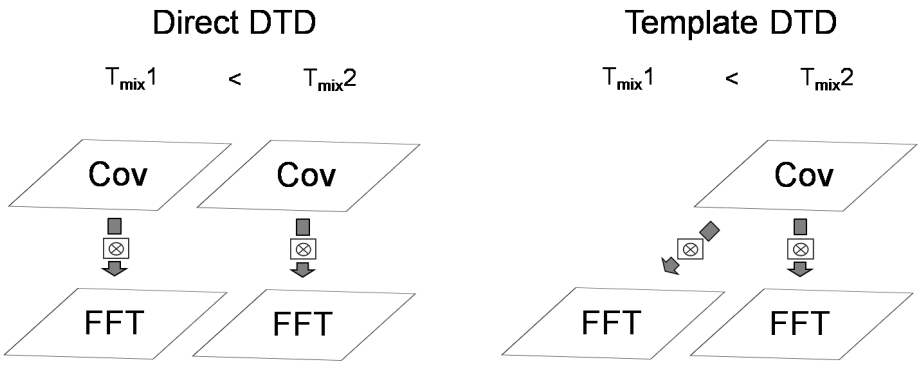

Figure 7.8: Schematic comparison of direct and template DTD: With direct DTD, both spectra resulting from covariance and FFT processing are multiplied for each mixing time as outlined in Figure 7.1. Template DTD transforms only the spectrum with the longest mixing time, showing all the crosspeaks that can be expected for the chosen mixing times, using covariance. This spectrum is then used as a template for multiplication with the FFT processed spectra of each mixing time recorded, resulting in a reduction of noise without compromising the relative peak intensities of the spectra with different mixing times.

peaks in the spectrum ranges from about 1 to 10 (Fig. 7.2b). In the following, the effect of DTD is discussed with respect to the denoising performance, the suppression of truncation artifacts and the fidelity of peak intensities.

7.4.1 Denoising

The DTD processed data set is shown in Fig. 7.2 c. A comparison to Fig. 7.2 b shows that the noise is significantly reduced in contrast to the Fourier transformed data set. The results of a data set populated by peaks of Gaussian shape showed similar results (data not shown). To evaluate the performance of DTD, the S/N ratios of the individual crosspeaks are plotted in Fig. 4a, for the FFT (see Fig. 7.2 b) and the DTD (see Fig. 7.2 c) processed sets. Here, the S/N for FFT and DTD is plotted against the number of scans representing the crosspeak intensities in Fig. 7.2. In the simulated spectra the denoising performance of DTD is readily visible. For the lowest number of scans given in Fig. 7.6 a the S/N is enhanced by a factor of 2.3. With increasing S/N, the relative enhancement of DTD over FFT grows, showing a strong exponential behavior in contrast to the well known $\sqrt{2}$ S/N dependency of the Fourier transform spectrum. An explanation for the dramatic rise in S/N is the multiplication of the covariance and FFT spectra. As the noise is generally small in the case of high S/N and uncorrelated between the two component spectra, multiplication has a much stronger effect on the denoising than addition would. To quantify this effect further, the result of a power processed spectrum (multiplying the spectrum with itself) is plotted in Fig. 7.6 a. It can be seen that, for low S/N ratios, the power spectrum (triangles) offers no significant advantage over the conventional FFT (squares), as the noise is squared with the signals. The DTD processing (circles), on the other hand, shows an increase in S/N as the noise in the two subspectra used for DTD is different, as outlined above. In the high S/N regime the effect of power processing more resembles that of the DTD.

Here, the reduction of noise gained by DTD is only of minor importance. The main effect stems from squaring the spectrum, as the large signals are proportionally enhanced more strongly than the weak noise. To evaluate the performance of DTD on spectra with a realistic distribution of peak intensities, radio frequency driven re-

coupling (RFDR) spectra of a three spin system were simulated using SIMPSON. Afterward the data set has been treated identical to the one generated with Scipy. The resultant data set is shown in Fig. 7.3. Here, different levels of Gaussian noise have been added to the spectrum to simulate strong, intermediate and weak noise contributions. Slices of these spectra are shown on the right, where the spectra processed with FFT are plotted in blue and the DTD spectra in green. The signal to noise for the crosspeak a), indicated in the left half of Fig. 7.3 are listed as an inset. The relative enhancements obtained for the RFDR spectra were similar to the ones for the data set generated with Scipy, suggesting that our previous findings were correct.

To confirm these simulations with experimental data, homo-nuclear correlation spectra of various S/N were recorded using PDSD spectra [33] of bradykinin. The results of DTD processing are compared to those obtained with FFT, as shown for the slices of three spectra recorded with 2, 8 and 32 scans in Fig. 7.4b. From these it can be seen that for 8 scans the S/N is strongly increased for the DTD processed spectrum, as compared to the FFT spectrum, whereas the noise is all but eliminated in the spectrum recorded with 32 scans using DTD processing. The evaluation of the S/N for the Cα-carbonyl crosspeak for all spectra recorded on bradykinin is shown in Fig. 7.6b, plotted over the number of scans for FFT (squares) and DTD (circles). As can be seen by comparison of the graphs in Fig. 7.6a and b, the plots of S/N(DTD) vs. S/N(FFT) agree well, as the general denoising is observed in both cases and shows the same trend with increasing S/N ratio.

7.4.2 Truncation

To inspect the effect of DTD processing on a truncated data set, a truncated the set shown in Fig. 7.2, which has been shortened to 256, 128, 64 and 32 increments. These spectra were subsequently processed using the conventional FFT (Fig. 7.7, upper row) and DTD (Fig. 7.7, lower row). It is apparent that the general shape of the spectrum is not as severely affected by truncation in the case of DTD as compared to FFT processing, even in the presence of strong noise. The same effect was observed on artificially truncated, experimental PDSD spectra (data not shown). This allowed a reduction of the number of increments, in an PDSD experiment on bradykinin, by up to a factor of 4 without introducing truncation artifacts into the spectrum. Thus DTD provides the advantages of denoising at the same time as fast NMR for which covariance was originally introduced. It is worth noting that the S/N ratio of the processed 2D spectra shown in Fig. 7.7 improves with fewer increments. This is a consequence of the short T_2 time chosen for the simulation and is a feature typical for most ssNMR spectra.

7.4.3 Measuring buildup curves using DTD

Although the denoising and artifact suppression characteristics of multiplication make this approach favorable, there are also drawbacks to this method. Peak integrals are no longer quantitative using direct multiplication of FFT and covariance spectra, and thus do not yield accurate buildup curves when different mixing times are used to record a set of homo-nuclear correlation spectra. This is not a problem when considering qualitative applications of homo-nuclear correlation spectroscopy (e.g. peak assignment), but can prove to be severely limiting if quantitative information is required. To solve this problem for buildup curve evaluation, a slightly different approach to the multiplication of spectra is proposed, which will be referred to in the following as template DTD (as opposed to the direct DTD discussed above). Instead of DTD processing all the spectra in the set, only the spectrum with the longest mixing time (thus showing all relevant crosspeaks) is DTD processed. The covariance transformed subspectrum is then used as a spectral template for denoising and artifact suppres-

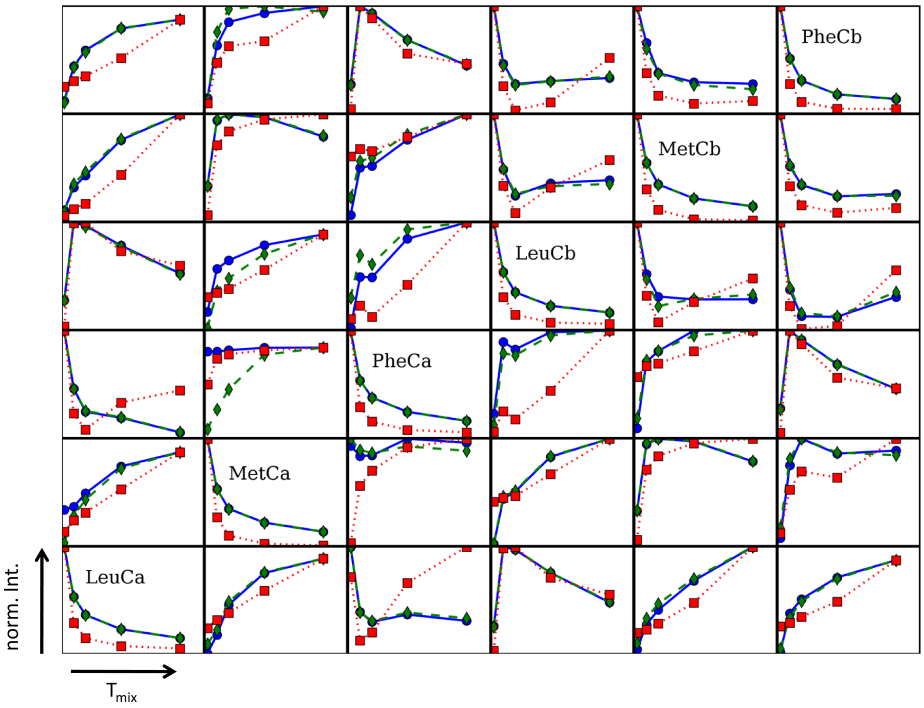

Figure 7.9: Comparison of the experimental $^{13}C - ^{13}C$ buildup rates (corresponding to 1, 5, 10, 25 and 50 ms) for DARR spectra on the tripeptide MLF. The buildup curves have been normalized individually. The FFT processed set of spectra is shown as blue circles (solid line). The FFT processed set multiplied with the covariance processed spectrum for the longest mixing time (50 ms) (template DTD) is shown as green diamonds (dashed line). The direct DTD processed set is shown as red squares (dotted line). The buildup curves of the direct DTD and FFT processed spectra show similar rates, but differences can be seen for the long range crosspeaks. The agreement of FFT and template DTD on the other hand is very good, as expected from the principle of template DTD processing.

sion by multiplication of all FFT spectra with this template spectrum, as indicated in Fig. 7.8. This gives far better buildup curves of the denoised data set, as it amounts to multiplying the individual spectral data points with the points in the covariance transformed spectrum. This factor is constant for the whole set, and thus eliminated if relative values are used for analysis. The resultant buildup curves of a set of $^{13}C^{13}C$ DARR spectra [81] are shown in Fig. 7.9 on the tripeptide MLF for the Cα and Cβ resonances. The blue circles (solid line) show the buildup curve derived from the FFT processed set, the green diamonds (dashed line) correspond to template DTD set and the red squares (dotted line) correspond to regular (direct) DTD processing of the individual spectra. For most crosspeaks, the template processed and the FFT sets are in very good agreement. Differences appear in the case of partial spectral overlap, as with the PheCα/Met-Cα crosspeak. In all cases, the agreement between template DTD and FFT is much better than between the direct DTD and the FFT sets. An exception to this behavior only occurred for long mixing times, as covariance spectra in general seem to be less affected by relaxation decay of the crosspeaks. This leads to a divergence of FFT and covariance buildup curves, and as a consequence between the pure FFT and the covariance multiplied sets at long mixing times (100, 150 and 200 ms, data not shown). This should not pose a problem as mixing times dominated by relaxation are normally excluded from structural calculations using the initial rate approximation. Thus the quantification of peaks is possible using template DTD, keeping the favorable property of denoising of the direct DTD. Caution is advised in the case of spectral truncation, as artifacts in the FFT spectrum could produce false correlations if the spectral template crosspeaks coincide with the artifact position. Another option to achieve quantitative buildup curves is using an FFT processed spectrum as a template for a set of covariance spectra. This option was not investigated in this work, as FFT is more widely used for quantitative analysis as compared to covariance processing, but this option could provide useful if spectra with strong truncation artifacts are to be analyzed.

7.4.4 Application of DTD to DGK Spectra

An example of the application of DTD to a homo-nuclear correlation spectrum of an integral membrane protein is shown in chapter 8, Fig. 8.23.

Solid state spectra of integral membrane proteins intrinsically carry the disadvantage of limited sensitivity. This is caused by several different factors. Firstly, the expression yield is generally low for membrane proteins, and the proteins have to be reconstituted into an membrane mimetic environment, if their natural surroundings are to be emulated. Although for most samples polarization enhancement of heteronuclei from ^{1}H can be used, proton detection is normally not possible in the solid state, as the homo-nuclear dipolar couplings lead to a severe broadening of the spectra. Most of the time, the interplay of several such factors makes measuring times unfeasibly long.

This was also the case for a $^{2}H\,-^{13}C\,-^{15}N$ labeled preparation of the integral membrane protein diacylglycerol kinase. For this sample, the amount of protein was limited and no polarization enhancement schemes could be used, due to the perdeuteration of the protein.

This resulted in a very limited sensitivity and the spectrum could only be acquired with 140 increments in the indirect dimension, as 2048 scans were needed per increment to obtain a workable signal to noise ratio. This number of increments is normally insufficient to obtain $^{13}C\,-^{13}C$ spectra of good quality, as the digital resolution in the indirect dimension is limited to about 200Hz, given the necessary spectral width. Still, the measuring time was approx. 6 days.

Dual Transformation Denoising presents an opportunity to increase the quality of spectra recorded for such difficult samples. It was therefore applied to the TOBSY

spectrum of $^{2}H\,-^{13}C\,-^{15}N$ labeled DGK shown in chapter 8, Fig. 8.23.

For the given spectrum, no additional or missing resonances could be detected upon DTD processing and no significant change of the line shapes in the direct dimension was observed.

7.5 Conclusion and Outlook

DTD has been demonstrated to be an effective tool which increases the S/N of a homo-nuclear spectrum, while at the same time reducing the number of necessary increments in a given two dimensional spectrum. This can lead to a significant reduction of measuring time for homo-nuclear 2D experiments, as was shown for the example of PDSD spectra of bradykinin, recorded in one fourth of the normal measuring time. Alternatively, the experimental time could be kept constant by increasing the number of scans per increment at the expense of the number of increments recorded. This would make use of the fact that the S/ N improves steeply with a growing number of scans for DTD processed spectra, while utilizing the suppression of truncation artifacts to compensate for the decreased number of increments. This should lead to spectra of high quality with an enhanced S/N ratio. Although DTD is demonstrated here using a combination of covariance and FFT on 2D data sets, spectra of higher dimensionality should show the same reduction of measuring time, if a homo-nuclear mixing period is included.

Chapter 8

Solid State NMR on the Integral Membrane Protein DGK

8.1 Introduction

Diacylglycerol Kinase (DGK) from *Escherichia coli* [122–124] is a small integral membrane protein, with 121 amino acids and a molecular weight of 13.2 kDa. It functions as a kinase, catalyzing the phosphorylation of diacylglycerol (DAG) by the transfer the γ-phosphate from ATP to DAG, to form phosphatidic acid (PA) and ADP.

In *E.coli*, the functionality of DGK has been shown to influence on the rate of cell proliferation under conditions of low osmolarity [125]. This observation is based on the role of DAG in the membrane derived oligosaccharide (MDO) cycle.

During the synthesis of MDOs, the pre-MDOs need to be ferried to the site of synthesis. This involves phosphatidylglycerol (PG) as a carrier molecule for the pre-MDOs.

After the pre-MDO has dissociated, DAG remains, which has been shown to accumulate in the membrane in the absence of DGK function [125].

Phosphorylation to PA by DGK recycles DAG, as PA can act as a precursor molecule for the biosynthesis of phosphatidylethanolamine (PE) and cardiolipin (CL). In this biochemical pathway, CDP-Diacylglycerol is formed from PA by CDP - Diacylglycerol Synthetase. One of the intermediate products in the CL synthesis pathway is PG, which can again be used by the cell for MDO biosynthesis as outlined above, closing the PG-DAG-PA catalytic cycle.

DGK spans the membrane three times as elucidated by Smith et al. [126] via β-lactamase and β-galactosidase fusion experiments and is mostly α-helical [127]. The topology is proposed [128] to consist of two small N-terminal amphipathic helices, followed by two transmembrane helices connected by a small loop of four amino acids. These domains are followed by a third amphipathic helix, containing most of the residues highly conserved in all procaryotic DGK sequences and proposed to be involved in the active site of the protein [128–130], which in turn is followed by a third transmembrane helix and the C-terminus.

The N-terminus of DGK is proposed to reside in the cytoplasm and the C-terminus is oriented towards the periplasm in *E.coli* [126]. This topology model was further refined by ^{19}F solution state NMR studies [128, 131].

DGK forms trimers [132] with transmembrane helix 2 acting as the center of three-

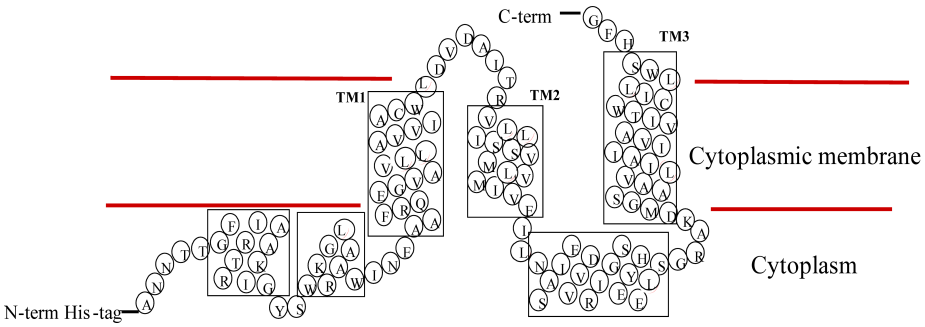

Figure 8.1: Schematic diagram of a diacylglycerol kinase monomer based on [134]. The protein forms trimers in its native state, with transmembrane helix 2 acting as a center of threefold symmetry.

fold symmetry [133] and three active sites per trimer, made up by residues from the different subunits [130].

DGK has several advantages that make it ideally suited as a target for solid state NMR studies. It can be obtained in large amounts by overexpression in E.coli cells and easily purified using Ion Metal Affinity Chromatography (IMAC) [132, 135, 136]. It can be reconstituted into lipid vesicles with high efficiency [136] and assayed for activity either in mixed micelles [129, 137–139] or reconstituted into lipid vesicles [140].

DGK has been studied before in a variety of publications concerning its activity in different environments [127, 133, 137, 138, 141–143], the correct folding of integral membrane proteins and their insertion into lipid bilayers and detergent micelles [136, 140, 144–146], its stability with respect to unfolding using detergent [135, 145] and its thermal stability in a variety of detergents [147].

Furthermore the stability of DGK in membranes has been assessed [122, 145, 148]. DGK has been investigated using a variety of methods such as glutaraldehyde cross linking [132, 133, 136, 140, 144], FT-IR [127], UV and CD spectroscopy [135, 140], solution [128, 131, 134, 141] and solid state NMR spectroscopy [6, 149]. The functional tolerance of DGK to mutation has been thoroughly investigated by mutation studies [150] and an extensive library of DGK single cysteine mutants is available [136].

8.2 Biochemistry

8.2.1 Materials

The plasmid pSD004 was a gift from from C. Sanders (Vanderbilt University, USA). Dihexanoylglycerol (DHG) was purchased from Cayman Chemicals (Ann Arbor, Michigan, USA). The detergents octyl-β-D-glucopyranoside (OG), n-Dodecyl-β-D-maltoside (DDM) and dodecylphosphocholine (DPC) were bought from Anatrace (Anatrace (Maumee, OH, USA). The Ni-NTA agarose resin was purchased from QIAgen. All lipids used were purchased from Avanti Polar Lipids (Alabaster, Alabama. USA). The labeled compounds U-^{13}C labeled glucose, $^{2}H^{13}C$ labeled glucose, $15N$ ammonium chloride and 2-^{13}C-glycerol were bought from Cambridge Isotopes (Cambridge, MA, USA) or through its subsidiary Euriso-Top (Saint Aubin Cedex, FR). All other chemicals were purchased either from Sigma Aldrich or Carl Roth GmbH+CoKG (Karlsruhe, DE).

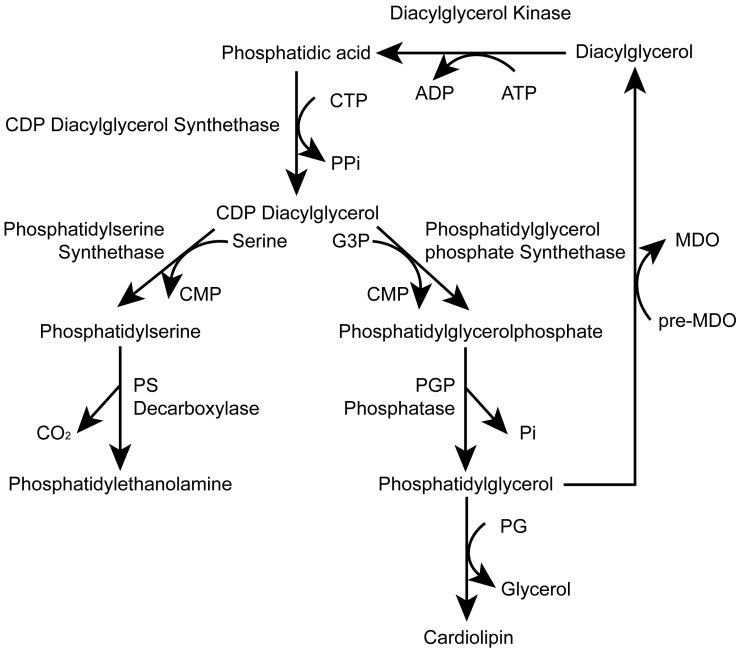

Figure 8.2: Schematic diagram of the role of DGK in the lipid and MDO metabolism of *E.coli*. DGK catalyzes the conversion of diacylglycerol produced in the synthesis of MDOs to phosphatidic acid, which is a precursor in the bacterial lipid metabolism.

8.2.2 Expression

DGK (Swiss-Prot number P00556) has been prepared according to [6]. *E.coli* BL21 cells harboring the pSD004 plasmid [135], encoding DGK with a added hexa-His tag, have been plated out from a glycerol stock on LB agar plates containing 100 $/mu$ g/ml ampicillin. After incubating these plates at 37°C overnight, a colony was picked and transferred to an overnight culture of M9 minimal medium. This culture was incubated at 220rpm and 37°C. M9 medium was prepared by adding 6g Na_2HPO_4, 3g KH_2PO_4, 0.5g $NaCl$ and 1g NH_4Cl to 1l of milliq H_2O. After autoclaving, 1ml of 0.1M $CaCl_2$, 1ml of 1M $MgSO_4$, 10ml 40% Glucose, 100mg ampicillin and 2ml vitamin mix were added to the medium (the vitamin mix was prepared by crushing 1.5g Centrum multivitamin tablets in a mortar, adding 20ml water, vortexing for 20min, centrifugation of the insoluble parts and sterile filtration of the supernatant).

The overnight culture was used to inoculate the main culture 1/100. For a $^{13}C-^{15}N$ labeled preparation of DGK, the glucose and ammonium chloride were substituted by ^{13}C-glucose and ^{15}N-ammonium chloride, in the main culture. The total amounts of glucose and ammonium chloride were kept constant, as any reduction lead to a decrease in the protein yield (data not shown).

The culture was induced with 200mg/l isopropyl β-D-thiogalactopyranoside (IPTG) after reaching an OD_{600} of 1. Expression was done overnight. The cells were harvested the next morning by centrifugation at 5000rpm for 20min at 4°C in a Beckmann Avanti J-E centrifuge and stored at -80°C. The protein yield after purification was typically 20mg/l of culture.

For the preparation of $^{2}H-^{13}C-^{15}N$ labeled DGK the protocol given above was slightly modified. The overnight culture was used to inoculate 100ml of M9 media at a ratio of 1/100, prepared in D_2O with unlabeled glucose. After reaching an OD_{600} of 0.5, this culture was used to inoculate the main culture of M9 media prepared in D_2O

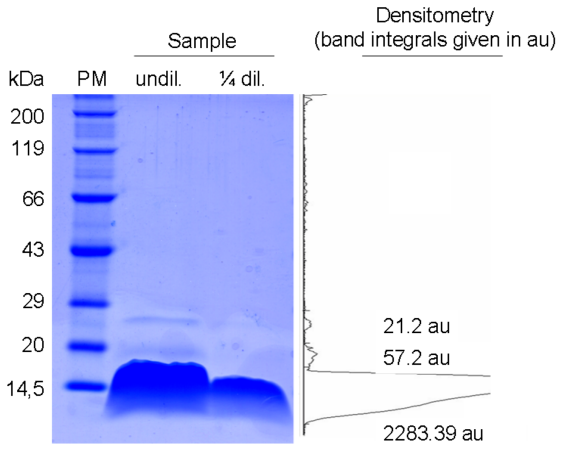

Figure 8.3: SDS-PAGE of purified DGK from BL21 cells grown in M9 media. The purified sample is shown undiluted and 1/4 diluted on the middle and right lane, respectively. The protein marker (PM) is shown on the left lane. The middle lane has been quantified via densiometry using the program ScionImage (www.scioncorp.com). From this, the bands not stemming from monomeric DGK can be estimated to amount to less than 3.5% of the total protein. These bands could stem from traces of other proteins or residual di- and trimers of DGK, which have not been properly unfolded by SDS.

and in which $^{2}H\,-^{13}\,C$ glucose was added. Here, the protein yield after purification was only 4.7 mg/l of culture.

8.2.3 Purification

The purification of DGK was conducted by thawing the cell pellet on ice and adding 26ml of buffer A (50mM sodium phosphate, 300mM NaCl, pH 7.5), one tablet of Roche Diagnostics protease inhibitor mini and 3% weight per volume of octyl β-D-glucopyranoside (OG), per 2g of wet cells. Then one spatula tip of DNase I and $MgCl_2$ was added to digest the cellular DNA and the mixture was stirred on ice for 2h.

Insoluble material was removed via centrifugation (Beckmann Allegra 21R with a F0850 rotor) at 10000rpm for 30min at 4°C. The supernatant was added to Ni-NTA resin for ion metal affinity chromatography (IMAC) purification and stirred on ice for 1h, after adding 2M imidazole pH 8.0 stock solution, to a final imidazole concentration of 30mM.

After the incubation, the resin was packed into a column and washed with buffer A + 1.5% OG + 30mM imidazole, until the absorption at 280nm was below 0.01. Then the detergent was exchanged by washing the column with buffer A + 0.5% dodecylphosphocholine (DPC) (10 column volumes). The protein was then eluted with buffer A containing 0.5% DPC and 250mM imidazole. Fractions were collected and the protein concentration measured by the absorption at 280nm according to the following formula, using a Jasco V-550 UV/Vis Spectrometer.

$$c[DGK] = \frac{abs_{280} \cdot pathlength^{-1} \cdot dilutionfactor}{1.8}$$

Fractions containing the protein were combined and immediately used for recon-

Figure 8.4: Incorporation of of DGK reconstituted into DOPC 1:25 using Protocol 2, as seen by freeze fracture electron microscopy. I thank Dr. Winfried Haase for the EM measurement.

stitution. The purity of the protein was checked with SDS-PAGE.

8.2.4 Reconstitution

Several different reconstitution protocols were used to assess the effect of the reconstitution conditions on the spectral quality of DGK. The first protocol used is outlined in [6]. Here, the lipid used for reconstitution (1,2-dioleoyl-sn-glycero-3-phospholcholine, DOPC) is suspended in 5ml buffer A, per 100mg of lipid. Then 10ml buffer A +0.5% DPC is added per 100mg lipid and the resulting mixture freeze thawed multiple times until it is clear. This lipid stock solution is then added to DGK in the elution buffer (buffer A + 0.5% DPC + 250mM imidazole) so that the DGK to lipid mol/mol ratio is about 1:100. The combined solution is then transferred into a SpectaPor 4 dialysis membrane with a molecular weight cutoff of 12-14kDa and dialyzed against a dialysis buffer containing 50mM HEPES, 10mM $MgCl_2$, 2mM NaATP, 1mM ethylene diamine tetraacetic acid (EDTA), 0.2mM dithiotreitol (DTT) at a pH of 7.0, at room temperature. The buffer has to be exchanged every day and the dialysis is complete after 7 days. This protocol will be referred to as protocol 1 in the following.

A second protocol, which was employed for most of the NMR experiments, reduces the lipid to DGK ratio to 1:50 (mol/mol) (I thank Dr. Sarika Shastri for providing me with this protocol, which is detailed in [151]). This increases the amount of protein that can be contained in the rotor by approx. a factor of 2. The preparation and elution conditions are the same as for protocol 1, but here the protein is dialyzed against a buffer containing 40mM sodium acetate, 20mM $MgCl_2$, 0.2mM DTT, 20% glycerol, 0.02% sodium azide at a pH of 4.5. This protocol will be referred to as protocol 2 in the following.

The third protocol used is described in [136]. This protocol was adopted for the $^{2}H\,^{-13}C\,^{-15}N$ DGK samples, as protocol 2 failed to give good reconstitution results with perdeuterated DGK. These problems were not observed using this protocol. Briefly, a lipid stock solution is prepared in a 50mM HEPES, 300mM NaCl, 1mM EDTA buffer (pH8.0), by adding 50mM DOPC and 200mM DPC and freeze thawing the solution until it is clear. This stock solution is then added to DGK in elution buffer, so that the final ratio of DGK to DOPC is 1:120 (mol/mol). This mixture is

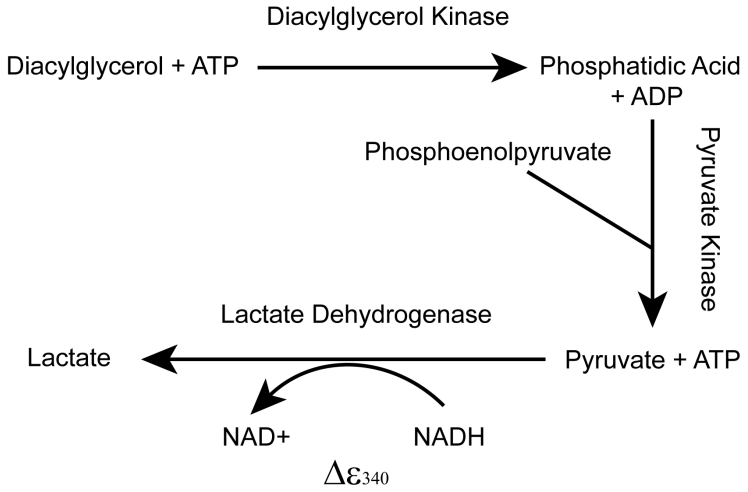

Figure 8.5: Schematic diagram of the coupled assay, as described in [152]. Briefly, the conversion of ATP to ADP by DGK is monitored by the conversion of NADH to NAD^+ through a coupled reaction with pyruvate kinase and lactate dehydrogenase. The reduction in NADH is observable as an absorption change at 340nm.

then dialyzed against 10mM imidazole, 0.5mM EDTA pH 8.0 at room temperature. The buffer is exchanged every day and the dialysis is complete after 4-5 days. This protocol will be referred to as protocol 3 in the following.

For all protocols the same dialysis membranes (SpectraPor 4, 12-14kDa cutoff) were used and the samples were snap frozen in liquid N_2 after reconstitution and stored at -80°C.

8.2.5 Activity

The activity of the reconstituted samples was tested using the assay described in [152] using dihexanoylglycerol (DHG) as the substrate.

Here, the generation of ADP from ATP by DGK is monitored via a coupled reaction, that leads to an oxidation of nicotine amide dinucleotide (NADH) to NAD^+ and a concomitant reduction of the absorption of the sample at a wave length of 340nm. This reaction is depicted in Fig. 8.5. First, DHG and ATP are converted to DHG-phosphate and ADP. This ADP is then converted back to ATP by pyruvate kinase, generating pyruvate from phosphoenolpyruvate. Pyruvate in turn acts, together with NADH, as a substrate for lactate dehydrogenase, forming lactate and NAD^+.

The reaction mixture containing 75mM PIPES (pH 6.9), 50mM LiCl, 0.1mM ethylene glycol tetraacetic acid (EGTA), 0.1mM EDTA, 0.2mM DTT, 1% DDM (w/v), 0.66mM CL, 0.95mM DHG, the coupling enzymes (20 units of each of lactate dehydrogenase and pyruvate kinase), 1mM phosphoenolpyruvate, 3mM ATP, 0.25 mM NADH and 15mM Mg^{2+}, is incubated for 5 min at 30°C prior to the experiment. Then the reaction mixture is transferred to a cuvette with a pathlenght of 3mm, in a Jasco V-550 Uv/Vis spectrometer. To this mixture reconstituted DGK is added, which has been diluted 1:10 into a 1% N-dodecyl-β-D-maltoside (DDM) solution.

The activity is measured by the absorption of NADH at 340nm, according to

$$\frac{u}{mg} = \frac{abs}{min} \cdot \eta_{NADH}^{-1} \cdot pathlength^{-1} \cdot reactionvolume \cdot proteinmass^{-1} \qquad (8.1)$$

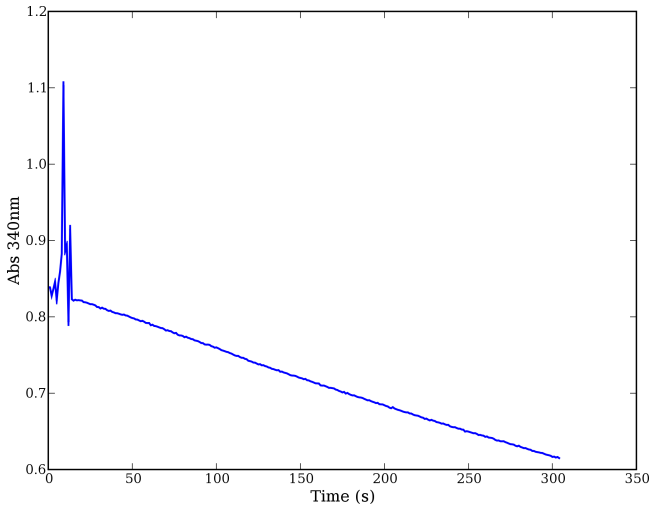

Figure 8.6: Activity trace of DGK reconstituted with protocol 3, using DOPC as the reconstitution lipid (protein/lipid ratio 1:120). The reaction catalyzed by DGK is monitored via the change of absorption at 340nm, through the coupled assay shown in Fig. 8.5, using dihexanoylglycerol as the substrate. The reaction volume was 103 μl, containing 0.11 μg ml^{-1} of reconstituted DGK, in a cuvette with a path length of 3mm. The measurement was conducted at room temperature. The spikes at the beginning of the trace stem from the pipet tip occluding the light path upon addition of the DGK sample to the reaction mixture, followed by short stirring. Using Eqn. 8.1 the measured activity computes to 23 units/mg.

It is important to add the DGK sample from the 1:10 DDM solution (typically 1μl) to the reaction mixture immediately following dilution, as it has been observed, that after approx. 30min the DDM leads to permeability of the lipid vesicles.

This can result in an overestimation of the protein activity, as the method used for reconstitution is non-directional and therefore approx. 50% of the active sites of the proteins are inaccessible to water soluble compounds, such as ATP, as long as the lipid vesicles are intact.

Keeping the 1 % DDM solution on ice and measuring the sample activity directly following dilution was found to circumvent this problem.

Thus, for this assay, only the activities measured immediately after dilution into 1% DDM are given. One example for such an activity trace is shown in Fig. 8.6.

Using a variant of the assay described above, in which dihexanoylglycerol is substituted by dibutyrylglycerol and which omits the detergent from the reaction mixture, an activity of 35 units/mg (one unit is defined as 1 μmol of substrate phosphorylated per minute) at 30°C was measured for DGK reconstituted using protocol 1. These measurements are detailed in [6]. The activity of the DGK reconstituted using protocol 2, with a protein to lipid ratio of 1:50 (mol/mol), was determined with the same assay used for protocol 1 to be 30 units/mg. The activities for protocol 3 reconstituted samples were measured using the assay with DHG as the substrate. The activities were 48 units/mg for DGK in mixed micelles and 23 units/mg after reconstitution, both measured at room temperature. The activity of the reconstituted sample was measured directly after dilution into 1% DDM and is shown in Fig. 8.6.

These numbers correspond well with the values reported in the literature, measured under similar conditions [140, 152, 153] (the activities measured at room temperature are expected to increase by approx. 50%, if the samples are measured at 30°C [154]).

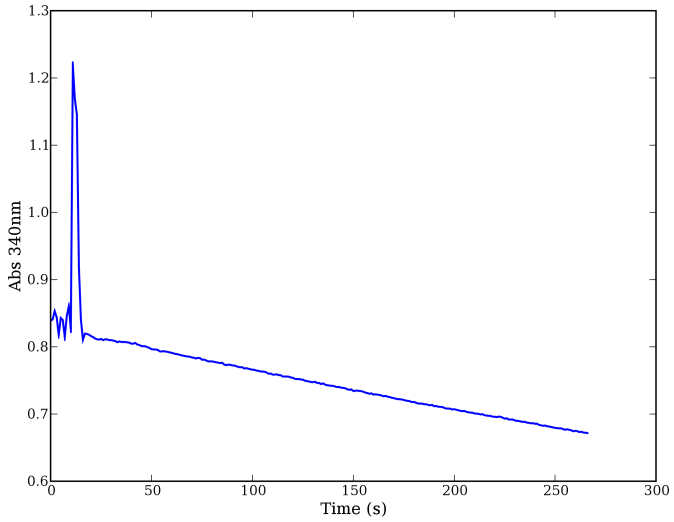

Figure 8.7: Activity trace of DGK reconstituted with protocol 3, using a 80:20 DOPC/DOPG lipid mixture for reconstitution (protein/lipid ratio 1:120). The assay used was the same as in Fig. 8.6. The reaction volume of 103 μl contained 0.09 μg ml^{-1} reconstituted DGK, in a cuvette with a path length of 3mm. The measurement was conducted at room temperature. Using Eqn. 8.1 the measured activity computes to 21.5 units/mg.

8.3 NMR

Although DGK has been investigated by solution, as well as solid state NMR before [6, 128, 131, 134, 141, 149] the three dimensional structure of the protein is still unknown. Complicating the studies of DGK with solution state NMR is the large size of the protein-detergent micelle of 90-110 kDa [134]. With solid state NMR, the rotation correlation time is not an issue, but DGK shows dynamics that lead to spectral broadening upon freezing the sample, as multiple, highly similar conformations are frozen out [6].

Solid state NMR studies of the sample in a non frozen state are perturbed by the dynamics of DGK, as motions on the NMR time scale interfere with the polarization transfer steps needed in the NMR experiments. To characterize this behavior further and to find ways to overcome these problems, the effects of a variety of different labeling, reconstitution and NMR techniques were tested. The results of these experiments are shown in the following.

The experiments conducted, the labeling schemes employed and the results obtained will first be summarized briefly in the following section. Then a more elaborate treatment of the individual techniques is given.

Although the conclusions drawn in this chapter were found exclusively on the integral membrane protein DGK, most of the basic principles are expected to be common to most α-helical integral membrane proteins.

8.3.1 Overview

The most common approach, when investigating a biological sample using solid state NMR, is to keep the, usually semi liquid, sample frozen during measurement. Using this approach, the speed of freezing is of utmost importance, as it might influence the number of distinct structural conformations present in the frozen sample. Unfortunately, freezing first and then packing the sample into a MAS rotor is very difficult, as small packing errors in the rotor might lead to an imbalance. A far more reliable way consists of packing the still semi liquid sample into the rotor, at 4°C and then rapidly freezing the sample, once it is homogeneously distributed in the rotor cavity. A drawback of this method is that the rotor walls (usually consisting of zirconium-oxide) isolate the sample from the coolant. This leads to a slow freezing of the sample. Still, the prospect of a spinning instability and possibly successive rotor crash, leads to the latter packing method being exclusively used for the experiments presented in this chapter.

The most pronounced effects apparent, when measuring a frozen sample, are twofold. Firstly, the signal intensity is relatively high, as the combination of MAS, cross polarization and low temperature complement each other, resulting in relatively short measurement times needed to arrive at a spectrum of a good signal to noise ratio.

The second effect observable concerns the width of the spectral resonances. Most resonances in the spectrum become rather broad (often greater than 100Hz line width at half height). This is most likely caused by the dynamics of the protein sample at room temperature, which results in a number of similar, but not identical structural conformations being populated. Freezing the sample leads to a distribution of the sample molecules in these different conformations, especially if the individual conformations are of similar energy, as in this case none of the conformations is strongly favored upon freezing the sample. This in turn leads to a slight structural heterogeneity in the frozen sample, resulting in a spread of isotropic chemical shifts of the individual spectral resonances.

This heavily complicates the study of the protein sample, because most amino acids display a limited structural chemical shift range and therefore the resonance shifts caused by the three dimensional structure of one conformation are superimposed on those of the other populated conformations. As resonance line widths are already rather broad in the solid state (which is mostly due to the influence of residual anisotropic interactions, see chapter 2), this leads to severe spectral overlap, which, in many cases, almost totally obscures the structural information contained in the spectrum. This data is shown in section 8.3.2 below.

One possibility to overcome the spectral degeneration, is the use of special labeling patterns. These can be employed to limit the number of NMR active nuclei in the sample and therefore reduce the spectral overlap. This possibility was studied using selective, extensive labeling [155] as shown in [6] or selective unlabeling [156], where a mixture of nonlabeled amino acids is supplemented to the bacteria during protein expression, leading to a significant reduction of specific resonances. This is shown in section 8.3.3. A potential problem with this approach is, that only certain amino acids can be selected for unlabeling. The reason for this is the biochemical interconversion of certain amino acids in the bacteria. This restriction to certain amino acids poses a limit to this method. In the present case this labeling technique was found to be insufficient to resolve especially crowded regions of the spectrum, such as the $C\alpha$ or CO regions.

Another solution for this problem, which is hard to mitigate at low temperatures, is the use of a sample temperature just above 0°C. The sensitivity and resolution of protein preparations studied at this temperature was investigated, to find a viable alternative to sample freezing and all its assorted problems.

Experiments conducted on semi solid samples present unique chances, as well as challenges to a solid state NMR spectroscopist. A major advantage gained by the study of a semi solid sample, is that structural states of the protein, which have similar energies and low interconversion barriers, are likely to rapidly interconvert. This leads to a single resonance line via a phenomenon spectroscopically similar to rapid chemical exchange, resulting in the observation of the average of the chemical shifts of all interconverting structures. This should in principle alleviate the problem of very large, inhomogeneous line widths, which is observed at lower temperatures. This is investigated in section 8.3.4.

Counterbalancing the superior resolution gained at higher measurement temperatures, is the very same effect leading to the line narrowing: the dynamics of the sample. Sample motion not only scales the anisotropic interactions, which are often beneficially employed in the solid state, such as the heteronuclear dipolar coupling for cross polarization, but may even interfere with the often sophisticated RF irradiation schemes employed to endow the spectral information.

This results in a overall low sensitivity of the experiment and/or incomplete encoding of spectral information in the recorded data set. In the present case of DGK, this often leads to whole groups of expected cross peaks to be missing from the spectra.

To overcome these limitations spectroscopically, the advantages of the nuclear Overhauser effect [72] and INEPT [22] in the semi solid state are investigated in sections 8.3.5 and 8.3.6, respectively. The heteronuclear Overhauser effect was found to be of great utility for polarization enhancement of flexible loop regions and more rigid transmembrane regions of the protein alike, whereas INEPT is useful for spectral editing, by selecting only the highly flexible loop regions of the protein.

Additionally, the performance of the symmetry based, heteronuclear transfer sequence R70, introduced in chapter 4, is assessed on two dimensional spectral of DGK in the semi solid state, as shown in section 8.3.7. Although the sensitivity of this sequence was not found to be significantly higher than INEPT in the present case, the relayed homo-nuclear through bond transfer, observed for the uniformly labeled preparation of DGK, is useful for amino acid type assignment. More importantly this information can be used to distinguish between genuine protein signals and natural abundance ^{13}C signals of the lipids.

A different way to enhance the quality of the spectra is to reduce the dynamics of the membrane protein, at temperatures above 0°C, via sample preparation.

One promising way to achieve this, is to control the environment of the protein. Here, especially the composition of the lipid matrix, in which the protein is embedded, is of importance. As some specific lipids might act as a scaffold for the protein and therefore stabilize a certain conformation, an effect on the protein dynamics can be expected.

This possibility is explored in section 8.3.8.

No significant change could be observed in the spectral properties of DGK, upon incorporation of a potential scaffolding lipid of DGK, DOPG, discussed in the literature [137, 138]. This implies, that the sample dynamics are not significantly changed by the presence DOPG in the DOPC lipid matrix.

Another possibility for the absence of certain groups of correlations from DGK spectra, could be interference of the sample dynamics with the ^{1}H decoupling. ^{1}H heteronuclear interactions are very strong and can easily dominate the spectrum in the solid state, if no precautions are taken. Interference of the sample dynamics with heteronuclear decoupling could therefore be a source of strong T_2 relaxation during the experiment, especially for the transmembrane parts of the protein.

To exclude this, a perdeuterated sample of DGK was prepared, as shown in section 8.3.9. Upon deuteration, a line narrowing was observable and heteronuclear decoupling was found to have little influence on the spectra. Still, the resonances groups missing from the TOBSY spectra of the protonated samples measured at temperatures above

0°C, were not detectable.

This implies that not insufficient heteronuclear decoupling, and concomitant relaxation of spectral resonances, is the cause for the absence of certain signals, but the polarization transfer sequence itself is adversely affected by the sample dynamics.

Further evidence for strong dynamics of the sample on the kHz time scale were found by deuterium echo experiments. The results of these measurements show a significant perturbation of the echo in the milli- to μ second range.

Unless otherwise noted, all samples were prepared with protocol 2, using DOPC as the reconstitution lipid. The spectrometer used for all experiments was a Bruker WB600 with an Avance console, again unless otherwise noted. The temperatures given for the experiments are always the values read out from the thermocouple of the spectrometer. The actual sample temperature is higher by approx. 1K per 1kHz of MAS spinning rate, due to friction.

8.3.2 Temperature Dependence of DGK Spectra

To assess the spectral resolution of the DGK samples several one dimensional spectra were recorded. To find the ideal temperature to conduct NMR experiments, first a cross-polarization (CP) spectrum was measured at 233K, which is well below the phase transition temperature of the lipids (253 K). Comparing the sensitivity of this spectrum with one recorded at 273K, it can be seen that at the higher temperature the CP efficiency is strongly reduced, even below the sensitivity of a spectrum recorded with direct polarization, using just a hard 90° pulse. This suggests strong dynamics of the protein, which partially average out the heteronuclear dipolar couplings. When comparing the direct polarization (DP) spectrum with the CP spectrum at 273K, it is apparent that several additional peaks with very narrow line width can be detected using DP. Some of these can be assigned to lipid resonances, but others stem from highly mobile regions of the protein, as will be shown later.

To further characterize the spectral resolution and the effect of temperature, a series of two dimensional proton driven spin diffusion (PDSD) experiments [33] were recorded at different mixing times and temperatures. As shown in Fig. 8.9, severe spectral overlap at low temperatures complicates the identification of individual resonances, even at a short mixing time of only 10ms. This problem is even more obvious at a longer mixing time of 100ms. These long mixing times are needed to obtain non-trivial through space constrains for three dimensional structure determination. For instance, the $C\alpha - C\alpha$ inter-residue cross peaks in the region from 52 to 68ppm carry a great deal of structural information, but severe spectral overlap makes an evaluation difficult.

Especially hydrophobic amino acids, such as isoleucine, show no fine structure in their respective cross peaks. This is caused by broad line widths, in combination with the high similarity of the chemical environment of the individual residues of that amino acid type.

To elucidate if higher temperatures can alleviate the problem of spectral overlap, for instance by reducing the observed line widths, a PDSD spectrum at 288K was recorded. For this experiment, the mixing time was 100ms and a 90° pulse was used for excitation, instead of cross polarization. An overlay of this spectrum, with the spectrum recorded at 233K with the same mixing time is shown in Fig. 8.10. Comparison of the spectra shows a reduction of the observed line widths for most resonances. An even more striking feature of the spectrum recorded at 288K is the overall low sensitivity, which results in the complete loss of several groups of cross peaks, even at this long mixing time. This indicates strong dynamics of the sample at this temperature, which is corroborated by the one dimensional CP and DP spectra.

In summary, the dynamics seen for DGK has several implications on the appearance of the NMR spectra. First, strong dynamics above 273K indicate a set of struc-

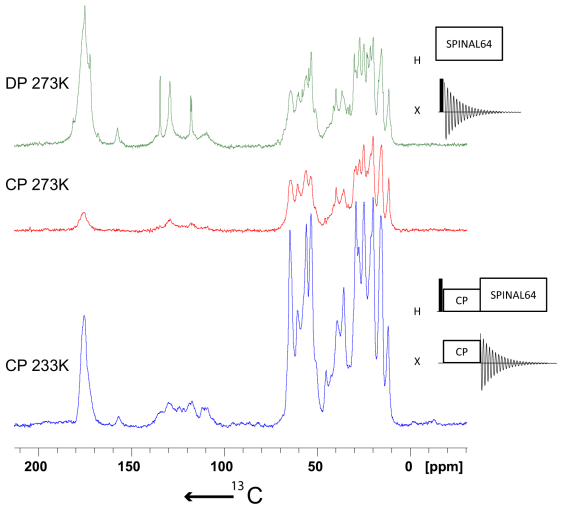

Figure 8.8: 1D spectra of DGK reconstituted 1:50 mol/mol in DOPC. All spectra were recorded with 256 scans, 10kHz MAS at the indicated temperature. All spectra were processed with an exponential line broadening of 20Hz. At low temperature, CP is efficient, but this efficiency drops considerably above the freezing point, indicating strong dynamics of the protein sample. Comparison with the DP spectrum suggests the existence of highly flexible regions of the protein, which are not cross polarized at 273K. The CP and DP pulse sequences used for the experiment are given as an inset to the right of the spectra.

tural conformations, which are very similar in conformational energy and that have low kinetic interconversion barriers. This leads to a superposition of a set of closely related structures in the NMR spectra, if the protein sample is frozen resulting in broad, nonlorentzian line shapes. Second, if the protein sample is measured in a non frozen state, the dynamics scale the homo- and heteronuclear dipolar couplings, which is highly perturbing for most classical solid state NMR experiments that rely on dipolar couplings such as CP and proton driven spin diffusion (PDSD).

Therefore, although the spectral resolution is enhanced, the loss in sensitivity and concomitant long measuring times, make the use of dipolar coupling mediated polarization transfer schemes a poor choice for structural elucidation of reconstituted DGK samples measured above 273K.

8.3.3 Selective Unlabeling

There are several ways to alleviate the aforementioned problem. One possible approach is to reduce the spectral overlap of the sample. This complicating factor for the study of integral membrane proteins by ssNMR, is mostly caused by the high fraction of hydrophobic amino acids, like alanine, leucine, isoleucine and valine in the protein sequence. As these amino acids typically reside in very similar chemical environments, the spectral degeneracy is considerable, complicating the analysis. It has therefore been proposed to 'selectively unlabel' certain ubiquitous amino acids [156–159], for which there is no significant metabolic turnover.

Using other amino acids would result in a 'scrambling' of the different isotopes, voiding the advantage of selective unlabeling. Although these problems could be partially alleviated by the use of auxotrophic *E.coli* strains, for the experiments shown in this section only the amino acids reported to be unproblematic in the context of

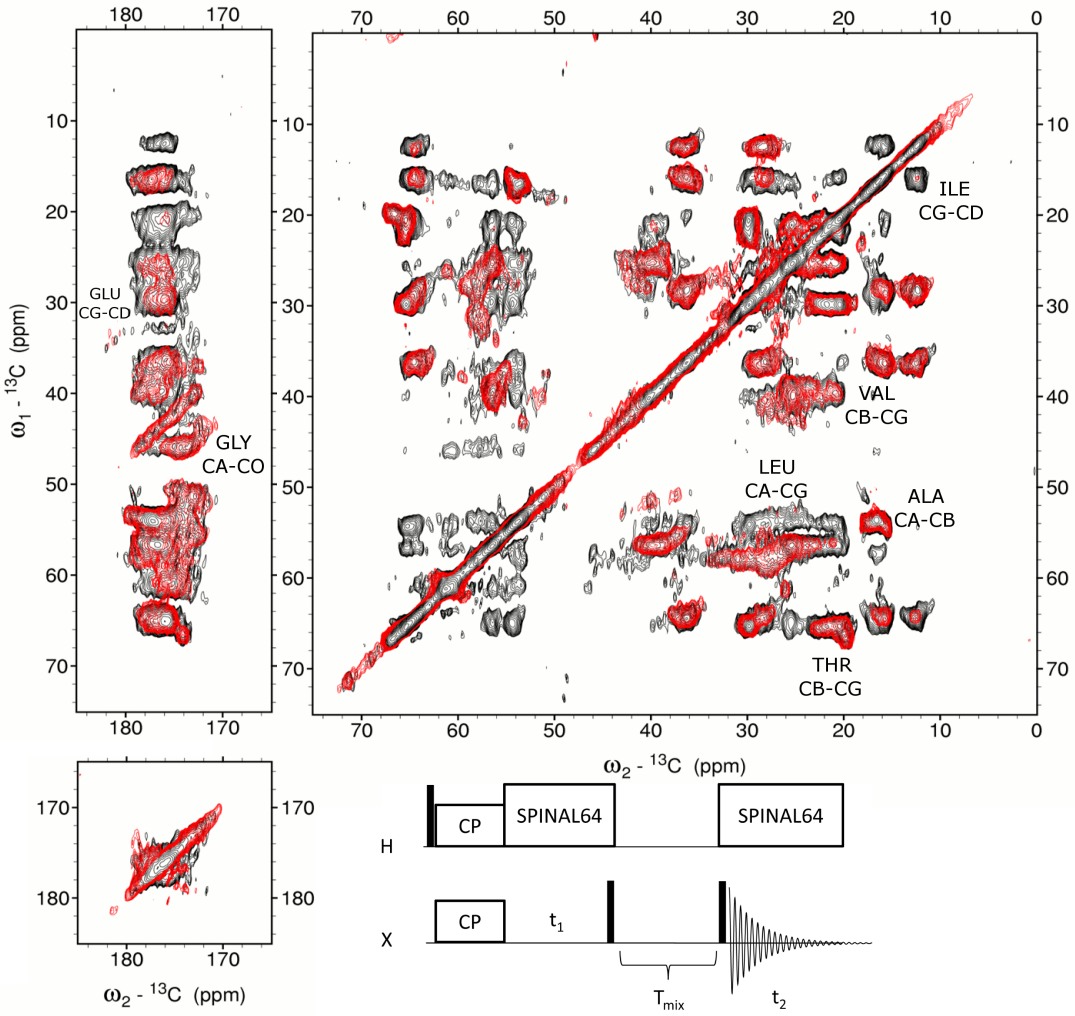

Figure 8.9: $^{13}C - ^{13}C$ correlation spectra of DGK recorded with PDSD. Spectra are shown for 100ms mixing time (black) and 10ms mixing time (red). The spectra where recorded using CP at 233K, 10 kHz MAS, 128 scans per increment and 384 increments in the indirect dimension. The spectra were processed with Gaussian window multiplication in both dimensions. At low temperature, severe spectral overlap complicates the identification of most resonances of the sample, a problem further aggravated by long mixing times, which are needed to obtain through space constrains. The PDSD pulse sequence used to record both spectra, is shown as an inset below the spectrum. Certain amino acid crosspeak regions have been labeled in the spectrum for later reference.

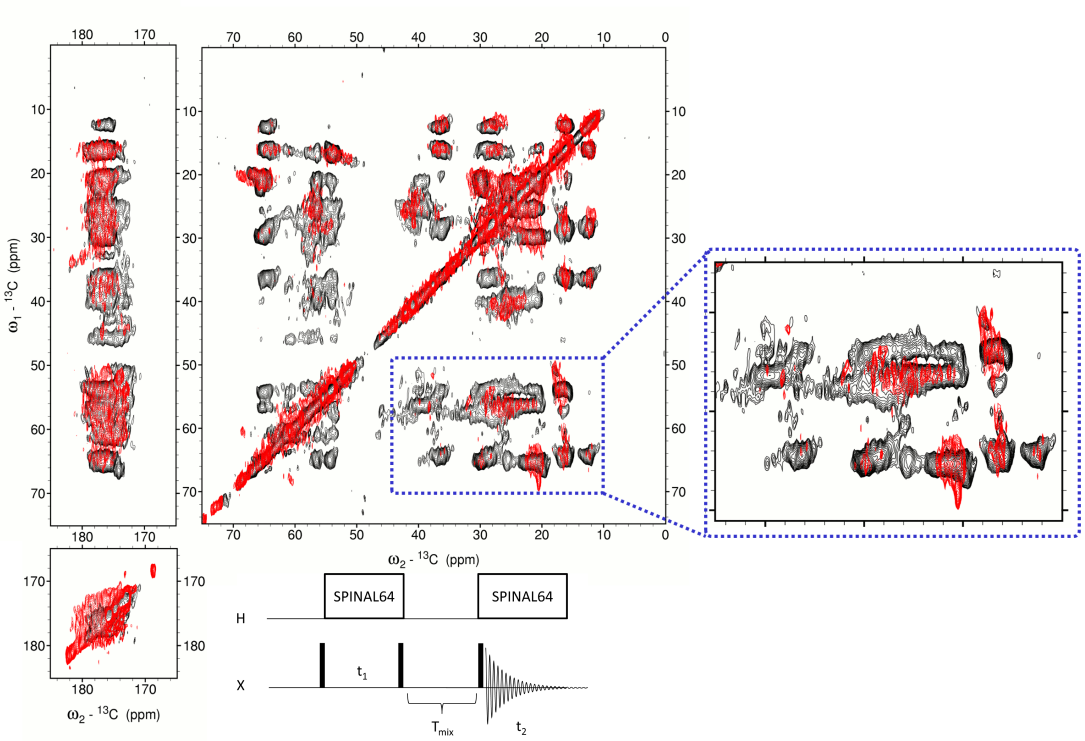

Figure 8.10: A cross polarized $^{13}C - ^{13}C$ PDSD spectrum of DGK compared to direct polarized PDSD. Spectra are shown for 100ms mixing time at 233K (black, CP spectrum) and 100ms mixing time at 288K (red, DP spectrum). The spectra where recorded using 10 kHz MAS, 128 scans per increment, 384 increments in the indirect dimension. From comparison of the spectra, it is apparent, that the line width is reduced at higher temperature, with a severe cost of sensitivity, leading to the loss of several groups of cross peaks. For better comparison, the $C\alpha - Sidechain$ crosspeak region of the spectrum has been zoomed in on the right. The PDSD pulse sequence used for the red spectrum recorded at 288K is shown as an inset. Here, the CP polarization enhancement was replaced by a 90° pulse on ^{13}C to increase the tolerance of the experiment to sample dynamics. The black spectrum was recorded with the sequence shown in Fig. 8.9.

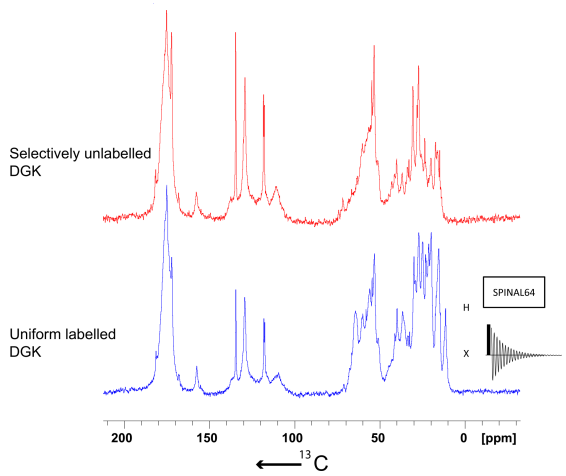

Figure 8.11: 1D DP spectra of reconstituted DGK, with and without selective unlabeling of the amino acids isoleucine and valine, as indicated in the figure. Both spectra were recorded at 273K, 10 kHz MAS and processed with 20Hz exponential line broadening. The blue spectrum was recorded with 256 and the red spectrum with 128 scans. The red spectrum was scaled to the same carbonyl intensity for better comparison, by a factor of 0.47. This is necessary due to differences in the receiver gain used for the two spectra. The success of selective unlabeling can be seen from the absence of the isoleucine $C\delta$ resonance at 11ppm. The DP pulse sequence employed, is shown to the right of the spectrum.

selective unlabeling have been used.

Using this approach, a sample was prepared in which isoleucine and valine have been selectively unlabeled. One dimensional spectra of these samples are shown in Fig. 8.11, where a fully labeled sample is compared to a selectively unlabeled sample. The success of the unlabeling is most easily seen by the absence of the isoleucine Cδ resonance at 11ppm.

A two dimensional spectrum of the selectively unlabeled sample is shown in Fig. 8.12. From the overlay of this spectrum, shown in red, with one recorded without selective unlabeling (black) at 233K and 100ms mixing time, it is apparent that several groups of cross peaks are missing from the spectra. Although this leads to an overall less complicated spectrum, the line widths of the remaining resonances are still too large to be resolved. Therefore it can be concluded that, although selective unlabeling helps with reducing the amount of detectable resonances, additional steps are required to arrive at a well resolved spectrum.

8.3.4 Through Bond Spectroscopy

Another approach to enhance the spectral resolution lies in spectroscopy at temperatures above 273K, as shown before. A drawback of this approach, using conventional solid state NMR techniques, is the partial averaging of the dipolar couplings, leading to an overall loss of sensitivity, especially for the cross peaks in PDSD spectra. One possible solution for this problem is the use of the isotropic J-coupling for $^{13}C-^{13}C$ correlation and for heteronuclear correlation of highly flexible residues of the protein.

Homonuclear correlation spectra of selectively unlabeled DGK have been recorded using the TOBSY sequence, introduced by Baldus and Meier [34, 160, 161] as shown in Fig. 8.13. A 90° pulse has been used for excitation instead of CP, as preselection

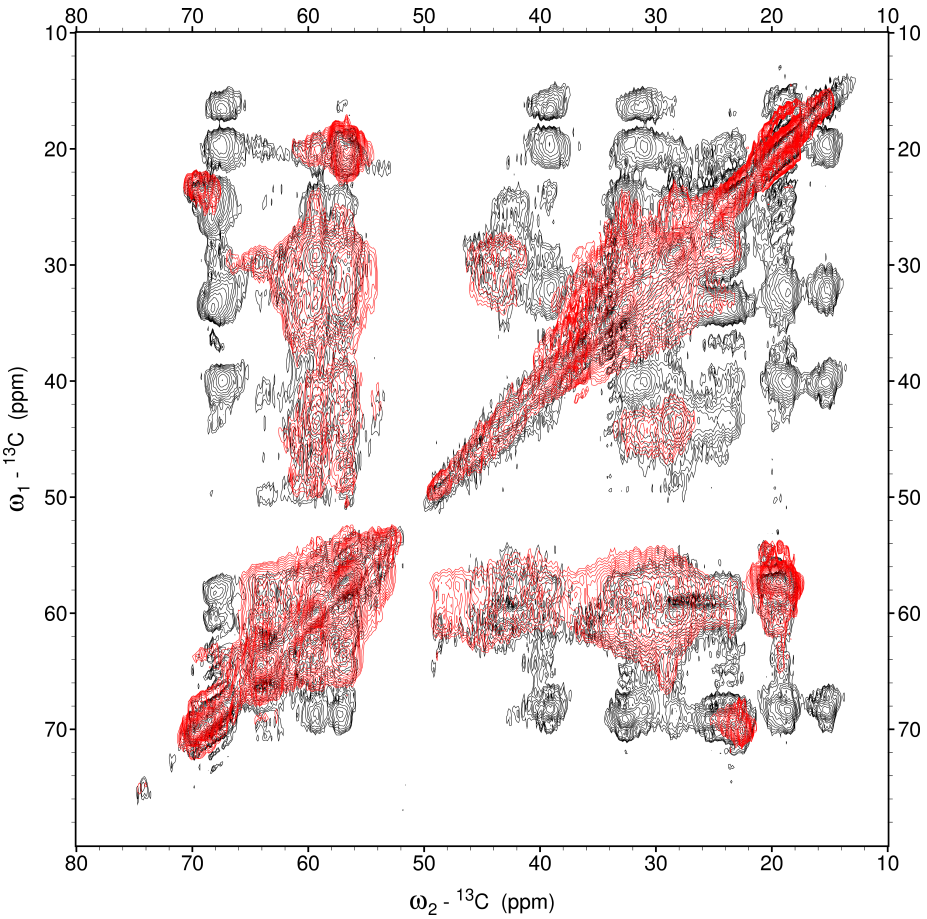

Figure 8.12: Proton driven spin diffusion spectra of fully labeled (black) and selectively unlabeled (red) DGK. Both spectra were recorded with a mixing time of 100ms, 10kHz MAS, 128 scans per increment, 384 increments in the indirect dimension at 233K. The red spectrum was processed with exponential line broadening (20Hz in the direct dimension, 50Hz in the indirect dimension) and the black spectrum Gaussian window multiplication. A comparison of the spectra with each other and with Fig. 8.9 reveals the absence of cross peaks in several regions of the spectrum, by merit of selective unlabeling. Other regions retain their high spectral overlap, indicating that additional measures have to be employed to arrive at a well resolved two dimensional correlation spectrum.

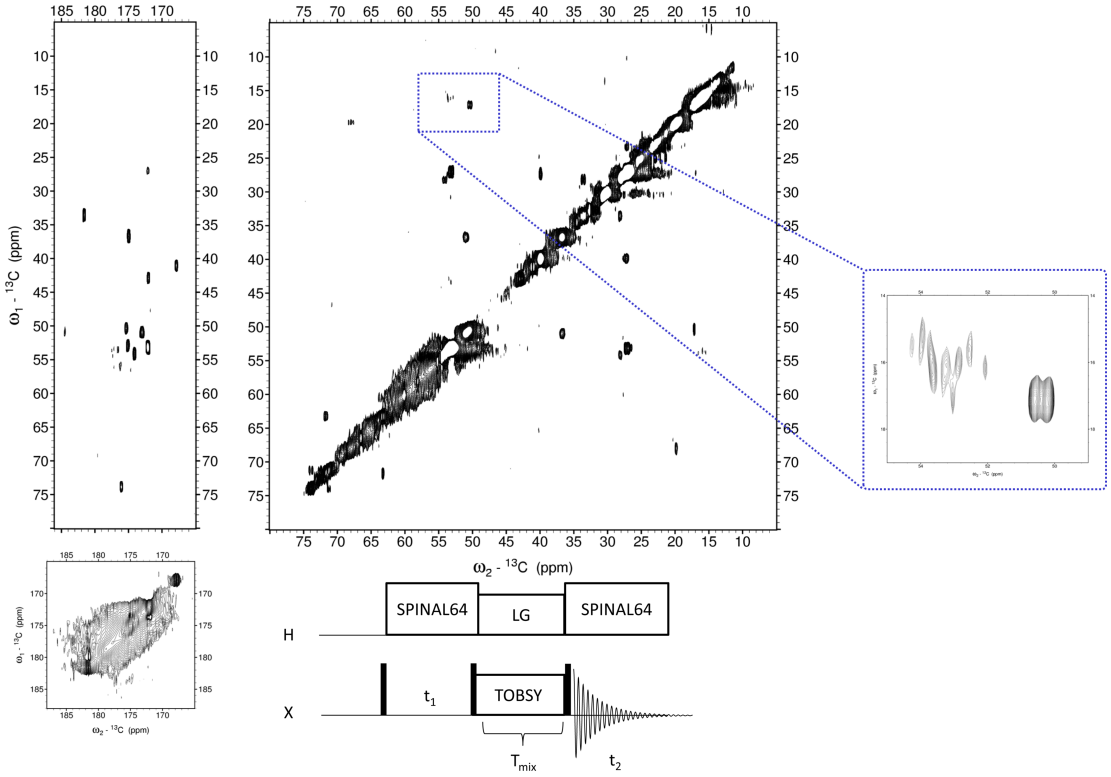

Figure 8.13: $^{13}C - ^{13}C$ correlation spectrum of DGK using TOBSY. A 90° pulse was used for excitation, as no preselection of dynamics was desired. The spectrum was recorded at 264K, using 10 kHz MAS, 320 scans per increment, 384 increments in the indirect dimension and a mixing time of 1,84ms. Although many resonances are absent from the spectra, the remaining resonances are well resolved. This is especially true for the alanine $C\alpha - C\beta$ resonances, shown to the right of the spectrum. The disappearance of so many resonances indicates a perturbation of the mixing sequence by relaxation, dynamics, or both. The TOBSY sequence used, employing a direct 90° pulse for resonance excitation on the ^{13}C channel, is shown below the spectrum.

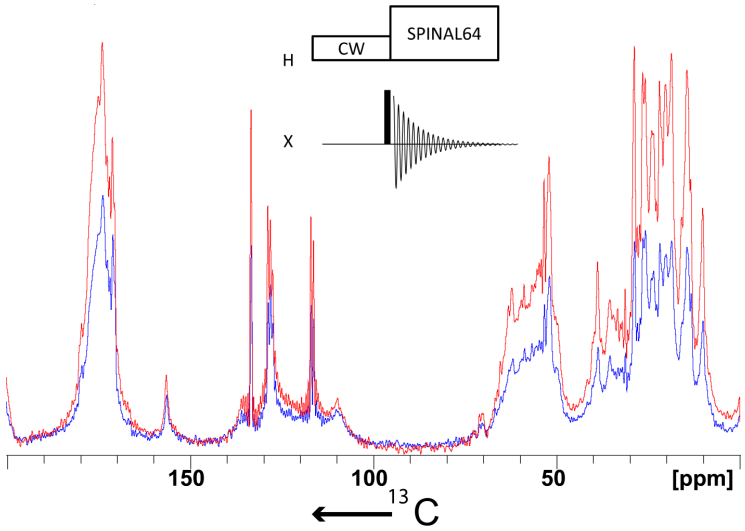

Figure 8.14: 1D spectra of reconstituted DGK with direct (blue) and hetNOE (red) excitation. Spectra were recorded with 32 scans, 10kHz MAS at 294K. An enhancement of approx. a factor of two was achieved for the hetNOE polarized spectrum, which was uniform for the broad and narrow resonances of the spectrum, indicating a motional insensitive polarization enhancement. The enhancement factor is consistent with the enhancement expected from the theory. The pulse sequence is shown as an inset above the spectra.

of dynamics was desired. Furthermore Lee-Goldburg [95] decoupling was used during the TOBSY transfer step. It is important to note that no frequency switching or phase modulation was employed for the LG decoupling, as this negatively influenced the TOBSY transfer.

In this spectrum it can be seen that, although many resonances are missing from the spectrum, the ones remaining are narrow and well resolved. This is especially true for the alanine $C\alpha - C\beta$ cross peaks, shown as an inset to the right of Fig. 8.13. The apparently higher sensitivity of these methyl group resonances could indicate a perturbation of the sequence during mixing by relaxation, dynamics on the NMR time scale, or both.

8.3.5 The Heteronuclear Overhauser Effect

As seen in the previous sections, ^{13}C spectra of non frozen samples show greatly enhanced line shapes and spectral resolution, but is often accompanied by a low overall sensitivity. This is mainly caused by the use of a single 90° pulse for resonance excitation. This excludes the benefits of ^{1}H polarization transfer and can lead to long measurement times. An alternative to this procedure is the use of polarization transfer schemes, that feature a reduced sensitivity with respect to motion.

The use of symmetry based polarization transfer schemes, with reduced sensitivity to motion and the heteronuclear Nuclear Overhauser Effect (hetNOE) were explored in this context [162–165]. The former will be detailed in section 8.3.7, and the effect of the latter is shown below in Fig. 8.14.

An enhancement of approx. a factor of two is seen, if the hetNOE is employed to polarize the spectrum. This factor did not change significantly for the broad and narrow resonances of the spectrum, indicating a motional insensitive polarization en-

hancement. The enhancement factor observed is consistent with the enhancement expected from theory.

As the hetNOE is easily implemented by adding a weak continuous wave irradiation during the recycle delay, all TOBSY spectra shown in the following were recorded with a modified pulse sequence, incorporating the hetNOE for polarization enhancement during preparation.

8.3.6 INEPT and HETCOR Spectra of DGK

INEPT [22] is an ideal complementary sequence to CP, as INEPT selects only highly mobile parts of the protein, whereas CP only polarizes immobile residues. INEPT spectroscopy has been used in solid state NMR before to selectively filter out highly dynamic moieties of membrane proteins [19].

Therefore, to further investigate the narrow resonances seen in Fig. 8.8 and to elucidate whether these stem from the protein or the lipids, DP and INEPT spectra were recorded on a Ile, Val selectively unlabeled DGK sample. These spectra, together with a reference spectrum of the reconstitution lipid DOPC are shown in Fig. 8.15.

Here it can be seen that some, but not all, of the narrow resonances stem from the protein, further corroborating the existence of highly flexible domains of DGK. These domains can be selected and studied via pulse sequences containing an INEPT step, greatly reducing the number of observable resonances, leading to a considerable simplification of the spectra.

To verify the results obtained so far, ^{15}N spectra of uniformly ^{15}N labeled DGK were recorded at 264K as shown in Fig. 8.16. Here, a picture similar to the one obtained with ^{13}C spectroscopy is observed. The DP spectra show a superposition of broad and narrow resonances in the backbone region between 100 and 120ppm, of which only the broad peaks are seen in the CP and the narrow lines appear in the INEPT. This indicates that for the residues observed with INEPT, the dynamics extend to the backbone of the protein.

As the INEPT sequence is known to be highly susceptible to residual dipolar coupling contributions, the appearance of resonances polarized with INEPT indicates a strong reduction of homo- and heteronuclear dipolar couplings through dynamics, for these residues. This could also cause narrow ^{1}H to be observable, which is normally not possible in solid state NMR, due to the strong broadening induced by the $^{1}H-^{1}H$ dipolar couplings.

To test this possibility, heteronuclear correlation (HETCOR) spectra of DGK were recorded, using INEPT as the polarization transfer step. These spectra are shown in Fig. 8.17 for a $^{1}H-^{13}C$ correlation and Fig. 8.18 for a $^{1}H-^{15}N$ correlation spectrum.

Both spectra feature nicely resolved ^{1}H, as well as $^{13}C/^{15}N$ resonances. The observation that addition of a ^{1}H evolution dimension does not eliminate the resonances from the spectrum further underlines the high degree of flexibility.

The clustering of resonances in the $^{1}H-^{15}N$ spectrum point to a random coil conformation of the observed residues. Although an assignment has not been conducted, these resonances most likely stem from the short loops, or the termini of the protein.

8.3.7 Application of R70 to DGK

Sample dynamics pose an intrinsic complication for classical homo- and heteronuclear transfer steps. PDSD is an example for the former, as it relies on homo-nuclear dipolar couplings to achieve mixing. These can be highly perturbed, if the sample shows dynamics beyond a certain degree, as was seen for the spectra shown in Fig. 8.10.

Hetero-nuclear transfer, on the other hand, is mostly done via cross polarization or INEPT transfer steps, for rigid and fluid systems, respectively. The efficiency of

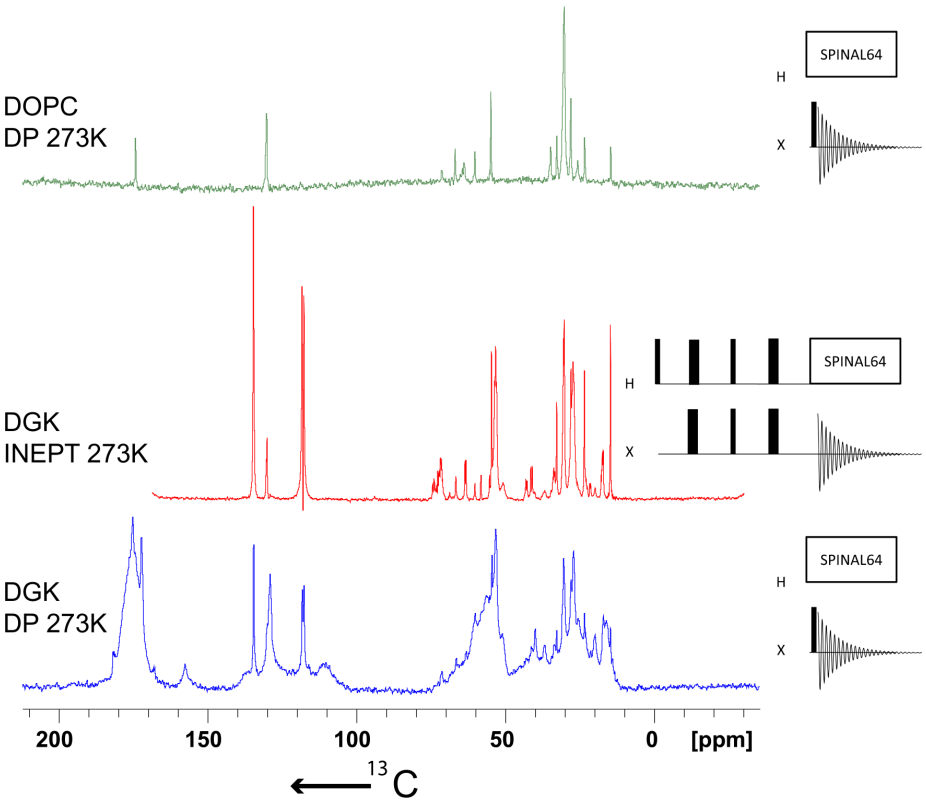

Figure 8.15: One dimensional spectra of Ile, Val selectively unlabeled DGK and the lipid DOPC. The spectra were recorded with 32, 2048 and 1024 scans for the blue, red and green spectra respectively, using 10kHz MAS at 273K in all cases. All spectra were processed with 20Hz exponential line broadening. Comparing the DP, INEPT and DOPC-DP reference spectra, it can be seen that some, but not all, of the narrow resonances stem from the lipid. This indicates the existence of highly flexible residues in the protein, that can be separated from the rest of the resonances via INEPT polarization transfer. For comparison the spectra have been scaled to the same height of the lipid chain resonances. This corresponds to a scaling factor of 0.214 and 0.3 for the red and green spectra, respectively. The sequences used, are depicted to the right of respective spectra.

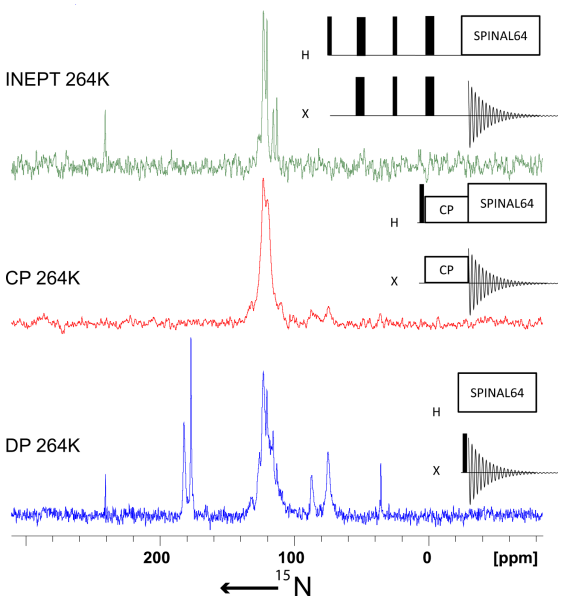

Figure 8.16: One dimensional ^{15}N spectra of uniformly $^{13}C-^{15}N$ labeled DGK. The spectra were recorded with 1024, 16 and 128 scans for the blue, red and green spectra respectively, using 8kHz MAS at 264K. The red spectrum was processed with 40Hz all other spectra with 20Hz exponential line broadening. Comparing the DP, CP and INEPT spectra, it can be seen that the narrow resonances that appear in the DP spectrum are selected in the INEPT spectrum, whereas the broad peaks appear in the CP spectrum. For comparison the spectra have been scaled to the same height. This corresponds to a scaling factor of 12 and 8 for the red and green spectra, respectively. The sequences used are depicted to the right of the respective spectra.

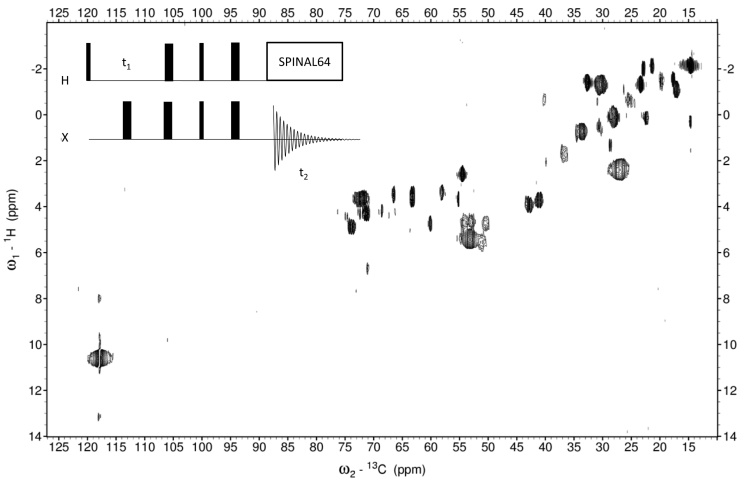

Figure 8.17: $^{1}H-^{13}C$ correlation spectrum of Ile, Val selectively unlabeled DGK via $^{1}H-^{13}C$ HETCOR. The spectrum was recorded with 192 scans in the direct dimension, 192 increments in the indirect dimension with 10kHz MAS at 264K. The spectrum was processed with exponential line broadening of 5Hz in the direct dimension and qsine (sine bell shift 3) in the indirect dimension. The pulse sequence used is shown as an inset in the spectrum.

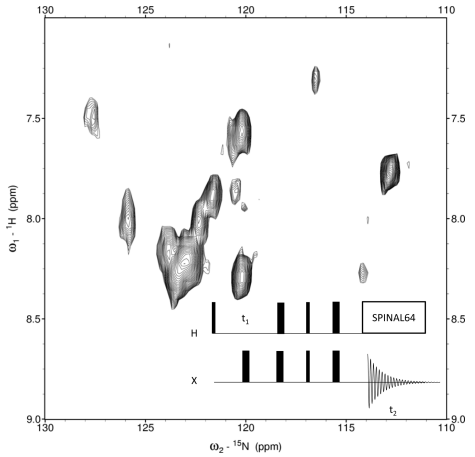

Figure 8.18: $^1H-^{15}N$ correlation spectrum of Ile, Val selectively unlabeled DGK via $^1H-^{15}N$ HETCOR. The spectrum was recorded with 192 scans in the direct dimension, 192 increments in the indirect dimension with 10kHz MAS at 264K. The spectrum was processed with exponential line broadening of 5Hz in the direct dimension and qsine (sine bell shift 4) in the indirect dimension. The pulse sequence used is shown as an inset in the spectrum.

both of these methods declines rapidly, if the dynamics of the sample is in between a rigid solid and an isotropic solution. CP, for instance, relies on the heteronuclear dipolar coupling to transfer magnetization between the nuclei and is perturbed by sample dynamics as seen in Fig. 8.8. INEPT, on the other hand, is susceptible to dipolar couplings during the transfer period, which lead to strong relaxation during free evolution.

Integral membrane proteins often feature both kinds of domains, rigid as well as solution like, in the form of transmembrane helices and flexible loops. Therefore methods, such as CP and INEPT, can be used as a filter to select certain regions of the protein, but cannot be employed to study the whole protein in a single experiment. This filtering characteristic can be appreciated in the spectra shown in Figs. 8.15 and 8.16.

The $R70_6^{16,16}$ sequence outlined in chapter 4 was designed to overcome these limitations, and to yield a more uniform excitation profile, with respect to motion. Two dimensional $^1H-^{13}C$ correlation spectra, with INEPT, R70 or CP as the heteronuclear transfer step, were recorded of DGK reconstituted into 80:20 DOPC/DOPG (mol/mol), as shown in Fig. 8.19.

Here, it can be seen that no phase errors or artifacts are introduced into the spectrum for R70 based heteronuclear correlation. A striking feature of the R70 spectra of DGK are the resonances in the carbonyl region. These originate from polarization relayed through the homo-nuclear $C\alpha-CO$ J-couplings in the fully ^{13}C labeled protein, a magnetization transfer pathway, which does not occur in the INEPT or CP spectra. This can simplify the identification of genuine protein resonances in the $C\alpha$ region in the presence of a lipid mixture, as the unlabeled lipids will generally not show transfer to their carbonyl groups, in contrast to the labeled protein.

It has to be noted, that no homo-nuclear decoupling was applied during the ^1H chemical shift evolution, which biases the observation towards mobile residues. This is most likely the cause for the limited amount of resonances observable in the spectra, where CP or R70 were used for polarization transfer. It is expected that more resonances appear upon incorporation of homo-nuclear ^1H decoupling during chemical

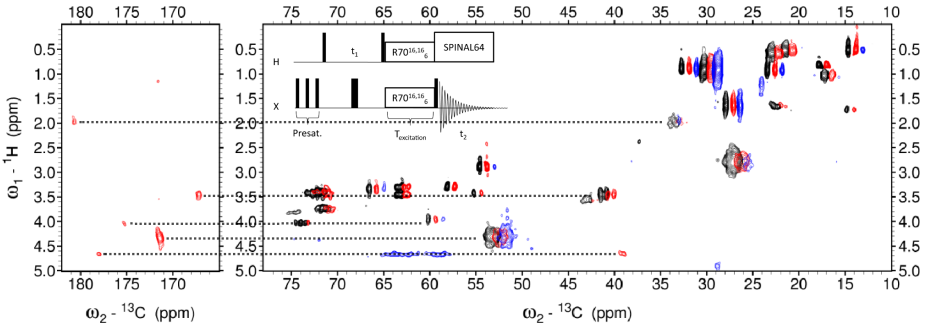

Figure 8.19: 2D ^{1}H-^{13}C heteronuclear correlation spectra of reconstituted DGK recorded at 277K and 5kHz MAS. The heteronuclear transfer step was INEPT for the black spectrum, $R70_6^{16,16}$ for the red and CP for the blue spectrum (the red and blue spectra have been offset by -0.8ppm and -1.6ppm, respectively). The spectra are similar, with exception of the carbonyl region, where $R70_6^{16,16}$ shows relayed transfer. This is due to homonuclear J-transfer active during mixing, leading to a relay of magnetization for the uniformly ^{13}C labeled protein. The pulse sequence employed is shown as an inset in the upper left corner of the spectrum. Protein peak pairs, created by relayed transfer, are indicated with black dotted lines.

shift evolution.

8.3.8 The Effect of Lipid Composition

In addition to spectroscopic techniques, sample preparation can have a tremendous influence on the quality of NMR spectra of a protein. To elucidate if the dynamics of the protein can be reduced via biochemical methods, using a different lipid composition, a sample was reconstituted into a lipid mixture of 80%DOPC and 20%DOPG. This mixture was chosen, as it has been reported that anionic lipids, such as DOPG, act as strong lipid activators of DGK in detergent micelles [137, 138]. The anionic lipid might stabilize a certain conformation and thus reduce the dynamics seen for non frozen samples of DGK.

The activity of the sample reconstituted into the lipid mixture was not significantly different from the previously measured activities, using a single lipid for reconstitution.

Though the activity was not higher than for the single lipid reconstituted samples, it was still in the range for a fully active preparation, and thus the sample was deemed suitable for NMR investigation. The activity trace for this sample is shown in Fig. 8.7.

The spectra of two samples, one with 100% DOPC and the other with 80:20 DOPC/DOPG (mol/mol) are shown in Fig. 8.20.

For the one dimensional spectra, no significant difference is apparent from the line shape of the resonances.

To further characterize this sample, a TOBSY spectrum has been recorded, as shown in Fig. 8.21. Although the resolution and sensitivity of the spectrum are good, no major improvement of the line shape or change in the dynamics and relaxation behavior of the sample could be observed. This indicates that, although anionic lipids such as DOPG act as an activator of enzymatic function of DGK in detergent, the dynamics of the reconstituted protein at room temperature are not significantly changed in presence of the lipid. Also, no significant peak shifts could be seen for the observed resonances. Whether this indicates no major changes in the protein structure, upon binding different lipids, or if the change takes place for residues not detected with the current set of experiments, remains to be seen.

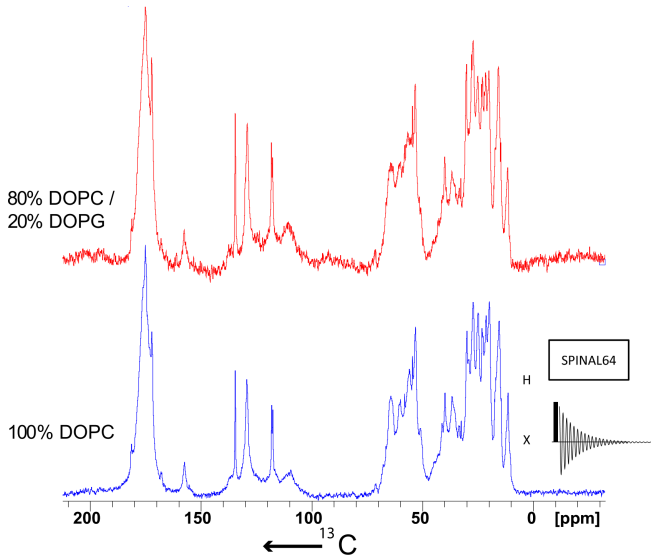

Figure 8.20: 1D spectra of DGK reconstituted in 1:50 mol/mol into the lipid mixture indicated next to the spectra. The blue spectrum was recorded with 256 scans, 10kHz MAS at 273K. The red spectrum was recorded with 8 scans, 11kHz MAS at 275K. Both spectra were processed with an exponential line broadening of 20Hz. From these spectra no obvious difference in the line shape is apparent, with the addition of 20% DOPG to the reconstitution lipid mixture. For better comparison the red spectrum was scaled to the same intensity for the carbonyl resonances (a factor of 5.2)

8.3.9 The Effect of Deuteration on DGK spectra

To explore, whether the losses observed during the correlation experiments are due to incomplete heteronuclear decoupling, a perdeuterated sample was prepared, as described in Section 8.2.4. DP spectra of protonated and deuterated DGK samples are shown in Fig. 8.22. As the yield of the $U-^{2}H-^{13}C-^{15}N$ labeled protein preparation was low (see Section 8.2.2) and no polarization enhancement from ^{1}H could be used, the sensitivity of the spectra is limited. Nevertheless a peak narrowing effect of the perdeuteration could be observed. It is worth noting, that the stronger relative contribution of the lipid resonances in the spectra stems from an increase of the reconstitution protein:lipid ratio from 1:50 to 1:120 (for details see Section 8.2.4).

The line narrowing effect can be seen more clearly in the two dimensional TOBSY spectrum shown in Fig. 8.23. Due to the low sensitivity of the measurement, the DTD method described in chapter 7, was applied to the spectrum. It is interesting to note that no additional (or missing) resonances can be seen for the $^{2}H-^{13}C-^{15}N$ labeled sample, as compared to $^{1}H-^{13}C-^{15}N$ DGK, while the line widths observed are reduced by approx. 20%. Changing the decoupler power during TOBSY mixing had no significant effect on the sensitivity of the spectra, as is to be expected from a perdeuterated sample (data not shown).

This suggests that relaxation is not the primary factor which causes the absence of resonances from the TOBSY spectra, but rather motions on the NMR timescale (μs-ms) which perturb the sequence during mixing.

It has to be noted that the chemical shifts observed for the $C\alpha$ and $C\beta$ resonances in the spectrum of ^{2}H labeled DGK were shifted by approx. 0.4ppm and 1ppm, respectively. Although an effect of the ^{2}H labeling on the reconstitution cannot be excluded with the present data, these shifts are indicative of an $^{1}\Delta^{13}C-\alpha(D)$ isotope

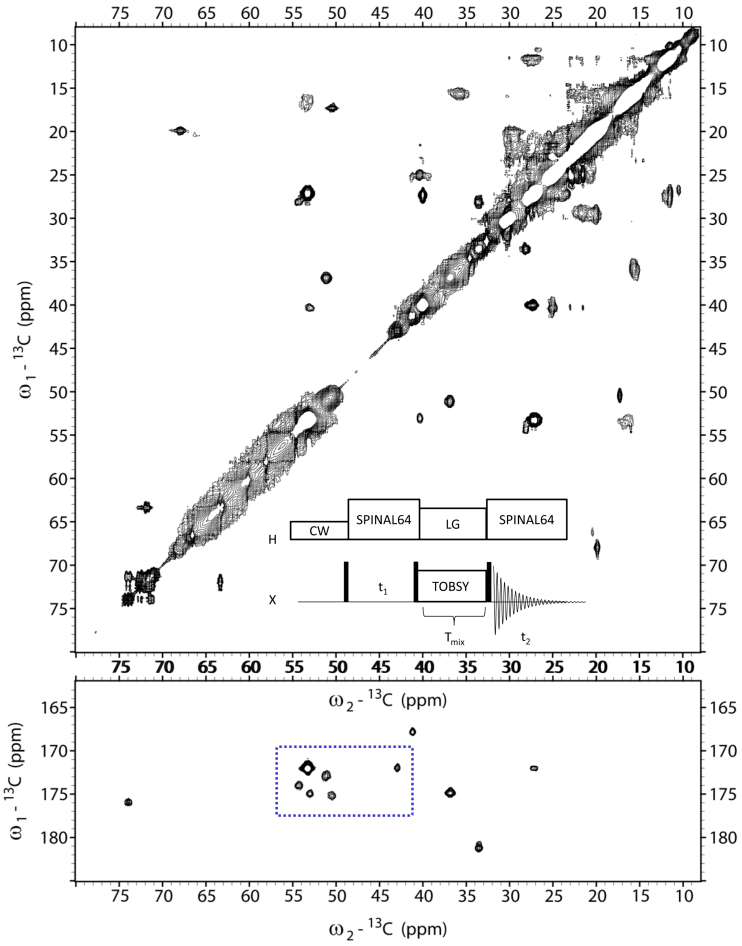

Figure 8.21: $^{13}C-^{13}C$ TOBSY spectrum of uniform ^{13}C labeled DGK, reconstituted at 1:50 protein to lipid molar ratio into 80%DOPC/20%DOPG. The spectrum was recorded at 264K, 10kHz MAS, 320 scans per increment, 384 increments along t1 and a mixing time of 1,84ms. Comparison of this spectrum with Fig. 8.13, indicates no obvious changes in the line shape, dynamics or relaxation parameters upon addition of 20%DOPG to the reconstitution lipid mixture. The TOBSY sequence modified to make use of the heteronuclear Overhauser effect is shown as an inset.

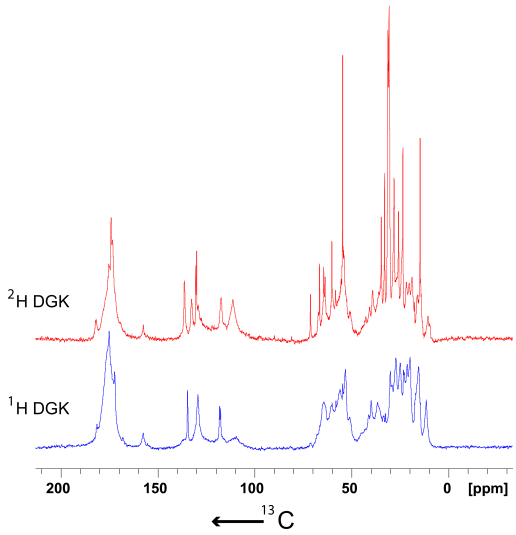

Figure 8.22: One dimensional DP spectra of uniformly $^{1}H-^{13}C-^{15}N$ labeled DGK (blue) and $^{2}H-^{13}C-^{15}N$ labeled DGK (red). The spectra were recorded with 256 and 1834 scans per increment, respectively, using 10kHz MAS at 273K for the blue and 270K for the red spectrum. Both spectra were processed with 20Hz exponential line broadening. The relatively stronger contribution of the lipid resonances to the red spectrum is caused by the protein to lipid ratio used for reconstitution (1:120 mol/mol)(see section 8.2.4)

effect, as reported in [166]. This would be consistent with the observation that most narrow resonances presumably stem from unstructured loop or terminal regions of the protein, which should only be lightly influenced by slight changes in the proteins overall fold.

To show the line narrowing effect of deuteration on the spectra more clearly, the $CO-C\alpha$ cross peak region of the TOBSY spectra shown in Fig. 8.21, and Fig. 8.23, have been overlayed and are shown in Fig.8.24. The exact region in the spectrum is indicated in Fig. 8.21 and Fig. 8.23 with blue boxes.

To investigate the dynamics of the protein further, ^{2}H static quadrupole echo experiments were recorded for the $^{2}H-^{13}C-^{15}N$ labeled DGK sample at 230 and 278K. These spectra are shown in Fig. 8.25.

When comparing the spectra, the appearance of an narrow isotropic peak at 278K and a scaling of the CD_3 group resonances by 4kHz are the most prominent features distinguishing the spectra recorded at 230 and 278K. This suggest a high molecular flexibility at higher temperatures.

Integration of both spectra, yields an increase of 130% in overall signal intensity from 230 to 278K. From the Boltzmann distribution an increase of only about 30% is expected. This indicates dynamics, that interfere with the refocusing during the time of the quadrupole echo (100 μs).

These results, together with the experiments shown before, imply strong dynamics of at least parts of the protein, on the NMR timescale (μs-ms).

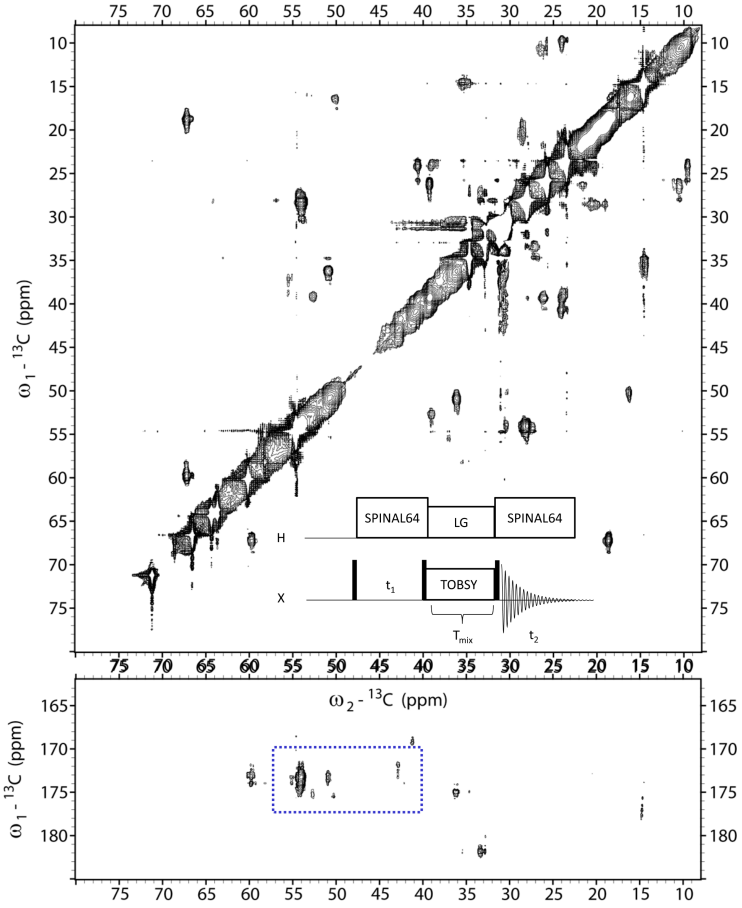

Figure 8.23: TOBSY $^{13}C-^{13}C$ correlation spectrum, of a $^{2}H-^{13}C$ DGK sample, reconstituted into 1:120 mol/mol DOPC. The spectrum was recorded with 10kHz MAS, at 270K, with 2048 scans per increment and 140 increments in the indirect dimension. The spectrum has been processed using dual transformation denoising (see chapter 7).

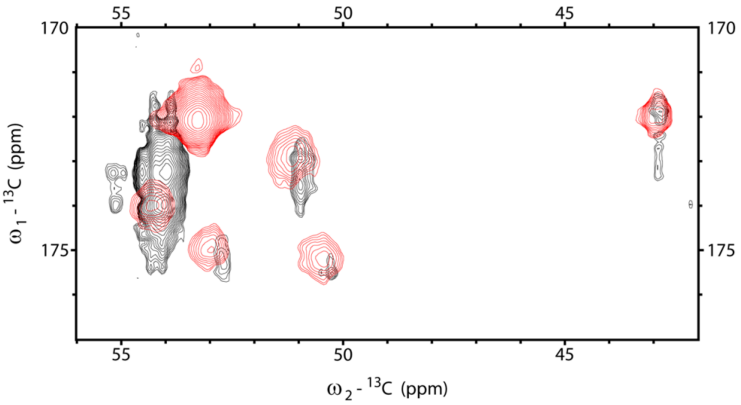

Figure 8.24: Overlay of the $CO-C\alpha$ crosspeak region of the spectra shown in Figs. 8.21 and 8.23, indicated with blue boxes in these figures.

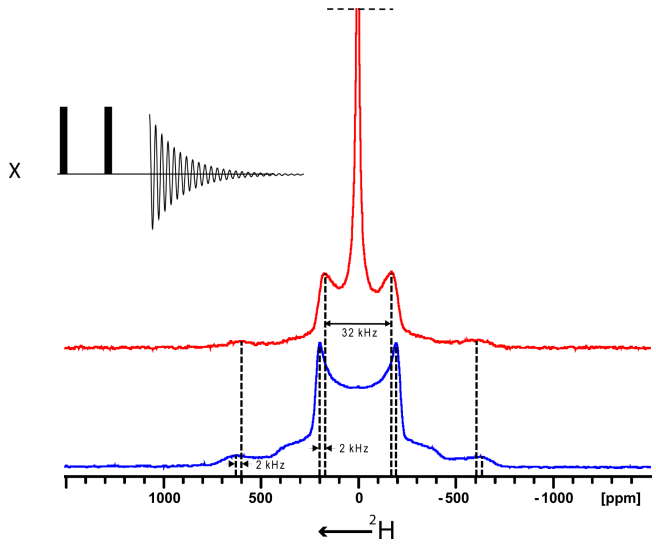

Figure 8.25: Comparison of static quadrupole echo experiments, with an echo time of 100μs, measured at 230K and 278K, for the blue and red spectra, respectively. Both spectra were recorded with 150k scans and a recycle delay of 0.5s. Comparison of the spectra shows a strong isotropic line at 278K as compared to 230K, as well as a reduction of the line width of the CD_3 powder pattern by 4kHz, suggesting strong dynamics of domains of the protein at higher temperatures. The 90-τ-90-τ-acq quadrupole echo sequence which was employed, is shown to the left of the spectra.

8.4 Conclusion

Diacylglycerol kinase is a protein that can be expressed in large quantities and reconstituted into lipid membranes. It has been thoroughly studied with a variety of methods and thus a plethora of biochemical, as well as NMR data is available.

This makes it ideally suited to elucidate the effect of sample preparation, labeling and experimental schemes on the spectra of integral membrane proteins investigated with solid state NMR.

Of particular interest are the dynamics of the protein, when the sample is studied at temperatures above 273K. These dynamics shed light on the broad resonances observed for frozen samples, as multiple similar conformations seem to coexist for the protein in its native state. Therefore it is advantageous to study the protein in a semi-solid state.

Nevertheless dynamics perturb most transfer schemes which are commonly used in solid state NMR. To overcome these problems, several different pulse sequences were tested, to investigate the influence of motion on the spectra of different residues of the protein.

It was found, that for samples with a high degree of dynamics, the heteronuclear Overhauser effect is the most reliable polarization transfer scheme for enhancing ^{13}C polarization. The TOBSY sequence was found to be effective for through bond homonuclear correlation experiments, as PDSD type schemes suffered from the scaling of the dipolar couplings, resulting in a sharply reduced sensitivity of the spectrum.

Still many resonances could not be observed, even employing schemes such as TOBSY. This, together with the results obtained from ^{2}H labeling of the protein, implies motion of the protein that results in an interference of the intrinsic dynamics with radio frequency irradiation, magic angle spinning or both.

These dynamics could not be significantly reduced upon modification of the lipid environment of the sample. Different sample preparation techniques, which might help to obtain a single conformation of the protein at temperatures where the dynamics are significantly reduced, could possibly present a solution to this problem. Although approaches like crystallization or controlled, slow freezing, have been attempted in the past [167], these studies have so far not yielded a significantly enhanced line shape of solid state NMR spectra of DGK.

Appendix A

Inversion Recoveries

Results of the selective and unselective inversion recovery experiments. Here the T_1 times for the selective inversion recovery experiments (sIR) are given, in which only a certain region of the spectrum is inverted, and the return of the magnetization to the positive z-axis is observed. For comparison, the T_1 times for the same resonance for the unselective inversion recovery (IR) are given in the next column. The final magnetization for the sIR experient is given in the column labelled $T_{max(sIR)}$, with the time needed for the magnetization in the unselective IR experiment to reach the same value given in $T_{max(IR)}$. The ratio of these times is given in the last column, yielding a measure of the enhancement in relaxation. This table is adapted from the diploma thesis of S. Asami [65].

Inverted Region	Observed Nucleus	Type	$T_{1(sIR)}$ [s]	$T_{1(IR)}$ [s]	$M_z(T_{max})$	$T_{max(sIR)}$ [s]	$T_{max(IR)}$ [s]	$\frac{T_{max(IR)}}{T_{max(sIR)}}$
C_α	C_α	F	0.0062 ± 0.0002	1.52 ± 0.06	0.41	0.05	2.41	48.2
C_α	C_α	L	0.0061 ± 0.0003	1.14 ± 0.07	0.48	0.05	2.53	50.5
C_α	C_α	M	0.0072 ± 0.0003	0.93 ± 0.06	0.38	0.05	1.86	37.3
C_α + C_β	C_α	F	0.0047 ± 0.0005	1.52 ± 0.06	-0.04	0.05	1.08	21.7
C_α + C_β	C_α	L	0.0095 ± 0.0007	1.14 ± 0.07	0.17	0.05	1.28	25.7
C_α + C_β	C_α	M	0.0120 ± 0.0005	0.93 ± 0.06	-0.00	0.05	0.84	16.8
C_α + C_β	C_β	L	0.0059 ± 0.0003	1.07 ± 0.07	0.21	0.05	1.29	25.8
C_α + C_β	C_β	M	0.0084 ± 0.0003	1.40 ± 0.06	0.06	0.05	1.22	24.3
C_α + C_β + C_R	C_α	F	0.0084 ± 0.0008	1.52 ± 0.06	-0.30	0.05	0.64	12.8
C_α + C_β + C_R	C_α	M	0.0023 ± 0.0006	0.93 ± 0.06	-0.43	0.05	0.31	6.2
C_α + C_β + C_R	C_β	L	0.0233 ± 0.0029	1.07 ± 0.07	-0.39	0.05	0.36	7.2
C_α + C_β + C_R	C_β	M	0.0115 ± 0.0008	1.40 ± 0.06	-0.20	0.05	0.74	14.9
C_α + C_β + C_R	C_δ	L	0.0015 ± 0.0003	0.77 ± 0.07	-0.22	0.05	0.40	8.1
C_α + C_β + C_R	C_γ	L	0.0219	0.85	-0.21	0.05	0.46	9.2

			± 0.0054	± 0.07				
$C_\alpha + C_\beta + C_R$	C_γ	M	0.0441 ± 0.0070	0.79 ± 0.07	-0.29	0.05	0.39	7.8
$C_\alpha + C_R$	C_α	F	0.0032 ± 0.0001	1.52 ± 0.06	0.25	0.05	1.78	35.7
$C_\alpha + C_R$	C_α	M	0.0034 ± 0.0001	0.93 ± 0.06	0.08	0.05	0.97	19.5
$C_\alpha + C_R$	C_δ	L	0.0336 ± 0.0034	0.77 ± 0.07	-0.25	0.05	0.38	7.6
$C_\alpha + C_R$	C_γ	L	0.0186 ± 0.0019	0.85 ± 0.07	-0.22	0.05	0.45	8.9
$C_\alpha + C_R$	C_γ	M	0.0092 ± 0.0008	0.79 ± 0.07	-0.00	0.05	0.73	14.7
C_β	C_β	L	0.0047 ± 0.0002	1.07 ± 0.07	0.75	0.05	2.91	58.2
C_β	C_β	M	0.0057 ± 0.0002	1.40 ± 0.06	0.43	0.05	2.34	46.8
$C_\beta + C_R$	C_β	L	0.0020 ± 0.0001	1.07 ± 0.07	-0.27	0.05	0.49	9.8
$C_\beta + C_R$	C_β	M	0.0055 ± 0.0002	1.40 ± 0.06	0.05	0.05	1.18	23.6
$C_\beta + C_R$	C_δ	L	0.0522 ± 0.0091	0.77 ± 0.07	-0.32	0.05	0.32	6.4
$C_\beta + C_R$	C_γ	L	0.0421 ± 0.0047	0.85 ± 0.07	-0.31	0.05	0.35	7.1
$C_\beta + C_R$	C_γ	M	0.0261 ± 0.0010	0.79 ± 0.07	-0.13	0.05	0.56	11.2
C'	C'	L	0.0116 ± 0.0005	1.68 ± 0.04	0.77	0.05	2.26	45.3
C'	C'	M	0.0114 ± 0.0003	1.27 ± 0.06	0.76	0.05	5.88	117.7
$C' + C_\alpha$	C_α	F	0.0129 ± 0.0011	1.52 ± 0.06	-0.03	0.05	1.11	22.2
$C' + C_\alpha$	C_α	L	0.0099 ± 0.0007	1.14 ± 0.07	0.25	0.05	1.49	29.7
$C' + C_\alpha$	C_α	M	0.0104 ± 0.0005	0.93 ± 0.06	0.14	0.05	1.11	22.2
$C' + C_\alpha$	C'	F	0.0256 ± 0.0011	1.52 ± 0.04	0.21	0.05	1.36	27.1
$C' + C_\alpha$	C'	L	0.0298 ± 0.0022	1.68 ± 0.04	0.38	0.05	1.49	29.8
$C' + C_\alpha$	C'	M	0.0248 ± 0.0010	1.27 ± 0.06	0.18	0.05	1.31	26.2
$C' + C_\alpha + C_\beta$	C_α	L	0.0158 ± 0.0017	1.14 ± 0.07	0.06	0.05	1.05	20.9
$C' + C_\alpha + C_\beta$	C_α	M	0.0260 ± 0.0027	0.93 ± 0.06	-0.17	0.05	0.59	11.8
$C' + C_\alpha + C_\beta$	C_β	L	0.0061 ± 0.0004	1.07 ± 0.07	0.16	0.05	1.16	23.2
$C' + C_\alpha + C_\beta$	C_β	M	0.0092 ± 0.0007	1.40 ± 0.06	-0.14	0.05	0.84	16.8
$C' + C_\alpha + C_\beta$	C'	F	0.0877 ± 0.0206	1.52 ± 0.04	-0.19	0.05	0.73	14.7
$C' + C_\alpha + C_\beta$	C'	L	0.0600 ± 0.0104	1.68 ± 0.04	-0.03	0.05	0.94	18.7
$C' + C_\alpha + C_\beta$	C'	M	0.1620 ± 0.0823	1.27 ± 0.06	-0.25	0.05	0.58	11.6
$C' + C_\alpha + C_\beta + C_R$	C_β	M	0.0180	1.40	-0.43	0.05	0.42	8.5

			± 0.0025	± 0.06				
$C' + C_\alpha + C_\beta + C_R$	C_δ	L	0.0007	0.77	-0.04	0.05	0.60	11.9
			± 0.0001	± 0.07				
$C' + C_\alpha + C_\beta + C_R$	C_ϵ	M	0.0006	1.25	0.23	0.05	1.35	26.9
			± 0.0003	± 0.04				
$C' + C_\alpha + C_\beta + C_R$	C_γ	L	0.0117	0.85	-0.22	0.05	0.45	9.0
			± 0.0029	± 0.07				
$C' + C_\alpha + C_\beta + C_R$	C_γ	M	0.0252	0.79	-0.36	0.05	0.32	6.5
			± 0.0034	± 0.07				
$C' + C_\alpha + C_R$	C_α	F	0.0037	1.52	-0.17	0.05	0.85	17.0
			± 0.0003	± 0.06				
$C' + C_\alpha + C_R$	C_α	L	0.0017	1.14	-1.09	0.05	-0.20	-4.0
			± 0.0001	± 0.07				
$C' + C_\alpha + C_R$	C_α	M	0.0031	0.93	-0.24	0.05	0.51	10.2
			± 0.0002	± 0.06				
$C' + C_\alpha + C_R$	C_δ	L	0.0334	0.77	-0.39	0.05	0.26	5.2
			± 0.0047	± 0.07				
$C' + C_\alpha + C_R$	C_γ	L	0.0163	0.85	-0.38	0.05	0.30	5.9
			± 0.0019	± 0.07				
$C' + C_\alpha + C_R$	C_γ	M	0.0067	0.79	-0.17	0.05	0.51	10.2
			± 0.0007	± 0.07				
$C' + C_\alpha + C_R$	C'	F	0.0261	1.52	-0.51	0.05	0.38	7.6
			± 0.0030	± 0.04				
$C' + C_\alpha + C_R$	C'	L	0.0469	1.68	-0.70	0.05	0.30	6.0
			± 0.0313	± 0.04				
$C' + C_\alpha + C_R$	C'	M	0.0264	1.27	-0.48	0.05	0.32	6.4
			± 0.0033	± 0.06				
$C' + C_\beta$	C_β	L	0.0041	1.07	0.59	0.05	3.33	66.7
			± 0.0002	± 0.07				
$C' + C_\beta$	C_β	M	0.0054	1.40	0.24	0.05	1.66	33.2
			± 0.0002	± 0.06				
$C' + C_\beta$	C'	F	0.0119	1.52	0.39	0.05	1.73	34.7
			± 0.0009	± 0.04				
$C' + C_\beta$	C'	L	0.0114	1.68	0.51	0.05	1.72	34.5
			± 0.0009	± 0.04				
$C' + C_\beta$	C'	M	0.0133	1.27	0.38	0.05	1.84	36.7
			± 0.0009	± 0.06				
$C' + C_\beta + C_R$	C_β	L	0.0024	1.07	-0.55	0.05	0.21	4.1
			± 0.0003	± 0.07				
$C' + C_\beta + C_R$	C_β	M	0.0055	1.40	-0.24	0.05	0.69	13.7
			± 0.0003	± 0.06				
$C' + C_\beta + C_R$	C_δ	L	0.0473	0.77	-0.42	0.05	0.24	4.8
			± 0.0065	± 0.07				
$C' + C_\beta + C_R$	C_γ	L	0.0353	0.85	-0.42	0.05	0.26	5.3
			± 0.0035	± 0.07				
$C' + C_\beta + C_R$	C_γ	M	0.0250	0.79	-0.32	0.05	0.36	7.2
			± 0.0019	± 0.07				
$C' + C_\beta + C_R$	C'	F	0.0026	1.52	-1.21	0.05	-0.19	-3.7
			± 0.0002	± 0.04				
$C' + C_\beta + C_R$	C'	M	0.0026	1.27	-1.13	0.05	-0.22	-4.4
			± 0.0001	± 0.06				
$C' + C_R$	C_δ	L	0.0321	0.77	-0.20	0.05	0.43	8.5
			± 0.0030	± 0.07				
$C' + C_R$	C_γ	L	0.0166	0.85	-0.18	0.05	0.50	9.9
			± 0.0012	± 0.07				

$C' + C_R$	C_γ	M	0.0092 ± 0.0006	0.79 ± 0.07	0.08	0.05	0.86	17.1
$C' + C_R$	C'	F	0.0049 ± 0.0001	1.52 ± 0.04	0.30	0.05	1.53	30.5
$C' + C_R$	C'	L	0.0037 ± 0.0003	1.68 ± 0.04	0.70	0.05	2.11	42.1
$C' + C_R$	C'	M	0.0051 ± 0.0002	1.27 ± 0.06	0.33	0.05	1.68	33.6
C_R	C_δ	L	0.0335 ± 0.0034	0.77 ± 0.07	-0.07	0.05	0.56	11.1
C_R	C_γ	L	0.0187 ± 0.0013	0.85 ± 0.07	-0.04	0.05	0.66	13.3
C_R	C_γ	M	0.0117 ± 0.0008	0.79 ± 0.07	0.26	0.05	1.28	25.6

Appendix B

Pulse programs

B.1 1D CP

```
"p30=p31-0.4u"

#include <lgcalc.incl>
#include <trigg.incl>
#include <prp15.prot>

;#include <praq.prot>

1 ze

2
   2u fq=cnst21:f2
   d1
   2u do:f2


  (p3 pl3 ph1):f2

  0.3u

  (p15 pl11 ph2):f1 (p15:spf0 pl22 ph10):f2

  (p1 pl1 ph3):f1

  1u pl12:f2
  2u cpds2:f2 ;cpds=cw or tppm15: pl12
  go=2 ph31  ;cpds=cwlgs       : pl13

  1m do:f2
  wr #0
HaltAcqu, 1m
exit

ph0= 0
ph1= 1 3
ph2= 0 0 2 2 1 1 3 3
ph3= 1 1 3 3 2 2 0 0
ph10= 0
ph31= 0 2 2 0 1 3 3 1
```

B.2 2D PDSD

```
"d31=1s/cnst31"
"d0=2u"
```

```
"p30=p31-0.4u"

"in0=inf1/2"

  ze
1 1m

2 d1 do:f2

  1m
  10u reset:f1
  2u fq=cnst21:f2
  10u:f1 ph0
  10u:f2 ph0
  10u pl1:f1
  10u pl12:f2
  (p3 pl3 ph1):f2

  0.2u

  (p15 pl11 ph2):f1 (p15:spf0 pl22 ph10):f2

  (d0 cpds2 pl12):f2

  0.3u do:f2

  (p1 pl1 ph4):f1

  d2

  (p1 pl1 ph5):f1

  (3u cpds2 pl12):f2
  go=2 ph31
  1m do:f2
  100m wr #0 if #0 zd
  id0
  1m
  lo to 1 times td1
HaltAcqu, 1m
exit

ph0= 0
ph1= 1 3
ph2= 1
ph4= 0
ph5= 0 0 2 2 1 1 3 3
ph10=0
ph31=0 2 2 0 1 3 3 1
```

B.3 2D DP-TOBSY

```
"cnst21=0"
"cnst22=cnst20/sqrt(2)+cnst24"
"cnst23=-cnst20/sqrt(2)+cnst24"

"p5=((294/360)/(cnst20))*1e6"
"p6=p5-.4u"

define pulse tau4
"tau4=((1s/cnst31)/7)"
define pulse tau1
"tau1=((0.25s/cnst31)/7)"
define pulse tau3
"tau3=((0.75s/cnst31)/7)"
"d31=1s/cnst31"
"d0=2u"
"p30=p31-0.4u"

"p11=1s/(24*cnst31)"
```

```
  ze
1 1m

2 10u do:f2
  1m rpp11
  1m rpp12

  10u reset:f1
  2u fq=cnst21:f2
  10u:f1 ph0
  10u:f2 ph0

  (d1 cw pl20):f1

  (p1 pl1 ph1):f1

  (d0 cpds2 pl12):f2

  0.3u do:f2

 (0.3u cpds1 pl27):f2


  (p1 pl1 ph4):f1

  3u pl17:f1
3     p11*1:f1 ph7
      p11*4:f1 ph8 ipp8
      p11*3:f1 ph7 ipp7
   lo to 3 times l0

  (p1 pl1 ph5):f1

  0.3u do:f2

  (3u cpds2 pl12):f2
  go=2 ph31
  1m do:f2
  100m wr #0 if #0 zd
  1m ip1
  id0
  1m
  lo to 1 times td1
HaltAcqu, 1m
exit

ph0= 0
ph1= 0 2
;ph1= 1 3
ph2= 1
ph4= 0
ph5= 0 0 2 2 1 1 3 3
ph7 = (16384) 0     1820  3641  5461  7282 9102 10923 12743 14566
ph8 = (16384) 8192 10012 11833 13653 15474 910  2730  4551  6371
ph10=0
ph11=(65536) 0 9362 18725 28087 37449 46811 56174
ph12=(65536) 32768 42130 51493 60855 4681 14043 23406
ph31=0 2 2 0 1 3 3 1
```

B.4 2D DOAM

```
"d31=1s/cnst31"
"d0=2u"

"p30=p31-0.4u"

define pulse tau1
"tau1=((1s/cnst31)/22)"
define pulse tau2
"tau2=((3s/cnst31)/22)"
```

```
  ze

1 d31

2 d1 do:f2

  1m rpp11
  1m rpp12
  1m rpp13
  1m rpp14
  1m rpp15
  1m rpp16
  1m rpp17
  1m rpp18

  10u reset:f1

  (p3 pl3 ph1):f2
  (p15 pl11 ph2):f1 (p15:spf0 pl22 ph10):f2


  (d0 cpds2 pl12):f2

  0.3u do:f2

  (p1 pl1 ph4):f1

  (d2 cw pl28):f2

  0.3u do:f2

 (1u cpds1 pl27):f2

   0.3u pl17:f1

3 tau1:f1 ph11:r ipp11
  tau2:f1 ph12:r ipp12
  tau1:f1 ph13:r ipp13
  tau2:f1 ph14:r ipp14
  lo to 3 times l0

  1u

4 tau1:f1 ph15:r ipp15
  tau2:f1 ph16:r ipp16
  tau1:f1 ph17:r ipp17
  tau2:f1 ph18:r ipp18
  lo to 4 times l0

 (p1 pl1 ph5):f1
   1u do:f2

  (3u cpds2 pl12):f2

 3u
  gosc ph31
  1m ip5
  1m ip15*16384
  1m ip16*16384
  1m ip17*16384
  1m ip18*16384
 1m do:f2
  lo to 2 times ns
 100m wr #0 if #0 zd
 1m ip2
 id0
 lo to 1 times td1
HaltAcqu, 1m
exit

ph0= 0
ph1= 1 1 1 1 3 3 3 3
ph2= 1
```

```
ph4= 0
ph5= 1
ph10=0

ph11=(65536) {13405}*11 {46173}*11
ph12=(65536) {46173}*11 {13405}*11
ph13=(65536) {52131}*11 {19362}*11
ph14=(65536) {19362}*11 {52131}*11

ph15=(65536) {13405}*11 {46173}*11
ph16=(65536) {46173}*11 {13405}*11
ph17=(65536) {52131}*11 {19362}*11
ph18=(65536) {19362}*11 {52131}*11

ph31= 3 2 1 0 1 0 3 2
```

B.5 2D DOPE

```
"d31=1s/cnst31"
"d0=2u"

"p30=p31-0.4u"

define pulse tau1
"tau1=((1s/cnst31)/22)"
define pulse tau2
"tau2=((3s/cnst31)/22)"

  ze

1 d31

2 d1 do:f2

  1m rpp11
  1m rpp12
  1m rpp13
  1m rpp14
  1m rpp15
  1m rpp16
  1m rpp17
  1m rpp18

  10u reset:f1

  (p3 pl3 ph1):f2
  (p15 pl11 ph2):f1 (p15:spf0 pl22 ph10):f2


 (1u cpds1 pl27):f2

 (p1 pl1 ph6):f1

   0.3u pl17:f1

3 tau1:f1 ph11:r ipp11
  tau2:f1 ph12:r ipp12
  tau1:f1 ph13:r ipp13
  tau2:f1 ph14:r ipp14
  lo to 3 times l0

  1u

4 tau1:f1 ph15:r ipp15
  tau2:f1 ph16:r ipp16
  tau1:f1 ph17:r ipp17
  tau2:f1 ph18:r ipp18
  lo to 4 times l0

 (p1 pl1 ph5):f1
   1u do:f2
```

```
 (d0 cpds2 pl12):f2

  0.3u do:f2

  (p1 pl1 ph4):f1

  (d2 cw pl28):f2

  0.3u do:f2

 (p1 pl1 ph7):f1

  (3u cpds2 pl12):f2

 3u
  gosc ph31
  1m ip5
  1m ip15*16384
  1m ip16*16384
  1m ip17*16384
  1m ip18*16384
 1m do:f2
  lo to 2 times ns
 100m wr #0 if #0 zd
 1m ip5
 id0
 lo to 1 times td1
HaltAcqu, 1m
exit

ph0= 0
ph1= 1 1 1 1 3 3 3 3
ph2= 1
ph4= 3 2 1 0
ph5= 1
ph6 =  2
ph7 = 0
ph10=0

ph11=(65536) {13405}*11 {46173}*11
ph12=(65536) {46173}*11 {13405}*11
ph13=(65536) {52131}*11 {19362}*11
ph14=(65536) {19362}*11 {52131}*11

ph15=(65536) {13405}*11 {46173}*11
ph16=(65536) {46173}*11 {13405}*11
ph17=(65536) {52131}*11 {19362}*11
ph18=(65536) {19362}*11 {52131}*11

ph31 = 0 0 0 0 2 2 2 2
```

B.6 1D $R70_6^{16,16}$

```
; Autogenerated Doublesyncronized R Sequence using
; generalized HH approach with N(70) v(16) n(6)
; YOU HAVE TO SET p15 TO TAU MANUALLY


"d31=1s/cnst31"
define delay tau
"tau=1s/(11.6666666667*cnst31*4)" ;set tau to SR Element and divide by 4 for 90Pulse
"p30=p31-0.4u"


1 ze


2
   2u fq=cnst21:f2
   d1
```

```
   2u do:f2
  tau
  1m


4
  (p1 pl1 ph4^):f1
  d20
  lo to 4 times l20


  10u reset:f1
  2u fq=cnst21:f2
  10u:f1 ph0
  10u:f2 ph0
  10u pl11:f1
  10u pl22:f2


3
      (p15 pl11 ph11):f1 (p15 pl22 ph11):f2
      (p15*3 pl11 ph12):f1 (p15*3 pl22 ph12):f2
      (p15 pl11 ph13):f1 (p15 pl22 ph13):f2
      (p15*3 pl11 ph14):f1 (p15*3 pl22 ph14):f2
   lo to 3 times l0


  (p1 pl1 ph3):f1
  1u pl12:f2
  2u cpds2:f2
  go=2 ph31
  1m do:f2
  wr #0
HaltAcqu, 1m
exit


ph0= 0
ph11 = (65536) 7489
ph12 = (65536) 40257
ph13 = (65536) 58045
ph14 = (65536) 25278
ph3= 0

ph4= (8) 3 1 4 2 5 1 6 3 5 7 3
ph10= 0
ph31= 0
```

B.7 CP with 180° selective pulse and mixing time

```
"d31=1s/cnst31"
"d0=2u"
"cnst2=0"

"p30=p31-0.4u"

define loopcounter count
"count= ns"

  ze
1 1m

2 d1 do:f2

  1m
  10u reset:f1
  2u fq=cnst21:f2
  10u:f1 ph0
```

```
  10u:f2 ph0
  10u pl1:f1
  10u pl12:f2
  (p3 pl3 ph1):f2

  0.2u

  (p15 pl11 ph2):f1 (p15:spf0 pl22 ph10):f2
  (p1 pl1 ph6):f1
4 d4 do:f2
  (3u cpds2 pl12):f2

  (p1 pl1 ph7):f1

  d0

  (p1 pl1 ph4):f1
  0.3u do:f2

  d2

  (3u cpds2 pl12):f2

  (p1 pl1 ph5):f1

  go=2 ph31

  1m do:f2
  wr #0
HaltAcqu, 1m
exit

ph0= 0
ph1= 1
ph2= 1
ph4= 0 2
ph5= 0
ph6= 0
ph7= 0 0 2 2
ph10=0
ph31=2 0 0 2
```

B.8 1D RELOAD CP

```
#include <lgcalc.incl>
#include <trigg.incl>
#include <prp15.prot>

"p30=p31-0.4u"
"p11 = p1*2"

  ze
1 1m

2 d1 do:f2

  (p3 pl3 ph1):f2

  0.3u

  (p15 pl11 ph2):f1 (p15:spf0 pl22 ph10):f2

  (p1 pl1 ph3):f1


4  d2 do:f2

  (p4:spf1 pl4 ph4):f1

  (3u cpds2 pl12):f2
  go=4 ph31
```

```
  1m do:f2
  wr #0

  lo to 2 times l0

HaltAcqu, 1m
exit



ph1= 1 3
ph2= 0
ph3= 3 1 ; for Iz
;ph3= 1 3 ; for -Iz
ph4= 0
ph10= 0
ph31= 1 3
```

B.9 2D RELOAD PDSD

```
"d31=1s/cnst31"
"d0=2u"
"cnst2=0"

"p30=p31-0.4u"
"in0=inf1/2"

define loopcounter count
"count= ns"

  ze
1 1m

2 d1 do:f2

  1m
  10u reset:f1
  2u fq=cnst21:f2
  10u:f1 ph0
  10u:f2 ph0
  10u pl1:f1
  10u pl12:f2
  (p3 pl3 ph1):f2

  0.2u

  (p15 pl11 ph2):f1 (p15:spf0 pl22 ph10):f2

  (p1 pl1 ph6):f1

  4 d4 do:f2
  (3u cpds2 pl12):f2
  1u fq=cnst1:f1
  (p4:spf1 pl4 ph7):f1

  d0

  (p4:spf1 pl4 ph4):f1
  1u fq=cnst2:f1
  0.3u do:f2

  d2

  (3u cpds2 pl12):f2

  1u fq=cnst1:f1
  (p4:spf1 pl4 ph5):f1
  1u fq=cnst2:f1
```

```
  goscnp ph31
  lo to 4 times l1  ; RELOAD cycle

  1m do:f2

  2u ipp4
  2u ipp7
  2u ipp31

  lo to 2 times count ; NS cycle

  100m wr #0 if #0 zd
  1m ip7
  id0
  1m
  lo to 1 times td1 ; 2D cycle
HaltAcqu, 1m
exit


ph0= 0
ph1= 1
ph2= 1
ph4= 0 0 2 2
ph5= 0
ph6= 0
ph7= 2 0
ph10=0
ph31=0 2 2 0
```

B.10 2D DoubleCP RELOAD

```
"d31=1s/cnst31"
"d0=2u"
"cnst2=0"

"p30=p31-0.4u"
"in0=inf1/2"

define loopcounter count
"count= ns"

  ze
1 1m

2 d1 do:f2

  1m
  10u reset:f1
  2u fq=cnst21:f2
  10u:f1 ph0
  10u:f2 ph0
  10u pl1:f1
  10u pl12:f2
  (p3 pl3 ph1):f2

  0.2u

  (p15 pl11 ph2):f3 (p15:spf0 pl22 ph10):f2
  (p1 pl1 ph6):f3
4 d4 do:f2
  (3u cpds2 pl12):f2
  1u fq=cnst1:f3

  (p14:spf2 pl14 ph7):f3

  d0

  (p14:spf2 pl14 ph4):f3
  1u fq=cnst2:f3
  0.3u do:f2
```

```
 (p1 pl1 ph11):f3

  1u pl27:f2
  1u cw:f2
  (p16 pl4 ph12):f1 (p16:spf1 pl5 ph13):f3
  1u do:f2
  (p1 pl1 ph14):f3



  (3u cpds2 pl12):f2


  goscnp ph31
  lo to 4 times l1  ; RELOAD cycle

  1m do:f2

  2u ipp4
  2u ipp7
  2u ipp11
  2u ipp31

  lo to 2 times count ; NS cycle

  100m wr #0 if #0 zd
  1m ip7
  id0
  1m
  lo to 1 times td1 ; 2D cycle
HaltAcqu, 1m
exit


ph0= 0
ph1= 1
ph2= 1
ph4= 0
ph5= 0
ph6= 0
ph7= 2 0
ph10=0
ph11=2
ph12=0
ph13=1
ph14=0
ph31=0 2
```

B.11 2D REDOR RELOAD

```
"p30=p31-0.4u"



"d3=3s/l31-p1*0.5-p11*1.5-1.5u" ;z-filter
"d21=(p11-p1)/2"
"d23=1.25s/l31-(p1/2)-0.5u"
"d24=0.25s/l31-(p11/2)-0.5u"
"d25=0.25s/l31-1u"
"d26=0.25s/l31-p12/2"
"d27=1.25s/l31-p2/2"
"d2=0.5s/l31"
"d28=300s/l31-p1"

"p30=p31-0.4u"
"in0=inf1/2"

"cnst2=0"
```

```
define loopcounter count
"count= ns"

#include <trigg.incl>


 ze ;accumulate into an empty memory
1 1m

2  1m do:f2
   2u fq=cnst21:f2
   d1 do:f2
   1m rpp5


  (p3 pl3 ph1):f2

  0.3u

  (p15 pl11 ph2):f1 (p15:spf0 pl22 ph3):f2

   (p5 pl5 ph12):f1


 8  d28 do:f2
    trigg


  1u pl12:f2
  2u cpds2:f2

 1u fq=cnst1:f1
   (p1:spf1 pl1 ph13):f1
 1u fq=cnst2:f1

  d25 pl1:f1  ;tr/4
3 d26:f3 ph5
  (p12 pl4 ph5^):f3         ;15N 180 deg. pulse
  d26
lo to 3 times l0     ;an even number


  d27:f1 ph6 ;tr/4
  d2     ;tr/2
  (p2 pl5 ph6):f1 ;13C 180 deg. pulse
  d2
  d27

4 d26:f3 ph5
  (p12 pl4 ph5^):f3     ;15N 180 deg. pulse
  d26
lo to 4 times l0
  0.5u pl1:f1
  0.5u pl4:f3
  (d24 ph9):f1 (d24 ph10):f3 ;phase switch

 1u fq=cnst1:f1
  (p1:spf1 pl1 ph9):f1
 1u fq=cnst2:f1


  d3 ;do:f2         ;z-filter
  (p11 pl4 ph10):f3 ;15N 90

  d0         ;t1

  (p11 pl4 ph4):f3 ;15N 90
  d3              ;z-filter


 1u fq=cnst1:f1
    (p1:spf1 pl1 ph11):f1
 1u fq=cnst2:f1
```

```
  d23 pl1:f1  ;tr/4
6 d26:f3 ph5
  (p12 pl4 ph5^):f3         ;15N 180 deg. pulse
  d26
lo to 6 times l0       ;an even number

  d27:f1 ph8   ;tr/4
  d2
  (p2 pl5 ph8):f1 ;13C refocus
  d2
  d27

7 d26:f3 ph5
  (p12 pl4 ph5^):f3       ;15N 180 deg. pulse
  d26
lo to 7 times l0
  d25

1u do:f2


  1u pl12:f2
  2u cpds2:f2

  goscnp ph31
  lo to 8 times l1   ; RELOAD cycle

  1m do:f2

  2u ipp4
  2u ipp13
  2u ipp31

  lo to 2 times count  ; NS cycle


  1m do:f2
  100m wr #0 if #0 zd
  1m ip10
  id0
  1m
  lo to 1 times td1


HaltAcqu, 1m
exit


ph0= 0
ph1= 0
ph2= 0
ph3= 1

ph5= 0 1 0 1 1 0 1 0 2 3 2 3 3 2 3 2

ph6=0
ph8=0

ph9= 0
ph10= 1
ph11= 2
ph12=3
ph13=1 3

ph4= 3 3 1 1

ph31=0 2 2 0
```

B.12 HEAT

```
"p30=p31-0.4u"
"p2=2*p1"
#include <lgcalc.incl>
#include <trigg.incl>
#include <prp15.prot>


1 ze
2 d1  do:f2
  2u do:f2

  10u reset:f1 reset:f2

  (p3 pl3 ph1):f2
  0.3u

  (p15 pl11 ph2):f1 (p15:spf0 pl22 ph10):f2
  1u pl12:f2
  2u cpds2:f2

  STARTADC
  RESETPHASE
  RGP_ADC_ON
  1u DWELL_GEN
  10u

  d6
  d3
  (p2 pl1 ph3):f1
  d3
  d6
  aq
  rcyc=2
  1m do:f2
  wr #0
exit


ph0= 0
ph1= 1 3
ph2= 0 0 2 2 1 1 3 3
ph3= 0 0 2 2 1 1 3 3
;ph3= 1 1 3 3 2 2 0 0
ph10= 0
ph31= 0 2 2 0 1 3 3 1
```

Appendix C

Software and Scripts

All the programs used for the generation of the data and plots discussed in chapters 7 and 4 are given below. Alternating processing schemes are also given, but commented out.

C.1 Symmetry based heteronuclear polarization transfer

C.1.1 SIMPSON

```
source NH.spinsys

# Nuclei
# 2: H
# 1: N


cluster {

  athena
#  mercury
#  achilles
#  ariadne2
#  poseidon
#  jason
  zeus
#  hermes
  ares
#  juno
}

par {

  proton_frequency 400e6
  start_operator   I2z+I3z
  detect_operator  I1z
  np    128*2


  crystal_file     rep20
  spin_rate    10000
  variable n    4
  gamma_angles    n

  variable rfmulti  1

  variable N       9
  variable v       3
  variable nr      1

  variable rfH     1
```

```
  variable rfN    1
  variable tp4     1
  variable tp3     1
  variable tp1     1
  sw    spin_rate/2
  verbose    1101
  method    direct
  use_cluster      1
  cluster_port     3265
}



proc pulseq {} {
  global par

  matrix set detect operator I1z
  acq
  matrix set detect operator I2z
  acq

   set ph [expr $par(v)*180.0/$par(N)]
   set phneg [expr $par(v)*(-180.0)/$par(N)]


  for {set i 1} {$i < [expr $par(np)/2]} {incr i} {



    if {$i == 1} {

      for {set j 0} {$j < $par(N)} {incr j} {
        pulse $par(tp1) $par(rfN) $ph $par(rfH) $ph
        pulse $par(tp3) $par(rfN) [expr $ph+180.0] $par(rfH) [expr $ph+180.0]
        pulse $par(tp1) $par(rfN) $phneg $par(rfH) $phneg
        pulse $par(tp3) $par(rfN) [expr $phneg+180.0] $par(rfH) [expr $phneg+180.0]
}

     store 1
   } else {
     prop 1
   }
   matrix set detect operator I1z
   acq
   matrix set detect operator I2z
   acq

 }
}

proc main {} {
  global par

  set f1 [fcreate -np [expr $par(np)/2] -sw $par(sw) \
       -type fid]
  set f2 [fcreate -np [expr $par(np)/2] -sw $par(sw) \
       -type fid]
#-------------------------------------
  for {set Na 1} {$Na <= 70} {incr Na 1} {

    file mkdir "RT_N[expr $Na*2]"
    cd "RT_N[expr $Na*2]"

  for {set va 1} {$va <= 30} {incr va 1} {
  for {set nra 1} {$nra <= 30} {incr nra 1} {
#-------------------------------------
  variable rfHa     [expr $Na*1.0*$par(spin_rate)/$nra]
  variable rfNa     [expr $Na*1.0*$par(spin_rate)/$nra]
  variable tp4a     [expr 1.0e6/$rfHa]
  variable tp3a     [expr 0.75e6/$rfHa]
  variable tp1a     [expr 0.25e6/$rfHa]

   set par(N)   $Na
   set par(v)   $va
```

```
   set par(nr)  $nra
   set par(rfH) $rfHa
   set par(rfN) $rfNa
   set par(tp4) $tp4a
   set par(tp3) $tp3a
   set par(tp1) $tp1a

 set f [fsimpson]

  for {set i 1} {$i <= [expr $par(np)/2]} {incr i} {
    set c [findex $f [expr 2*($i-1)+1]]
    fsetindex $f1 $i [lindex $c 0] [lindex $c 1]
    set c [findex $f [expr 2*($i-1)+2]]
    fsetindex $f2 $i [lindex $c 0] [lindex $c 1]

  }

  fsave $f1 NH_R_N-N([expr $Na*2])v($va)n($nra).fid -xreim
  fsave $f2 NH_R_H-N([expr $Na*2])v($va)n($nra).fid -xreim

}
}
  cd ..
}
}
```

C.1.2 Evaluation scripts

```
#!/usr/bin/tclsh

# set maximum values for the symmetry numbers

set N_max 70
set a_max 30
set b_max 30

# matrix loop to keep them 3 dimensional
for {set N 1} {$N <= $N_max} {incr N} {

# open outputfile
set output_file [open "IntMatrix_N[expr $N*2]_J.mat" w]
set text_file [open "Selected_Sequences.txt" w]

  cd "RT_N[expr $N*2]"
# matrix generating loops
for {set a 1} {$a <= $a_max} {incr a} {

for {set b 1} {$b <= $b_max} {incr b} {


# open infiles (v in inner loop for red. dim. matrix evaluation)
set input_file  [open "NH_R_N-N([expr $N*2])v($b)n($a).fid" r]

puts stdout "Opened data file NH_R_N-N([expr $N*2])v($b)n($a).fid"

set maxintensity 0
set maxtime 0

# read in data and compare for maximum intensity
    while { ![eof $input_file] } {
       gets $input_file line
       scan $line %f%f%f x y z
       if {abs($y) > $maxintensity} {
   set maxintensity $y
set maxtime $x
}
    }


# write out file in gnuplot matrix format

if {$maxintensity > 1.5 && $maxtime > 0.003 && [expr $N/$a] < 8 } {
puts $output_file "$b $a $maxintensity"
puts $text_file "\"RT_N[expr $N*2]/NH_R_N-N([expr $N*2])v($b)n($a).fid\""
```

```
} else {
puts $output_file "$b $a 0"
}


    puts stdout "Written to data file IntMatrix_N[expr $N*2]_J.mat "

# close files
close $input_file

}
}
  cd ..
close $output_file
}



#!/usr/bin/tclsh

# set maximum values for the symmetry numbers

set N_max 70
set v_max 30
set n_max 30

# open outputfile
set output_file [open "MetaIntMatrix.mat" w]

# matrix loop to keep them 3 dimensional
for {set N 1} {$N <= $N_max} {incr N} {


# open infiles
set input_file  [open "IntMatrix_N[expr $N*2].mat" r]

puts stdout "Opened data file IntMatrix_N[expr $N*2].mat"

#set maxpower 0
#set maxn 1
  #set n 0
# read in data and compare for maximum intensity

for {set n 1} {$n <= $n_max} {incr n} {

      set maxpower 0.0
#     incr n 1
for {set v 0} {$v < $v_max} {incr v} {
       gets $input_file line
       scan $line %f%f%f x y z

           if {$z > $maxpower} {
set maxpower $z
 #                set maxn $y
         }
    }
    puts $output_file "$N $n $maxpower"

  }

# write out file in gnuplot matrix format

#   set inversetime [expr 1/$maxtime]



   puts stdout "Written to data file MetaIntMatrix.mat "

# close files
close $input_file

}

close $output_file
```

C.1.3 Pulse program generation script

```
#!/usr/bin/tclsh

# Autogenerate Symmetry Based R-Transfersequence for bruker avance spectrometers
# -ck- last changed 16.08.2006

if { $argc != 3 } {
    puts stdout "The TCL script requires three symmetrynumbers N v n ."
    puts stdout "Please try again."
    return
} else {
    set sym_N [lindex $argv 0]
    set sym_v [lindex $argv 1]
    set sym_n [lindex $argv 2]
    }


# open outputfile
set output_file [open "DRTransfer_N($sym_N)v($sym_v)n($sym_n).av.cg" w]

puts stdout "Autogenerating DRTransfer Sequence with N=$sym_N v=$sym_v n=$sym_n"

#Calculate necessary variables

#factor 1 is for SR (otherwise it would be 0.5)
set timing [expr ($sym_N*1.0)/$sym_n]

set phasepos [expr (32768*$sym_v/$sym_N)%65535]
set phaseneg [expr (-32768*$sym_v/$sym_N)%65535]

set phasepos180 [expr ((32768*$sym_v/$sym_N)+(65536/2))%65535]
set phaseneg180 [expr ((-32768*$sym_v/$sym_N)+(65536/2))%65535]


#for {set a 0} {$a < $sym_N} {incr a} {
#
#append phase [expr ($phaseinc*$a)%65535]
#append phase "\t"
#
#append phase180 [expr ($phaseinc*$a+32768)%65535]
#append phase180 "\t"
#
#}



#generate Pulseprogram File

puts $output_file "; Autogenerated Doublesyncronized R Sequence using"
puts $output_file "; generalized HH approach with N($sym_N) v($sym_v) n($sym_n) "

puts $output_file "; YOU HAVE TO SET p15 TO TAU MANUALLY"

puts $output_file "\n"
puts $output_file "\"d31=1s/cnst31\""

puts $output_file "define delay tau"
puts $output_file "\"tau=1s/($timing*cnst31*4)\" ;set tau to SR Element and divide by 4 for 90Pulse"

puts $output_file "\"p30=p31-0.4u\""

puts $output_file "\n"

puts $output_file "1 ze ;accumulate into an empty memory"
puts $output_file "\n"

puts $output_file "2"
puts $output_file "   2u fq=cnst21:f2"
puts $output_file "   d1  ;recycle delay, decoupler off in go-loop"
puts $output_file "   2u do:f2"

puts $output_file "  tau"
puts $output_file "  1m"
```

```
puts $output_file "\n"

puts $output_file "4                        ; Saturationpulse Loop"
puts $output_file "  (p1 pl1 ph4):f1"
puts $output_file "  d20"
puts $output_file "  lo to 4 times l20 "
puts $output_file "\n"
puts $output_file "  10u reset:f1  "
puts $output_file "  2u fq=cnst21:f2"
puts $output_file "  10u:f1 ph0"
puts $output_file "  10u:f2 ph0"

puts $output_file "  10u pl11:f1"
puts $output_file "  10u pl22:f2"
puts $output_file "\n"

puts $output_file "3 ;SR excitation     "
puts $output_file "      (p15 pl11 ph11):f1 (p15 pl22 ph11):f2"
puts $output_file "      (p15*3 pl11 ph12):f1 (p15*3 pl22 ph12):f2"
puts $output_file "      (p15 pl11 ph13):f1 (p15 pl22 ph13):f2"
puts $output_file "      (p15*3 pl11 ph14):f1 (p15*3 pl22 ph14):f2"
puts $output_file "   lo to 3 times l0"
puts $output_file "\n"
puts $output_file "  (p1 pl1 ph3):f1"


puts $output_file "  1u pl12:f2"
puts $output_file "  2u cpds2:f2 ;cpds=cw or tppm15: pl12"
puts $output_file "  go=2 ph31  ;cpds=cwlgs       : pl13"

puts $output_file "  1m do:f2 ;decoupler off"
puts $output_file "  wr #0 ;save data to disk"
puts $output_file "HaltAcqu, 1m ;jump address for protection files"
puts $output_file "exit ;quit"

puts $output_file "\n"
puts $output_file "ph0= 0 "
puts $output_file "ph11 = (65536) $phasepos "
puts $output_file "ph12 = (65536) $phasepos180 "
puts $output_file "ph13 = (65536) $phaseneg"
puts $output_file "ph14 = (65536) $phaseneg180"
puts $output_file "ph3= 0"
puts $output_file ";ph4= 0 2"
puts $output_file "ph4= (8) 3 1 4 2 5 1 6 3 5 7 3"
puts $output_file "ph10= 0"
puts $output_file "ph31= 0"
```

C.2 Dual Transformation Denoising

Programs are listed in the order of execution

C.2.1 Generate synthetic data using python

```
#!/bin/python
import sys
import scipy
import pylab
import random
import FFT
import random
from pylab import *
import random
from scipy import *
from pylab import load
import RandomArray as ra



#def main():
```

```
# Define matrix parameters

nr_of_points = 2048

#noise_std_deviantion = 0.000000001
noise_std_deviantion = 0.00001

minimum = -1000.0
maximum = 1000.0

# Calculate matrix parameters

in_steps_of = abs(maximum - minimum)/nr_of_points

x = pylab.arange(minimum, maximum, in_steps_of)
y = pylab.arange(minimum, maximum, in_steps_of)

print len(x)

peaks_list = scipy.array([ 100.0, 200.0, 300.0, 400.0, 500.0, 600.0, 700.0, 800.0, 900.0  ])

linewidth = 0.0165 * abs(maximum - minimum) / len(peaks_list)



X, Y = pylab.meshgrid(x, y)


# Generate signal matrix



signal_sum = linewidth / (((X-10.0)**2.0+(Y-10.0)**2.0)+(linewidth**2.0))



for xindex in range(len(peaks_list)):
xpeak = peaks_list[xindex]
for yindex in range(len(peaks_list)):

ypeak = peaks_list[yindex]
# amp = 1/(1+(1.0*abs(xindex-yindex)))
amp = 1 /(1.4**(abs(xindex-yindex)))
signal1 = amp * linewidth / (((X-xpeak)**2.0+(Y-ypeak)**2.0)+(linewidth**2.0))
signal_sum = signal_sum + signal1

# Inverse FFT


Zreal = scipy.real(FFT.inverse_fft2d(signal_sum,s=None,axes=(-2,-1)))
Zimag = scipy.imag(FFT.inverse_fft2d(signal_sum,s=None,axes=(-2,-1)))
Zcomp = FFT.inverse_fft2d(signal_sum,s=None,axes=(-2,-1))

# Generate noise

noise1 = map(lambda x:x[:], [[0]*nr_of_points]*nr_of_points)
noise2 = map(lambda x:x[:], [[0]*nr_of_points]*nr_of_points)

for n in range(nr_of_points):

noise1[n] = ra.normal(0,noise_std_deviantion,nr_of_points)

noise2[n] = ra.normal(0,noise_std_deviantion,nr_of_points)

#noise1 = (randn(nr_of_points,nr_of_points)-0.5)*0.000005
#noise2 = (randn(nr_of_points,nr_of_points)-0.5)*0.000005

# Generate noisy matrices

Zreal_noise = Zreal + noise1
Zimag_noise = Zimag + noise2
Zcomp_noise = Zcomp + noise1
```

```
# Save data in SIMPSON format

outfile = open("LorentzianMatrix.simp.fid","w")

outfile.write("SIMP\n")
outfile.write("NP=" + str(len(x)) + "\n")
outfile.write("SW=" + str((abs(maximum)+abs(minimum))) + "\n")
outfile.write("NI=" + str(len(y)) + "\n")
outfile.write("SW1=" + str((abs(maximum)+abs(minimum))) + "\n")
outfile.write("TYPE=FID\n")
outfile.write("DATA\n")

# normalize matrices

# Zreal_norm = Zreal*(1/max(max(Zreal)))
# Zimag_norm = Zimag*(1/max(max(Zreal))) # use same number here as the matrices must stay coherent
# Zreal_noise_norm = Zreal_noise*(1/max(max(Zreal)))
# Zimag_noise_norm = Zimag_noise*(1/max(max(Zreal)))

for ind_x in range(len(x)):
for ind_y in range(len(y)):

outfile.write('%f ' % Zreal_noise[ind_x][ind_y])
outfile.write('%f \n' % Zimag_noise[ind_x][ind_y])



# Zsig = scipy.real(FFT.fft2d(Zcomp,s=None,axes=(-2,-1)))
# pylab.contour(Zsig, 32)

outfile.write("END\n")
outfile.close()

# check plotting options with gnuplot

# plotfile = open("GnuPlotFileNoise.mat","w")
#
# Zcomp_noise = Zcomp + noise1
# Zsig = scipy.real(FFT.fft2d(Zcomp_noise,s=None,axes=(-2,-1)))
#
# for inde_x in range(len(x)):
# for inde_y in range(len(y)):
#
# plotfile.write('%i %i %f\n' % ((inde_y+1), (inde_x+1), Zsig[inde_y][inde_x]))
#
# if inde_y == (len(y)-1):
#
# plotfile.write('\n')
#
# plotfile.close()
#
# save("PlotTest.txt",Zsig)

#x = signal_sum[563,550:590]

#np = len(x)
#maximum = max(x)
#m = maximum/2


#for n in range(np):

# if x[n]> m:
# leftlim = (n-1)
# break
#
#
#
#for n in range(np-1,-1,-1):

# if x[n]> m:
# rightlim = (n-1)
# break
#
```

```
#
#print(rightlim-leftlim)

#spectrum = real(FFT.fft2d(Zcomp_noise,s=None,axes=(-2,-1)))

#contour(spectrum)
#pylab.show()
#main()
```

C.2.2 Convert to NMRPipe format using SIMPSON

```
proc main {} {

  set f [fload "LorentzianMatrix.simp.fid"]
  fsave $f LM.fid -nmrpipe

}
```

C.2.3 Process data with NMRPipe

```
#!/bin/csh

#
# Process a Bruker AM States-Mode 2D:
#  "FT -bruk" is used to transform Sequential Detection Mode.
#  "POLY -time" is used for solvent subtraction.
#  "REV" (reverse) was needed in this case for the indirect axis.
#
#  Separate Polynomial baseline corrections are used for the
#  left and right halfs of the data after 2D transform.

nmrPipe -in LM.fid \
#| nmrPipe -fn POLY -time -ord 6              \
#| nmrPipe -fn SP -off 0.5 -pow 2 -c 0.5      \
| nmrPipe -fn FT                      \
#| nmrPipe -fn PS -p0 -14.2 -p1 13.2 -di -verb \
| nmrPipe -fn TP                             \
#| nmrPipe -fn SP -off 0.5 -pow 2 -c 0.5      \
#| nmrPipe -fn ZF -auto                       \
| nmrPipe -fn FT                         \
#| nmrPipe -fn REV                            \
#| nmrPipe -fn PS -p0 14.0 -p1 -24.0 -di -verb \
| nmrPipe -fn TP                             \
#| nmrPipe -fn Ext -x1 250 -xn 512     \
#| nmrPipe -fn Ext -x1 250 -xn 512 -y1 250 -yn 512    \
#| nmrPipe -fn TP \
#| nmrPipe -fn POLY -auto -xn 50%             \
#| nmrPipe -fn POLY -auto -x1 50%             \
   -out LM.fft -verb -ov



nmrPipe -in LM.fid \
#| nmrPipe -fn EM  -lb 100.0 -c 1.0                                \
#| nmrPipe  -fn ZF -auto                          \
| nmrPipe  -fn FT                        \
#| nmrPipe  -fn PS -p0 0.00 -p1 0.00 -di -verb         \
#| nmrPipe  -fn POLY -auto      \
   -ov -out LM.ft2

covNMR -N1 2048 -N2 2048 <LM.ft2> LM.cov2

nmrPipe -in ./LM.cov2           \
#| nmrPipe -fn Ext -x1 250 -xn 512    \
#| nmrPipe -fn Ext -x1 250 -xn 512 -y1 250 -yn 512    \
#| nmrPipe  -fn POLY -auto                \
   -verb -ov -out ./LM.cov


addNMR -in1 LM.fft -in2 LM.cov -out LM.conv -mul
```

```
#pipe2ucsf LM.fft LM.fft.uscf
pipe2txtv2.tcl LM.fft > LM.fft.ascii
pipe2txtv2.tcl LM.conv > LM.conv.ascii
```

C.2.4 Convert resulting spectrum to GNUPlot using Python

```
#!/usr/bin/env python
from pylab import *
import random
from scipy import *
from pylab import load
import sys
import pylab
import string


infile = open("LM.fft.noabs.ascii")
outfile = open("TestPlot.fft.noabs.mat","w")
infile2 = open("LM.conv.noabs.ascii")
outfile2 = open("TestPlot.conv.noabs.mat","w")


last = int(0)

# convert nmrpipe txt file to gnuplot matrix

#size = 263

#for line in infile.readlines():
# linesplit = string.split(line)
#
# if linesplit[0] == str(size):
#
# outfile.writelines(string.join([linesplit[0],linesplit[1],linesplit[2],"\n","\n"]))
#
# else:
# outfile.writelines(string.join([linesplit[0],linesplit[1],linesplit[2],"\n"]))

for line in infile.readlines():
linesplit = string.split(line)

if (int(linesplit[1])%2) == 1:

if int(linesplit[0]) < int(last):
outfile.writelines("\n")
outfile.writelines(string.join([linesplit[0],str(int(linesplit[1])/2),linesplit[2],"\n"]))
last = int(0)
else:
outfile.writelines(string.join([linesplit[0],str(int(linesplit[1])/2),linesplit[2],"\n"]))
last = linesplit[0]

last = int(0)

for line in infile2.readlines():
linesplit = string.split(line)
linescale = str(1000*float(linesplit[2]))

if (int(linesplit[1])%2) == 1:

if int(linesplit[0]) < int(last):
outfile2.writelines("\n")
outfile2.writelines(string.join([linesplit[0],str(int(linesplit[1])/2),linescale,"\n"]))
last = int(0)
else:
outfile2.writelines(string.join([linesplit[0],str(int(linesplit[1])/2),linescale,"\n"]))
last = linesplit[0]



print("Conversion from nmrPipe to GnuPlot complete")

infile.close()
outfile.close()
```

```
infile2.close()
outfile2.close()
```

C.2.5 Automatic evaluation using Python

```
#!/usr/bin/env python
from pylab import *
import random
from scipy import *
from pylab import load
import sys
import pylab
import string


# Create Python Matrix out of pipe2txtv2.tcl file

infile = open("LM.fft.ascii")
infile2 = open("LM.conv.ascii")

size = 2048

A = map(lambda x:x[:], [[0]*size]*size)

# the if statement has to be done that way because pipe2txt chops the data up only using every other point

for line in infile.readlines():
linesplit = string.split(line)
if (int(linesplit[1])%2) == 1:

A[int(linesplit[0])-1][(int(linesplit[1])/2)-1]= float(linesplit[2])




# isolate slice to be analyzed

B = A[1126][1024:]

# isolate peaks from slice


peaklist = [101,204,306,408,511,613,716,818,920]


PeakHeight = []

for element in peaklist:

PeakHeight.append(B[element])


#peak = map(lambda x:x[:], [[0]*100]*9)
#PeakHeight = [0]*9
#PeakPos = [0]*9
#PeakWidth = [0]*9


#for n in range(9):

# peak[n] = B[(70+(104*n)):(170+104*n)]


# determine max intensity and peak position

#for n in range(9):

# PeakHeight[n] = max(peak[n])
#
# for i in range(len(peak[n])):
#
# if max(peak[n]) == peak[n][i]:
#
```

```
# PeakPos[n] = i
#
#for n in range(9):
#
# for i in range(PeakPos[n],100,1):
#
# if float(peak[n][i])<=float((PeakHeight[n]/2)):
#
# rightlim = i
# break
#
# for i in range(PeakPos[n],-1,-1):
#
# if float(peak[n][i])<=float((PeakHeight[n]/2)):
#
# leftlim = i
# break
#
# PeakWidth[n] = rightlim-leftlim
#
#print("The Peak Heights are: "+str(PeakHeight))
#print("The Peak Widths are: "+str(PeakWidth))


# Calculate root mean square noise

mn = 0
rms = 0

NoiseSlice = A[20] [500:1500]

for element in NoiseSlice:

mn = mn + element

meanNoise = mn/len(NoiseSlice)

for element in NoiseSlice:

rms = rms + ((element - meanNoise)**2)

rms1 = rms/len(NoiseSlice)
rmsNoise = sqrt(rms1)

PeakSN = [0]*9

#for n in range(9):
#
# PeakSN[n]= (PeakHeight[0])/((rmsNoise*2)*(1.4**n))
#
for n in range(9):

PeakSN[n]= (PeakHeight[n])/(rmsNoise*2)


print("The FFT Peak Signal to Noise ratios are: "+str(PeakSN))

D = B

PeakSNFFT = PeakSN

infile.close()


# for the second infile


A = map(lambda x:x[:], [[0]*size]*size)

# the if statement has to be done that way because pipe2txt chops the data up only using every other point

for line in infile2.readlines():
```

```
linesplit = string.split(line)
if (int(linesplit[1])%2) == 1:

A[int(linesplit[0])-1][(int(linesplit[1])/2)-1]= float(linesplit[2])



# isolate slice to be analyzed

B = A[1126][1024:]

# isolate peaks from slice


peaklist = [101,204,306,408,511,613,716,818,920]


PeakHeight = []

for element in peaklist:

PeakHeight.append(B[element])



# Calculate root mean square noise

mn = 0
rms = 0

NoiseSlice = A[20] [500:1500]

for element in NoiseSlice:

mn = mn + element

meanNoise = mn/len(NoiseSlice)

for element in NoiseSlice:

rms = rms + ((element - meanNoise)**2)

rms1 = rms/len(NoiseSlice)
rmsNoise = sqrt(rms1)

PeakSN = [0]*9

#for n in range(9):
#
# PeakSN[n]= (PeakHeight[0])/((rmsNoise*2)*(1.4**n))
#
for n in range(9):

PeakSN[n]= (PeakHeight[n])/(rmsNoise*2)



print("The Cov x FFT Peak Signal to Noise ratios are: "+str(PeakSN))


C = [0]*len(B)

for n in range(len(B)):

C[n] = B[n]*250

PeakSNCONV = PeakSN

infile2.close()

plot(PeakSNFFT)
plot(PeakSNCONV)
save("PeakSNFFT.txt",PeakSNFFT)
```

```
save("PeakSNCONV.txt",PeakSNCONV)
show()
```

Appendix D

Expression Media

D.1 Media

D.1.1 Defined Medium

0,5g Alanine
0,4g Arginine
0,4g Aspartic Acid
0,05g Cysteine
0,4g Glutamine
0,65g Glutamic Acid
0,55g Glycine
0,1g Histidine
0,23g Threonine
0,17g Tyrosine
0,23g Valine
0,23g Isoleucine
0,42g Lysine Hydrochloride
0,25g Methionine
0,13g Phenylalanine
0,1g Proline
2,1g Serine
0,23g ^{15}N Leucine

0,5g Adenine
0,65g Guanosine
0,2g Thymine
0,5g Uracile
0,2g Cytosine
1,5g Sodiumacetate
1,5g Succinate
0,5g NH_4Cl
0,85g NaOH
10,5g K_2HPO_4

fill up with 950ml milliq H_2O, pH 7,2

after autoclaving:

50ml 40% Glucose
4ml 1M $MgSO_4$
1ml 0,01M $FeCl_3$
and 10ml filter sterilized solution containing:
2mg $CaCl_2$ / 2 H_2O
2mg $ZnSO_4$ / 7 H_2O
2mg $MnSO_4$ / H_2O
50mg l-Tryptophane
50mg Thiamine
50mg Niacin
1mg Biotin
100mg Ampicillin

D.1.2 M9 Medium

6g Na_2HPO_4
3g KH_2PO_4
0,5g NaCl
1g NH_4Cl
fill up to 1l with milliq H_2O, pH 7,0

after autoclaving add:

1ml 0,1M $CaCl_2$
1ml 1M $MgSO_4$ / $7H_2O$
10ml 40% Glycerine (w/w)
100mg Ampicillin

0,01% Thiamine (w/v)
or 2ml Centrum Mix
(made from 1,5g pulverized Centrum multivitamin pills in 20ml milliq H_2O, vortex, centrifuge and sterile filter supernatant)

D.2 Buffers

D.2.1 SDS-PAGE

Gel Buffer

3M Tris
0,3% SDS (v/v)
pH 8,45

Cathode Buffer

0,1M Tris
0,1M Tricine
0,1% SDS (v/v)
pH 8,25

Anode Buffer

0,2M Tris
pH 8,9

Separation Gel 8%

4ml Gelbuffer with Glycerine (2,5:1)
2ml 40% Acrylamide / Bisacrylamide (37,5 : 1)
3ml milliq H_2O
15μl TEMED
15μl APS

Stacking Gel 4%

600μl 40% Acrylamide / Bisacrylamide (37,5 : 1)
1,2ml Gel Buffer
4ml milliq H_2O
15μl TEMED
15μl APS

Sample Buffer

50mM Tris
3% SDS (v/v)
0,2% Bromphenolblue (w/v)
200mM DTT
20% Glycerine (w/v)

Coomassie Blue Solution

1,1g Coomassie Brilliant Blue
50ml Acetic Acid
250ml Methanol
200ml milliq H_2O

Destain Solution

10% Acetic Acid (v/v)
20% Methanol (v/v)
70% milliq H_2O (v/v)

D.2.2 Preparation Buffers

Buffer A

50mM Sodiumphosphate
300mM NaCl
pH 7,5

Washing Buffer

750mg OG
750μl 2M Imidazole Solution (pH 8,0)
fill to 50ml with Buffer A

DM (DPC) Buffer

250mg DM (DPC)
fill to 50ml with Buffer A

Elution Buffer

250mg DM (DPC)
6,25ml 2M Imidazole Solution (pH 8,0)
fill to 50ml with Buffer A

Dialysis Buffer

50mM HEPES
0,2mM DTT
1mM EDTA
10mM $MgCl_2$
pH 7,0

Gelfiltration Buffer

50mM Tris
20mM NaCl
0,02% DM
pH 8,0

Appendix E

Materials

E.1 Chemicals Used

Chemical	Supplier
1,2-Dioleoyl-sn-Glyero-3-Phosphocholine (DOPC)	Avanti Polar Lipids
1,4-Dithiothreitol	Roth
^{13}C 1,2-Glycine	Cambridge Isotope Laboratories
^{13}C Glutamic Acid (fully labeled)	Cambridge Isotope Laboratories
^{13}C Glycerine (fully labeled)	Chemotrade
2-^{13}C Glycerine	Chemotrade
$^{15}NH_4Cl$	Chemotrade
2-Mercapthoethanol	BioRad
2-Isopropanol	Roth
Acetone	Roth
Acrylamide-Stocksolution (37,5:1)	Roth
Adenine	Sigma
Adenosine Triphosphate DiSodium Salt	Sigma
Ammoniumchloride	Sigma
Ammoniumhydroxide	Sigma
Ammoniumperoxodisulfate (APS)	BioRad
Ammoniumpersulfate (APS)	Roth
Ampicillin, Sodiumsalt	Roth
Biotin	Sigma
Calciumchloride	Sigma
Coomassie Brillant Blue R250	Roth
Cytosine	Sigma
D-(+)-Glucose	Sigma
D-(+)-Saccharose	Roth
DNaseI	Roche
Dodecylphosphocholine (DPC)	Avanti Polar Lipids
EDTA	Sigma
Fe-chloride	Sigma
Acetic Acid	Sigma
Ethanol	Roth
Glycine	Sigma
Guanosine	Sigma
HEPES	Sigma
Imidazole	Sigma
Isopropyl-β-D-thiogalactoside (IPTG)	Roth
Potassiumacetate	Roth
Potassiumchloride	Roth
Potassiumhydrogenphosphate	Sigma
Complete protease inhibitor cocktail tablets	Roche Dagnostics
Complete mini protease inhibitor cocktail tablets	Roche Dagnostics
L-Alanine	Sigma
L-Arginine	Sigma
L-Asparagine	Sigma
L-Aspartate	Sigma
L-Cysteine	Sigma
L-Glutamine	Sigma

L-Glutamic Acid	Sigma
L-Histidine	Sigma
L-Isoleucine	Sigma
L-Leucine	Sigma
L-Lysine	Sigma
L-Methionine	Sigma
L-Phenylalanine	Sigma
L-Proline	Sigma
L-Serine	Sigma
L-Threonine	Sigma
L-Tryptophane	Sigma
L-Tryptophane	Sigma
L-Tyrosine	Sigma
L-Tyrosine	Sigma
L-Valine	Sigma
LB-Medium	Roth
$LiCl_2$	Sigma
Mg-ATP	Sigma
Mg-Chloride	Sigma
Mg-Sulfate	Roth
Mn-Sulfate	Sigma
Methanol	Roth
N,N,N',N'-Tetramethylendiamine (TEMED)	Roth
Nicotineamideadeninedinucleotide	Sigma
Sodiumacetate	Sigma
Sodiumchloride	Roth
Sodiumdodecylsulfate (SDS)	Roth
Sodiumhydroxide	Sigma
Sodiumnitrite	Sigma
Sodiumphosphate	Sigma
n-Dodecyl-β-D-Maltoside (DM)	Glycon Biochemicals GmbH
Niacin	Sigma
Ni-NTA Agarose	Qiagen
Octyl β-D-Glucopyranoside	Glycon Biochemicals GmbH
Phosphoenolpyruvate	Fluka
Pyruvate Kinase / L-Lactate Dehydrogenase	Roche Diagnostics
PIPES	Sigma
HCl 37	Roth
Succinate	Sigma
Thiamine	Sigma
Thymine	Sigma
Tricine	Roth
Tris-Hydrochloride	Roth
Uracile	Sigma

E.2 Instruments

Instrument	Manufacturer
4mm MAS-Rotor	Bruker
Analysis Balance Explorer	Ohaus
Autoklave Varioklav 65 T	H+P Labortechnik
Incubator Incucell	Medcenter Einrichtungen GmbH
Dialysis Tubes Spectra/Por, MWCO 12-14.000	Spectrum Laboratories
Elektrophoresis System Minigel Mini-Protean 3 Cell	Biorad
Extruder	Northern Lipids Extruder
Filter membrane 25mm Diameter 50kDa Cutoff	Millipore
Fluorescence Spectrometer FP-6300	Jasco
Gelfiltration Column Superose 12 PC 3.2 / 30	Pharmacia
Magnetic Stirrer	Fisher Bioblock Scientific
Incubator Innova 4230	New Brunswick Scientific
Incubator Innova 4430	New Brunswick Scientific
Concentration Cell Amicon 8010	Millipore
Laboratory balance Adventurer	Ohaus
pH-Meter MP 200	Mettler Toledo
Reaction Vessels, 1,5 und 2 ml	Roth
milliQ Water System Nanopure Diamond	Barnstead
Columns 1,5 / 15	Amersham Biosciences
Cleanbench Antair	AYSID
Ultrasonic Bath	Merck
UV/VIS Spectrometer V-550	Jasco
Vortexer Genie 2	Scientific Industries
Biofuge pico	Heraeus
Allegra 21R Centrifuge	Beckman Coulter
Avanti J-E Centrifuge	Beckman Coulter

E.3 NMR Spectrometer

Spectrometer:

Bruker Avance 600WB
Windows Workstation (PC) with Topspin

Bruker Avance 400WB
Windows Workstation (PC) with Topspin

Appendix F

Eidesstattliche Erklärung

Ich erkläre hiermit, dass ich mich bisher keiner Doktorprüfung unterzogen habe.

Frankfurt am Main, den .....

Unterschrift .....

Eidesstattliche Versicherung

Ich erkläre hiermit an Eides Statt, dass ich die vorgelegte Dissertation über

"Improving methods for the study of membrane proteins by solid-state NMR"

selbständig angefertigt und mich anderer Hilfsmittel als der in ihr angegebenen nicht bedient habe, insbesondere, dass aus Schriften Entlehnungen, soweit sie in der Dissertation nicht ausdrücklich als solche mit Angabe der betreffenden Schrift bezeichnet sind, nicht stattgefunden haben.

Frankfurt am Main, den .....

Unterschrift .....

Appendix G

Acknowledgments

I thank my supervisor Prof. Glaubitz for his support throughout my thesis and the opportunity to learn a great deal about the theory, as well as the hard- and software behind NMR. Furthermore I thank him for always being open to new ideas and not dismissing my sometimes out of the box way of thinking.

I thank Dr. Jakob Lopez for his ample support and the productive working environment during our shared projects. I will fondly remember the many hours spent in front of the spectrometers looking at spectral noise and composing haiku.

I thank Nicole Pfleger for her friendship and help during our thesis and the good times we had.

I thank Dr. Sarika Shastri for her support in the biochemistry lab and our pleasant work relationship. In particular I want to thank her for sharing DGK preparation tips with me.

I thank Dr. Frank Löhr and Dr. Christian Richter for their help and support with all things NMR related.

I thank Dr. Winfried Haase for taking freeze fracture electromicroscope pictures for me and helping me to understand what they meant.

I thank Ingrid Weber for her help in the biochemistry lab and will continue to admire her for her uncanny ability to know the location of the most esoteric chemical in the whole lab by heart. I also thank her for our Jujutzu training and teaching me that it is a good idea to block straight punches to the face.

I thank Simone Kobylka for always being friendly and ready to help out.

Am meisten möchte ich meinen Eltern Günther and Evelyn Kaiser danken. Ohne ihre besondere Unterstützung wäre ich nicht in der Lage gewesen die Dinge zu erreichen, die ich erreicht habe. Dies gilt im Besonderen für die vorliegende Doktorarbeit.

Bibliography

[1] Bockmann, A., Lange, A., Galinier, A., Luca, S., Giraud, N., Juy, M., Heise, H., Montserret, R., Penin, F., and Baldus, M. *Journal of Biomolecular NMR* **27**(4), 323–339 (2003).

[2] Franks, W. T., Zhou, D. H., Wylie, B. J., Money, B. G., Graesser, D. T., Frericks, H. L., Sahota, G., and Rienstra, C. M. *Journal of the American Chemical Society* **127**(35), 12291–12305 (2005).

[3] Igumenova, T. I., McDermott, A. E., Zilm, K. W., Martin, R. W., Paulson, E. K., and Wand, A. J. *Journal of the American Chemical Society* **126**(21), 6720–6727 (2004).

[4] Igumenova, T. I., Wand, A. J., and McDermott, A. E. *Journal of the American Chemical Society* **126**(16), 5323–5331 (2004).

[5] Seidel, K., Lange, A., Becker, S., Hughes, C. E., Heise, H., and Baldus, M. *Physical Chemistry Chemical Physics* **6**(22), 5090–5093 (2004).

[6] Lorch, M., Fahem, S., Kaiser, C., Weber, I., Mason, A. J., Bowie, J. U., and Glaubitz, C. *Chembiochem* **6**(9), 1693–1700 (2005).

[7] Castellani, F. *Nature* **420**, 98–102 (2002).

[8] Castellani, F., van Rossum, B. J., Diehl, A., Rehbein, K., and Oschkinat, H. *Biochemistry* **42**(39), 11476–11483 (2003).

[9] van Rossum, B. J., Castellani, F., Rehbein, K., Pauli, J., and Oschkinat, H. *Chembiochem* **2**(12), 906–914 (2001).

[10] Zech, S. G., Wand, A. J., and McDermott, A. E. *Journal of the American Chemical Society* **127**(24), 8618–8626 (2005).

[11] Ishii, Y. *Journal of Chemical Physics* **114**(19), 8473–8483 (2001).

[12] Petkova, A. T., Leapman, R. D., Yau, W. M., and Tycko, R. *Biophysical Journal* **86**(1), 506a–506a (2004).

[13] Heise, H., Hoyer, W., Becker, S., Andronesi, O. C., Riedel, D., and Baldus, M. *Proceedings of the National Academy of Sciences of the United States of America* **102**(44), 15871–15876 (2005).

[14] Siemer, A. B., Ritter, C., Ernst, M., Riek, R., and Meier, B. H. *Angewandte Chemie-International Edition* **44**(16), 2441–2444 (2005).

[15] Siemer, A. B., Ritter, C., Steinmetz, M. O., Ernst, M., Riek, R., and Meier, B. H. *Journal of Biomolecular NMR* **34**(2), 75–87 (2006).

[16] Hiller, M., Krabben, L., Vinothkumar, K. R., Castellani, F., van Rossum, B. J., Kuhlbrandt, W., and Oschkinat, H. *Chembiochem* **6**(9), 1679–1684 (2005).

[17] Lehner, I., Basting, D., Meyer, B., Haase, W., Manolikas, T., Kaiser, C., Karas, M., and Glaubitz, C. *J. Biol. Chem.* **283**(6), 3281 (2008).

[18] Luca, S. *Proceedings of the National Academy of Sciences of the United States of America* **100**(19), 10706–10711 (2003).

[19] Andronesi, O. *Journal of the American Chemical Society* **127**, 12965–12974 (2005).

[20] Etzkorn, M., Martell, S., Andronesi, O. C., Seidel, K., Engelhard, M., and Baldus, M. *Angewandte Chemie Intnational Edition Engl* **46**(3), 459–62 (2007).

[21] Hartmann, S. and Hahn, E. *Physical Reviews* **128**, 2042–2053 (1962).

[22] Morris, G. A. and Freeman, R. *Journal of the American Chemical Society* **101**(3), 760–762 (1979).

[23] Carravetta, M., Eden, M., Zhao, X., Brinkmann, A., and Levitt, M. H. *Chemical Physics Letters* **321**(3-4), 205–215 (2000).

[24] Brinkmann, A. and Levitt, M. H. *Journal of Chemical Physics* **115**(1), 357-384 (2001).

[25] Huster, D., Arnold, K., and Gawrisch, K. *Journal of Physical Chemistry B* **103**(1), 243–251 (1999).

[26] Meiboom, S. and Gill, D. *The Review of Scientific Instruments* **29**(2), 688–691 (1958).

[27] Bruschweiler, R. *Journal of Chemical Physics* **121**(1), 409–414 (2004).

[28] Bruschweiler, R. and Zhang, F. L. *Journal of Chemical Physics* **120**(11), 5253–5260 (2004).

[29] Prisner, T. and Kckenberger W. *Applied Magnetic Resonance* **34**(3-4), 213–218 (2008).

[30] Denysenkov V.P., Prandolini M.J. and Prisner T. *Applied Magnetic Resonance* **34**(3-4), 289–299 (2008).

[31] Prandolini M.J., Denysenkov V.P. and Prisner T. *Journal of the American Chemical Society* **131**(17), 6090–6092 (2009).

[32] Anet, F. A. L. and Bourn, A. J. R. *Journal of the American Chemical Society* **87**, 5250 (1965).

[33] Szeverenyi, N. M., Sullivan, M. J., and Maciel, G. E. *Journal of Magnetic Resonance* **47**(3), 462–475 (1982).

[34] Baldus, M., Iuliucci, R. J., and Meier, B. H. *Journal of the American Chemical Society* **119**(5), 1121–1124 (1997).

[35] Levitt, M. H. *Journal of Chemical Physics* **128**(5), 052205 (2008).

[36] Carravetta, M., Eden, M., Johannessen, O. G., Luthman, H., Verdegem, P. J. E., Lugtenburg, J., Sebald, A., and Levitt, M. H. *Journal of the American Chemical Society* **123**(43), 10628–10638 (2001).

[37] Brinkmann, A. and Levitt, M. H. *Journal of Chemical Physics* **115**(1), 357–384 (2001).

[38] Kristiansen, P. E., Carravetta, M., Lai, W. C., and Levitt, M. H. *Chemical Physics Letters* **390**(1-3), 1–7 (2004).

[39] Kristiansen, P. E., Carravetta, M., van Beek, J. D., Lai, W. C., and Levitt, M. H. *Journal of Chemical Physics* **124**(23), – (2006).

[40] Franks, W. T., Kloepper, K. D., Wylie, B. J., and Rienstra, C. M. *Journal of Biomolecular NMR* **39**(2), 107–31 (2007).

[41] Bajaj, V. S., Farrar, C. T., Hornstein, M. K., Mastovsky, I., Vieregg, J., Bryant, J., Elena, B., Kreischer, K. E., Temkin, R. J., and Griffin, R. G. *Journal of Magnetic Resonance* **160**(2), 85–90 (2003).

[42] Hu, K. N., Yu, H. H., Swager, T. M., and Griffin, R. G. *Journal of the American Chemical Society* **126**(35), 10844–5 (2004).

[43] Mak-Jurkauskas, M. L., Bajaj, V. S., Hornstein, M. K., Belenky, M., Griffin, R. G., and Herzfeld, J. *Proceedings of the National Academy of Sciences* **105**(3), 883–8 (2008).

[44] Rosay, M., Lansing, J. C., Haddad, K. C., Bachovchin, W. W., Herzfeld, J., Temkin, R. J., and Griffin, R. G. *Journal of the American Chemical Society* **125**(45), 13626–7 (2003).

[45] Rosay, M., Weis, V., Kreischer, K. E., Temkin, R. J., and Griffin, R. G. *Journal of the American Chemical Society* **124**(13), 3214–5 (2002).

[46] Linser, R., Chevelkov, V., Diehl, A., and Reif, B. *Journal of Magnetic Resonance* **189**(2), 209–16 (2007).

[47] Pintacuda, G., Giraud, N., Pierattelli, R., Bockmann, A., Bertini, I., and Emsley, L. *Angewandte Chemie-International Edition* **46**(7), 1079–1082 (2007).

[48] Trbovic, N., Smirnov, S., Zhang, F. L., and Bruschweiler, R. *Journal of Magnetic Resonance* **171**(2), 277–283 (2004).

[49] Zhang, F. L. and Bruschweiler, R. *Chemphyschem* **5**(6), 794–796 (2004).

[50] Zhang, F. L. and Bruschweiler, R. *Angewandte Chemie-International Edition* **46**(15), 2639–2642 (2007).

[51] Blinov, K. A., Larin, N. I., Kvasha, M. P., Moser, A., Williams, A. J., and Martin, G. E. *Magnetic Resonance in Chemistry* **43**(12), 999–1007 (2005).

[52] Zhang, F. L. and Bruschweiler, R. *Journal of the American Chemical Society* **126**(41), 13180–13181 (2004).

[53] Zhang, F. L., Trbovic, N., Wang, J. B., and Bruschweiler, R. *Journal of Magnetic Resonance* **174**(2), 219–222 (2005).

[54] Main, J. Taylor, H. S. *Journal of Physics A* **33**, 1247–1263 (2000).

[55] Kunikeev, S., T. H. S. *Journal of Physical Chemistry A* **108**, 743–753 (2004).

[56] Kunikeev, S., M. C. *Journal of Organometallic Chemistry* **690**, 2644–2650 (2005).

[57] Kaiser, C., L. J. B. W. G. C. *Biochimica et Biophysica Acta* **1768**, 3107–3115 (2007).

[58] Hong, M., G. R. G. *Journal of the American Chemical Society* **120**, 7113–7114 (1998).

[59] Rienstra, C. M., Hohwy, M., Hong, M., and Griffin, R. G. *Journal of the American Chemical Society* **122**(44), 10979–10990 (2000).

[60] Schanda, P., B. B. *Journal of the American Chemical Society* **127**, 8014–8015 (2005).

[61] Schanda, P., B. B. *Journal of Biomolecular NMR* **33**, 199–211 (2005).

[62] Schanda, P., B. B. *Journal of the American Chemical Society* **128**, 9042–9043 (2006).

[63] Friedrich, J., F. R. *Journal of Magnetic Resonance* **75**, 390 (1987).

[64] Emsley, L. and Bodenhausen, G. *Chemical Physics Letters* **165**(6), 469–476 (1990).

[65] Asami, S. Diploma Thesis J.W. Goethe University, Frankfurt (2008).

[66] Schaefer, J., Mckay, R. A., and Stejskal, E. O. *Journal of Magnetic Resonance* **34**(2), 443–447 (1979).

[67] Baldus, M., Geurts, D. G., Hediger, S., and Meier, B. H. *Journal of Magnetic Resonance Series A* **118**(1), 140–144 (1996).

[68] Baldus, M., Petkova, A. T., Herzfeld, J., and Griffin, R. G. *Molecular Physics* **95**(6), 1197–1207 (1998).

[69] Gullion, T., S. J. *Journal of Magnetic Resonance* **81**, 196 (1989).

[70] Pines, A., Gibby, M. G., and Waugh, J. S. *Journal of Chemical Physics* **59**(2), 569–590 (1973).

[71] Katoh, E., Takegoshi, K., and Terao, T. *Journal of the American Chemical Society* **126**(11), 3653–7 (2004).

[72] Takegoshi, K. and Terao, T. *Journal of Chemical Physics* **117**(4), 1700–1707 (2002).

[73] Elena, B., Lesage, A., Steuernagel, S., Bockmann, A., and Emsley, L. *Journal of the American Chemical Society* **127**(49), 17296–17302 (2005).

[74] Lee, Y. K., Kurur, N. D., Helmle, M., Johannessen, O. G., Nielsen, N. C., and Levitt, M. H. *Chemical Physics Letters* **242**(3), 304–309 (1995).

[75] Zhao, X., Hoffbauer, W., auf der Gunne, J. S., and Levitt, M. H. *Solid State Nuclear Magnetic Resonance* **26**(2), 57–64 (2004).

[76] Hohwy, M., Jakobsen, H. J., Eden, M., Levitt, M. H., and Nielsen, N. C. *Journal of Chemical Physics* **108**(7), 2686–2694 (1998).

[77] Nagle, J. *Annual Reviews Physical Chemistry* **31**, 157–195 (1980).

[78] Bak, M. *Journal of Magnetic Resonance* **147**, 296–330 (2000).

[79] Vosegaard, T., Malmendal, A., and Nielsen, N. C. *Monatshefte Fuer Chemie* **133**(12), 1555–1574 (2002).

[80] Fung, B. M., Khitrin, A. K., and Ermolaev, K. *Journal of Magnetic Resonance* **142**(1), 97–101 (2000).

[81] Takegoshi, K., Nakamura, S., and Terao, T. *Chemical Physics Letters* **344**(5-6), 631–637 (2001).

[82] Lange, A., Luca, S., and Baldus, M. *Journal of the American Chemical Society* **124**(33), 9704–9705 (2002).

[83] Lopez, J. J., Shukla, A. K., Reinhart, C., Schwalbe, H., Michel, H., and Glaubitz, C. *Angewandte Chemie International Edition English* **47**(9), 1668–71 (2008).

[84] Lehner, I., Basting, D., Meyer, B., Haase, W., Manolikas, T., Kaiser, C., Karas, M., and Glaubitz, C. *Journal of Biological Chemistry* **283**(6), 3281–8 (2008).

[85] Creuzet, F., Mcdermott, A., Gebhard, R., Vanderhoef, K., Spijkerassink, M. B., Herzfeld, J., Lugtenburg, J., Levitt, M. H., and Griffin, R. G. *Science* **251**(4995), 783–786 (1991).

[86] Guo, W., Groesbeek, M., Salmon, A., Smith, S. O., and Hamilton, J. A. *Biophys J* **70**(2), Su326–Su326 (1996).

[87] Creemers, A. F. L., Kiihne, S., Bovee-Geurts, P. H. M., DeGrip, W. J., Lugtenburg, J., and de Groot, H. J. M. *Proceedings of the National Academy of Sciences* **99**(14), 9101–9106 (2002).

[88] Weliky, D. P., Bennett, A. E., Zvi, A., Anglister, J., Steinbach, P. J., and Tycko, R. *Nature Structural Biology* **6**(2), 141–145 (1999).

[89] Bax, A., Freeman, R., and Kempsell, S. P. *Journal of the American Chemical Society* **102**(14), 4849–4851 (1980).

[90] Munowitz, M. and Pines, A. *Science* **233**(4763), 525–531 (1986).

[91] Munowitz, M. and Pines, A. *Adv Chem Phys* **66**, 1–152 (1987).

[92] Munowitz, M., Pines, A., and Mehring, M. *Journal of Chemical Physics* **86**(6), 3172–3182 (1987).

[93] Kaiser, C., Lopez, J., Shastri, S., and Glaubitz, C. *Journal of Biomolecular NMR* **41**(2), 97–104 (2008).

[94] Hohwy, M., Rienstra, C. M., Jaroniec, C. P., and Griffin, R. G. *Journal of Chemical Physics* **110**(16), 7983–7992 (1999).

[95] Lee, M. and Goldburg, W. I. *Physical Review* **140**(4A), 1261 (1965).

[96] Vinogradov, E., Madhu, P. K., and Vega, S. *Chemical Physics Letters* **314**(5-6), 443–450 (1999).

[97] Bodenhausen, G., Kogler, H., and Ernst, R. R. *Journal of Magnetic Resonance* **58**(3), 370–388 (1984).

[98] Keller, R., Grace, C. R. R., and Riek, R. *Magnetic Resonance in Chemistry* **44**, S196–S205 (2006).

[99] Jones, E., Oliphant, T., and Peterson, P. (2002).

[100] Shastri, S., Vonck, J., Pfleger, N., Haase, W., Kuehlbrandt, W., and Glaubitz, C. *Biochim Biophys Acta* **1768**(12), 3012–9 (2007).

[101] Hong, M., Gross, J. D., Rienstra, C. M., Griffin, R. G., Kumashiro, K. K., and Schmidt-Rohr, K. *Journal of Magnetic Resonance* **129**(1), 85–92 (1997).

[102] Rienstra, C. M., Tucker-Kellogg, L., Jaroniec, C. P., Hohwy, M., Reif, B., McMahon, M. T., Tidor, B., Lozano-Perez, T., and Griffin, R. G. *Proceedings of the National Academy of Sciences* **99**(16), 10260–5 (2002).

[103] Ratnala, V. R., Kiihne, S. R., Buda, F., Leurs, R., de Groot, H. J., and DeGrip, W. J. *Journal of the American Chemical Society* **129**(4), 867–72 (2007).

[104] Larsen, F. H., Jakobsen, H. J., Ellis, P. D., and Nielsen, N. C. *Journal of Physical Chemistry A* **101**, 8597–8606 (1997).

[105] Frydman, L. *Proceedings of the National Academy of Sciences* **99**(25), 15858–15862 (2002).

[106] Frydman, L., Lupulescu, A., and Scherf, T. *Journal of the American Chemical Society* **125**(30), 9204–9217 (2003).

[107] Blechta, V. and Freeman, R. *Chemical Physics Letters* **215**(4), 341–346 (1993).

[108] Kupce, E., Nishida, T., and Freeman, R. *Progress in Nuclear Magnetic Resonance Spectroscopy* **42**(3-4), 95–122 (2003).

[109] Ziessow, D. and Blumich, B. *Berichte Der Bunsen-Gesellschaft-Physical Chemistry Chemical Physics* **78**(11), 1168–1179 (1974).

[110] Szyperski, T., Luginbuhl, P., Otting, G., Guntert, P., and Wuthrich, K. *Journal of Biomolecular NMR* **3**(2), 151–164 (1993).

[111] Ding, K. Y. and Gronenborn, A. M. *Journal of Magnetic Resonance* **156**(2), 262–268 (2002).

[112] Kupce, E. and Freeman, R. *Journal of the American Chemical Society* **126**(20), 6429–6440 (2004).

[113] Barna, J. C. J., Laue, E. D., Mayger, M. R., Skilling, J., and Worrall, S. J. P. *Journal of Magnetic Resonance* **73**(1), 69–77 (1987).

[114] Marion, D. *Journal of Biomolecular NMR* **32**(2), 141–150 (2005).

[115] Schmieder, P., Stern, A. S., Wagner, G., and Hoch, J. C. *Journal of Biomolecular NMR* **3**(5), 569–576 (1993).

[116] Stern, A. S., Li, K. B., and Hoch, J. C. *Journal of the American Chemical Society* **124**(9), 1982–1993 (2002).

[117] Tugarinov, V., Kay, L. E., Ibraghimov, I., and Orekhov, V. Y. *Journal of the American Chemical Society* **127**(8), 2767–2775 (2005).

[118] Chen, Y. B., Zhang, F. L., Bermel, W., and Bruschweiler, R. *Journal of the American Chemical Society* **128**(49), 15564–15565 (2006).

[119] Eric Jones, Travis Oliphant, P. P. et al. (2001).

[120] Regoli, D. and Barabe, J. *Pharmacological Reviews* **32**(1), 1–46 (1980).

[121] Delaglio, F., Grzesiek, S., Vuister, G. W., Zhu, G., Pfeifer, J., and Bax, A. *Journal of Biomolecular NMR* **6**(3), 277–293 (1995).

[122] Pieringe, R. and Kunnes, R. S. *Journal of Biological Chemistry* **240**(7), 2833 (1965).

[123] Lightner, V. A., Bell, R. M., and Modrich, P. *Journal of Biological Chemistry* **258**(18), 856–861 (1983).

[124] Loomis, C. R., Walsh, J. P., and Bell, R. M. *Journal of Biological Chemistry* **260**(7), 4091–4097 (1985).

[125] Raetz, C. R. H. and Newman, K. F. *Journal of Biological Chemistry* **253**(11), 3882–3887 (1978).

[126] Smith, R. L., Otoole, J. F., Maguire, M. E., and Sanders, C. R. *Journal of Bacteriology* **176**(17), 5459–5465 (1994).

[127] Sanders, C. R., Czerski, L., Vinogradova, O., Badola, P., Song, D., and Smith, S. O. *Biochemistry* **35**(26), 8610–8618 (1996).

[128] Oxenoid, K., Sonnichsen, F. D., and Sanders, C. R. *Biochemistry* **41**(42), 12876–12882 (2002).

[129] Badola, P. and Sanders, C. R. *Journal of Biological Chemistry* **272**(39), 24176–24182 (1997).

[130] Lau, F. W., Chen, X., and Bowie, J. U. *Biochemistry* **38**(17), 5521–5527 (1999).

[131] Luchette, P. A., Prosser, R. S., and Sanders, C. R. *Journal of the American Chemical Society* **124**(8), 1778–1781 (2002).

[132] Vinogradova, O., Badola, P., Czerski, L., Sonnichsen, F. D., and Sanders, C. R. *Biophysical Journal* **72**(6), 2688–2701 (1997).

[133] Nagy, J. K., Lau, F. W., Bowie, J. U., and Sanders, C. R. *Biochemistry* **39**(14), 4154–4164 (2000).

[134] Oxenoid, K., Kirn, H. J., Jacob, J., Sonnichsen, F. D., and Sanders, C. R. *Journal of the American Chemical Society* **126**(16), 5048–5049 (2004).

[135] Lau, F. W. and Bowie, J. U. *Biochemistry* **36**(19), 5884–5892 (1997).

[136] Gorzelle, B. M., Nagy, J. K., Oxenoid, K., Lonzer, W. L., Cafiso, D. S., and Sanders, C. R. *Biochemistry* **38**(49), 16373–16382 (1999).

[137] Walsh, J. P. and Bell, R. M. *Journal of Biological Chemistry* **261**(14), 6239–6247 (1986).

[138] Walsh, J. P. and Bell, R. M. *Journal of Biological Chemistry* **261**(32), 5062–5069 (1986).

[139] Walsh, J. P., Fahrner, L., and Bell, R. M. *Journal of Biological Chemistry* **265**(8), 4374–4381 (1990).

[140] Nagy, J. K., Lonzer, W. L., and Sanders, C. R. *Biochemistry* **40**(30), 8971–8980 (2001).

[141] Vinogradova, O., Sonnichsen, F., and Sanders, C. R. *Journal of Biomolecular NMR* **11**(4), 381–386 (1998).

[142] Pilot, J. D., East, J. M., and Lee, A. G. *Biochemistry* **40**(28), 8188–8195 (2001).

[143] Pilot, J. D., East, J. M., and Lee, A. G. *Biochemistry* **40**(49), 14891–14897 (2001).

[144] Nagy, J. K., Hoffmann, A. K., Keyes, M. H., Gray, D. N., Oxenoid, K., and Sanders, C. R. *Febs Letters* **501**(2-3), 115–120 (2001).

[145] Nagy, J. K. and Sanders, C. R. *Biochemistry* **41**(29), 9021–9025 (2002).

[146] Nagy, J. K. and Sanders, C. R. *Biochemistry* **43**(1), 19–25 (2004).

[147] Zhou, Y. F. and Bowie, J. U. *Journal of Biological Chemistry* **275**(10), 6975–6979 (2000).

[148] Raetz, C. R. H., Kantor, G. D., Nishijima, M., and Jones, M. L. *Journal of Biological Chemistry* **256**(5), 2109–2112 (1981).

[149] Yamaguchi, S., Tuzi, S., Bowie, J. U., and Saito, H. *Biochimica Et Biophysica Acta-Proteins and Proteomics* **1698**(1), 97–105 (2004).

[150] Wen, J. A., Chen, X., and Bowie, J. U. *Nature Structural Biology* **3**(2), 141–148 (1996).

[151] Shastri, S. *PhD Thesis.* PhD thesis, J.W. Goethe University, Frankfurt/Main, (2008).

[152] Sanders, C. structbio.vanderbilt.edu/sanders/Resources/.

[153] Shastri, S. (2008)

[154] Czerski, L. and Sanders, C. R. *Analytical Biochemistry* **284**(2), 327–333 (2000).

[155] Hong, M. *Journal of Biomolecular NMR* **15**(1), 1–14 (1999).

[156] Atreya, H. S. and Chary, K. V. R. *Current Science* **79**(4), 504–507 (2000).

[157] Putter, I., Barreto, A., Markley, J. L., and Jardetzk.O. *Proceedings of the National Academy of Sciences* **64**(4), 1396 (1969).

[158] Arrowsmith, C. H., Pachter, R., Altman, R. B., Iyer, S. B., and Jardetzky, O. *Biochemistry* **29**(27), 6332–6341 (1990).

[159] Reisman, J. M., Hsu, V. L., Jarielencontre, I., Lecou, C., Sayre, M. H., Kearns, D. R., and Parello, J. *European Journal of Biochemistry* **213**(2), 865–873 (1993).

[160] Hardy, E. H., Verel, R., and Meier, B. H. *Journal of Magnetic Resonance* **148**(2), 459–464 (2001).

[161] Hardy, E. H., Detken, A., and Meier, B. H. *Journal of Magnetic Resonance* **165**(2), 208–218 (2003).

[162] White, J. L. and Haw, J. F. *Journal of the American Chemical Society* **112**(15), 5896–5898 (1990).

[163] Higgins, J. S., Hodgson, A. H., and Law, R. V. *Journal of Molecular Structure* **602**, 505–510 (2002).

[164] Takegoshi, K. and Terao, T. *Journal of Chemical Physics* **117**(4), 1700–1707 (2002).

[165] Katoh, E., Takegoshi, K., and Terao, T. *Journal of the American Chemical Society* **126**(11), 3653–3657 (2004).

[166] Hansen, P. E. *Magnetic Resonance in Chemistry* **38**(1), 1–10 (2000).

[167] Kaiser, C. Diploma Thesis J.W. Goethe University, Frankfurt (2004).